



LUND UNIVERSITY

Excited state dynamics in low-dimensional perovskite nanocrystals

Lin, Weihua

2022

[Link to publication](#)

Citation for published version (APA):

Lin, W. (2022). *Excited state dynamics in low-dimensional perovskite nanocrystals*. Chemical Physics, Lund University.

Total number of authors:

1

General rights

Unless other specific re-use rights are stated the following general rights apply:

Copyright and moral rights for the publications made accessible in the public portal are retained by the authors and/or other copyright owners and it is a condition of accessing publications that users recognise and abide by the legal requirements associated with these rights.

- Users may download and print one copy of any publication from the public portal for the purpose of private study or research.
- You may not further distribute the material or use it for any profit-making activity or commercial gain
- You may freely distribute the URL identifying the publication in the public portal

Read more about Creative commons licenses: <https://creativecommons.org/licenses/>

Take down policy

If you believe that this document breaches copyright please contact us providing details, and we will remove access to the work immediately and investigate your claim.

LUND UNIVERSITY

PO Box 117
221 00 Lund
+46 46-222 00 00

Excited state dynamics in low-dimensional perovskite nanocrystals

WEIHUA LIN

CHEMICAL PHYSICS | FACULTY OF SCIENCE | LUND UNIVERSITY

We are so excited!



Excited state dynamics in low-dimensional perovskite nanocrystals

Excited state dynamics in low-dimensional perovskite nanocrystals

Weihua Lin



LUND
UNIVERSITY

DOCTORAL DISSERTATION

Doctoral dissertation for the degree of Doctor of Philosophy (Ph.D.) at the Faculty of Science at Lund University to be publicly defended on 29 November 2022 at 9.15 am. in Lecture Hall A of Kemicentrum, Department of Chemistry, Naturvetarvägen 16, 22362 Lund

Faculty opponent

Dr. Matthew C. Beard

National Renewable Energy Laboratory, United States

Organization LUND UNIVERSITY Division of Chemical Physics Department of Chemistry P. O. BOX 124, SE-22100 Lund, Sweden		Document name Doctoral Dissertation
Author(s) Weihua Lin		Date of issue 29th November 2022
Title and subtitle Excited state dynamics in low-dimensional perovskite nanocrystals		Sponsoring organization
Abstract Two-dimensional (2D) perovskites have emerged as promising building blocks for optoelectronic applications. To fabricate high-performance devices, the relation between the material structures and their function in terms of excited state and charge carrier dynamics need to be well understood. In this thesis, we investigate photophysics of 2D lead halide perovskite with different compositions to reveal the relation between lattice distortion and electronic properties. Firstly, we found that the threshold of the Goldschmidt tolerance factor is relaxed and thereby the range of possible composition for forming stable 2D perovskite is extended compared to 3D perovskite. In addition, lattice distortion is greater when containing large cations inside octahedral cages and the formed 2D perovskite has a larger band gap and higher trap state density. The link between lattice distortion and modification of electronic structure shows a potential approach to designing and developing high-performance PV materials. To further evaluate the influence of local lattice distortion on the electronic properties of 2D perovskite, we analyze fluorescence signals from different facets of samples with different spacers. We found that free carriers dominate in the in-plane facet (IF) while self-trapped excitons (STE) are the main emitters from the facet perpendicular to the 2D layer (PF). The strain accumulated along the 2D layers leads to enhanced carrier-phonon coupling and facilitates STE formation in PF, while in IF the separated flexible spacers contribute to releasing the strain accumulation. To directly characterize the electronic structure at different areas of a 2D perovskite single crystal, electrons emitted from Pb 5d and I 4d core levels are mapped at the edge and the bulk areas by using X-ray photoemission electron microscopy. The observed asymmetric shifts of the emission spectra of 2D perovskite indicate different degrees of lattice distortion at the edge and the bulk areas since the internal strain accumulation is released at the edge area. The different shift in Pb 5d core level emission between edge and bulk areas at 2D perovskites with different layer thickness confirms the contribution of spacers in releasing accumulated strain. In addition, we investigated the ultrafast hot carrier (HC) relaxation dynamics in 2D perovskite single crystals by employing transient absorption (TA) spectroscopy and time-resolved two-photon photoemission (TR-2PPE) spectroscopy. With TR-2PPE, the distribution of hot electrons and their dynamics in the conduction band can be directly visualized. The different cooling rates of HC observed in the two techniques reflect the spatial sensitivity of relaxation dynamics across the 2D perovskite single crystal. We believe the comprehensive study on HC relaxation in 2D perovskite provides an effective approach to compare the potential of different materials in hot carrier solar cell (HCSC) applications and can extend thermoelectric applications based on 2D perovskites. We also investigated the influence of transition metal doping on electronic and phononic features of three-dimensional perovskite by studying the HC relaxation processes in Mn ²⁺ -doped and undoped CsPbI ₃ nanocrystals (NCs). The Mn ²⁺ doping leads to the enlarged phononic gap between longitudinal optical (LO) – acoustic phonons, enhanced carrier-LO phonon coupling strength, and additional Mn orbitals within the original bands of the undoped sample, which are beneficial for establishing a hot quasi-equilibrium to recycle the energy from HC relaxation to reheat cold carriers. The results present a methodology to optimize HC dynamics by element doping and are meaningful for guiding the future development of HCSC applications.		
Keywords Two-dimensional perovskite, Ultrafast spectroscopy, Single crystal, Nanocrystals, Hot carrier cooling		
Classification system and/or index terms (if any)		
Supplementary bibliographical information		Language English
ISSN and key title		ISBN Printed version: 978-91-7422-916-5 Digital version: 978-91-7422-917-2
Recipient's notes	Number of pages 74	Price
	Security classification	

I, the undersigned, being the copyright owner of the abstract of the above-mentioned dissertation, hereby grant to all reference sources permission to publish and disseminate the abstract of the above-mentioned dissertation.

Signature *weihua Lin*

Date 19th October 2022

Excited state dynamics in low-dimensional perovskite nanocrystals

Weihua Lin



LUND
UNIVERSITY

Coverphoto by Juanzi Shi and Weihua Lin

Copyright pp i-74 © Weihua Lin

Paper 1 © 2022 The Authors.

Paper 2 © 2020 American Chemical Society.

Paper 3 © 2021 The Authors, licensed under CC-BY 4.0. Published by American Chemical Society.

Paper 4 © 2022 The Authors, licensed under CC-BY 3.0. Published by Royal Society of Chemistry.

Paper 5 © 2022 The Authors.

Faculty of Science
Department of Chemistry

ISBN

978-91-7422-916-5 (Print)

978-91-7422-917-2 (Digital)

Printed in Sweden by Media-Tryck, Lund University
Lund 2022



Media-Tryck is a Nordic Swan Ecolabel certified provider of printed material. Read more about our environmental work at www.mediatryck.lu.se

MADE IN SWEDEN 

Table of Contents

Abstract	i
Popular Science Summary	iii
Acknowledgement	v
List of Publications	vii
Abbreviations	xii
1 Introduction	1
1.1 Solar Cell	1
1.2 Metal Halide Perovskite	3
1.2.1 Three-Dimensional Perovskite	4
1.2.2 Two-Dimensional Perovskite	6
1.3 Hot Carrier Relaxation.....	8
1.3.1 General Pathway of Hot Carrier Cooling	8
1.3.2 Mechanisms for Slowing Down Hot Carrier Relaxation.....	12
2 Experimental Methods	21
2.1 Time-Correlated Single Photon Counting	21
2.2 Transient Absorption Spectroscopy.....	25
2.3 Time-Resolved Two-Photon Photoemission Spectroscopy.....	28
3 Results and Discussion	33
3.1 Electronic Structure and Trap States of Two-Dimensional Perovskite Single Crystal – Paper II	33
3.2 Free Carriers and Self-trapped Excitons at Different Facets of Two-Dimensional Perovskite Single Crystal – Paper III.....	37
3.3 Local Electronic Properties of Two-Dimensional Perovskite Single Crystal – Paper V	42
3.4 Hot Carrier Cooling in Two-Dimensional Perovskite Single Crystal – Paper I	46
3.5 Hot Carrier Cooling in Mn-Doped Inorganic Perovskite Nanocrystals– Paper IV	51

4	Conclusions	57
	References	61

Abstract

Two-dimensional (2D) perovskites have emerged as promising building blocks for optoelectronic applications. To fabricate high-performance devices, the relation between the material structures and their function in terms of excited state and charge carrier dynamics need to be well understood.

In this thesis, we investigated photophysics of 2D lead halide perovskite with different compositions to reveal the relation between lattice distortion and electronic properties. Firstly, we found that the threshold of the Goldschmidt tolerance factor is relaxed and thereby the range of possible composition for forming stable 2D perovskite is extended compared to 3D perovskite. In addition, lattice distortion is greater when containing large cations inside octahedral cages and the formed 2D perovskite has a larger band gap and higher trap state density. The link between lattice distortion and modification of electronic structure shows a potential approach to designing and developing high-performance PV materials. To further evaluate the influence of local lattice distortion on the electronic properties of 2D perovskite, we analyzed fluorescence signals from different facets of samples with different spacers. We found that free carriers dominate in the in-plane facet (IF) while self-trapped excitons (STE) are the main emitters from the facet perpendicular to the 2D layer (PF). The strain accumulated along the 2D layers leads to enhanced carrier-phonon coupling and facilitates STE formation in PF, while in IF the separated flexible spacers contribute to releasing the strain accumulation. To directly characterize the electronic structure at different areas of a 2D perovskite single crystal, electrons emitted from Pb $5d$ and I $4d$ core levels are mapped at the edge and the bulk areas by using X-ray photoemission electron microscopy. The observed asymmetric shifts of the emission spectra of 2D perovskite indicate different degrees of lattice distortion at the edge and the bulk areas since the internal strain accumulation is released at the edge area. The different shift in Pb $5d$ core level emission between edge and bulk areas at 2D perovskites with different layer thickness confirms the contribution of spacers in releasing accumulated strain.

In addition, we investigated the ultrafast hot carrier (HC) relaxation dynamics in 2D perovskite single crystals by employing transient absorption (TA) spectroscopy and time-resolved two-photon photoemission (TR-2PPE) spectroscopy. With TR-2PPE, the distribution of hot electrons and their dynamics in the conduction band can be directly visualized. The different cooling rates of HC observed in the two techniques reflect the spatial sensitivity of relaxation dynamics across the 2D perovskite single

crystal. We believe the comprehensive study on HC relaxation in 2D perovskite provides an effective approach to compare the potential of different materials in hot carrier solar cell (HCSC) applications and can extend thermoelectric applications based on 2D perovskites. We also investigated the influence of transition metal doping on electronic and phononic features of three-dimensional perovskite by studying the HC relaxation processes in Mn^{2+} -doped and undoped CsPbI_3 nanocrystals (NCs). The Mn^{2+} doping leads to the enlarged phononic gap between longitudinal optical (LO) -acoustic phonons, enhanced carrier-LO phonon coupling strength, and additional Mn orbitals within the original bands of the undoped sample, which are beneficial for establishing a hot quasi-equilibrium to recycle the energy from HC relaxation to reheat cold carriers. The results present a methodology to optimize HC dynamics by element doping and are meaningful for guiding the future development of HCSC applications.

Popular Science Summary

For a more sustainable future, we need to switch to renewable energy sources, and utilizing solar energy is a promising and realistic long-term solution. The record for power conversion efficiency of solar cells has grown steadily in the past whilst with insufficient speed. Alternative solar technologies which can radically boost the device performance are desired in the field, with refreshing strategies for harvesting and storing solar energy. Many new solar technologies are proposed for exceeding the Shockley-Queisser limit, such as multiple exciton generation, singlet exciton fission and hot carrier (HC, carriers with excess energy) injection. The latter is closely related to hot carrier solar cells (HCSC), whose fundamental idea is to recycle the energy from HC relaxation before heat dissipation. A key to fabricating high-quality HCSC devices is finding a suitable absorber material.

Metal halide perovskite is an up-rising star in solar cell applications, and it has many outstanding photophysics properties but suffers from poor stability towards moisture. By inserting the long-chain organic spacing cations in the structure, the two-dimensional perovskite can be formed with significantly improved stability. The hydrophobic spacers work like an umbrella preventing the penetration of water into the octahedral layers (unit cell of 3D perovskite). In addition, because the spacers are soft and flexible, the octahedral cage in 2D perovskite can contain larger or smaller cations (A-site cation), in comparison to the limited available A-site cations with fixed sizes to be chosen when forming stable 3D perovskite. We found that the too large A-site cations result in greater lattice distortion and lead to changes in the electronic properties of the material. We also found that flexible spacers contribute to compensating the strain accumulated in rigid octahedral layers. We prepared bulky single crystals of 2D perovskite with different spacers to further 'zoom in' to the spacer effects. The millimeter-scale samples enable us to measure photoluminescence (PL) signals from the surface of each targeted facet. The strain is accumulated along the octahedral layer and released to the edge, so that the degree of lattice distortion at the edge and bulk areas are different which will result in different interactions with the lattice. By comparing PL spectra from the facets parallel and perpendicular to the octahedral layer, we conclude that different charge carrier species dominate in the two facets and confirm that local structural distortion can modify the electronic structure of 2D perovskite. We also vary the thickness of octahedral layers in one unit cell of 2D perovskite, where one unit cell equals n -layers of octahedral layer sandwiched by spacing cations. But this time instead of

measuring the photophysics of sample and speculating the change in electronic structure, we directly map the electrons emitted from core levels of Pb and I atoms at different areas of single crystals. The results indicate that when each 2D unit only contains one or two octahedral layers, the contribution of spacers in compensating the accumulated strain is more efficient than when in the case with three octahedral layers. In conclusion, we conduct a series of investigations on 2D perovskite with different compositions and at different areas at single crystals to reveal the relation between structural distortion and electronic structure in 2D perovskite.

In addition, we use ultrafast spectroscopies to investigate the HC relaxation in 2D perovskite. The two techniques we used are transient absorption (TA) spectroscopy and time-resolved two-photon photoemission (TR-2PPE) spectroscopy. TA spectroscopy has been widely used in investigating 3D perovskite, but the standard analysis method is sometimes problematic. TR-2PPE spectroscopy, on the other hand, has many experimental demands but can provide direct visualization of hot electron distribution. By comparing the results obtained from these two techniques, we can reveal the different HC cooling dynamics across the 2D perovskite single crystal, which is beneficial for thermoelectric applications based on 2D perovskites in the future. In addition, we also investigated the effect of transition metal doping on the properties of 3D perovskite nanocrystals ($1 \text{ nm} = 10^{-9} \text{ m}$). The difference in HC relaxation rates observed in doped and undoped samples points out what we can expect from doping methodology on the path towards HCSCs.

Acknowledgement

After recalling the experience of the past four years, I feel very grateful and lucky that I come to Lund for my Ph.D. study. Although sometimes it feels like time has been stolen by the epidemic, I still have seen a lot of beautiful scenery in my life journey.

The Chapter Lund of the journey started with the first meeting with my supervisor Tõnu Pullerits in Beijing, when I was still doing the master project at the University of Science and Technology Beijing (USTB). Thank you for meeting with me and providing the opportunity for me to study abroad. I vaguely remember that during the meeting I was not able to talk in English fluently, but I am quite certain that I enjoyed the scientific discussion and the chat with you. I still can picture that day - you were drawing on a whiteboard to explain the physics to me, while I was sitting on the sofa trying to figure out what words you just said. During the four years of upgrading – next to the whiteboard in your office, I have learned a great many things from you and keep realizing there is more I can learn from you than I imagined.

I arrived in Lund on a Friday morning in September 2018 and met my co-supervisor Kaibo Zheng during Division Fika. The kind and friendly chat with Kaibo made me almost forget the discomfort caused by jet lag and felt excited about exploring Europe. Thank you for providing extensive help in scientific projects and tips about living in Lund, as well as including me in many group activities in Denmark. The first meeting with my mentor Eva Åkesson happened in December 2021, and we started arranging meetings every month afterward. Thank you for your patience and caring - listening to my problems and providing valuable suggestions every time, especially when I start writing the thesis and planning the defence. I have enjoyed each meeting and the relaxing atmosphere.

Thanks to all the people who have helped me during the past four years. Yang and Li, my ‘chef’ friend and gaming pal, thanks for all the joy you have brought in the first two years. Hope we can meet again soon and have fun like old times. Chen, Fan, Jingyuan and Xianshao, thanks for the company, helping me in my endless loop of moving-in and moving-out, and inviting me to various delightful activities. Qi, thanks for helping me settle down in Lund when I arrived and for all the life tips. Sol, thank you for all the happy hours we spent together in theme parks and for showing me around Copenhagen. Mingli and Jie, thank you for all the help with projects and valuable discussions. Zehan and Yue, thank you for helping in the

division kitchen and inviting me to your place. Thanks to my ‘tofu box’ mates, Albin, Edoardo A. and Linnea for all the fun times in our office and for inviting me to many other activities. Thanks to Alireza, Pavel and Torbjorn for the extensive help in the Millennia lab. Thanks to all members of Tõnu’s group, Zhengjun, Yanmei, Junsheng and Anurag for all the valuable group meetings and discussions. Thanks to all members of Kaibo’s group at the Technical University of Denmark (DTU), Qian and Qinying. Thanks to Shraddha, Romain, Chuanshuai, Yong, Sudipta, Lintang, Yen and Edoardo D. for all the delightful chatting in the division. Thanks to Donatas, Ivan, Arkady, Ebbe, Per and Jens for help and discussions in the course and seminars. Thanks to Maria for all the helpful emails during defence planning. I would like to also thank Sophie, Yuran, and all collaborators for helping with projects and extensive discussions.

Thanks to all the friends who have been helping in proofreading.

Juanzi, thank you for all the caring and support in work and in life, especially for giving me a push when I am unmotivated on writing the thesis. Looking forward to having more adventures with you.

My greatest thanks to my family, my parents, grandparents, aunts, uncles, cousins, niece and nephew. Your love teaches me how to embrace love and gives me the bravery to start new journey. A lot has happened at home since my last return, and it would be impossible for me to persevere in my Ph.D. study without your comfort and encouragement. I sincerely hope the reunion can happen soon in the future.

祝愿大家：身康体健，小得盈满。

List of Publications

This doctoral thesis is based on the following papers, which will be referred to in the text by their Roman numerals.

- I. Combining Two-Photon Photoemission and Transient Absorption Spectroscopy to Resolve Hot Carrier Cooling in 2D Perovskite Single Crystals: the Effect of Surface Layer

W. Lin[†], M. Liang[†], Y. Niu, Z. Chen, M. Cherasse, J. Meng, X. Zou, Q. Zhao, H. Geng, E. Papalazarou, M. Marsi, L. Perfetti, S. E. Canton, K. Zheng, T. Pullerits.

Accepted by *J. Mater. Chem. C.* (2022).

I developed a procedure for preparing 2D perovskite flakes, suitable for optical measurements and carried out transient absorption studies of the flakes. With help of co-authors we performed time-resolved two-photon photoemission spectroscopy and low-energy electron diffraction measurements. I analysed the data and discussed interpretation of the results with KZ and TP. I wrote the first version of the manuscript and participated in finalizing it.

- II. Electronic Structure and Trap States of Two-Dimensional Ruddlesden–Popper Perovskites with the Relaxed Goldschmidt Tolerance Factor

M. Liang[†], W. Lin[†], Z. Lan, J. Meng, Q. Zhao, X. Zou, I. E. Castelli, T. Pullerits, S. E. Canton, K. Zheng.

ACS Appl. Electron. Mater. **2020**, 2 (5), 1402-1412.

I carried out the optical measurements and performed the related analysis together with ML. I participated in the discussions and wrote parts of the article related to the Raman measurements.

III. Free Carriers versus Self-Trapped Excitons at Different Facets of Ruddlesden–Popper Two-Dimensional Lead Halide Perovskite Single Crystals

M. Liang, W. Lin, Q. Zhao, X. Zou, Z. Lan, J. Meng, Q. Shi, I. E. Castelli, S. E. Canton, T. Pullerits, K. Zheng.

J. Phys. Chem. Lett. **2021**, *12* (20), 4965-4971.

I performed optical measurements and related analyses together with ML.

IV. Optimizing the quasi-equilibrium state of hot carriers in all-inorganic lead halide perovskite nanocrystals through Mn doping: fundamental dynamics and device perspectives

J. Meng, Z. Lan, W. Lin, M. Liang, X. Zou, Q. Zhao, H. Geng, I. E. Castelli, S. E. Canton, T. Pullerits, K. Zheng.

Chem. Sci. **2022**, *13* (6), 1734-1745.

I performed transient absorption measurements and participated in the related discussions about the data interpretation.

V. Spatially Resolved Local Electronic Properties of Two-Dimensional Lead Halide Perovskite Single Crystals Studied by X-ray Photoemission Electron Microscopy

M. Liang[†], W. Lin[†], Q. Zhao, L. Zhu, B. Sarpi, A. Zakharov, T. Pullerits, Y. Niu, S. E. Canton, K. Zheng

Manuscript. (2022).

I performed the measurements together with ML under the supervision of the beamline scientist YN. I participate in the discussions and manuscript writing.

Publications not included in this thesis:

VI. Revisiting the structure and the carrier-dynamics of lead-free bismuth perovskite nanocrystals processed by a modified hot injection method

H. Geng, Z. Huang, H. Geng, S. Liu, M. A. Naumova, R. Salvia, S. Chen, J. Wei, L. Zhang, X. Zou, W. Lin, X. Cai, M. Yuan, Z. Hu, K. Zheng, X. Shen, R. Yu, S. E. Canton, X. Fu.

Manuscript. (2022).

- VII. N-doping of nonfullerene bulk-heterojunction organic solar cells strengthens photogeneration and exciton dissociation
J. Xie, W. Lin, G. C. Bazan, T. Pullerits, K. Zheng, Z. Liang.
J. Mater. Chem. A **2022**, DOI: 10.1039/d2ta05078a.
- VIII. Inorganic ligands-mediated hole attraction and surface structural reorganization in InP/ZnS QD photocatalysts studied via ultrafast visible and midinfrared spectroscopies
Y. Liu, Y. Zhou, M. Abdellah, W. Lin, J. Meng, Q. Zhao, S. Yu, Z. Xie, Q. Pan, F. Zhang, T. Pullerits, K. Zheng.
Sci. China Mater. **2022**, 65 (9), 2529–2539.
- IX. Ultrafast charge transfer dynamics in 2D covalent organic frameworks/Re-complex hybrid photocatalyst
Q. Pan, M. Abdellah, Y. Cao, W. Lin, Y. Liu, J. Meng, Q. Zhou, Q. Zhao, X. Yan, Z. Li, H. Cui, H. Cao, W. Fang, D. A. Tanner, M. Abdel-Hafiez, Y. Zhou, T. Pullerits, S. E. Canton, H. Xu, K. Zheng.
Nat. Commun. **2022**, 13, 845.
- X. Charge Carrier Diffusion Dynamics in Multisized Quaternary Alkylammonium-Capped CsPbBr₃ Perovskite Nanocrystal Solids
S. Gutiérrez Álvarez, W. Lin, M. Abdellah, J. Meng, K. Žídek, T. Pullerits, K. Zheng.
ACS Appl. Mater. Interfaces **2021**, 13 (37), 44742-44750.
- XI. The piezotronic effect on carrier recombination processes in InGaN/GaN multiple quantum wells microwire
X. Zou, J. Dong, K. Zhang, W. Lin, M. Guo, W. Zhang, X. Wang.
Nano Energy **2021**, 87, 106145.
- XII. Manipulating crystallization dynamics through chelating molecules for bright perovskite emitters
Y. Zou, P. Teng, W. Xu, G. Zheng, W. Lin, J. Yin, L. Kobera, S. Abbrent, X. Li, J. A. Steele, E. Solano, M. B. J. Roeffaers, J. Li, L. Cai, C. Kuang, I. G. Scheblykin, J. Brus, K. Zheng, Y. Yang, O. F. Mohammed, O. M. Bakr, T. Pullerits, S. Bai, B. Sun, F. Gao.
Nat. Commun. **2021**, 12, 4831.

- XIII. Ultrafast Spectroelectrochemistry Reveals Photoinduced Carrier Dynamics in Positively Charged CdSe Nanocrystals
A. Honarfar, P. Chabera, W. Lin, J. Meng, H. Mourad, G. Pankratova, L. Gorton, K. Zheng, T. Pullerits.
J. Phys. Chem. C **2021**, *125* (26), 14332-14337.
- XIV. Graphitic Carbon Nitride/CdSe Quantum Dot/Iron Carbonyl Cluster Composite for Enhanced Photocatalytic Hydrogen Evolution
C. Li, X. Zou, W. Lin, H. Mourad, J. Meng, Y. Liu, M. Abdellah, M. Guo, K. Zheng, E. Nordlander.
ACS Appl. Nano Mater. **2021**, *4* (6), 6280-6289.
- XV. Mixed halide perovskites for spectrally stable and high-efficiency blue light-emitting diodes
M. Karlsson, Z. Yi, S. Reichert, X. Luo, W. Lin, Z. Zhang, C. Bao, R. Zhang, S. Bai, G. Zheng, P. Teng, L. Duan, Y. Lu, K. Zheng, T. Pullerits, C. Deibel, W. Xu, R. Friend, F. Gao.
Nat. Commun. **2021**, *12*, 361.
- XVI. Manganese doped eco-friendly CuInSe₂ colloidal quantum dots for boosting near-infrared photodetection performance
R. Guo, J. Meng, W. Lin, A. Liu, T. Pullerits, K. Zheng, J. Tian.
Chem. Eng. J. **2021**, *403*, 126452.
- XVII. Photoexcitation Dynamics in Electrochemically Charged CdSe Quantum Dots: From Hot Carrier Cooling to Auger Recombination of Negative Trions
A. Honarfar, H. Mourad, W. Lin, A. Polukeev, A. Rahaman, M. Abdellah, P. Chábera, G. Pankratova, L. Gorton, K. Zheng, T. Pullerits.
ACS Appl. Energy Mater. **2020**, *3* (12), 12525-12531.
- XVIII. Exploring the light-induced dynamics in solvated metallogrid complexes with femtosecond pulses across the electromagnetic spectrum
M. A. Naumova, A. Kalinko, J. W. L. Wong, S. Alvarez Gutierrez, J. Meng, M. Liang, M. Abdellah, H. Geng, W. Lin, K. Kubicek, M. Biednov, F. Lima, A. Galler, P. Zalden, S. Checchia, P.-A. Mante, J. Zimara, D. Schwarzer, S. Demeshko, V. Murzin, D. Gosztoła, M. Jarenmark, J. Zhang, M. Bauer, M. L. Lawson Daku, D. Khakhulin, W. Gawelda, C. Bressler, F. Meyer, K. Zheng, S. E. Canton.
J. Chem. Phys. **2020**, *152* (21), 214301.

- XIX. Mechanistic Investigation into Dynamic Function of Third Component Incorporated in Ternary Near-Infrared Nonfullerene Organic Solar Cells
Z. Wang, J. Ji, W. Lin, Y. Yao, K. Zheng, Z. Liang.
Adv. Funct. Mater. **2020**, *30* (31), 2001564.
- XX. Modulating Charge-Carrier Dynamics in Mn-Doped All-Inorganic Halide Perovskite Quantum Dots through the Doping-Induced Deep Trap States
J. Meng, Z. Lan, M. Abdellah, B. Yang, S. Mossin, M. Liang, M. Naumova, Q. Shi, S. L. Gutierrez Alvarez, Y. Liu, W. Lin, I. E. Castelli, S. E. Canton, T. Pullerits, K. Zheng.
J. Phys. Chem. Lett. **2020**, *11* (9), 3705-3711.
- XXI. Electron Transfer Mediated by Iron Carbonyl Clusters Enhance Light-Driven Hydrogen Evolution in Water by Quantum Dots
C. Li, A. Rahaman, W. Lin, H. Mourad, J. Meng, A. Honarfar, M. Abdellah, M. Guo, M. G. Richmond, K. Zheng, E. Nordlander.
ChemSusChem **2020**, *13* (12), 3252-3260.
- XXII. Revealing Hot and Long-Lived Metastable Spin States in the Photoinduced Switching of Solvated Metallogrid Complexes with Femtosecond Optical and X-ray Spectroscopies
M. A. Naumova, A. Kalinko, J. W. L. Wong, M. Abdellah, H. Geng, E. Domenichini, J. Meng, S. A. Gutierrez, P.-A. Mante, W. Lin, P. Zalden, A. Galler, F. Lima, K. Kubicek, M. Biednov, A. Britz, S. Checchia, V. Kabanova, M. Wulff, J. Zimara, D. Schwarzer, S. Demeshko, V. Murzin, D. Gosztola, M. Jarenmark, J. Zhang, M. Bauer, M. L. Lawson Daku, W. Gawelda, D. Khakhulin, C. Bressler, F. Meyer, K. Zheng, S. E. Canton.
J. Phys. Chem. Lett. **2020**, *11* (6), 2133-2141.
- XXIII. Defect State Assisted Z-scheme Charge Recombination in Bi₂O₂CO₃/Graphene Quantum Dot Composites For Photocatalytic Oxidation of NO
Y. Liu, Y. Zhou, S. Yu, Z. Xie, Y. Chen, K. Zheng, S. Mossin, W. Lin, J. Meng, T. Pullerits, K. Zheng.
ACS Appl. Nano **2020**, *3* (1), 772-781.

Abbreviations

2D	two-dimensional
BBO	beta barium borate
CB	conduction band
CBM	conduction band minimum
DFT	density functional theory
DJ	Dion–Jacobson
DOS	density of state
EA	electron affinity
EF	Fermi level
ESA	excited-state absorption
ESC	energy selective contact
FE	free exciton
FWHM	full width at half maximum
GSB	ground-state bleach
HC	hot carrier
HCSC	hot carrier solar cell
IE	ionization energy
IRF	instrument response function
KE	kinetic energy
LA	longitudinal acoustic
LEED	low-energy electron diffraction
LES	low-energy edge states
LO	longitudinal optical
LR	long-range

MHP	metal halide perovskite
MQW	multiple quantum well
NCs	nanocrystals
PCE	power conversion efficiency
PeLED	perovskite light-emitting diodes
PL	photoluminescence
PSC	perovskite solar cell
PV	photovoltaic
QY	quantum yield
RP	Ruddlesden–Popper
SE	stimulated emission
SPAD	single photon avalanche diode
SQ	Shockley-Queisser
SR	short-range
STE	self-trapped excitons
TA	transient absorption
TCSPC	time-correlated single photon counting
tr-ARPES	time-resolved angle-resolved photoelectron spectroscopy
tr-2PPE	time-resolved two-photon photoemission
TRPL	time-resolved photoluminescence
VAC	vacuum level
VB	valence band
VBM	valence band maximum
WF	work function
XANES	X-ray absorption near edge spectroscopy
XAS	X-ray absorption spectroscopy
XPEEM	X-ray photoemission electron microscopy
XPS	X-ray photoelectron spectroscopy
XRD	X-ray diffraction

1 Introduction

1.1 Solar Cell

Due to climate change and increasing demand for energy, the green, low-carbon, diversified and sustainable energy sources have attracted much attention. Techniques for acquiring renewable energy such as hydroelectricity, biomass, geothermal, wind and solar energy have been developed over decades. Because of the enormous amount of available sunlight, a photovoltaic (PV) device, that can directly convert solar energy into electricity, has wide developmental and applied prospects.¹⁻⁴ Generally PVs can be divided into multijunction cells, single-junction gallium arsenide solar cells, crystalline silicon solar cells, thin film solar cells and new-generation solar cells. The latter include perovskite-based solar cells, polymer-based solar cells, quantum dot solar cells and dye-sensitized solar cells. To compare the different solar cell devices, power conversion efficiency (PCE) is often used as a critical characteristic. PCE has been steadily improved through the efforts of researchers. The development of PVs is shown in **Figure 1.1**. Nowadays, the PCE of multijunction cells can reach as high as 47.1%, but commercial use of such cells is so far limited due to their high manufacturing complexity and cost. Therefore, new-generation PV technologies are emerging targeting cheap alternatives and simple fabrication methods.

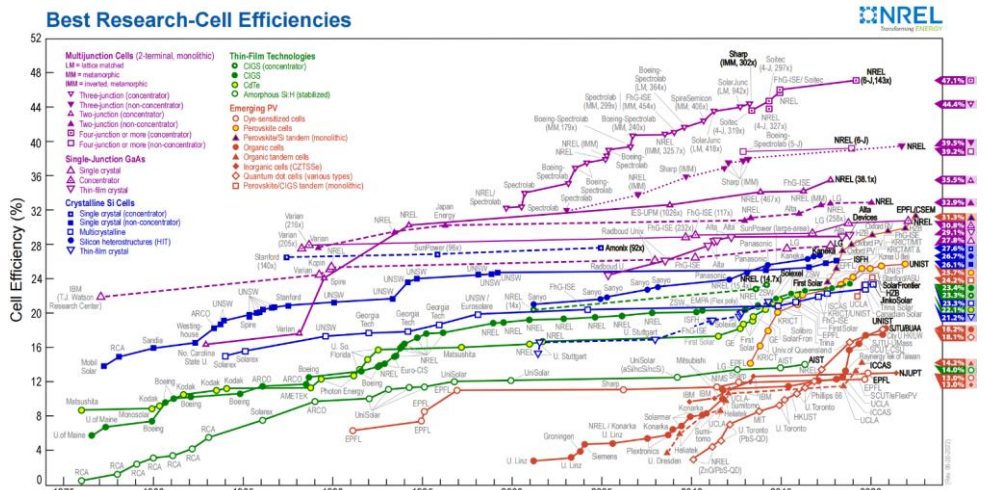


Figure 1.1 Power conversion efficiencies for photovoltaic technologies since 1976. This plot is courtesy of the National Renewable Energy Laboratory, Golden, CO.

Based on Shockley-Queisser (SQ) theory,⁵ the maximum efficiency that a single junction cell with ~ 1.3 eV bandgap under AM1.5 illumination can reach is theoretically predicted as 33%. To overcome the SQ limit, several strategies are investigated to minimize the fundamental loss channels. For example carrier multiplication⁶⁻⁷ where extra carriers are generated to enhance photocurrent, and hot carrier extraction⁸⁻⁹ where the lost energy is recycled to lift photovoltage. The latter idea is the fundamental principle of hot carrier solar cells (HCSCs).¹⁰⁻¹² The structure of HCSC is simplified as a hot carrier absorber material sandwiched by two energy selective contacts (ESC), as shown in **Figure 1.2a**. The energy diagram of HCSC is shown as **Figure 1.2b**. The idea of HCSC was proposed by Ross and Nozik in 1982,¹³ where the photogenerated carriers are extracted via ESCs before their excess energy is mostly lost. A great portion of absorbed energy might be wasted as heat (25%) as shown in **Figure 1.2c**. The PCE of HCSC can be pushed above 50%, which is much exceeding the SQ limit. This has drawn the wide attention of researchers who are trying to understand the intrinsic mechanisms of suitable materials for developing HCSC.

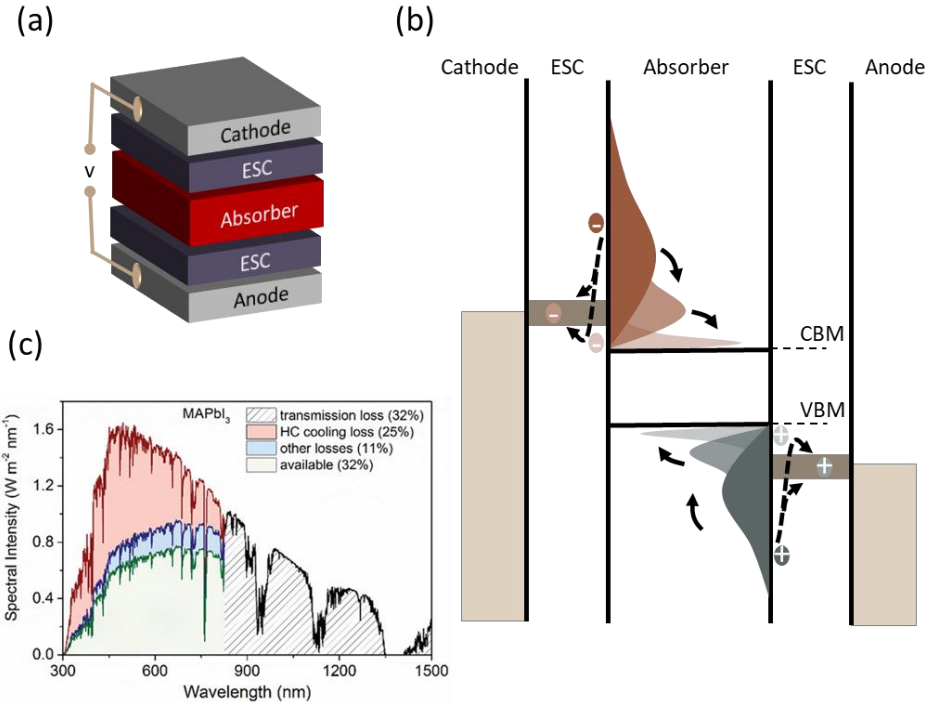


Figure 1.2 Principle of hot carrier solar cell (HCSC). (a) Schematic diagram of HCSC device, where ESC represents energy selective contact. (b) Energy schematic of HCSC, where conduction band minimum CBM and valence band maximum VBM are marked. The extraction energy of ESC needs to be suitably narrow, so that the HC can reheat cold carriers for improving device efficiency. (c) Illustration of losses in a single junction perovskite solar cell over the solar spectrum. Figure was adapted from Ref 12 with permission. The fundamental idea of HCSC lies in recycling the energy wasted in HC cooling and pushing the power conversion efficiency of the device above the Shockley-Quissier limit.

1.2 Metal Halide Perovskite

In 1839, the calcium titanate (CaTiO_3) mineral was discovered by Gustav Rose and was named as perovskite in honor of mineralogist Lev Perovski.¹⁴ Later the usage of name was extended to describe compounds with the same type of crystal structure. Inorganic lead halide perovskite was synthesized by Wells in 1893,¹⁵ and organic-inorganic hybrid perovskite was first reported by Weber in 1978.¹⁶ In the last decade metal halide perovskite (MHP) has become an up-rising star in the optoelectronic device field, including perovskite solar cells,^{3, 17-18} light-emitting diodes,¹⁹⁻²⁰ lasers and photodetectors²¹. The perovskite-based PV devices have been developed over years, such as perovskite solar cells (PSCs) with PCE of more than 25% as shown

in **Figure 1.1**, and metal halide perovskite light-emitting diodes (PeLEDs) with boosted external quantum efficiency above 20%.²² The simple and low-cost solution process in perovskite preparation enables its potential of substituting for presently commercial photovoltaic technologies.²³ In recent years, perovskite also has received wide attention as a suitable absorber material for HCSC devices.

1.2.1 Three-Dimensional Perovskite

The chemical formula of MHPs can be described as ABX_3 , where anion X is a halogen (e.g. Cl⁻, Br⁻, I⁻), the A is a monovalent cation (e.g. MA = CH₃NH₃⁺, FA = CH(NH₂)₂⁺, Cs⁺, Rb⁺) and B is a divalent metal cation (e.g. Pb²⁺, Sn²⁺). The crystal structure of perovskite can be viewed as A cation centered in the corner-shared (BX₆)⁴⁻ octahedra cage, as shown in **Figure 1.3a**. For different A-site cations, the MHPs can be classified as organic-inorganic hybrid perovskites or inorganic perovskites. If the ions are too small or too big, the crystal structure is unstable. The empirical Goldschmidt's tolerance factor (t) and octahedral factor (μ) are widely used to predict the formation and stability of perovskite structure.²⁴

$$t = \frac{r_A + r_X}{\sqrt{2}(r_B + r_X)}, \quad (1.1)$$

$$\mu = \frac{r_B}{r_X}, \quad (1.2)$$

where r_A , r_B and r_X are the ionic radii for A, B and X ions in ABX_3 perovskite, respectively. For APbI₃ perovskite, the range of tolerance factor is generally between 0.8 and 1.0, and octahedral factor is larger than 0.41.²⁵ The tolerance factors of MHPs with different A cations are listed in **Figure 1.3b**, which charts the systems with a too low or too high tolerance factors that are not able to form a stable perovskite structure.²⁶⁻²⁷ In addition, different perovskites have diverse phase transition temperatures.²⁸⁻²⁹ The influence of phase transition needs to be carefully considered when analyzing charge carrier dynamics since it can alter the electronic band structure significantly.³⁰⁻³¹ For the archetypal hybrid perovskite MAPbI₃, the transitions from cubic phase to tetragonal phase to orthorhombic phase occur at 330 K and 160 K, respectively.³²

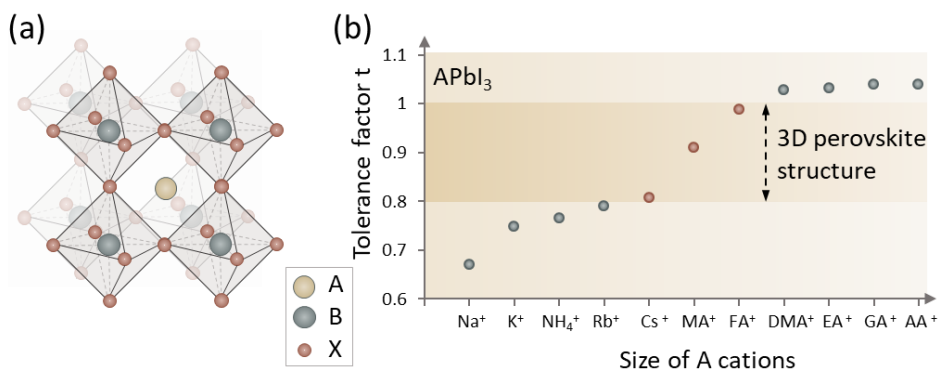


Figure 1.3 Structure of metal halide perovskite (MHP). (a) Crystal structure of MHPs with formula as ABX_3 . (b) Tolerance factors of MHPs with different A cations, where the B cation is Pb^{2+} and halogen X is I, and range of tolerance factor is between 0.8 and 1.0 for forming stable three-dimensional (3D) perovskite structure.

The performance of perovskite in solar cell applications is approaching the best inorganic PV materials, due to its effective light absorption, narrow and tunable emission bandwidth, balanced charge carrier transport, slow charge carrier recombination rate, high photoluminescence quantum yield, etc.³³⁻³⁸ Its high-quality properties are unexpected for a material produced from solution process at low temperature and the functional material properties are preserved with mitigated impact from crystalline defects – thus labeled as defect tolerant material.³⁹ The band structure of perovskite gives a hint about the reasons for its defect tolerance and unique optoelectronic properties.

As shown in **Figure 1.4**, the conduction band minimum (CBM) and valence band maximum (VBM) originate from antibonding orbitals of lead and halide atoms, arising from hybridization as $Pb(6p)-I(5p)$ and $Pb(6s)-I(5p)$, respectively. Even though the bottom of conduction band (CB) does not match the optimal bonding character for defect tolerance, the strong spin-orbit coupling effect in perovskite leads to the beneficial band broadening and shifts the CBM to be below $Pb(6p)$ atomic orbital and increase the possibility of defects forming intra-CB states.⁴⁰ It is also found that defects in perovskite can appear as shallow traps (near the band edge), which are not detrimental to device performance compared with deep trap states.⁴¹ In addition, the direct bandgap (silicon has indirect bandgap) and high transition probability between edges of CB and valence band (VB) (about two orders of magnitude higher than GaAs) enable the application of ultrathin perovskite film as an efficient absorber layer.⁴² There are other outstanding properties of perovskite correlating to its electronic structure, such as electrically-benign grain boundaries, long and balanced charge carrier diffusion length and slow carrier recombination.⁴³

The high-quality optoelectronic properties, composition-tunability, inexpensive and simple solution processing method qualify perovskite as a superior material for solar cell applications. It encourages researchers to further explore and develop perovskite solar cells.

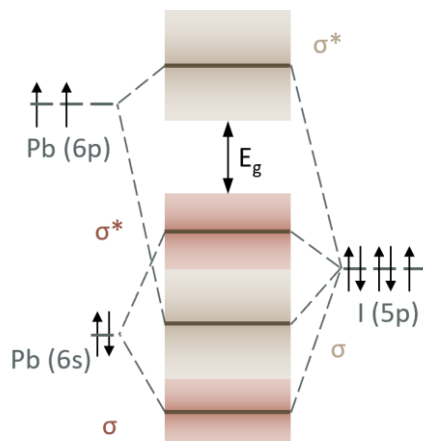


Figure 1.4 Schematic representation of bonding and band structure of APbI₃ perovskite. σ represents the bonding and σ^* represents the antibonding of orbitals.

1.2.2 Two-Dimensional Perovskite

Perovskite solar cells have been developed unprecedentedly in the past decade, but many challenges still remain, especially the poor thermal and moisture stability.⁴⁴ To improve the long-term stability, many studies are conducted on optimizing perovskite absorbers and device fabrication.⁴⁵⁻⁴⁷ Among all, inserting large organic spacing cations in between inorganic slabs can greatly improve the device stability when subjected to light, heat and humidity.⁴⁸ The resulting perovskites have a self-assembled multiple-quantum-well (MQW) structure and are named as two-dimensional (2D) perovskite, or quasi-2D perovskite, within which the inorganic sheets and organic spacer are alternately arranged in one direction. The MQW structure makes 2D perovskite an interesting material for various optoelectronic applications.⁴⁹⁻⁵⁰ 2D perovskites with Ruddlesden–Popper (RP) phases and Dion–Jacobson (DJ) phases are commonly reported.⁵¹⁻⁵² The difference between these two phases is that the RP phase contains two monocationic spacers while DJ phase contains only one dication spacer in one unit cell.⁵³ The general formula of 2D RP perovskite is $(A')_2A_{n-1}B_nX_{3n+1}$, where A' is the monovalent organic spacer (e.g., *n*-butylamine (BA⁺), phenylethylammonium (PEA⁺)), A is the cation inside the octahedra cage (e.g., methylammonium (MA⁺)), B is the metal cation (e.g. Pb²⁺), X is a halogen (e.g. I) and the n -value represents the number of octahedral layers (**Figure 1.5**).

Since the first report of 2D perovskite solar cell with PCE of 4.73%,⁵⁴ the efficiency was significantly improved over years to above 21%.⁵⁵ Apart from using pure-2D perovskite as absorber material, the profound potential lies in mixing perovskites with different n -values (including 3D perovskite as $n = \infty$) as a favorable ‘energy funnel/cascade’ structure.⁵⁶ The bandgap of 2D perovskite can be adjusted by varying the thickness of inorganic sublattice and the photoexcitations can be funneled into the lowest-bandgap emitter in the device.⁵⁷ In addition, the selection of composition for stable structure is extended compared to 3D perovskite, because the Goldschmidt tolerance factor requirement is relaxed in 2D perovskites due to the flexible structure, meaning that the large cations can be contained in the octahedra cage with lattice distorted.⁵⁸

All in all, the natural MQW structure, tunability of optical and electronic properties, flexible structure and enhanced stability make 2D perovskite an attractive candidate for exploring photoelectronic applications and further developing perovskite solar cell devices.⁵⁶

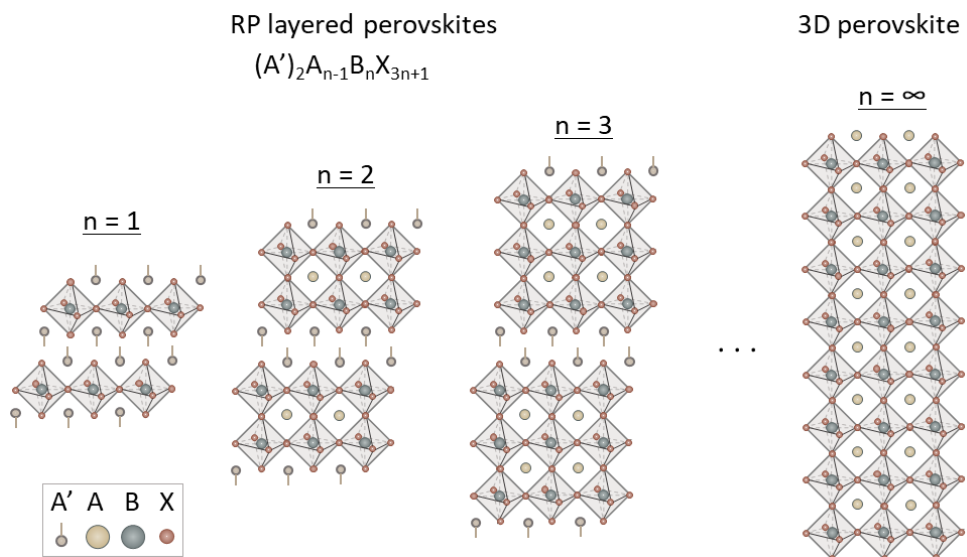


Figure 1.5 Crystal structure of two-dimensional Ruddlesden-Popper (RP) perovskite and three-dimensional perovskite. A' is the long-chain organic spacers, A is the cation in the octahedral cage, B is the metal cation, X is the halide anion and n represents the number of octahedral layers in one unit cell.

1.3 Hot Carrier Relaxation

As mentioned before, HCSC is a promising concept to exceed SQ limit and within which the selection of absorber material is a critical part to fabricate high-quality HCSC. Materials with high absorption coefficient, long carrier diffusion length and slow charge carrier recombination are generally preferred for PV applications. A special requirement for absorber material in HCSC application is that its HC lifetime should be sufficiently long for recycling the energy before heat dissipation. The potential of various materials being decent candidates have been investigated over years.⁵⁹ Illustration of HC cooling in HCSC is shown in **Figure 1.2b**. To improve the PCE, the rate of HC cooling needs to be slower than carrier separation and transportation for increasing photovoltage,⁶⁰⁻⁶¹ or the rate of impact ionization (i.e. inverse Auger effect) for increasing photocurrent.⁶²⁻⁶³ In most conventional semiconductors, the lifetime of hot carriers is limited in sub-ps timescale, but lead halide perovskite might be an exception according to current reports.⁶⁴⁻⁶⁵ To address the potential of perovskite and related mechanisms, fundamental processes involved in HC relaxation will be first introduced.

1.3.1 General Pathway of Hot Carrier Cooling

After the absorption of a photon with energy higher than the band gap, an electron is generated in the conduction band and leaves behind a hole in the valence band. The energy difference between the excitation and band gap is named as excess energy, which will be distributed to electron and hole as:⁶⁶

$$\Delta E_e = (h\nu - E_g)[1 + m_e^*/m_h^*]^{-1}, \quad (1.3)$$

$$\Delta E_h = (h\nu - E_g) - \Delta E_e, \quad (1.4)$$

where the m_e^* and m_h^* are the effective masses of electrons and holes, ΔE_e is the energy difference between the initial excited level of photogenerated electron and CBM, and ΔE_h is the energy difference between the initial excited level of photogenerated hole and VBM. The excess energy of system shows as the kinetic energy of charge carriers. When the photon energy is significantly greater than the band gap, the carriers populate far from the band edge and are at non-equilibrium status. The charge carriers with excess energy will lose energy via various scattering processes and eventually equilibrate with environmental (lattice) temperature.

- *Dephasing*

After the photoexcitation with an ultrashort laser pulse, there will be a regime where the oscillations of free e-h pairs are in phase before the first collision happens (mainly involve either another carrier or a phonon), considering the carrier recombination happens in a very late timescale. The coherent behavior is lost at an

extremely fast rate and the decay rate can be described by dephasing time. The four-wave mixing measurement can be conducted for observing the ultrafast coherence decay. Based on many measurements on samples with different morphology or temperature, the upper limit of the coherence timescale of 3D perovskite can be put as within 20 fs at room temperature.⁶⁷⁻⁶⁸

- *Carrier-carrier scattering*

Hot carriers will exchange energy among themselves after photoexcitation, which will not cause the loss of total system energy but affect the HC relaxation indirectly. In addition, the strong carrier-carrier scattering can limit the carrier mobility under high excitation densities. The process in which charge carriers exchange the energy towards forming a thermal distribution, is labeled as carrier thermalization in the ultrafast field, even though in other fields it can be used to represent the overall cooling of HC in semiconductors. With the help of two-dimensional electronic spectroscopy with high energy resolution, the initial carrier distribution can be visualized and the scattering rates which lead to the HC re-distribution can be obtained.⁶⁹ The results show that the carrier thermalization rate in perovskite depends on the excess energy and density of carriers, unlike GaAs, indicating the dominant mechanism being the carrier-carrier scattering (< 100 fs under moderate excitation intensity). The carrier thermalization is faster in perovskite than GaAs under similar excitation conditions, which could be due to the weak Coulomb screening effect in perovskite.⁷⁰⁻⁷¹ The previous description is based on pulse laser excitation. The situation will be different under continuous excitation, for example standard sunlight illumination. If the carrier lifetime is long enough or the HC extraction is designed inefficiently, the cold population of carriers in the bottom of conduction band will cause the rapid loss of excess energy of HC and will play a significant role in defining the timescale of carrier thermalization.⁶⁹

After elastic carrier-carrier scattering, the energetic carriers thermalize to a quasi-equilibrium state which can be characterized by Fermi-Dirac distribution. It can be approximated as a Boltzmann distribution because carriers locate in the high energy regime (excess energy \gg quasi-Fermi energy E_f). At this status, the Boltzmann distribution of carriers can be determined by the system temperature (separately assign the electron and hole temperature). The carriers with excess energy of at least kT , meaning that their initial carrier temperatures are above the lattice temperature, are labeled as ‘hot’ carriers.

- *Carrier-phonon scattering and phonon decay*

After carrier-carrier scattering, carriers with elevated temperatures will further lose energy by equilibrating to lattice via carrier-phonon scattering, where the excess energy of carriers is transferred to phonons. Phonons are quasiparticles with discrete energy $\hbar\omega$, used to represent modes of vibrations in the elastic and periodic arrangement of atoms in the semiconductors.⁷² The phonons are labeled as *acoustic*

when neighboring atoms move collectively towards one direction with relative position unchanged, whereas they are *optical* phonons, when the atoms undergo relative change in their positions. In addition, based on the displacement direction being parallel or perpendicular to wave-vector k , phonons can be classified into *longitudinal* and *transverse*. The schematic of longitudinal optical (LO) phonon and longitudinal acoustic (LA) phonon are shown in **Figure 1.6**.

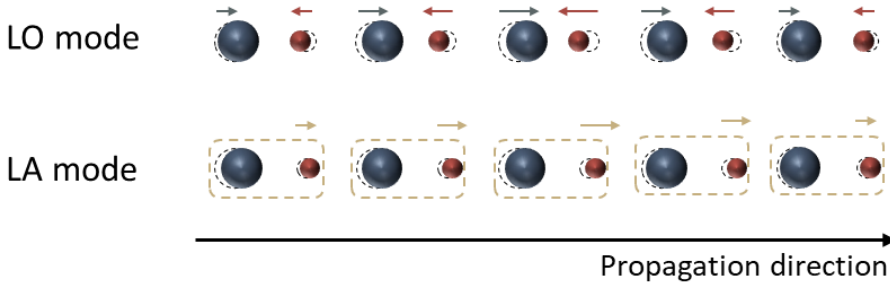


Figure 1.6 Schematic of longitudinal optical (LO) phonon and longitudinal acoustic (LA) phonon. In optical mode, the atoms of the unit cell oscillate in respect of each other, while in acoustic mode, the unit cells oscillate with respect to each other. Longitudinal waves mean that the vibration of the lattice is parallel to the wave propagation.

In general, there are different ways that lattice vibration can affect the charge carrier motions, such as Fröhlich interaction with LO phonons, deformation potential interaction with optical and acoustic phonons, and piezoelectric interaction with acoustic phonons.⁷³ In polar semiconductors, Fröhlich interaction which is the Coulomb interaction between carriers and longitudinal electric field from LO phonons, is generally agreed for governing the HC relaxation in the early cooling stage.⁷⁴⁻⁷⁵ This intra-band HC cooling results in the emission of LO phonons, and the energy and momentum are conserved during the cooling processes in the combination of electron and emitted phonons. The carriers interact with the macroscopic electric field arising from the out-of-phase displacement of oppositely charge atoms (LO phonon mode) via Coulomb interaction. The interactions between free carriers and phonons cover only a small wave-vector range, $k \approx 0$. Following, the emitted zone-center optical photons can re-heat the free electrons or further decay to counterpropagating acoustic phonons due to lattice anharmonicity via Klemens,⁷⁶ Ridley,⁷⁷⁻⁷⁸ Vallée-Bogani,⁷⁹ and other channels.⁸⁰⁻⁸¹ The routes of LO phonon decay are shown in **Figure 1.7**. The decision of mechanisms is based on a relatively simple (symmetric) crystal structure and thus the decrease in the symmetry will increase the complexity of decay routes.

Among all decay routes, Klemens decay is the most efficient channel in polar semiconductors.⁸² During Klemens decay, an optical phonon with k_0 decays into two acoustic phonons, which must fulfill momentum and energy conservation as $k_0 = k_1 + k_2$ and $\hbar\omega_O(k_0) = \hbar\omega_A(k_1) + \hbar\omega_A(k_2)$. Therefore, the zone-center LO phonon will decay into two acoustic phonons half of its energy, as well as equal and opposite

momenta. Klemens decay can be hindered significantly if the phononic band gap is greater than twice the highest energy of acoustic phonon.⁵⁹

In the next cooling stage, the energy is released as heat through acoustic phonon and eventually the lattice equilibrates to the environment temperature. Meanwhile, it is not significant in polar semiconductors that HC will cool down via acoustic phonon emission, since the acoustic phonons have rather small energies for the k -vectors of interest. In addition, energy loss through heat dissipation from the LO phonon to environment is considered negligible due to its negligible group velocity (low thermal conductivity).⁸³

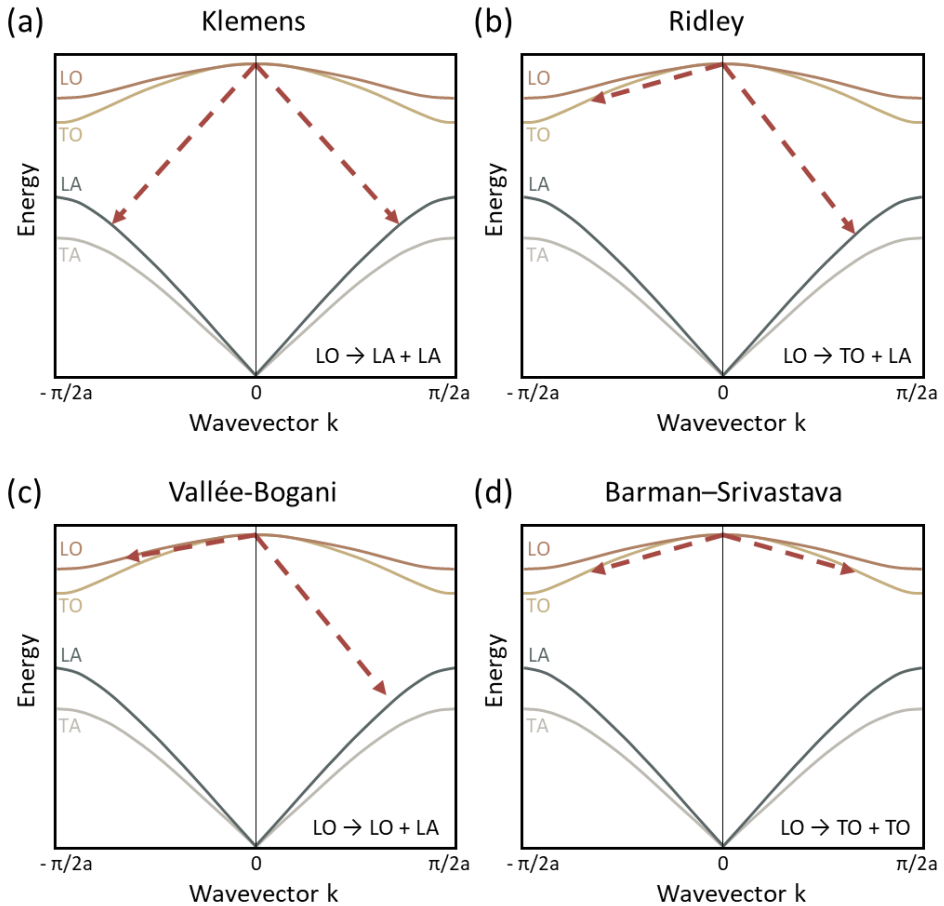


Figure 1.7 Phonon decay routes from zone-centre LO phonons to phonons with smaller energies, where Klemens decay is the most efficient channel in polar semiconductors.

- *Carrier recombination*

The electrons and holes will recombine, radiatively or non-radiatively, and the system can reach a complete relaxation situation with the carrier population same as before photoexcitation. The photons generated by direct recombination can be re-absorbed by ground state transitions and are beneficial for retarding HC cooling. But the photons from this process will not be included in the discussion of photoexcitation since they are usually near the band edge and have a longer absorption length than the photons which initially created electron-hole pairs.⁸⁴ In addition, the carrier recombination will not be included in the discussion of HC relaxation since its timescale is much later than the carrier cooling processes discussed above and the carriers close to the band edge might not have enough energy to be beneficial for improving the efficiency of HCSC.

1.3.2 Mechanisms for Slowing Down Hot Carrier Relaxation

In general, there are two pronounced HC cooling stages presented in investigations on lead halide perovskite after dephasing and carrier thermalization.^{12, 85} In the first stage, the HC loses energy via Fröhlich interaction in a sub-picosecond to few ps regime, which mainly occurs between carriers and lead-halide bonds.⁸⁶⁻⁸⁷ The second stage lies on the several tens of picoseconds to nanosecond scale, where the phonon decay from LO phonon to acoustic phonon plays a role, as well as the further heat dissipation from acoustic phonon to the environment. The timescales for typical photoexcited status are marked in **Figure 1.8**. Noteworthy, the timescale of different regions will overlap and can be significantly affected by the material composition, applied techniques and experimental parameters.

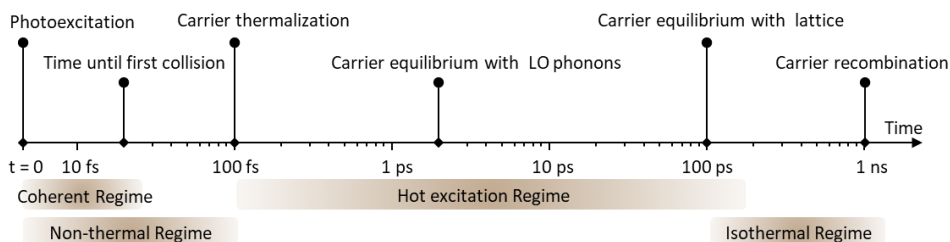


Figure 1.8 Timescale of four temporally-overlapping HC relaxation regimes in perovskite with typical status marked.

There are some effects that can significantly affect the HC lifetime in perovskite, including the screening effect, hot phonon bottleneck and Auger heating effect. The screening effect, e.g. polaron formation, can be observed at low fluence with carrier density as around 10^{17} cm^{-3} .⁶⁴ The HC cooling can be significantly slowed down by a few orders of magnitude with carrier density being above $5 \times 10^{17} \text{ cm}^{-3}$ due to hot phonon bottleneck,⁸⁸ which is different compared to the case in GaAs (an order of

magnitude lower in critical carrier density with three orders of magnitude longer HC lifetime in perovskite).⁸⁸ At high carrier density ($> 10^{19} \text{ cm}^{-3}$),⁸⁹ the Auger heating effect is found to prolong HC lifetime significantly in the later timescale with the average carrier temperature close to lattice temperature.

- *Hot phonon bottleneck*

Under strong excitation, it is observed that the carrier cooling rate is reduced due to a non-equilibrium population of phonon bath, and the HC lifetime is significantly prolonged.⁸⁵ The effect is named as ‘hot phonon bottleneck’. Noteworthy, it is different from the phonon bottleneck effect that was expected in QDs due to the discrete electronic band feature originated from the strong quantum confinement.⁹⁰

Phonon bottleneck: When the inter-level energy gap is substantially higher than the energy of LO phonons,⁹¹ the intra-band electronic transitions require multiple phonon emissions and the carriers are compelled to remain at excited levels with slow relaxation.⁹² However, the ultrafast spectroscopic measurements and theoretical calculation show that the lifetime of hot electrons in various types of QDs is in sub-ps to few ps range.⁹³⁻⁹⁷ The multiple phonon emission pathway is bypassed by interstate transitions that require only one emitted phonon followed by a cascade of single phonon intrastate transitions.^{92, 98-100} Among possible mechanisms, the most prominent is the Auger-type energy transfer where the excessive energy of a hot electron is transferred to the hole and cools rapidly due to its larger effective mass and smaller energy-level spacing.⁹⁵⁻⁹⁶ On the other hand, when fabricating the HCSC device, the discrete density of state (DOS) might be a problem for efficient light absorption over a broad spectral range.¹⁰¹ All in all, the potential of QDs in HCSC application and suppressing Auger-like relaxation are still under investigation.

Hot phonon bottleneck, on the other hand, is confirmed as a comprehensive effect that leads to the prolonged lifetime of HC under high excitation intensity, as shown in **Figure 1.9a**. Under strong external perturbations (e.g., laser excitation), the system will be driven out of equilibrium, and form a non-equilibrium hot phonon population if the main HC relaxation process is via phonon emission. In reverse, it is also possible for the phonon disturbances to feed back to the carrier system, as phonon reabsorption. The energy of the system is not necessarily removed by the phonon emission if the possibility of phonon reabsorption by the carriers is high enough. The hot phonon bottleneck effect has been observed in other polar semiconductors such as GaAs and CdSe.¹⁰² It is found that the hot phonon bottleneck effect has a dependence on carrier density (involve e-ph scattering rate) and environmental temperature relating to the ph-ph scattering rate (decreased at low temperature) due to the lower phonon occupancy.^{89, 103} The possibility of phonon reabsorption increases with increasing carrier density, and therefore the hot phonon bottleneck effect is expected to be more significant in high excitation density measurements. Generally hot carrier relaxation kinetic has two cooling stages under moderate or high excitation fluence due to the hot phonon bottleneck

effect, as shown in **Figure 1.9b**, with initial carrier temperature in the later stage being higher under high excitation fluence.

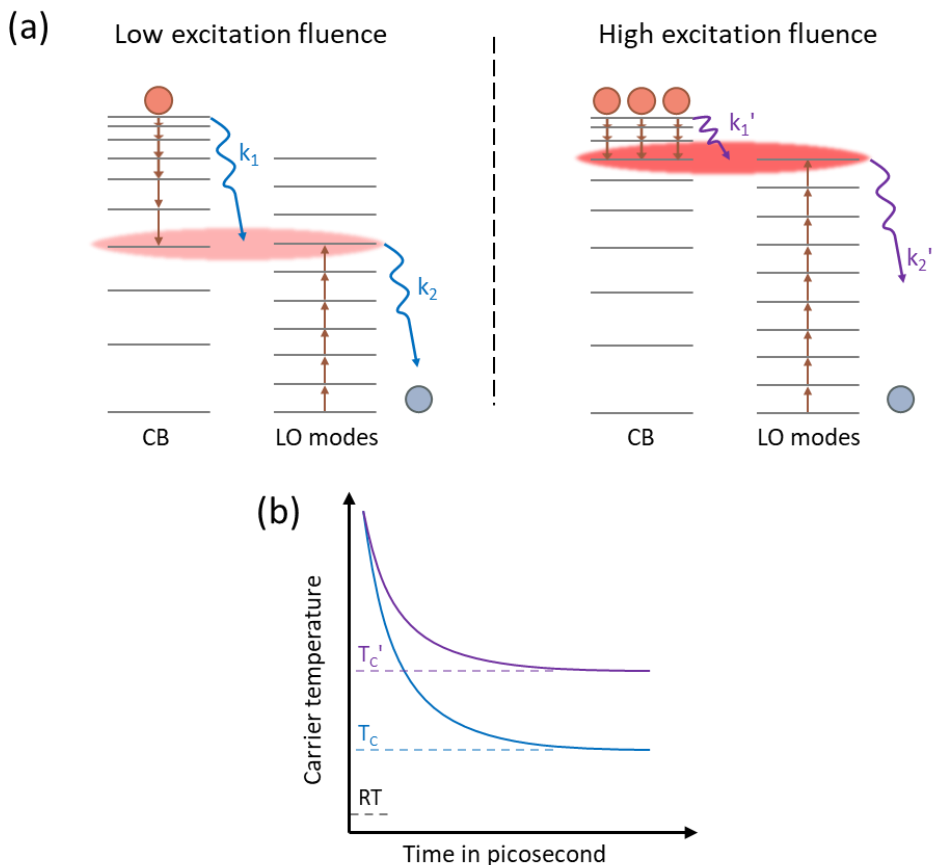


Figure 1.9 Schematic for hot phonon bottleneck. (a) Illustration of equilibrium between carriers and LO phonons under low and high excitation fluence. CB represents conduction band, k_1 and k_1' represent rate constant of establishing carrier-LO phonon equilibrium, and k_2 and k_2' represent HC relaxation after in the later stage until reaching environmental temperature, under low and high excitation fluence respectively. (b) Hot carrier cooling dynamics under low (blue line) and high excitation fluence (purple line). Two cooling stages are generally observed due to the hot phonon bottleneck effect and the initial carrier temperature of the later stage is higher under high excitation fluence compared to under low excitation fluence ($T_c' > T_c$).

In perovskite, the LO phonons are emitted via carrier-phonon scattering and warmed up by abundant HC. When the energy flow from HC to LO phonons is equal to the phonon reabsorption (backward flow), the population of hot LO phonons hinders the HC relaxation at an elevated carrier temperature like a bottleneck in sub-picosecond. Since the equilibrium between HC and hot LO phonons is reached, the

further cooling rate is corresponding to the phonon decay, which will be in the timescale of few picoseconds. The bottleneck observation in this stage, for example the slow-down of HC relaxation under high excitation intensity, means the carrier density can affect the phonon decay or the heat dissipation to environment, and is also included in the discussion of hot phonon bottleneck effect in some previous references.^{88, 104} One possible scenario is that HC relaxation is slowed down because of the partial heating of acoustic phonons,¹⁰⁵ possibly results from the inefficient thermal conductivity of sample.⁸⁵

- *Factors influencing hot phonon bottleneck*

The previously mentioned suppressed LO phonon decay is a possible influencing factor.⁸⁹ In this case, the LO phonon emission rate is faster than the phonon decay rate from LO phonon to acoustic phonons, and further leads to the accumulation of non-equilibrium hot LO phonon which can reheat the cooled carriers.¹⁰⁶ Hence, materials whose phonon decay can be hindered would be expected to exhibit a more significant hot phonon bottleneck effect and slowed HC cooling rate.¹⁰⁷ As discussed above, the Klemens decay channel ($LO \rightarrow 2LA$) can be suppressed if the phononic band gap is twice greater than the energy of acoustic phonons, which is fulfilled in the perovskites. Take organic-inorganic lead halide perovskite $MAPbI_3$ as an example for calculation, the energy of LO phonon is around 8 meV and of LA phonon is around 2.5 meV.⁸⁹ In addition, in the room-temperature 2D electronic spectra analysis, the existence of beating signal corresponding to a coherent optical phonon with long dephasing time suggests the strong coupling between this optical phonon(s) to the electron transition, but weak interaction with other phonon modes.¹⁰⁸

Another possible scenario is that the non-equilibrium accumulation of LO phonons is enhanced due to the acoustic-optical phonon up-conversion.⁸⁵ A-site organic cation plays a significant role in this possible channel, providing low-energy optical phonons that have a wide band overlap and strong thermal coupling with acoustic phonons. Based on the discovery of the “hybrid phonon” modes due to the existence of organic cation, acoustic phonon can be facilitated to up-convert optical phonon before dissipating the local lattice heat to the surroundings, and the HC relaxation can be slowed down.⁸⁵ However, this mechanism is argued by the investigation on coherent phonon oscillations,¹⁰⁸ which indicates the contribution of this mechanism to the HC lifetime can only happen in the timescale greater than 10 ps.

Nanostructuring, for example multiple-quantum-well (MQW) structure, can also be beneficial to enhancing the hot phonon bottleneck effect.¹⁰ The phononic bandgap between LO phonons and acoustic phonons might be opened up because the LO phonons might be reflected by the barrier¹⁰⁹⁻¹¹⁰ or the minigaps in frequency spectrum are formed preferably¹¹¹⁻¹¹².

- *Auger heating*

At high carrier density above 10^{19} cm^{-3} , the HC cooling lifetime in perovskite has been reported to be significantly prolonged up to several hundreds of picoseconds.⁸⁹ The credit has been given to Auger heating (non-radiative Auger recombination), where the released energy (\approx bandgap E_g) from electron-hole recombination is transferred to another carrier. The effect is more significant with high carrier density due to the more efficient carrier-carrier scattering.⁸⁹ In addition, Auger heating is expected to be more observable in the material with a smaller band gap or with nanostructure due to the quantum confinement effect.^{89, 113} Illustration of Auger heating is shown in **Figure 1.10**, in comparison with Auger-type energy transfer where the total energy of the e-h pair is unchanged.

Under low excitation fluence, in the investigations of conventional inorganic semiconductor nanocrystals (NCs), the hot carrier cooling is fast in smaller NCs which is assigned to Auger-type energy transfer, e.g. the excess energy of the hot electron is transferred to heat the cooled hole.¹¹⁴ However, perovskite NCs have an opposite trend in size-dependence of HC relaxation rate under low pump fluence, as well as the HC lifetime is significantly prolonged compared to conventional NCs.¹⁰⁴ This phenomenon indicates that the Auger-type energy transfer is suppressed in perovskite NCs (intrinsic phonon bottleneck), possibly due to the smaller carrier effective mass, symmetric energy dispersion and other factors.⁴²

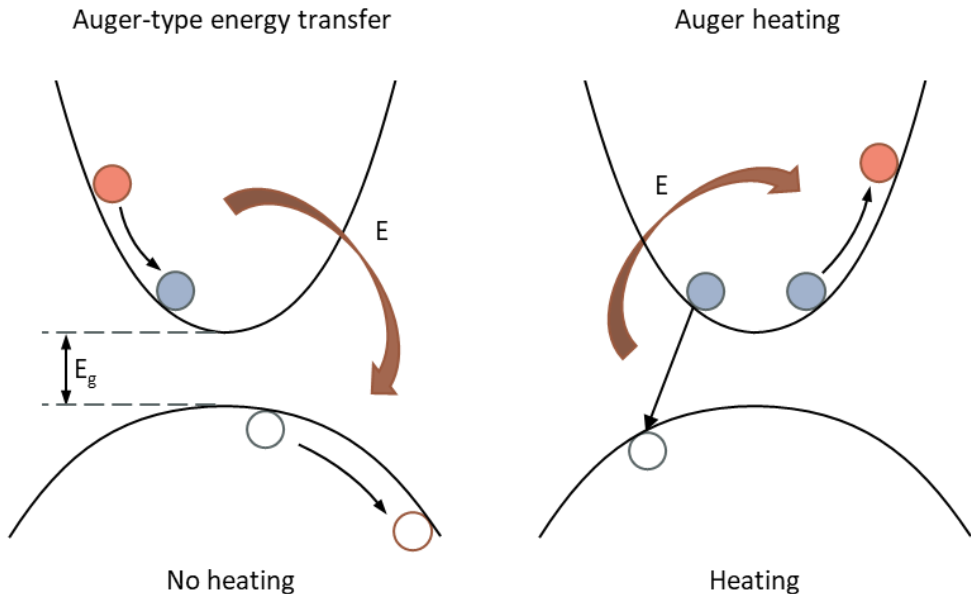


Figure 1.10 Illustration of Auger-type energy transfer and Auger heating (Auger recombination). Bandgap E_g is marked.

- *Polaron formation*

As mentioned before, the influence of the screening effect on HC relaxation is negligible compared to the hot phonon bottleneck effect at moderate or high carrier density. Therefore, the contribution of free carrier screening effect is generally observed at low carrier density ($< 10^{17} \text{ cm}^{-3}$), such as polaron formation due to the deformation of PbX_3^- inorganic framework and indirect modulation from organic cation.¹¹⁵⁻¹¹⁶

The genesis of polaron is often ascribed to a paper published by Landau in 1933 for considering the charge carrier moving slowly through an ionic solid.¹¹⁷ The general use of the term ‘polaron’ refers to the charge carrier and the altered atomic motions induced by it, as shown in **Figure 1.11a**. It can be divided into strong-coupling polaron and weak-coupling polaron by whether the electronic carriers are self-trapped or not (considered as a perturbation in the weak-coupling approach). In the class of strong-coupling polaron, it can be further divided into large polaron and small polaron by whether the spatial extent of its polarization cloud can extend over several sites or be confined to a single site. In addition, large and small polarons have different transport behavior and temperature dependency of mobility due to the different interaction ranges of carrier-phonon coupling.¹¹⁸⁻¹¹⁹ With rising temperature, the mobility of large polaron will decrease and the mobility of small polaron will increase.¹¹⁸⁻¹¹⁹ In general, a charge carrier in a deformable lattice induces an attractive potential well, where the carrier can be momentarily trapped. Depending on the strength and type of electron-lattice coupling, the time scale and spatial localization of lattice deformation can vary in a wide range.

Two essential driving forces need to be considered for polaron formation: long-range Coulomb potential (V^{LR}) associated with an ionic displacement polarization, and short-range deformation potential (V^{SR}) related to the carrier-induced strain.¹²⁰ If the former is the only important interaction, the charge carrier can remain ‘free’ and can travel in the lattice dressed with a phonon cloud. If the latter mechanism dominates, the deformation potential induced by the change in local bonding (e.g., lattice distortion induced due to the existence of carrier), the carrier will be strongly localized within one unit cell. The Coulomb potential can be given as

$$V^{LR}(\mathbf{r}) = - \left[\frac{1}{\epsilon_r(\infty)} - \frac{1}{\epsilon_r(0)} \right] \frac{e^2}{|\mathbf{r}|\epsilon_0}, \quad (1.5)$$

where \mathbf{r} is the vector between an electron and an ionic site. In the case of perovskite, with the large difference between static and optical dielectric constants $\epsilon_r(0) \gg \epsilon_r(\infty)$,¹²¹ the Coulomb potential might play an important role in hybrid perovskite for forming large polaron.

Polaron formation is proposed as a possible reason for slow carrier recombination and modest carrier mobility in perovskite, since the two oppositely charged polarons need to remove their “protective shield” for recombination.⁶⁴ As an outcome, the interaction between carriers, or with defects or LO phonons, is screened with weakened scattering strength. Many researchers suggest the ‘large polaron’ is

formed in hybrid perovskite,^{74, 116} as shown in **Figure 1.11b**, which is likely to be formed in three-dimensional polar or ionic medium when the self-trapped carriers interact with the displaceable ions mainly via long-range (Fröhlich) interaction.¹¹⁹ The ‘large’ in the term stands for the polaron size, meaning the moderate lattice deformation extending over several unit cells. The self-trapping timescale is extremely short (on the order of 100 fs) for large polaron, and therefore large polaron is sometimes expressed as an increase in the effective mass of the carrier. Various investigations have been conducted in exploring the reason for polaron formation.¹²²⁻¹²⁵ Is it related to the disorder and rotational degrees of freedom of organic cations or originating from macroscopic polarization induced by ion displacement? The predominant reason for polaron formation generally is the deformation of inorganic sublattice, with indirect contribution from organic cations.^{116, 126} It is also suggested in some references, that the dipolar fluctuations due to anharmonicity of the halide displacement have a more significant impact on carrier mobility than due to organic cations.¹²⁷⁻¹²⁸ The latter might participate indirectly.¹²⁹ However, the type of cation can affect the polaron formation time,^{64, 130} for e.g., 0.3 ps for mixed-cation lead halide perovskite MAPbBr₃ and 0.7 ps for all-inorganic perovskite CsPbBr₃.¹¹⁶ Large polaron is formed mainly due to the deformation of PbX₃⁻ sublattice, while the motions of organic cations coupled to the inorganic cage are responsible for the faster formation rate in hybrid perovskite compared to all-inorganic perovskite. Dynamic disorder (orientation) of molecules produces a random potential on inorganic sublattice, besides indirectly participating in polaron formation,¹³¹ it can modulate electronic properties and suppress the electron-hole recombination since they are spatially localized at different locations.^{123, 132-134} Theoretical and experimental results show that the charge carriers are stabilized and localized in the hybrid perovskite on the order of 0.1 ps,¹³⁵⁻¹³⁷ with a polarization cloud spanning many unit cells.^{135, 138}

In addition to the size of polaron and reasons for polaron formation, the lattice response under injection of a hot electron or hole is different.¹²³ This may be due to a different sensitivity of the valence band and conduction band in response to vibrations of inorganic sublattice.¹¹⁶

In the consideration of large polaron in perovskite, as self-trapped carriers with surrounding atoms, it is suggested by some researchers that the ability of self-trapping tends to be diminished with increasing carrier density, since they compete to displace the same atoms.¹³⁹⁻¹⁴¹ The phenomenon was labeled as ‘polaron overlap’, and more investigations are needed to clear its relation with hot phonon bottleneck effect.¹⁴²

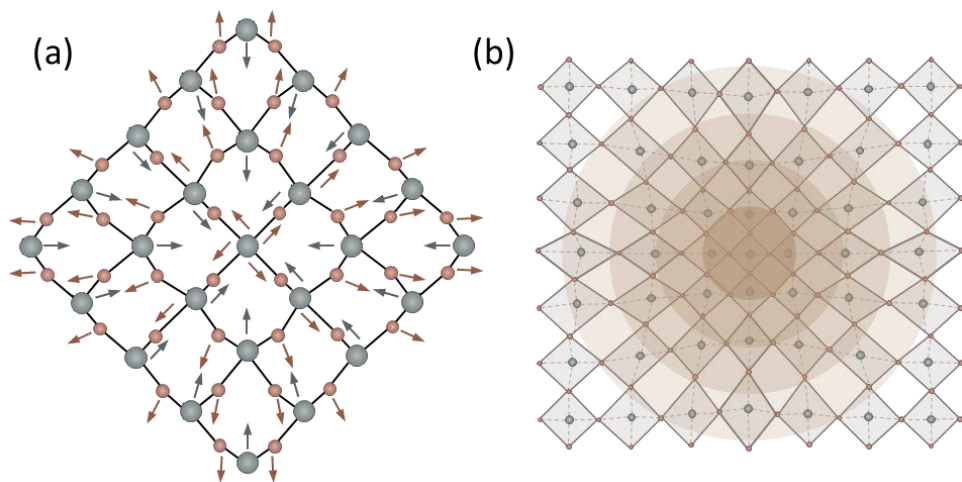


Figure 1.11 Schematics of polaron. (a) Illustrations of polaron formation, include the charge carrier and the altered atomic motion induced by it, and (b) a schematic of large polaron in perovskite.

2 Experimental Methods

Time-resolved spectroscopies enable the investigations of temporal changes inside the material. Alike using fast shutter cameras for capturing the motion of a horse in the 19th century, by applying ultrafast laser pulses and detectors with high temporal resolution, the generation and relaxation of transient species in ultrafast timescale can be recorded. This chapter mainly discusses time-resolved fluorescence spectroscopy, transient absorption spectroscopy, and time-resolved two-photon photoemission spectroscopy. Different kinds of ultrafast spectroscopies aim at collecting diverse information, more comprehensive information can be obtained through combination of techniques.

2.1 Time-Correlated Single Photon Counting

Time correlated single photon counting (TCSPC) setup is a useful tool for studying fluorescence decay in the time domain, with the time resolution typically in the range of picoseconds to nanoseconds. The detection range can be further extended to microseconds by employing an external trigger to synchronize the laser. After a pulse of light (excitation), the photons emitted from the fluorescent sample will be collected as a function of time. Based on the analysis of temporal evolution of the de-excitation behavior of the excited sample, important information, e.g. fluorescence lifetime, can be evaluated.

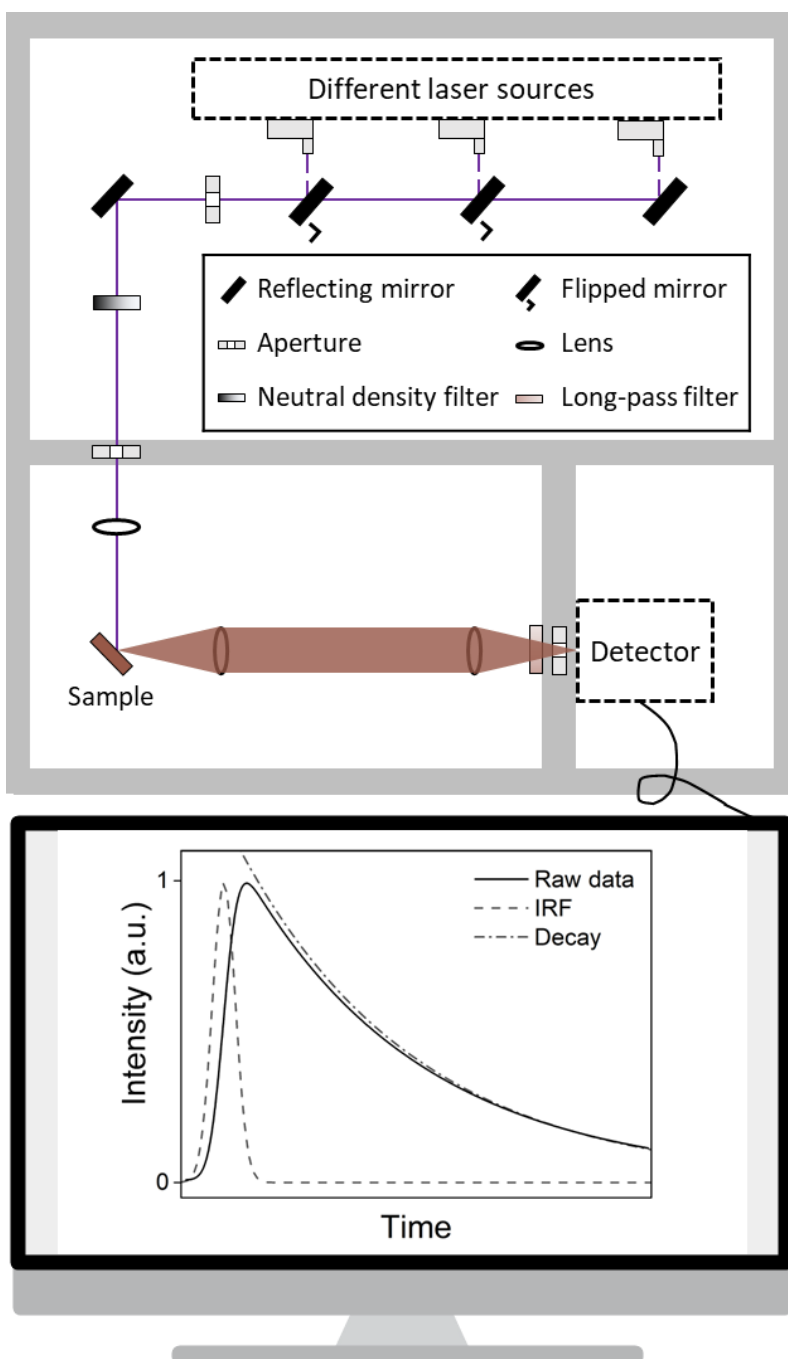
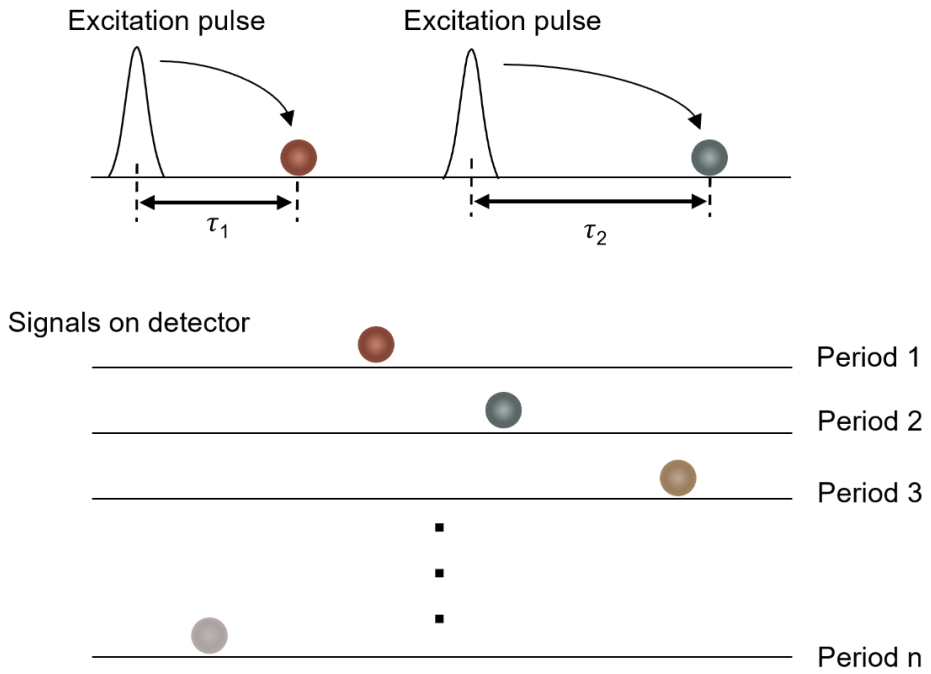


Figure 2.1 Illustration of time-correlated single photon counting setup.

The scheme of the TCSPC setup is shown in **Figure 2.1**. Several picosecond pulsed sources (laser diodes, LDH-series, PicoQuant) are used for excitation, with an adjustable repetition rate of up to 80 MHz and a pulse duration of 20 ps. The excitation pulse is directed onto the sample typically via a neutral density filter, for not only attenuating the laser pulse (preventing sample damage) but also suppressing false triggers from stray light on the detector. The single photon avalanche diode (SPAD, PicoQuant) is used as a detector with a timing resolution as short as 50 ps. The picosecond diode laser driver (Sepia II, PicoQuant) and TCSPC module & multichannel picosecond event timer (HydraHarp 400, PicoQuant) are used for controlling the laser and recording data. To characterize the overall timing resolution of the setup, the attenuated scattering of water is measured with the cutoff filter removed (generally long-pass filter) as the instrument response function (IRF) of setup, which contains contributions from the laser, detector, optics and electronics. The full width at half maximum (FWHM) of IRF is around 300 ps, when using a 375 nm laser source with a repetition rate set as 20 MHz. The observed decay profile is a convolution of the intrinsic decay with IRF. Therefore, the influence of IRF needs to be considered cautiously during measurements, especially when the fluorescence lifetime of the sample is close to the timing resolution. The light is attenuated so that only one photon can be received by the detector per excitation cycle to guarantee that the histogram of photon arrivals can represent the PL decay dynamic of the sample.

The principle of TCSPC, as shown in **Figure 2.2**, is detecting the single photon events (one emitted photon per excitation pulse) and their arrival time with respect to the excitation. The arrival time is determined based on signals from the excitation pulse (start time) and from the emission from the sample (stop time). Once an emitted photon is detected, the detector will stop collecting the rest of the photons. By employing the pulsed laser with a high repetition rate, the collection process is efficiently repeated many times to obtain a well-resolved histogram of photon distribution as a function of time. Choosing a high repetition rate can help minimize the pile-up effects in TCSPC measurements (emitted photons lost at a high photon count rate) but can also cause trouble when the sample has a fluorescence lifetime longer than (or equal to) the pulse period.



Result after many periods

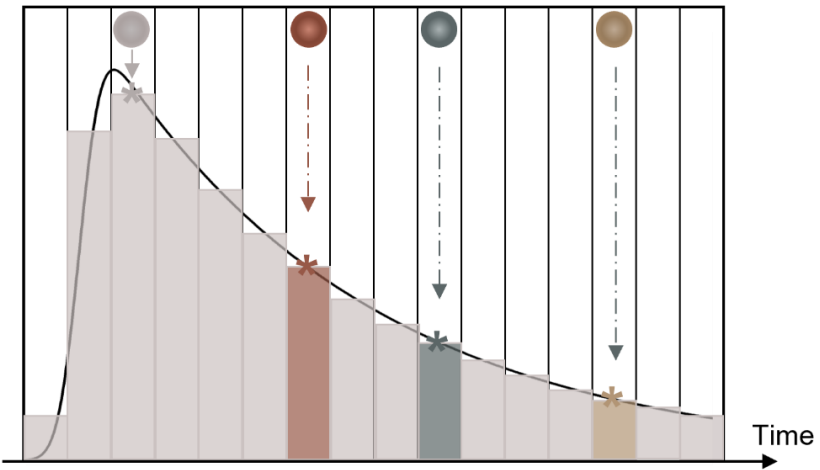


Figure 2.2 The principle of time-correlated single photon counting. The balls with different colors represent photons detected at different detection periods.

2.2 Transient Absorption Spectroscopy

Transient absorption spectroscopy (TA) is a powerful technique for investigating light-matter interaction in ultrafast timescales. The pump-probe configuration enables it to detect the change in material absorption as a function of wavelength and delay time, and the related spectrum and kinetics of transient species can be resolved after analysis. The TA spectrogram (ΔA) is calculated as the absorption spectrum of material under excitation (excited state) minus the absorption spectrum of material without excitation (ground state). Therefore, the information related to non-emissive states can also be accessed, unlike the case with time-resolved fluorescence spectroscopy.

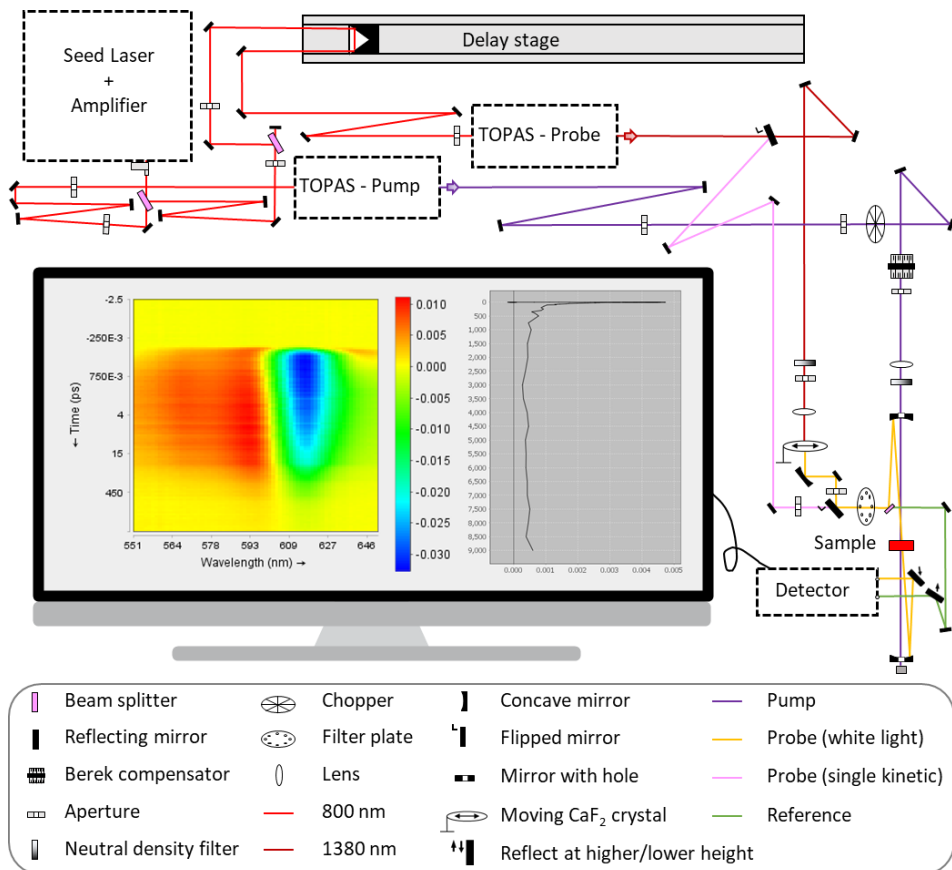


Figure 2.3 Illustration of transient absorption spectroscopy setup.

The scheme of TA spectroscopy is shown in **Figure 2.3**. The seed laser (femtosecond oscillator Mai Tai from Spectra Physics) is injected into the regenerative amplifier (Spitfire XP Pro, Spectra Physics) for producing a

fundamental beam with 800 nm wavelength, 1kHz repetition rate, 6 mJ/pulse, and 80 fs pulse duration. The fundamental beam is incident on the beam splitter for generating pump and probe beams. The single-wavelength pump beam can be obtained from the fundamental beam via second harmonic generation (400 nm) on a beta barium borate (BBO) crystal or via an optical parametric amplifier (TOPAS-C, Light Conversion). The probe beam can be single-wavelength (for single kinetic measurements) or broadband white light by sending the near-infrared beam (adjusted by TOPAS) through a CaF₂ crystal. The CaF₂ crystal is mounted on a computer-controlled motorized translation stage to prevent thermal damage. The switch between pump-on and pump-off status in TA measurement is achieved by chopper, and the variation in delay time is controlled by the delay stage (up to 9 ns). The Berek compensator is placed in the light path of the pump beam to set the polarization between the pump and probe beams to be the magic angle (54.7°). For single kinetic measurements, the photodiode is used as a detector. For spectral measurements, the prism and photodiode array is used in the detector.

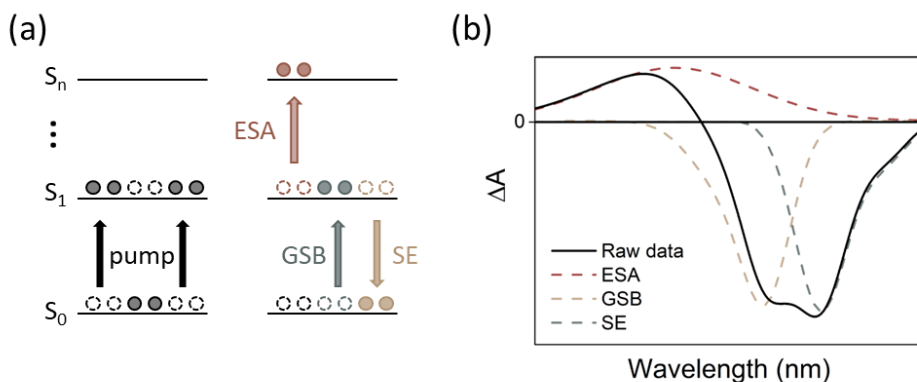


Figure 2.4 Schematic of contributions in the transient absorption spectrum. Schematic of (a) transitions and (b) example spectra related to excited-state absorption (dash-dot line), ground-state bleach (dash line) and stimulated emission (dot line). The influence of the probe beam on the population of excited state S_1 is exaggerated for a clear illustration. The raw data (solid line) represents the sum of three contributions.

Three main contributions to the TA spectrum are ground-state bleach (GSB), stimulated emission (SE), and excited-state absorption (ESA), as shown in **Figure 2.4**. The measured TA spectra are the superposition of all contributions. Due to photoexcitation, species are partially excited to excited state S_1 , and the population of species at ground state S_0 is decreased compared to the pump-off status. Therefore, a negative signal (GSB) in the TA spectra appeared in the related wavelength region (ground state absorption). By absorbing the probe beam, the excited species at S_1 state can be further excited to a higher excited state S_n and a positive signal (ESA) appears due to the occurrence of absorption of the probe beam in a related wavelength window. Apart from absorption, the excited species at S_1 are not stable

and the probe beam might induce SE, resulting in the transition of excited species from excited state S_1 to ground state S_0 . The photon generated from SE follows the direction of the probe beam and results in increased light intensity on the detector, corresponding to a negative signal in TA spectra (ΔA) in the related wavelength range (fluorescence spectrum).¹⁴³

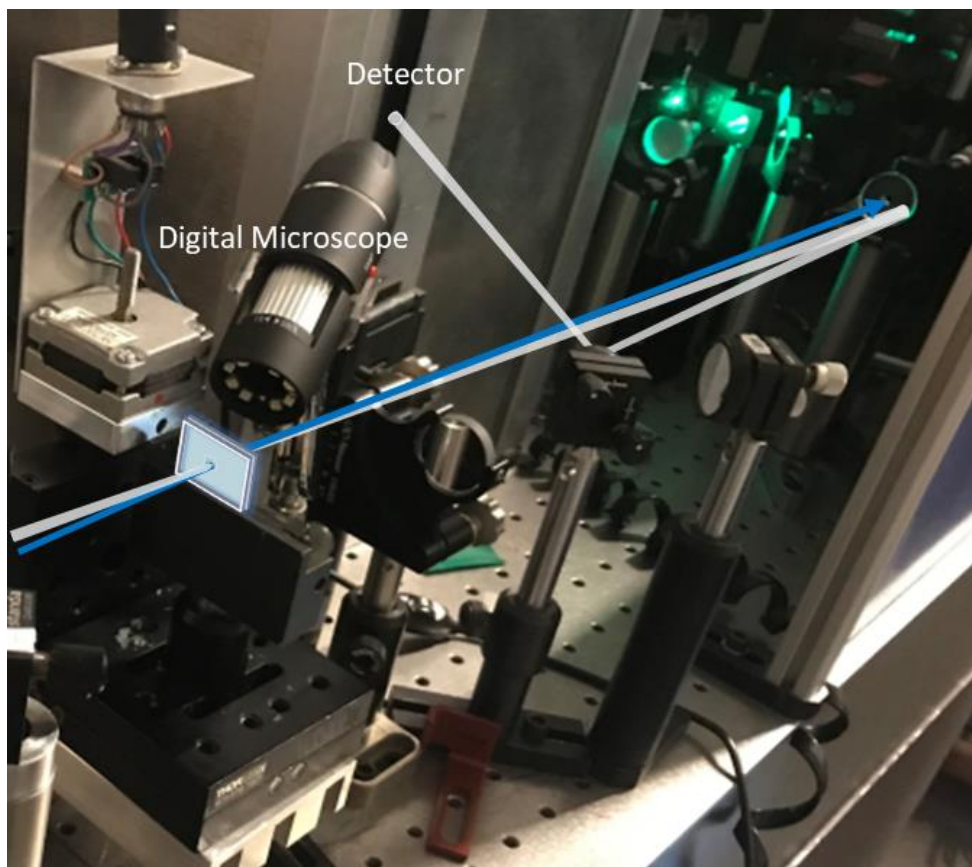


Figure 2.5 Schematic of in-situ transient absorption measurements. The blue and white lines represent the pump and probe beams, respectively.

A flake with a size of around a hundred micrometers can be located and in-situ measured with the assistance of a commercial digital microscope embedded in TA spectroscopy, as shown in **Figure 2.5**. The flake is selected under an optical microscope and the picture including the surroundings is taken to mark the location, as shown in **Figure 2.6a**. Then based on the pattern of surrounding bulky crystals and relative distances, the location of the target flake can be determined and the overlapping of beams on the sample can be confirmed, as shown in **Figure 2.6b** and **Figure 2.6c**.

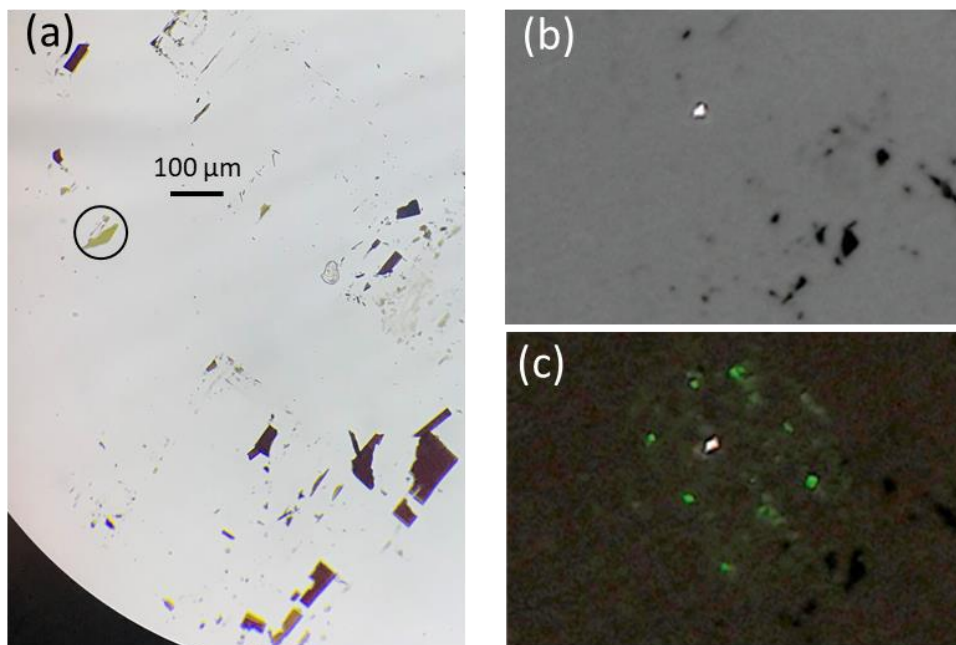


Figure 2.6 Location of the target flake. (a) Optical microscope image of the flake and surroundings as marks. Digital microscope image of the flake (b) under probe beam and (c) under both probe and pump beams. In this figure, the pump is 560 nm and the probe is white light. The contrast of figures is adjusted for clearer observation.

2.3 Time-Resolved Two-Photon Photoemission Spectroscopy

The time-resolved two-photon photoemission (tr-2PPE) spectrum can be obtained from (laser-based) time- and angle-resolved photoelectron spectroscopy (tr-ARPES) with the momentum distribution integrated. The configuration is also pump-probe, but unlike transient absorption, the probe used here has higher energy to excite electrons from the conduction band to the vacuum. The photo-emitted electrons with different kinetic energies are collected and analyzed in an electron analyzer under different time delays, and therefore the temporal evolution of the distribution of photoexcited electrons in the conduction band (by pump) can be directly visualized.

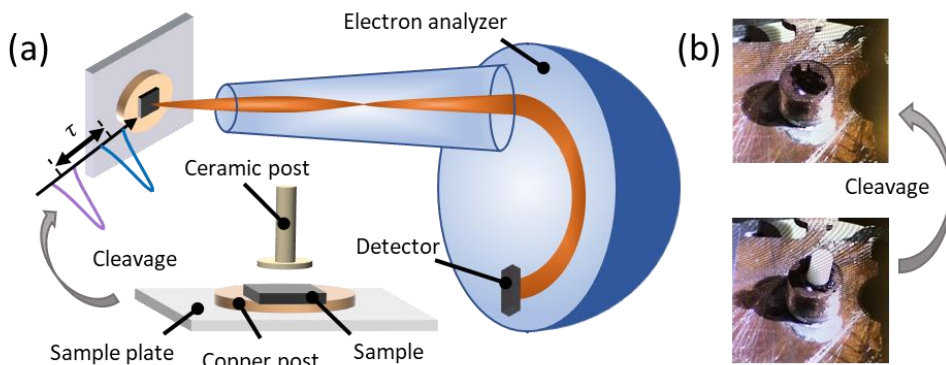


Figure 2.7 Schematic of time-resolved two-photon photoemission spectroscopy. (a) Illustration of time-resolved two-photon photoemission setup. (b) Images of sample on sample holder before and after cleavage.

The tr-2PPE setup is shown in **Figure 2.7a**. A Ti:Sapphire system (RegA, Coherent) is used to generate a fundamental beam with an energy of 1.55 eV (800 nm), a repetition rate of 250 kHz and an intensity of 6 $\mu\text{J}/\text{pulse}$. A beam splitter is used in the fundamental light path for obtaining pump and probe beams. The fundamental beam is incident on a BBO crystal for generating a 3.1 eV (400 nm) pump beam via second harmonic generation. The probe beam is 4.65 eV or 6.2 eV via third and fourth harmonic generation respectively. The pump and probe beams are spatially overlapped on the sample. A hemispherical electron analyzer (Phoibos 150, Specs) is used for collecting and recording the temporal population of photo-emitted electrons as a function of kinetic energy and angle. Note that the distribution on electron emission angles is integrated for tr-2PPE spectroscopy. A delay stage is used to control the time delay between the pump and probe beams. The temporal resolution of the setup is around 100 fs and the energy resolution is around 50 meV. Due to the mean free path of photoelectrons, the setup has a high surface sensitivity as few nanometers where the unscattered photoelectrons come mostly from.

A clean and atomically flat surface is needed for measurements, and thus a cleavage is typically required, as shown in **Figure 2.7b**. Two sides of the crystal are glued on the copper post and ceramic post respectively with electrically conductive adhesives (e.g. silver epoxy). Then the whole sample is coated with graphite for avoiding the charging effect during measurements. After loading the sample holder into the preparation chamber (high vacuum environment), the ceramic post is knocked down by a wobble stick for obtaining a fresh and flat surface. This method is practically useful on a layered material since the Van der Waals force between the interlayers is weak. A commercial microscope (Bresser) is equipped to confirm the sample preparation, and the sample can be further transferred to the main chamber (ultra-high vacuum environment) for measurements.

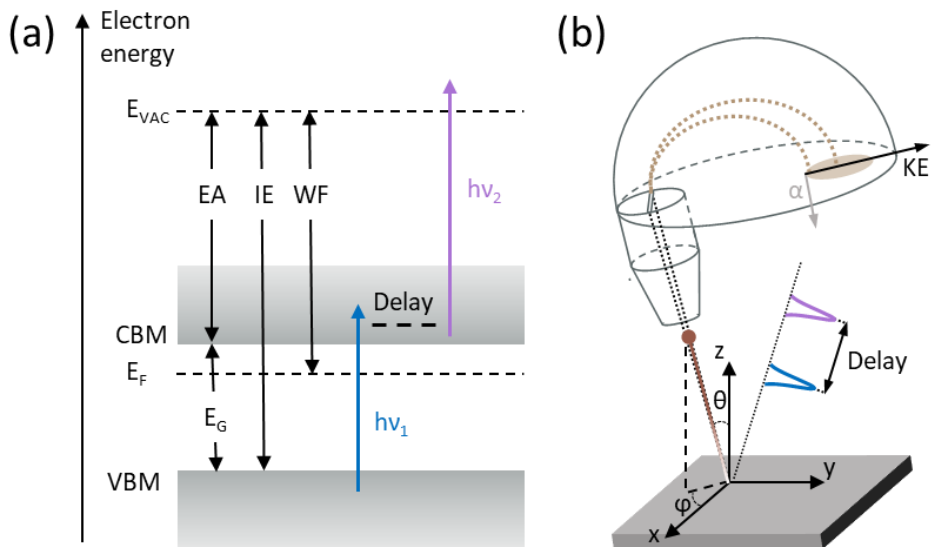


Figure 2.8 Principle of time-resolved two-photon photoemission spectroscopy (tr-2PPE). (a) Energy diagram of a semiconductor and transitions due to pump and probe beams. (b) Experimental geometry for tr-2PPE where the angle-related distribution from time- and angle-resolved photoelectron spectrogram is integrated. Vacuum level E_{VAC} , conduction band minimum CBM , valence band maximum VBM , Fermi level E_F , electron affinity EA , energy gap E_G , ionization energy IE , work function WF , polar angle θ and azimuthal angle ϕ of photoemission direction, momentum α and kinetic energy KE are marked. The blue line represents the pump beam and the purple line represents the probe beam.

Electrons at the material surface are naturally prevented to escape to the vacuum level (E_{VAC}), where an electron is ‘few nanometers’ outside the material surface.¹⁴⁴ According to the photoelectric effect, incident light with minimum frequency (energy) is required for electrons to start emitting from a metal surface. As shown in the energy diagram of a semiconductor (**Figure 2.8a**), the work function ($WF = E_{VAC} - E_F$) represents the minimum energy needed to remove an electron from the Fermi level (E_F) to the outside of surface. The local vacuum level, as well as the work function, is strongly dependent on the nature of surface. For example, surface conditions (contamination or surface reactions) can commonly induce changes on the order of 1 eV on work function, due to the formation of surface electric dipoles. Note, from another perspective, it emphasizes the surface sensitivity of photoemission spectroscopy.

When the sample is irradiated by one beam with photon energy exceeding the work function, the rest of the energy will contribute to the kinetic energy of photoelectron, apart from overcoming the atomic bonding. Due to energy conservation, the kinetic energy E_{kin} of photoelectron emitted from an energy level that is below Fermi level with binding energy E_B can be calculated as:

$$E_{kin} = h\nu - |E_B| - \phi_{sample} , \quad (2.1)$$

where ϕ_{sample} is the work function of sample and $h\nu$ is the photon energy.¹⁴⁵

While in the case of two-photon photoemission spectroscopy (our measurements), the pump beam cannot induce direct photoemission but excite an electron into an intermediate state (i.e. in the conduction band). After a certain delay, the excited electron is further pushed by the probe beam to a final state above the vacuum level. The calculation of the kinetic energy of photoelectrons can be modified as:

$$E_{kin} = E_{pump} + E_{probe} - |E_B| - \phi_{sample} , \quad (2.2)$$

where the E_{pump} and E_{probe} represent the photon energy of pump and probe beams. Since the kinetic energy can reflect information relating to intermediate states, the temporal evolution of electrons in the conduction band can be evaluated by varying the delay time between pump and probe beams.

3 Results and Discussion

3.1 Electronic Structure and Trap States of Two-Dimensional Perovskite Single Crystal – Paper II

Photovoltaic devices based on metal halide perovskites have been widely investigated over the years due to their advantageous properties. However, the developments suffer from poor structural stability, especially when facing moisture. By inserting the hydrophobic long-chain organic cation between inorganic sublattice, the two-dimensional perovskites can be formed with the formula $(A')_2A_{n-1}B_nX_{3n+1}$, where A' is the organic spacer (e.g. n-butylamine ($n\text{-BA}^+$)), A is the cation inside the inorganic cage (e.g. methylammonium (MA^+), ethylammonium (EA^+), guanidinium (GA^+)), B is the metal cation (e.g. Pb^{2+}), X is the halogen (e.g. I^-) and n is the number of octahedral layers. The electronic properties can be adjusted by varying the thickness of the inorganic sublattice. The variable composition and natural multiple-quantum-well structure of two-dimensional (2D) perovskite have drawn significant attention in recent years.

Goldschmidt tolerance factor (τ) is widely used to predict the formation of stable perovskite structure, with a range generally between 0.8 and 1.0.¹⁴⁶ Thus, only a few cations with suitable sizes can be employed in lead halide perovskites, such as MA^+ , FA^+ and Cs^+ . However, the strict requirement of tolerance factor on 3D perovskites is relaxed in 2D perovskite, and A-site cations with larger sizes can be accommodated by the octahedral cage with greater structural distortions, such as EA^+ and GA^+ .

This paper reports the influence of structural distortion on electronic properties and photo-physics by comparing $(n\text{-BA})_2(\text{MA})_2\text{Pb}_3\text{I}_{10}$ (BMAPI) and $(n\text{-BA})_2(\text{EA})_2\text{Pb}_3\text{I}_{10}$ (BEAPI) single crystals. The molecular compositions of the two target materials are similar, while the A-cation in BEAPI (effective radius $r_{\text{EA}} = 274$ pm) is larger than in BMAPI (effective radius $r_{\text{MA}} = 217$ pm). The stable formation of BEAPI ($\tau = 1.031$) shows the relaxation of the tolerance factor threshold in 2D perovskite and compensation for strain accumulation (increased distortion of the inorganic octahedron) is attributed to separated flexible organic spacers.¹⁴⁷ Based on single-crystal X-ray diffraction (XRD) measurements and calculations in this

work, the magnitude of octahedral distortion in the inner layer and outer layers of BMAPI and BEAPI are compared in detail. Five essential parameters (average lead-halide bond distance $\langle D \rangle$, distance distortion ζ , tilting distortion Δ , torsional distortion Θ and angle distortion Σ) are used for characterizing lattice distortion, whose values are overall greater for BEAPI than BMAPI. The long-chain spacers work as a ‘buffer’ to the rigid inorganic sublattice and compression on the organic layer is increased in BEAPI for accommodating larger EA cation in the cage. The compression is confirmed by the shortened layer distance in BEAPI, as shown in **Figure 3.1**. Noteworthy, the organic cations interact with the inorganic unit via N-H \cdots I hydrogen bond, whose average lengths and NH₃ vibration frequency are similar in BMAPI and BEAPI, showing that interaction between the organic cation and inorganic units is unlikely to be the dominating reason for the difference in BMAPI and BEAPI.

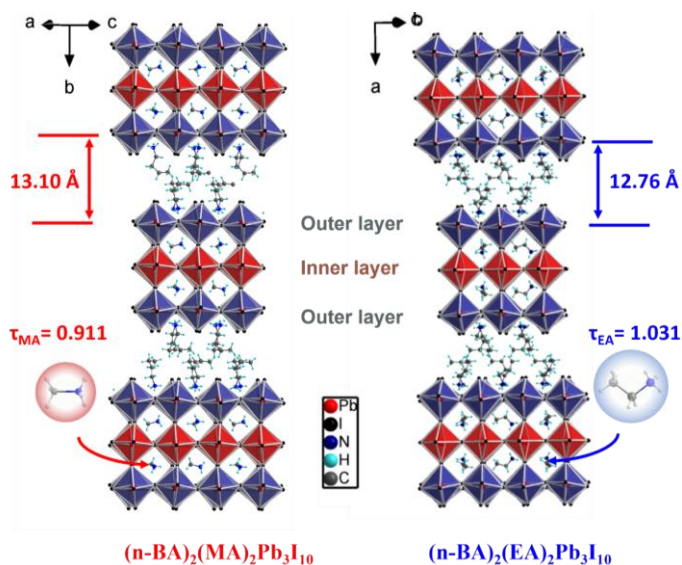


Figure 3.1 Structure of $(n\text{-BA})_2(\text{MA})_2\text{Pb}_3\text{I}_{10}$ (BMAPI) and $(n\text{-BA})_2(\text{EA})_2\text{Pb}_3\text{I}_{10}$ (BEAPI) with marked tolerance factors and layer distances, respectively.

The change in the lattice structure can affect the electronic properties, especially the electronic band-edges. The optical band gap E_g is determined by steady state absorption measurements and the exciton binding energy is evaluated from the temperature-dependent photoluminescence (PL) measurements. The position of the valence band maximum (VBM) with respect to the Fermi level is determined by X-ray photoelectron spectroscopy (XPS). The energy diagrams of BMAPI and BEAPI are presented in **Figure 3.2a**, showing a ~ 0.2 eV difference in band gap and VBM position, confirmed by the band structure calculated based on density functional

theory (DFT). In the XPS measurements of the core levels, the core-level binding energy of Pb 4*f* core levels in BEAPI is ~ 0.2 eV lower than BMAPI, as shown in **Figure 3.2b**. It suggests the electronic density around Pb atoms is more pronounced in BMAPI than in BEAPI due to the shortened Pb-I bond. In addition, the identical XPS spectra on I 3*d* core level indicate a similar chemical environment around I centers, as shown in **Figure 3.2c**. The electronic structure near the band edges in 2D perovskite is sensitive to the details of the octahedral unit structure, while the organic cation influences the states which are located deep in the valence band or conduction band.¹⁴⁸ The VBM consists of anti-bonding of Pb 6*s* and I 5*p* orbitals, and conduction band minimum (CBM) consists of anti-bonding of Pb 6*p* and I 5*p* orbitals. The existence of lone-pair 6*s*² electrons and off-center Pb²⁺ distortion suggest the non-spherical electronic distribution around Pb²⁺ atom.¹⁴⁸⁻¹⁵⁰ The shorter average Pb-I bond length in BMAPI than BEAPI suggests stronger interaction of the related orbitals possibly leading to more pronounced charge delocalization due to the hybridization between Pb 6*s* and I 5*p* orbitals. Thus, the energy difference between bonding and anti-bonding states (Pb 6*s* and I 5*p*) is enlarged and the energy position of VBM is higher in BMAPI than BEAPI, whilst the CBM is being less affected by the change in Pb-I bond length.

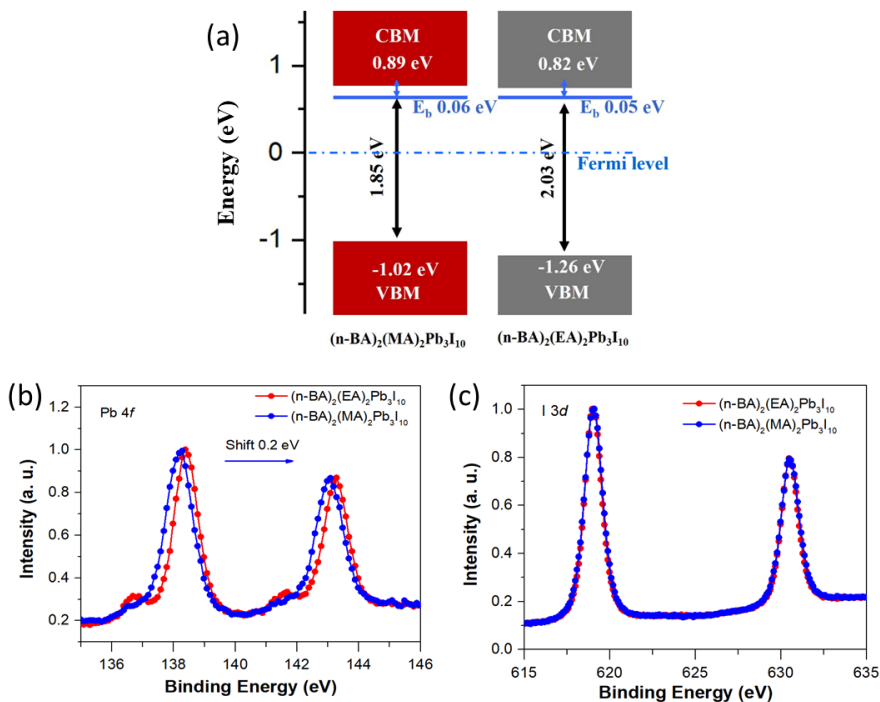


Figure 3.2 (a) Band alignment of BMAPI and BEAPI. XPS core level emission spectra of (b) Pb 4*f* doublet and (c) I 3*d* doublet in BMAPI and BEAPI, respectively.

As mentioned above, the constraint on the tolerance factor is relaxed in 2D perovskite. To study its impact on the photo-physics properties, we conduct time-resolved photoluminescence (TRPL) measurements on BMAPI and BEAPI. The kinetics can be fitted with three exponential components, including fast (t_1), medium (t_2) and slow (t_3) components. It is shown that the PL lifetime of BMAPI is significantly longer than that of BEAPI, as shown in **Figure 3.3a**. Based on the Saha-Langmuir equation taking into the exciton binding energy and excitation density of the system,¹⁵¹ the majority of photogenerated species are free carriers, and thus the slow component (t_3) is assigned to intrinsic bimolecular recombination. The other two faster components are often assigned to nonradiative trap-mediated recombination due to various possible mechanisms.¹⁵²⁻¹⁵³ To further investigate the trap properties, the PL lifetimes under different excitation intensities are measured to monitor the trap-filling effect, which occurs when the lifetime of trap is significantly longer than the time interval between laser pulses. Based on global fitting, the amplitudes (A_1 , A_2 and A_3) of the three components at different excitation densities (N_c) are obtained, and the result suggests the existence of two types of traps, that one causes trap filling phenomenon (long lifetime) and the other is immune to trap filling effect (faster depopulation time).¹⁵³ The ratio of amplitudes (A_1 / A_2) can be used to determine the fraction of charge carriers being trapped by two different traps and equals the initial ratio of unfilled trap density ($n_{\text{uncT1}} / n_{\text{uncT2}}$). Thus, the ratio $A_1 / (A_1 + A_2)$ as a function of excitation density N_c (**Figure 3.3b**) can be fitted to obtain total concentrations of trap 1 and trap 2 (N_{T1} and N_{T2}) and the ratio between trap population and depopulation rates (R_1).

The obtained timescales for each transition are marked in **Figure 3.3c**, and the total trap concentrations of trap 1 in BMAPI and BEAPI are $\sim 2.18 \times 10^{16}$ and $\sim 3.76 \times 10^{16} \text{ cm}^{-3}$, respectively. The higher trap concentration in BEAPI compared to BMAPI might be due to the stronger interfacial lattice distortion when containing the larger EA cation inside the octahedral cage. The faster trapping and detrapping rates in BEAPI also indicate that the traps might be much shallower than in BMAPI. The combination of the shallower traps and higher trap density can be the main reason for the shorter PL lifetime in BEAPI.

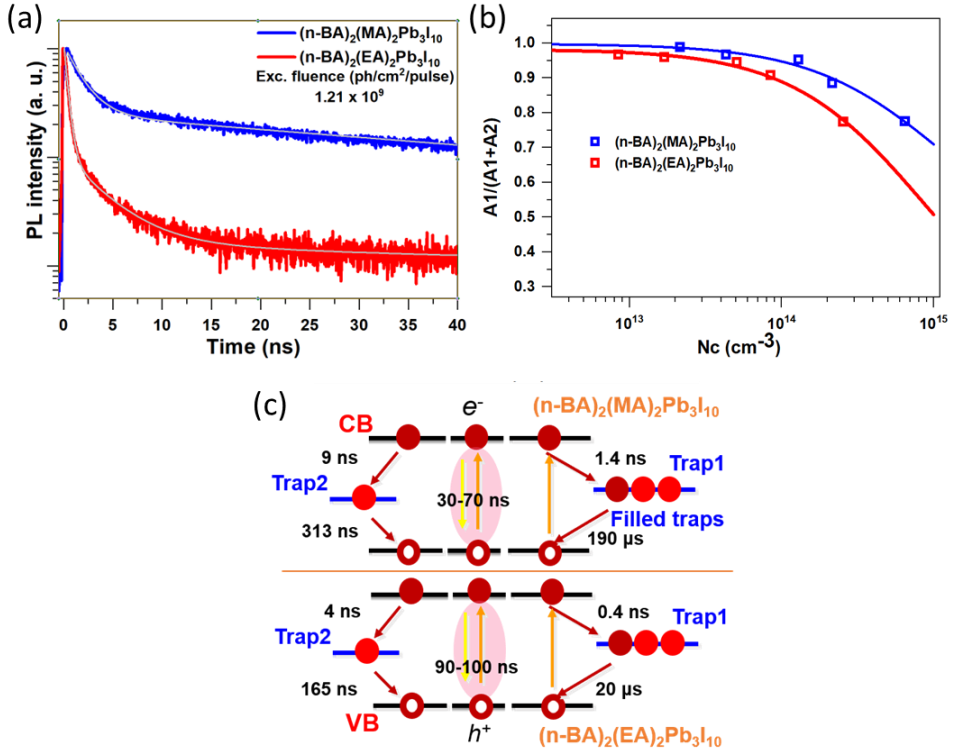


Figure 3.3 (a) TRPL spectra of BMAPI and BEAPI crystals. (b) Amplitude ratio $A_1/(A_1+A_2)$ as a function of initial charge carrier density N_c for BMAPI and BEAPI, where amplitudes are extracted from multi-exponential fitting on PL decay profile. (c) Schematic of trap-mediated charge carrier recombination in BMAPI and BEAPI, respectively.

3.2 Free Carriers and Self-trapped Excitons at Different Facets of Two-Dimensional Perovskite Single Crystal – Paper III

By comparing the photophysics of (n-BA)₂(MA)₂Pb₃I₁₀ and (n-BA)₂(EA)₂Pb₃I₁₀ single crystals, we conclude the influence of structural distortion on electronic properties. The stable formation of the latter crystal confirms the relaxed threshold of tolerance factor in 2D perovskite, with flexible spacers contributing to releasing the accumulated strain. In the following study, we further investigate the relationship between local structural distortion, i.e. bulk volume and edge area, on electronic properties.

2D perovskites have great potential in developing photoelectronic applications, such as laser, photodetectors and etc,⁵⁰ due to their remarkable electronic properties at room temperature. The properties different from the three-dimensional counterparts are enabled by the natural multiple-quantum-well structure of two-dimensional perovskite.¹⁵⁴ For future applications, the elementary photo excitations need to be understood, for example the origin of the observed broad sub-bandgap emission has been debated.¹⁵⁵⁻¹⁵⁶ One possible scenario is that the low-energy edge states (LES) are observed at the edges of the 2D perovskite single-crystal flakes. Theoretical results suggest that the formation of LES is an evidence of interface strain release at different areas (bulk and edge) in 2D perovskite.¹⁵⁷⁻¹⁵⁸ This means that the different degrees of distortion in bulk volume and edge area will lead to different electronic properties. In addition, in materials with soft lattice and strong electron-phonon interaction, self-trapped excitons (STE) can occur, whose fingerprint is a broad emission spectrum and large Stokes shift.¹⁵⁹⁻¹⁶⁰ The strong electron-phonon coupling leads to elastic distortions in the surrounding lattice and the photogenerated carriers will be 'self-trapped'. The relationship among lattice distortion, STE and LES needs to be revealed by investigating local photogenerated species in bulk and edge areas.

As suggested by theoretical studies,¹⁵⁷ the interface strain in the bulk area is released towards the spacer and the strain accumulation along the direction of the layer is relaxed at the edge area, as shown in **Figure 3.4a**. Thus, the optical measurements are conducted on in-plane facets (IF) and facet perpendicular to the octahedral layer (PF) for investigating charge dynamics in bulk and edge areas, respectively. Since the spacer plays a significant role in strain relaxation, the formation of LES can be modulated by varying spacers. Therefore, in this study perovskite single crystal with similar molecular formula $((A')_2A_{n-1}B_nX_{3n+1})$ where A is MA^+ , B is Pb^{2+} , X is Br^{2+} and $n = 2$) but different spacer such as iso-butylamine (iso-BA), n-butylamine (n-BA), and n-pentylamine (n-PA)) are employed and labeled as iso-BAPB, n-BAPB and n-PAPB, respectively. The structures of the three samples having different layer spacers are shown in **Figure 3.4b-d**. The powder-XRD and calculations indicate that the octahedron of perovskite lattice in n-PAPB is the most distorted and has the smallest internal lattice mismatch compared to other 2D perovskites. This observation suggests that the lattice distortion releases the accumulated strain inside the crystal and eases the mismatch in comparison to the lattice of 3D perovskite ($MAPbBr_3$).

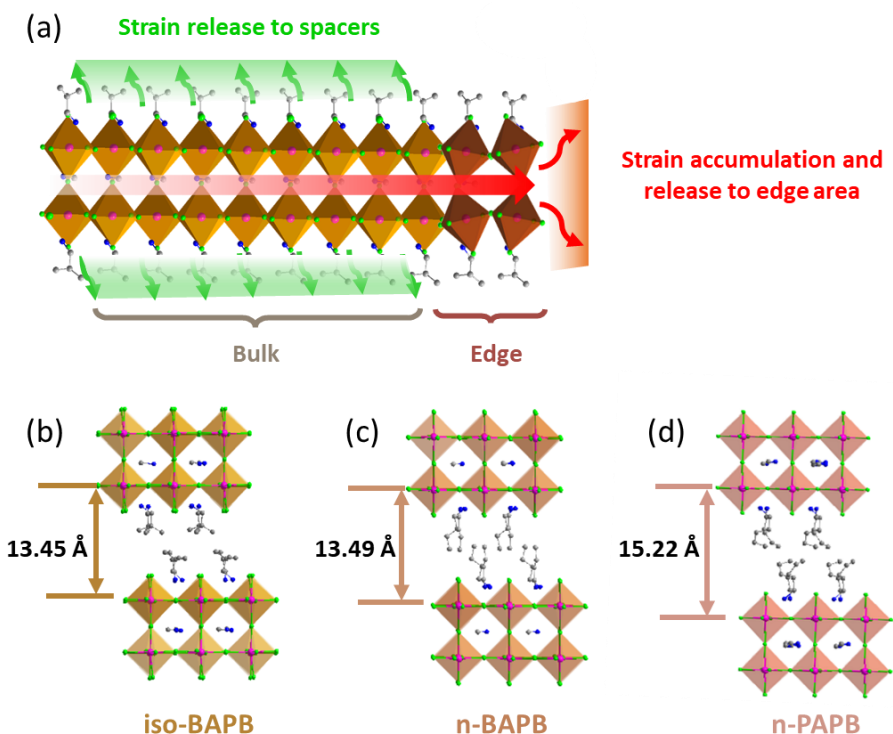


Figure 3.4 Structure of 2D perovskites. (a) Illustration for strain release in 2D perovskite in bulk and edge areas with different release directions. (b-d) Lattice structures of iso-BAPB, n-BAPB and n-PAPB with different layer distances.

The 2D perovskite single crystals are grown to be large enough for measuring PL signals from the surface of each targeted facet, as shown in **Figure 3.5a** and **Figure 3.5c**, for investigating the change in the electronic structure induced by local structural distortion. The difference in PL signals from the two facets are observed as different color emissions, as shown in **Figure 3.5b** and **Figure 3.5d**. A red shift of the emission of around 0.4 eV is observed on the PF facet of n-BAPB compared to the IF facet. The large energy shift implies that the octahedral distortion-induced modification on electronic structure around the band edge is not the only reason, which leads to the shift of the PL within 0.2 eV.¹⁶¹ We propose that the formation of STE is contributing to the red-shifted emission, as the photogenerated carriers are quickly self-trapped into a more stable state compared to the mobile state. To clarify the processes, we performed the temperature-dependent PL measurements on single crystals, and the results suggest that the exciton dissociation and STE formation dominate in IF and PF, respectively. The high-energy PL corresponding to the band edge emission becomes more significant in PF at low temperatures, which can be attributed to the hindered transition from free exciton (FE) to STE, as shown in

Figure 3.5e. With the formation of STEs, the energy of exciton will decrease and the energy difference between before and after STE formation is called self-trapping energy E_{st} . To confirm our explanation of the temperature dependence, the time-resolved photoluminescence spectra are collected for studying the dynamics of photogenerated species, i.e. STEs which are usually responsible for the red-shifted emission.

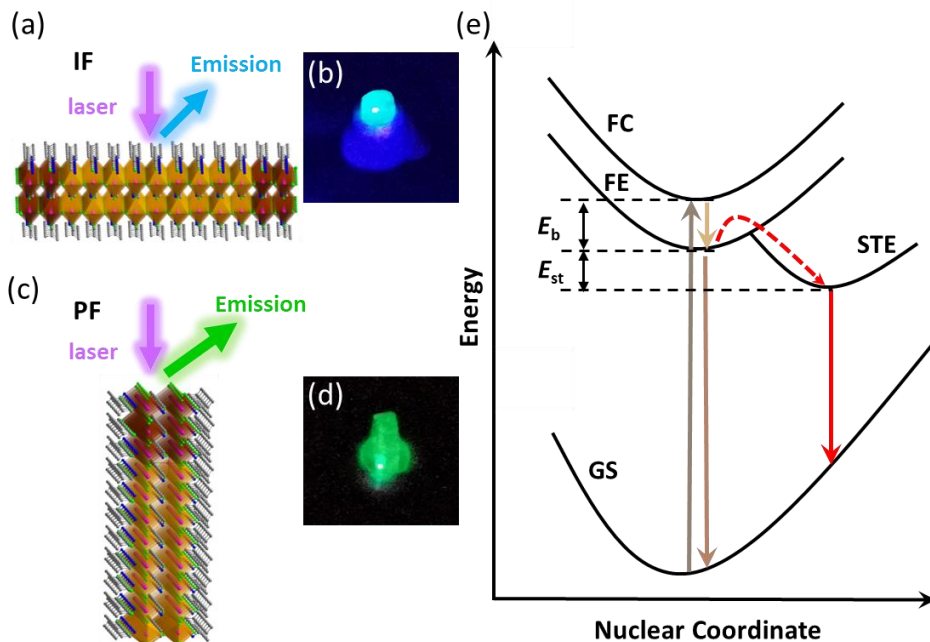


Figure 3.5 Charge carrier dynamics at in-plane facet (IF) and facet perpendicular to octahedral layer (PF). Illustration of steady-state PL measurements on (a) IF facets and (c) PF facets, and picture of *n*-BAPB single crystal under laser excitation with (b) blue emission and (d) green emission. (e) Illustration of energy level structure of STE. Free exciton state FE, free carrier state FC, ground state GS, self-trapped exciton state, exciton binding energy E_b and self-trapping energy E_{st} are marked.

At the IF of *n*-BAPB, the PL lifetime increases with excitation density, as shown in **Figure 3.6a**. The phenomenon can be attributed to the trap filling effect which is widely observed in perovskite single crystals,^{151,153} and the trap density is estimated to be $2.9 \times 10^{16} \text{ cm}^{-3}$. The observation is evidence that the majority of the photogenerated species in IF are free carriers, which is further confirmed by modeling based on the Saha-Langmuir equation. On the contrary, the PL lifetime decreases with increasing excitation density in PF of *n*-BAPB as shown in **Figure 3.6b**, suggesting the existence of another recombination process. In the picture of

STE formation, the greater lattice distortion in PF leads to small polaron formation as self-trapping.¹⁶² The distance between the traps obtained from the trap density is 32 nm. From this, we conclude that it is hard to capture the STE by the trap states at PF under low excitation density because of the relatively long mean distance between traps and the reduced mobility due to self-trapping. Thus, the dominating depopulation pathway of photoexcitations under low excitation fluence is the radiative recombination of STEs, as shown in **Figure 3.6c**. However, the motion of STEs is enhanced with increasing excitation density, illustrated in **Figure 3.6d**, confirmed by the decreased relative PL quantum yield (QY). This could be explained by the decreased stability of STEs¹⁶³ or the increased mobility of collective polaron behavior¹⁶⁴.

In conclusion, by investigating the PL dynamics at two different facets of the 2D perovskite single crystals with different spacing cations, we have obtained a better understanding of the relationship between the local structure and the pathways of photogenerated species.

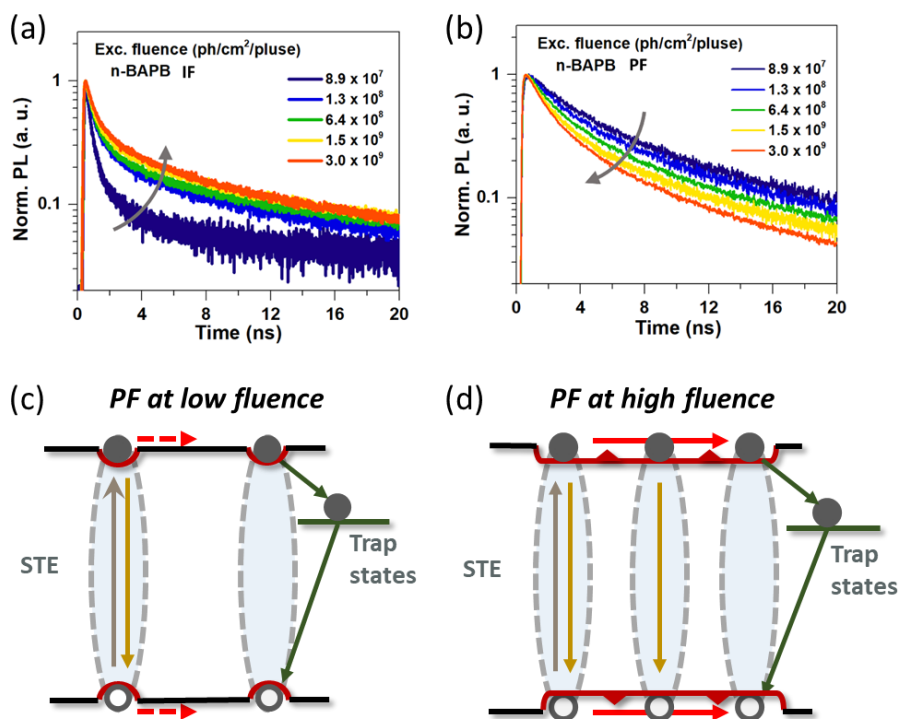


Figure 3.6 Schematic of STE in 2D perovskite single crystal. Time-resolved photoluminescence measurements on (a) IF facet and (b) PF facet. Schematics of charge carrier recombination processes in PF under (c) low excitation density and (d) high excitation density.

3.3 Local Electronic Properties of Two-Dimensional Perovskite Single Crystal – Paper V

In the above-discussed papers, the relationship between structural distortion and electronic properties is investigated by comparing photophysics in samples with different compositions or different facets of one single crystal. In the following study, we provide additional arguments by directly characterizing the electronic structure at different areas of samples by mapping the photoelectrons from Pb $5d$ and I $4d$ core levels.

The two-dimensional (2D) lead halide perovskites have drawn great attention due to their unique properties and natural quantum well structure with a formula as $(A')_2A_{n-1}B_nX_{3n+1}$, where A' is the organic spacer, A is the cation inside the octahedral cage, B is Pb^{2+} , X is the halogen and n is the number of octahedral layers.¹⁶⁵ The photo- and chemical stability of 2D perovskite is significantly improved compared to conventional three-dimensional perovskites.⁴⁸ In addition, it is found that the photophysical properties of 2D perovskite correlate with the local structure, e.g., low-energy edge states (LES) are observed at the edge area of single crystal flake, which possibly facilitates exciton dissociation into long-lived charge carriers and improves device performance.^{155, 166} The formation of LES has been debated for years and the direct characterization of local electronic structure at the edge and in the bulk area of crystal flake is urgently needed.^{157, 167-169}

In this paper, we conducted X-ray photoemission electron microscopy (XPEEM) measurements on exfoliated $(BA)_2(MA)_{n-1}Pb_nI_{3n+1}$ ($n = 1, 2, 3$) single crystal flakes. Based on the results, we can spatially resolve differences in elementary compositions and electronic structure at edge and bulk areas by mapping the Pb $5d$ and I $4d$ core levels. With varying the n -value of 2D perovskites, the relation between lattice distortion and edge states can be studied in detail.

The structure models of 2D perovskites are shown in **Figure 3.7 (a-c)** with sample images in **Figure 3.7 (d-e)**. The high quality of single crystals is confirmed by XRD measurements, and the bulky single crystal is exfoliated several times to flakes for removing potential surface contaminations before measurements. The fresh flakes are transferred on a silicon substrate and the surface of a flake is exfoliated again in the preparation chamber with high vacuum. To confirm that the long-range lattice order remains in the flakes, low-energy electron diffraction (LEED) measurements are performed on three samples and the results are consistent with the theoretical predictions on Pb-Pb distances.

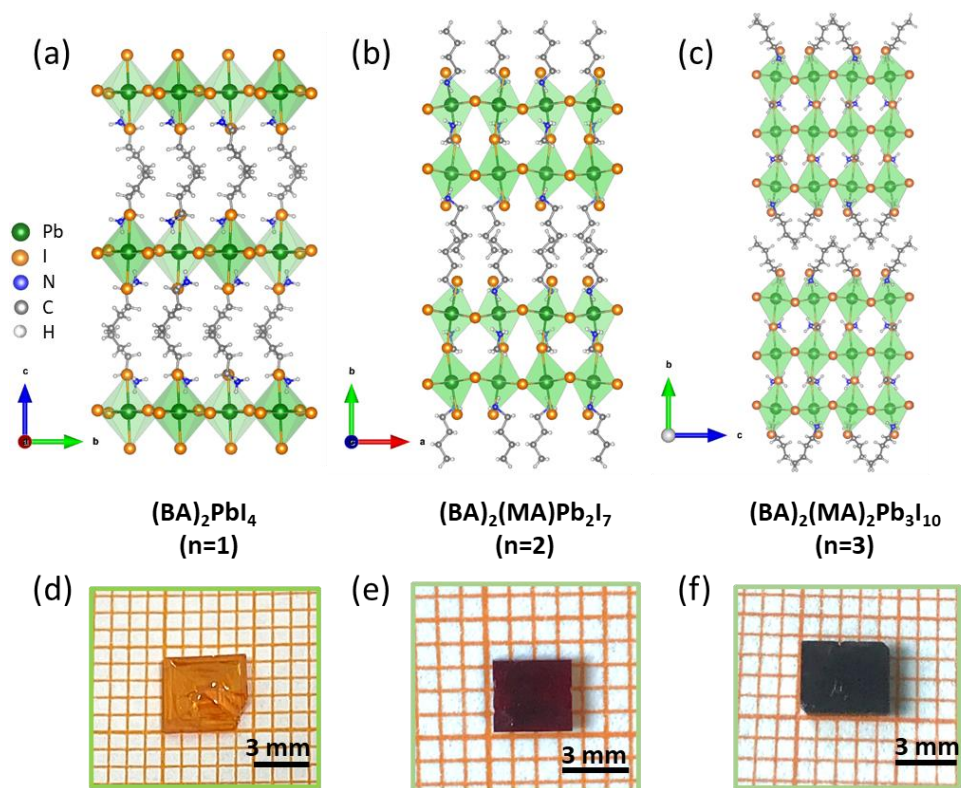


Figure 3.7 Structures and images of 2D perovskite. (a-c) Schematic of 2D perovskite lattice with different n -value, and (d-f) images of corresponding single crystals.

The XPEEM measurements on 2D perovskites focus on mapping the core electron emission at the edge and the bulk areas marked as two rectangular zones in **Figure 3.8 (a-c)**. The X-ray source used in XPEEM measurements has a photon energy of 80 eV and the energy resolution of the setup is around 0.2 eV. The results of Pb 5*d* and I 4*d* core level emission are presented in **Figure 3.8 (d-i)** for different 2D perovskites. The Pb 5*d* core level emission at the edge area is blue-shifted (to higher core-level binding energies) compared to bulk areas in all three samples by different amount, i.e. ~ 0.2 eV in $(\text{BA})_2\text{PbI}_4$ ($n = 1$) and $(\text{BA})_2(\text{MA})\text{Pb}_2\text{I}_7$ ($n = 2$), and ~ 1.0 eV in $(\text{BA})_2(\text{MA})_2\text{Pb}_3\text{I}_{10}$ ($n = 3$). The shifts of I 4*d* core level emission are negligible ($\ll 0.2$ eV) in all samples. To summarize, the Pb 5*d* core level emission is blue-shifted at the edge area compared to the bulk area, and the shift is more significant with thicker octahedral layers ($n = 3$), while the shift of I 4*d* core level emission is negligible and independent of n -value.

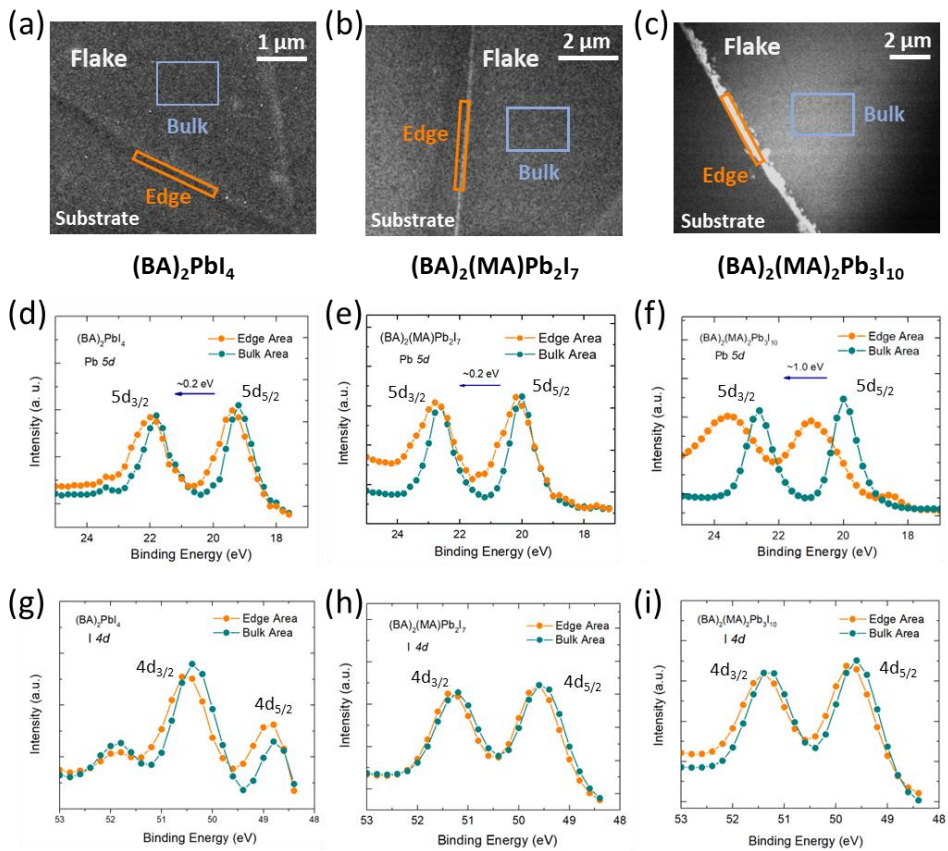


Figure 3.8 X-ray photoemission electron microscopy (XPEEM) results on 2D perovskites with different n -value. (a-c) XPEEM mapping images of $(\text{BA})_2(\text{MA})_{n-1}\text{Pb}_n\text{I}_{3n+1}$ ($n = 1, 2$ and 3), corresponding (d-f) $\text{Pb } 5d$ and (g-i) $\text{I } 4d$ core level emission spectra at edge and bulk areas.

As for the possible reason for the blue shifts in $\text{Pb } 5d$ core level emission, the change of chemical composition at the edge state is first ruled out. Considering the Pb atom as an electron donor and the I atom as an electron acceptor via Pb-I bond, an opposite shift in $\text{I } 4d$ core level emission (compare to $\text{Pb } 5d$) should be observed if the ratio between Pb and I is changed due to additional composition.

Since the lattice distortion difference in edge and bulk area has a significant impact on electronic properties, the lattice mismatch theory can be used to explain the asymmetric shifts in core-level emissions.¹⁵⁷ The lattice strain in the octahedral layer can be released in different directions, i.e. perpendicular or parallel to the plane. In the out-of-plane direction (perpendicular to the octahedral layer), the soft and flexible spacers participate in releasing strain. However, in the in-plane direction

(parallel to the octahedral layer), the lattice strain is accumulated at a long distance inside the octahedral layer and released at the edge area. The resulted local surface structural reconstruction at the edge area, as shown in **Figure 3.9a**. Therefore, the edge states are formed and are dependent on the n -value. In 2D perovskites with thin octahedral layers, i.e. $n = 1$ or 2, the accumulation of in-plane lattice strain can be significantly buffered by spacers and hinder the formation of the edge states. As a result, the core level emissions at the edge area and bulk area are more identical. In 2D perovskites with thick octahedral layers, i.e. $n = 3$ in our study, the surface structural reconstruction may lead to a larger overlap between outer electron orbitals of Pb and I atoms. The Coulomb attraction of the Pb nucleus on electrons at core levels is enhanced and results in higher core-level binding energy in core-level emissions at the edge area than at the bulk area, as shown in **Figure 3.9b**.

On the other hand, the identical I $4d$ core level emission at the edge and bulk areas might be attributed to the contribution of N-H...I hydrogen bonds. The reorganization of charge distribution within the Pb-I metavalent bond is balanced and thus the core level emission from the I atom is independent of n -value and local structure distortion.

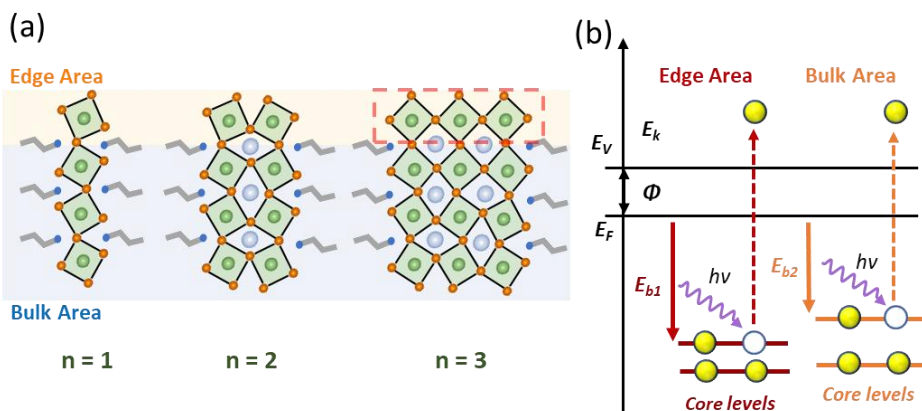


Figure 3.9 Illustration of core level emission at edge and bulk area. (a) Schematic of local structure at edge and bulk areas for 2D perovskites with different n -value. (b) Energy diagram of electron emission from Pb core levels at edge and bulk areas, with related transitions marked. $h\nu$ is the energy of excitation, E_k is the kinetic energy of generated electrons, ϕ is the work function, E_v is the vacuum level, E_F is Fermi level, E_{b1} and E_{b2} are the core-level binding energies of target Pb core levels at edge and bulk areas.

3.4 Hot Carrier Cooling in Two-Dimensional Perovskite Single Crystal – Paper I

The previous studies focus on revealing the electronic properties of 2D perovskites with different compositions or at different areas of single crystal samples. In the following study, we target hot carrier (HC) relaxation processes in 2D perovskites and link the observation to the spatial sensitivity of cooling dynamics across the sample.

Metal halide perovskites have various outstanding properties which make them good candidates for solar cell applications.¹⁸ 2D perovskite, which has a natural multiple-quantum-well structure,⁴⁹ improved stability^{50, 154} and extended variable compositions compared to 3D perovskites,⁵⁸ has drawn interest widely as building blocks for solar cell applications.¹⁷⁰ For solar cells with power conversion efficiency exceeding the Shockley-Queisser limit, a promising concept is hot carrier solar cell (HCSC) with theoretical efficiency reaching 66%.¹³ The essential idea of the concept lies in reducing heat loss during device operation, which is the most pronounced loss channel in solar cells. The excess energy released from hot photogenerated carriers is used to heat the “cold” carriers close to the band edge. If the carrier energies can stay high, which corresponds to elevated temperature, long enough for continuous extraction via electrodes significant efficiency improvement can be achieved. For this to work, materials whose photogenerated carriers cool down slowly would be needed.

3D perovskite has drawn increasing attention as a potential material candidate for HCSC applications, e.g. large phononic bandgap between optical and acoustic phonon branches.^{89, 104} Klemens decay, the most efficient channel of phonon decay in polar semiconductors,⁸² can be hindered if the Two-dimensional perovskite as a promising building block for solar devices, has unique properties that might potentially hinder the hot carrier relaxation and enable hot quasi-equilibrium states with long lifetime. For example, the propagation of acoustic phonons might be hindered due to the existence of soft and long-chain spacers and the hot phonon bottleneck effect may be enhanced due to the multiple-quantum-well (MQW) structure.^{10, 171}

On the other hand, extensive researches have been conducted for investigating mechanisms of hot carrier relaxation based on ultrafast spectroscopy, such as transient absorption spectroscopy (TA) and time-resolved photoluminescence spectroscopy. However, standard analysis requires the selective fitting of the high energy tail part of the spectra, which might lead to errors when using different fitting ranges or equations.¹⁷² A technique with which the population and energy

distribution of hot carriers can be directly observed is needed to make a universal comparison among different samples.

All in all, a comprehensive study of 2D perovskite with direct observation of hot carrier distribution, is needed. In this paper, the hot carrier relaxation process in exfoliated (BA)₂(MA)₂Pb₃I₁₀ single-crystal flakes is investigated by employing transient absorption (TA) spectroscopy and time-resolved two-photon photoemission (TR-2PPE) spectroscopy. Signals from the two techniques provide information about carrier dynamics in surface and bulk areas, which allow us to relate HC relaxation mechanisms to the material properties of 2D perovskite single crystal.

To prevent the influence of moisture and oxygen on sample properties, the single crystal is exfoliated into flakes (diameter around 100 μm and thickness around 100 nm) and capsuled between two quartz plates in the glove box. The TA spectra of 2D perovskite single crystal flake are shown in **Figure 3.10a**, where the sample is photoexcited at 3.1 eV (400 nm) and probed by a white light. Since the TA signal reflects the population of photogenerated carriers in excited states, the carrier temperature (system energy) can be extracted by fitting the high energy tail of ground-state bleaching with the Boltzmann distribution.

$$\frac{\Delta T}{T} = A_1 + A_2 \exp\left(-\frac{E - E_f}{k_B T_C}\right) \quad (3.1)$$

The method has been widely reported in literature.^{88, 173} Since the effective masses of electron and hole are similar, the calculated carrier temperature T_C represents the average temperature of the system. The decay of carrier temperature over time after carrier thermalization (~ 0.3 ps) is shown in **Figure 3.10b** and fitted by the single exponential function. The HC lifetime is in the range of a few picoseconds, and the hot carrier relaxation is slowed down with increasing excitation density.

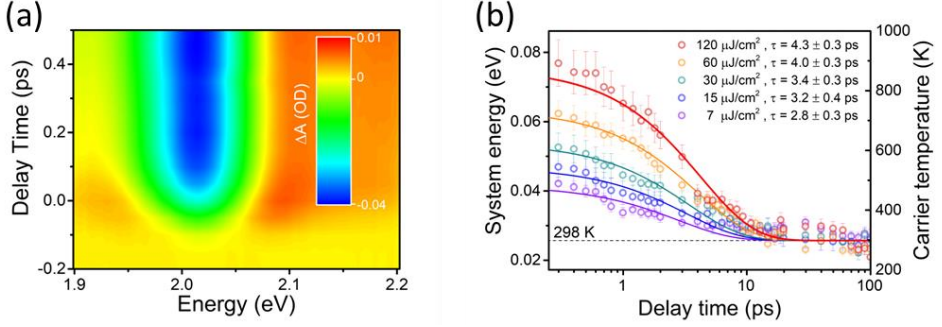


Figure 3.10 Transient absorption measurements for investigating hot carrier relaxation rate. (a) TA spectrum of 2D perovskite single crystal flake, where the pump is 3.1 eV with the intensity of 30 $\mu\text{J}/\text{cm}^2$, and the probe is white light. (b) Decay of hot carrier temperature as a function of time delay under different excitation densities.

By pumping crystal with the same excitation (3.1 eV) but probing it with a middle ultraviolet probe beam, electrons in the conduction band can be further excited to vacuum and collected by the analyzer showing electron distribution along momentum and energy axis. The crystal is cleaved inside the preparation chamber with high vacuum to produce an atomically flat and clean surface, since the TR-2PPE measurements are highly surface-sensitive. The mean escape depth of photoelectrons is around 3 nm,¹⁷⁴ and thus the very surface layer plays a significant role in providing signals, as shown in **Figure 3.11a**. Compared to the case in TA measurements where the whole bulk volume (100 nm thickness) of flake is probed, the TR-2PPE only monitors the hot electron distribution at the surface layer. The spectrogram is presented in **Figure 3.11b** which clearly shows two cooling stages. The average excess energy $E_x(t)$, calculated by integrating the overall excess energy distribution.

$$E_x(t) = \frac{\int E[I(E, t) - I(E, -)]dE}{\int [I(E, t) - I(E, -)]dE} \quad (3.2)$$

The average excess energy can be used to represent the system energy at different time delays as shown in **Figure 3.11c**. Fitting the decay profile of average excess energy with bi-exponential function, two stages of electron relaxation. First a rapid cooling in sub-picosecond timescale takes place, followed by a slower component in few picosecond range.

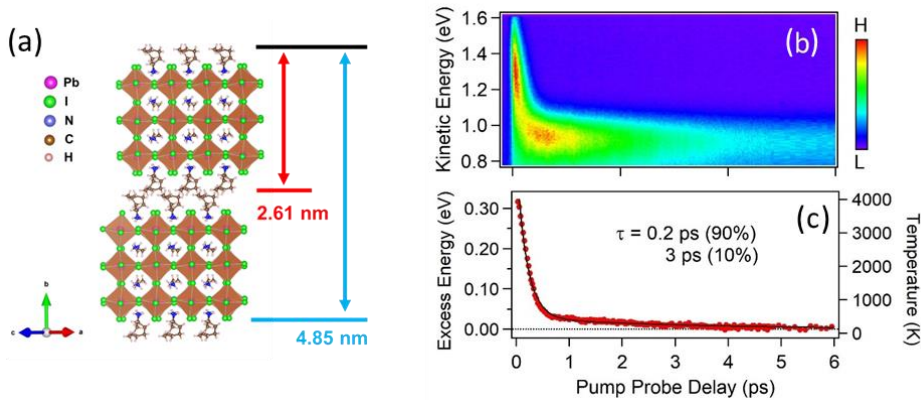


Figure 3.11 Surface-sensitive time-resolved two-photon photoemission measurements for investigating hot carrier relaxation rate. (a) Schematic of the 2D perovskite structure. (b) TR-2PPE spectrogram of 2D perovskite single crystal flake, where the pump is 3.1 eV with excitation intensity of $100 \mu\text{J}/\text{cm}^2$ and probed is 4.65 eV. (c) Decay of average excess energy of the system as a function of time delay.

The results from TA and TR-2PPE are summarized in **Figure 3.12a**, where the carrier temperature T_c and average excess energy $E_x(t)$ are converted into system energy for simplifying the comparison. Since the carrier temperature cannot be quantified before carrier thermalization, the initial system energy value from TR-2PPE is adopted as a starting point in TA analysis and the two time constants of HC relaxation are calculated to be ≤ 0.1 ps and 4.3 ps. Two main differences in TA and TR-2PPE results are a faster cooling rate in Stage I and a higher amplitude of Stage II in TA analysis.

The clear observation of two stages in HC relaxation can be attributed to the hot phonon bottleneck. As HCs warm up longitudinal optical (LO) phonons and reach an equilibrium with these phonons, the further cooling of HCs is slowed down and corresponds to the energy flow from the LO phonons to acoustic phonons. Stage I can be assigned to the carrier-LO phonon scattering and Stage II is related to the relaxation of LO phonons to acoustic phonons. The different HC relaxation rate in TA and TR-2PPE in Stage I has several possible reasons. One significant difference between these two techniques is that the signal in TR-2PPE dominantly comes from the surface layer, while the whole bulk volume is probed in the TA measurements. The faster relaxation rate in TA analysis suggests stronger carrier-LO phonon coupling strength or larger density of states of LO phonons in bulk volume. It is reported that the lattice distortions at the surface and in the bulk are different based on the scanning tunneling microscopy investigations,¹⁷⁵ and the carrier-phonon coupling strength can be enhanced due to the strain-accumulated area based on our

previous study¹⁷⁶. Thus, the relaxed steric hindrance in the surface layer can lead to a weaker carrier-phonon coupling than in bulk volume. In addition, the soft and flexible spacer attached to the surface layer might result in reduced availability of the ‘regular phonons’ for HCs to couple to and leads to a reduced efficiency of HC relaxation at the surface at Stage I. Another possible reason is that the environmental temperatures in TA (room temperature) and tr-2PPE (135 K) measurements are different, which changes the thermal population of LO phonons and affects the cooling efficiency. However, the spacer modification can change vibrational frequencies,¹⁷⁷ therefore the effect of the environmental temperature on HC relaxation cannot be clearly evaluated due to the uncertain LO phonon energy.¹⁷⁸⁻¹⁷⁹ A further difference between the two experiments is that only hot electrons are probed in tr-2PPE measurements, while both electrons and holes contribute to the signal in TA measurements. The slightly lighter effective mass of electrons than holes can lead to different Fröhlich coupling constant,¹⁸⁰ whilst as a minor influencing factor on HC cooling rate. As for the higher initial carrier temperature of the Stage II in TA analysis, we speculate that the LO phonon density of states is higher at the surface, thus can accommodate more energy and the hot phonon bottleneck effect appears at a lower temperature compared to the bulk area.

Our investigation provides information about spatial-sensitive HC relaxation dynamics in 2D perovskite single crystal by conducting two comprehensive spectroscopic measurements, which may benefit HCSC application when using 2D perovskites as building blocks. In addition, TR-2PPE shows its potential in investigating HC relaxation with direct visualization of relaxation stages.

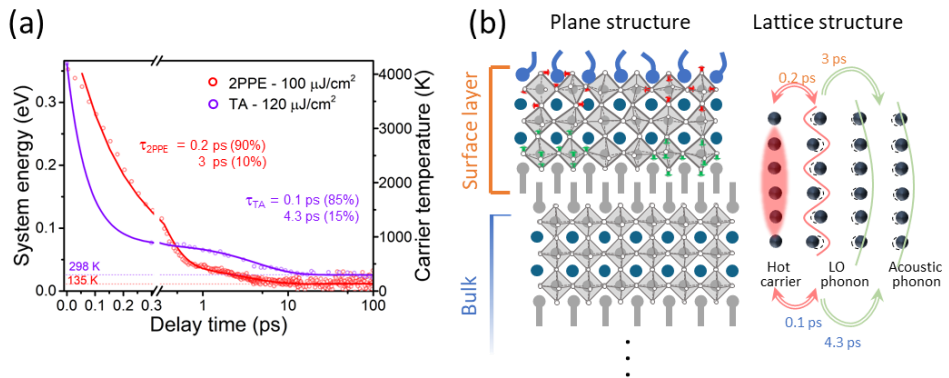


Figure 3.12 Illustration of the different observed HC decay dynamics from TA and TR-2PPE measurements. (a) Decay dynamics of HC temperature extracted from analysis on TA and TR-2PPE measurements. (b) Schematic of hot carrier relaxation processes in surface and bulk areas.

3.5 Hot Carrier Cooling in Mn-Doped Inorganic Perovskite Nanocrystals– Paper IV

The previous articles present the characterization of 2D perovskite single crystals, the relation between structure and electronic properties, and the relaxation dynamics of hot carriers in 2D perovskites. In the following study, we investigate the influence of transition metal doping on electronic and phononic properties in 3D perovskite nanocrystals and the resulting modification of hot carrier relaxation dynamics.

The concept of hot carrier solar cells (HCSCs) is established for producing solar cells with efficiency exceeding the Shockley-Queisser limit.¹³ The photogenerated carrier with high excess energy relaxes via several processes until reaches equilibrium with the environment. To improve the power conversion efficiency of devices, the hot carriers need to be kept at quasi-equilibrium status for a sufficiently long time so that they can be extracted. Various mechanisms are proposed for slowing down hot carrier relaxation, e.g. hot phonon bottleneck,⁸⁸ polaron formation⁶⁴ and Auger heating⁸⁹. The origin of mechanisms is highly dependent on material properties and experimental conditions. Investigating hot carrier relaxation in different materials is helpful for establishing general selection criteria of material candidates as HCSC absorbers. In addition, optimizing the HC extraction is required for recycling the released energy from the relaxation of HC towards band edge. One way to achieve the goal is to develop energy-selective contacts to limit the energy range of extracted HC and thus avoid the waste of HC excess energy. However, the perfect energy alignment between the absorber and electrodes is challenging. Another way is adjusting the material composition to alter HC relaxation dynamics and create a long-lived quasi-equilibrium status, while the HC excess energy can be used to reheat cold carriers. The generally involved processes in HC relaxation in polar materials are carrier-carrier scattering, carrier-LO phonon scattering and decay of LO phonon.⁸⁹ A material with enhanced carrier-LO phonon interaction and hindered LO phonon decay is desired, since the former interaction is contributing to establishing the mentioned quasi-equilibrium while the last process is dissociating such quasi-equilibrium.

Lead halide perovskite (LHP) is a promising material candidate for HCSC with various appreciated properties, such as efficient HC extraction, long HC lifetime and transportation distance.^{37, 104, 181} Furthermore, transition metal doping is found to have a significant impact on the properties of LHP.¹⁸²⁻¹⁸⁴ The doping results in long-lived triplet luminescence after charge or energy transfer from host to Mn²⁺.¹⁸⁵⁻¹⁸⁶ In addition, local structural distortion is induced due to the partial replacement of Pb²⁺ by Mn²⁺, as shown in **Figure 3.13**, which has a different cation radius. X-

ray absorption (XAS) spectroscopy is used to confirm Mn^{2+} doping in perovskite lattice instead of presenting as Mn^0 clusters on samples with different doping concentrations.

Since the HC relaxation processes are determined by the electronic structure and phononic structure of the material, it is expected that the Mn^{2+} doping can significantly modulate HC relaxation dynamics and help establish the preferred quasi-equilibrium. Thus, in this work, the HC relaxation dynamics in Mn-doped $CsPbI_3$ nanocrystals (NCs) are investigated in detail by employing transient absorption (TA) spectroscopy on samples with different doping concentrations.

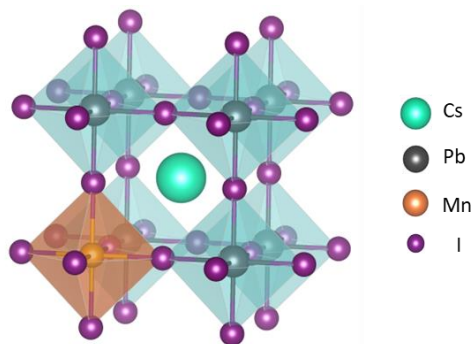


Figure 3.13 Schematic of incorporation of Mn^{2+} ion in perovskite lattice.

The transient absorption spectroscopy is used to characterize the HC relaxation dynamics in Mn-doped perovskite NCs under different excitation energies and intensities. After carrier-carrier scattering within 100 fs timescale, the HC redistributes and reaches Fermi-Dirac distribution with system energy being much higher than lattice temperature. The carrier temperature can be quantized by fitting the high energy tail of the beaching signal to the Boltzmann distribution. The analysis of HC cooling dynamics starts after a delay of 0.3 ps to ensure that HCs have redistributed their energies and reached the quasi-equilibrium status. Considering the similar effective masses of electrons and holes, the contribution from hot electrons and hot holes are assumed equal.

The HC relaxation dynamics of undoped and doped perovskite NCs under different excitation densities are presented as **Figure 3.14 (a-b)**. It is observed that HC relaxation is slowed down with increasing carrier densities in both samples. The kinetics can be well fitted with bi-exponential function, where the fast component is assigned to the HC relaxation via carrier-LO phonon coupling and the LO phonon decay is involved in explaining the slow component. The phenomenon is also observed under other excitation energies and can be explained by the enhanced hot

phonon bottleneck effect under high excitation intensity. The HC cooling dynamics of undoped and doped CsPbI₃ NCs under different excitation energies are shown as **Figure 3.14 (c-d)**, with fitted average HC lifetimes inserted inside figures. The 2.18 eV excitation is close to the energy of the bandgap and photogenerated HC has less excess energy compared to under 3.1 eV excitation. To have a clear observation of HC relaxation at different stages, the power loss rate as a function of carrier temperature is calculated as $P = d(1.5k_B T_C) / dt$. In summary, the HC relaxation in doped NCs is slower under 2.18 eV but faster under 3.1 eV excitation compared to undoped NCs.

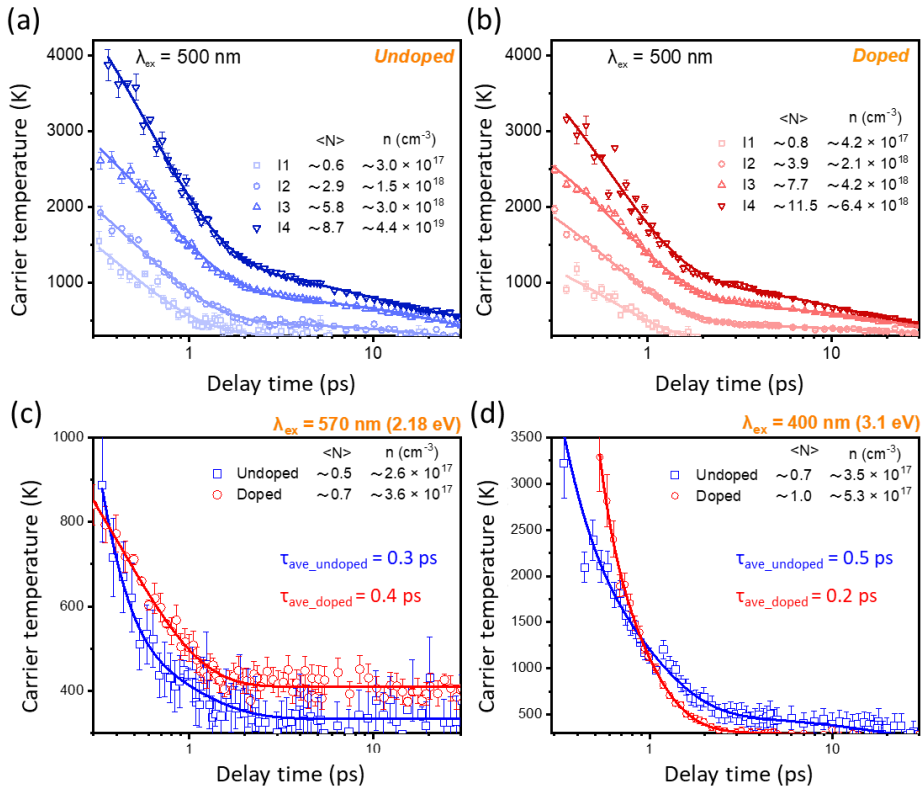


Figure 3.14 TA results and analysis of carrier temperature in Mn-doped CsPbI₃ NCs. (a-b) Carrier temperature as a function of time delay under 500 nm (2.48 eV) excitation at different excitation intensities in undoped and doped perovskite NCs. (c-d) Carrier temperature decay profiles in undoped and doped perovskite NCs under 570 nm (2.18 eV) and 400 nm (3.1 eV) excitation.

Two distinct slopes represent two HC relaxation stages, related to equilibrium between HC and LO phonons and equilibrium among HC, LO phonons and acoustic

phonons, respectively. The difference in relaxation rate in the two regions is highly dependent on material properties, i.e. electronic and phononic structure.

The electronic band structures of undoped and doped NCs are calculated using DFT, as shown in **Figure 3.15 (a-b)**. The effective masses of electrons and holes in doped NCs are greater than in undoped NCs due to the perturbation in the periodicity of Pb $6p$ orbital with Mn-doping. Due to the relation between Fröhlich coupling strength and effective masses, faster HC cooling is expected in doped NCs.⁸⁹ The strengthened carrier-LO phonon coupling is also confirmed by the temperature-dependent PL measurements. In addition, the calculation of density of states (DOS) in undoped and doped NCs shows that additional Mn orbitals are added into the original perovskite electronic structure (mainly Pb and I orbitals), which are marked in pink in the **Figure 3.15b**. As a result, when the sample is under high-energy excitation, more channels are possibly available for HC relaxation.

The projected phononic band structures of undoped and doped NCs are presented in **Figure 3.15 (c-d)**, with which we can evaluate the efficiency of LO phonons decay to acoustic phonons. The most efficient phonon decay channel is Klemens decay, where one LO phonon decays to two acoustic phonons with opposite wave vectors.¹⁸⁷ It can be significantly slowed down when the phononic bandgap between LO phonon and acoustic phonon is larger than the maximum energy of acoustic phonons, and results in a non-equilibrium population of LO phonons (hot phonon bottleneck). The phononic bandgap is enlarged in Mn-doped NCs due to the strain induced by Mn doping in local structure¹⁸⁸ and the requirement for hindering Klemens decay is fulfilled. Therefore, the LO phonon decays via other less efficient channels and potentially leads to a larger non-equilibrium population of LO phonons.

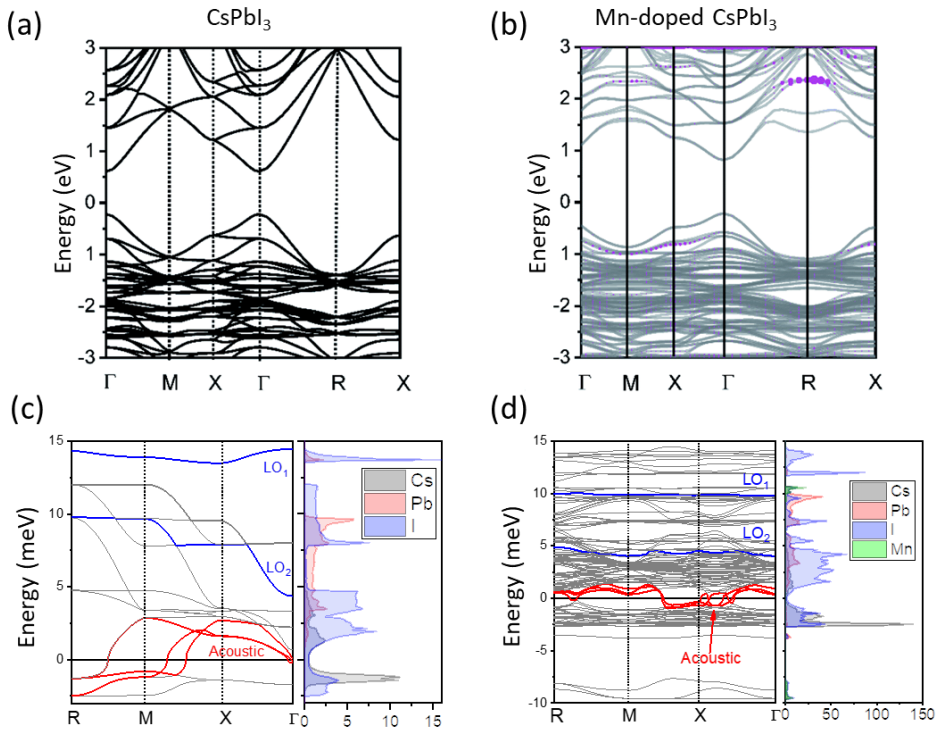


Figure 3.15 Density functional theory (DFT) calculations on undoped and doped CsPbI_3 NCs. (a-b) Electronic band structures of undoped and doped perovskite NCs with corresponding (c-d) phonon energy as a function of phonon momentum and density of states.

The influence of doping, carrier-LO phonon coupling and phonon decay on HC relaxation are summarized in **Figure 3.16 (a-b)**. Under 2.18 eV excitation (close to bandgap), the additional Mn orbitals have a minor impact on HC relaxation since they locate at higher excited states, as shown in **Figure 3.15b**. However, the increased phononic bandgap still plays a role in slowing down HC relaxation leading to a longer average HC lifetime in **Figure 3.14c**. Under high energy excitations, i.e. 2.48 eV and 3.1 eV, more factors need to be considered, as listed in **Figure 3.16b**. The faster relaxation rate in doped NCs is resulted from competition among the influence of additional Mn orbitals, enhanced carrier-LO phonon coupling and enlarged phononic bandgap. The output of competition is beneficial to establish the desired quasi-equilibrium state for HC extraction.

The influence of Mn doping on average HC lifetime is summarized in **Figure 3.16 (c-e)**. Under low energy excitation (2.18 eV), the HC relaxation is slowed down with increasing doping concentration as **Figure 3.16c**, with combined influence from the altered phononic structure and e-ph coupling. The change originates from

local lattice disordering around Mn atoms as confirmed by X-ray absorption near edge spectroscopy (XANES) characterization. Under high energy excitations, the average HC lifetime decreases with doping concentration under 2.48 eV excitation as **Figure 3.16d**, but first decreases and then increases with doping concentration under 3.1 eV as **Figure 3.16e**. As indicated by XANES measurements that the distortion of Mn-I bonds monotonously increases with doping concentration, the mixing (overlap) between orbitals of Mn and I are possibly altered, and the change significantly affects available states related to HC relaxation pathways. In addition, the dependence indicates the influence of addition pathways due to Mn orbitals dominates HC relaxation under low doping concentrations, while the enlargement in phononic bandgap dominates HC relaxation under high doping concentrations.

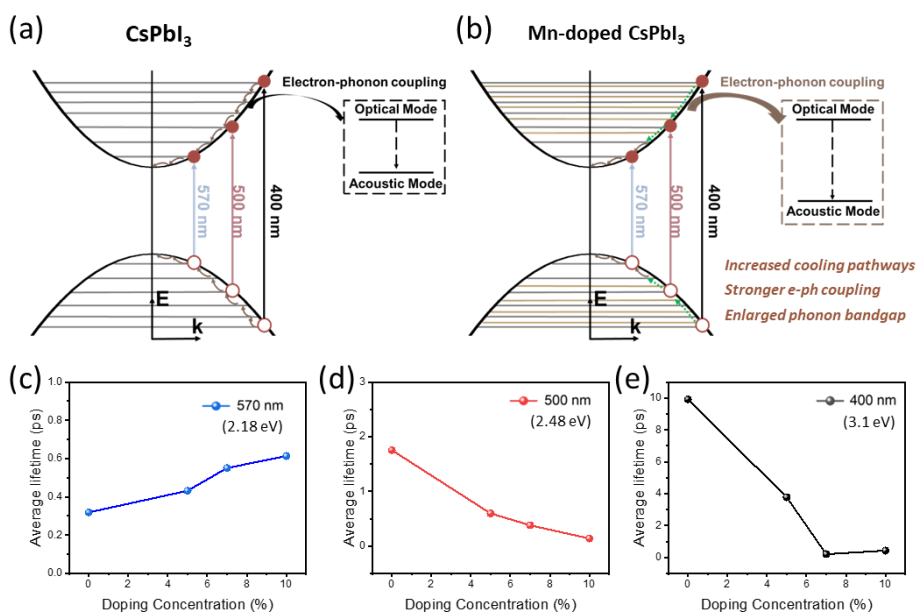


Figure 3.16 Schematic of HC relaxation processes in undoped and doped CsPbI₃ NCs. (a-c) Average HC lifetime in Mn-doped CsPbI₃ perovskite NCs with different doping concentrations under 400 nm (3.1 eV), 500 nm (2.48 eV) or 570 nm (2.18 eV) excitation energies, respectively. (d-e) Illustration of HC relaxation in undoped and doped CsPbI₃ NCs with different excitation energies, where the organic lines represent the contribution of Mn orbitals in the electronic band structure.

4 Conclusions

Paper I, II, III and V is a series of comprehensive investigations on the photophysics of two-dimensional (2D) perovskite single crystals, by carefully assessing the charge carrier dynamics and revealing the relation between structural distortion and electronic structure. Two key approaches we applied in the investigations: (1) comparing photophysics properties of 2D perovskite single crystals with different compositions and different facets of the crystal, and (2) applying various ultrafast spectroscopy techniques to provide information on hot carrier relaxation from different aspects.

The formula of lead halide two-dimensional perovskites can be presented as $(A')_2A_{n-1}B_nX_{3n+1}$, where A' is the long-chain organic spacer, A is the cation inside the octahedral cage, B is the Pb^{2+} cation, X is the halogen and n is the number of octahedral layers in one unit cell. The existence of spacers enables the ability to extend the selection range of molecular compositions in 2D perovskite compared to its 3D alternatives. In this thesis, different targeted samples are used with varying the A' spacer cation (Paper III), A -site cation (Paper II) and n -value (Paper V).

In Paper II, we characterize the lattice and electronic structure of $(n-BA)_2(MA)_2Pb_3I_{10}$ (BMAPI) and $(n-BA)_2(EA)_2Pb_3I_{10}$ (BEAPI) single crystals. Two samples have different degrees of lattice distortion and we confirm the relaxed threshold on tolerance factor in 2D perovskite, with accumulated strain in rigid octahedral layers being compensated by the flexible long-chain spacers. In addition, we find that BEAPI, which has greater lattice distortion, has a larger band gap and higher trap state density compared to BMAPI.

In Paper III, we further extend the investigation on the link between structure and photophysics in 2D perovskites by studying PL signals from different facets of bulky $(iso-BA)_2(MA)Pb_2Br_7$ (iso-BAPB), $(n-BA)_2(MA)Pb_2Br_7$ (n-BAPB), and $(n-PA)_2(MA)Pb_2Br_7$ (n-PAPB) single crystals. Based on structure characterization, we find that internal lattice mismatch varies in samples with different spacers, which provides evidence that the spacers contribute to releasing internal strain accumulation. In all samples, a red shift around 0.4 eV in PL spectra is observed on the facet perpendicular to the 2D layer (PF), in comparison to the in-plane facet (IF). We propose that the free carriers dominate the emission from IF and STE are the main emitters from the PF of 2D perovskite single crystals.

In Paper V, we directly characterize the electronic structure at different areas of samples with different n -value, with formula as $(\text{BA})_2\text{PbI}_4$, $(\text{BA})_2(\text{MA})\text{Pb}_2\text{I}_7$ and $(\text{BA})_2(\text{MA})_2\text{Pb}_3\text{I}_{10}$. Based on X-ray photoemission electron microscopy measurements, photoelectrons emitted from Pb $5d$ and I $4d$ core levels are mapped at the edge and bulk areas of single crystals. The emissions from the Pb $5d$ core level at edge areas are blue-shifted compared to bulk areas in all samples, with the most significant ~ 1.0 eV shift observed in the $n = 3$ sample. However, no significant shift is observed in emission from I $4d$ core level at edge and bulk areas. We believe the asymmetric shifts in core level emission can be attributed to the different degrees of lattice distortion at edge and bulk areas, where the strain accumulated along the 2D layer is released at the edge area. In addition, the shift in Pb $5d$ core level emission from edge and bulk areas depends on the n -value of samples, and is because the in-plane lattice strain in samples with $n = 1$ and 2 can be efficiently buffered by spacers, which is not the case in the sample with $n = 3$.

In the above-mentioned papers, we focus on studying the relation between lattice structure and electronic structure, by comparing 2D perovskite with different compositions or detecting signals from different areas of the sample.

In Paper I, we explore the ultrafast charge carrier dynamics (hot carrier relaxation) in 2D perovskite using transient absorption (TA) spectroscopy and time-resolved two-photon photoemission (TR-2PPE) spectroscopy. The distribution of hot electrons can be directly mapped in TR-2PPE measurements, as well as its relaxation dynamics in the conduction band. The hot carrier decay kinetics obtained from the two techniques both have two cooling stages due to the hot phonon bottleneck effect, while a faster cooling rate in Stage I and a higher initial carrier temperature in Stage II are observed in TA analysis. Since the whole bulk area is probed in TA measurements while TR-2PPE signals mainly come from the outermost layer, we believe the spatial sensitivity of cooling dynamics across the 2D perovskite single crystal contributes to the different cooling rates in Stage I observed in two techniques.

2D perovskite has shown its potential in solar cell applications as a promising building block, and we perform a series of investigations on 2D perovskite single crystals to characterize its intrinsic properties and relation with lattice structure.

In Paper IV, we investigate the impact of transition metal doping on electronic and phononic properties in 3D perovskite nanocrystals and the resulted change in hot carrier relaxation kinetics between doped and undoped samples under different excitation intensities and energies. In Mn^{2+} -doped CsPbI_3 nanocrystals, the phononic gap between longitudinal optical (LO) – acoustic phonon is enlarged, the coupling strength of carrier-LO phonon interaction is enhanced and additional HC relaxation pathways are added via Mn orbitals within bands, compared to the undoped sample. The phenomenon is optimal for hot carrier solar cell application,

where a high-temperature thermal quasi-equilibrium is established for recycling the energy from the hot carrier relaxation to reheat the cold carriers.

References

- (1) Snaith, H. J. Present status and future prospects of perovskite photovoltaics. *Nat. Mater.* **2018**, *17*, 372-376.
- (2) Green, M. A.; Bremner, S. P. Energy conversion approaches and materials for high-efficiency photovoltaics. *Nat. Mater.* **2017**, *16*, 23-34.
- (3) Green, M. A.; Ho-Baillie, A.; Snaith, H. J. The emergence of perovskite solar cells. *Nat. Photonics* **2014**, *8*, 506-514.
- (4) Green, M. A. Third generation photovoltaics: solar cells for 2020 and beyond. *Physica E* **2002**, *14*(1-2), 65-70.
- (5) Shockley, W.; Queisser, H. J. Detailed Balance Limit of Efficiency of p-n Junction Solar Cells. *J. Appl. Phys.* **1961**, *32*(3), 510-519.
- (6) Rao, A.; Friend, R. H. Harnessing singlet exciton fission to break the Shockley–Queisser limit. *Nat. Rev. Mater.* **2017**, *2*, 17063.
- (7) Semonin, O. E.; Luther, J. M.; Choi, S.; Chen, H. Y.; Gao, J.; Nozik, A. J.; Beard, M. C. Peak External Photocurrent Quantum Efficiency Exceeding 100% via MEG in a Quantum Dot Solar Cell. *Science* **2011**, *334*(6062), 1530-1533.
- (8) Paul, K. K.; Kim, J.-H.; Lee, Y. H. Hot carrier photovoltaics in van der Waals heterostructures. *Nat. Rev. Phys.* **2021**, *3*, 178-192.
- (9) Liu, C.; Lu, Y.; Shen, R.; Dai, Y.; Yu, X.; Liu, K.; Lin, S. Dynamics and physical process of hot carriers in optoelectronic devices. *Nano Energy* **2022**, *95*, 106977.
- (10) Conibeer, G.; Shrestha, S.; Huang, S.; Patterson, R.; Xia, H.; Feng, Y.; Zhang, P.; Gupta, N.; Tayebjee, M.; Smyth, S.; Liao, Y.; Lin, S.; Wang, P.; Dai, X.; Chung, S. Hot carrier solar cell absorber prerequisites and candidate material systems. *Sol. Energy Mater. Sol. Cells* **2015**, *135*, 124-129.
- (11) Hirst, L. C.; Lumb, M. P.; Hoheisel, R.; Bailey, C. G.; Philipps, S. P.; Bett, A. W.; Walters, R. J. Spectral sensitivity of hot carrier solar cells. *Sol. Energy Mater. Sol. Cells* **2014**, *120*, 610-615.
- (12) Li, M.; Fu, J.; Xu, Q.; Sum, T. C. Slow Hot-Carrier Cooling in Halide Perovskites: Prospects for Hot-Carrier Solar Cells. *Adv. Mater.* **2019**, *31*(47), 1802486.
- (13) Ross, R. T.; Nozik, A. J. Efficiency of hot -carrier solar energy converters. *J. Appl. Phys.* **1982**, *53*(5), 3813-3818.
- (14) Chakhmouradian, A. R.; Woodward, P. M. Celebrating 175 years of perovskite research: a tribute to Roger H. Mitchell. *Phys. Chem. Miner.* **2014**, *41*(6), 387-391.
- (15) Wells, H. L. Über die Cäsium- und Kalium-Bleihalogenide. *Z. Anorg. Chem.* **1893**, *3*(1), 195-210.

- (16) Weber, D. $\text{CH}_3\text{NH}_3\text{PbX}_3$, ein Pb(II)-System mit kubischer Perowskitstruktur / $\text{CH}_3\text{NH}_3\text{PbX}_3$, a Pb(II)-System with Cubic Perovskite Structure. *Z. Naturforsch. B* **1978**, 33(12), 1443-1445.
- (17) Correa-Baena, J.-P.; Saliba, M.; Buonassisi, T.; Grätzel, M.; Abate, A.; Tress, W.; Hagfeldt, A. Promises and challenges of perovskite solar cells. *Science* **2017**, 358(6364), 739-744.
- (18) Snaith, H. J. Perovskites: The Emergence of a New Era for Low-Cost, High-Efficiency Solar Cells. *J. Phys. Chem. Lett.* **2013**, 4(21), 3623-3630.
- (19) Chen, J.; Xiang, H.; Wang, J.; Wang, R.; Li, Y.; Shan, Q.; Xu, X.; Dong, Y.; Wei, C.; Zeng, H. Perovskite White Light Emitting Diodes: Progress, Challenges, and Opportunities. *ACS Nano* **2021**, 15(11), 17150–17174.
- (20) Zhang, K.; Zhu, N.; Zhang, M.; Wang, L.; Xing, J. Opportunities and challenges in perovskite LED commercialization. *J. Mater. Chem. C* **2021**, 9(11), 3795-3799.
- (21) Ahmadi, M.; Wu, T.; Hu, B. A Review on Organic–Inorganic Halide Perovskite Photodetectors: Device Engineering and Fundamental Physics. *Adv. Mater.* **2017**, 29(41), 1605242.
- (22) Liu, X.-K.; Xu, W.; Bai, S.; Jin, Y.; Wang, J.; Friend, R. H.; Gao, F. Metal halide perovskites for light-emitting diodes. *Nat. Mater.* **2021**, 20, 10-21.
- (23) Razza, S.; Castro-Hermosa, S.; Di Carlo, A.; Brown, T. M. Research Update: Large-area deposition, coating, printing, and processing techniques for the upscaling of perovskite solar cell technology. *APL Mater.* **2016**, 4(9), 091508.
- (24) Goldschmidt, V. M. Die Gesetze der Krystallochemie. *Die Naturwissenschaften* **1926**, 14(21), 477-485.
- (25) Ji, D.; Feng, S.; Wang, L.; Wang, S.; Na, M.; Zhang, H.; Zhang, C.; Li, X. Regulatory tolerance and octahedral factors by using vacancy in APbI_3 perovskites. *Vacuum* **2019**, 164, 186-193.
- (26) Fu, Y.; Zhu, H.; Chen, J.; Hautzinger, M. P.; Zhu, X. Y.; Jin, S. Metal halide perovskite nanostructures for optoelectronic applications and the study of physical properties. *Nat. Rev. Mater.* **2019**, 4, 169-188.
- (27) Han, G.; Hadi, H. D.; Bruno, A.; Kulkarni, S. A.; Koh, T. M.; Wong, L. H.; Soci, C.; Mathews, N.; Zhang, S.; Mhaisalkar, S. G. Additive Selection Strategy for High Performance Perovskite Photovoltaics. *J. Phys. Chem. C* **2018**, 122(25), 13884-13893.
- (28) Kirschner, M. S.; Diroll, B. T.; Guo, P.; Harvey, S. M.; Helweh, W.; Flanders, N. C.; Brumberg, A.; Watkins, N. E.; Leonard, A. A.; Evans, A. M.; Wasielewski, M. R.; Dichtel, W. R.; Zhang, X.; Chen, L. X.; Schaller, R. D. Photoinduced, reversible phase transitions in all-inorganic perovskite nanocrystals. *Nat. Commun.* **2019**, 10, 504.
- (29) Jain, P.; Dalal, N. S.; Toby, B. H.; Kroto, H. W.; Cheetham, A. K. Order–Disorder Antiferroelectric Phase Transition in a Hybrid Inorganic–Organic Framework with the Perovskite Architecture. *J. Am. Chem. Soc.* **2008**, 130(32), 10450-10451.
- (30) Parrott, E. S.; Milot, R. L.; Stergiopoulos, T.; Snaith, H. J.; Johnston, M. B.; Herz, L. M. Effect of Structural Phase Transition on Charge-Carrier Lifetimes and Defects in $\text{CH}_3\text{NH}_3\text{SnI}_3$ Perovskite. *J. Phys. Chem. Lett.* **2016**, 7(7), 1321-1326.

- (31) Quarti, C.; Mosconi, E.; Ball, J. M.; D'Innocenzo, V.; Tao, C.; Pathak, S.; Snaith, H. J.; Petrozza, A.; De Angelis, F. Structural and optical properties of methylammonium lead iodide across the tetragonal to cubic phase transition: implications for perovskite solar cells. *Energy Environ. Sci.* **2016**, 9(1), 155-163.
- (32) Poglitsch, A.; Weber, D. Dynamic disorder in methylammoniumtrihalogenoplumbates (II) observed by millimeter - wave spectroscopy. *J. Chem. Phys.* **1987**, 87(11), 6373-6378.
- (33) Wehrenfennig, C.; Liu, M.; Snaith, H. J.; Johnston, M. B.; Herz, L. M. Homogeneous Emission Line Broadening in the Organo Lead Halide Perovskite $\text{CH}_3\text{NH}_3\text{PbI}_{3-x}\text{Cl}_x$. *J. Phys. Chem. Lett.* **2014**, 5(8), 1300-1306.
- (34) Shi, D.; Adinolfi, V.; Comin, R.; Yuan, M.; Alarousu, E.; Buin, A.; Chen, Y.; Hoogland, S.; Rothenberger, A.; Katsiev, K.; Losovyj, Y.; Zhang, X.; Dowben, P. A.; Mohammed, O. F.; Sargent, E. H.; Bakr, O. M. Low trap-state density and long carrier diffusion in organolead trihalide perovskite single crystals. *Science* **2015**, 347(6221), 519-522.
- (35) Chen, Y.; Yi, H. T.; Wu, X.; Haroldson, R.; Gartstein, Y. N.; Rodionov, Y. I.; Tikhonov, K. S.; Zakhidov, A.; Zhu, X. Y.; Podzorov, V. Extended carrier lifetimes and diffusion in hybrid perovskites revealed by Hall effect and photoconductivity measurements. *Nat. Commun.* **2016**, 7, 12253.
- (36) Stranks, S. D.; Eperon, G. E.; Grancini, G.; Menelaou, C.; Alcocer, M. J. P.; Leijtens, T.; Herz, L. M.; Petrozza, A.; Snaith, H. J. Electron-Hole Diffusion Lengths Exceeding 1 Micrometer in an Organometal Trihalide Perovskite Absorber. *Science* **2013**, 342(6156), 341-344.
- (37) Guo, Z.; Wan, Y.; Yang, M.; Snaider, J.; Zhu, K.; Huang, L. Long-range hot-carrier transport in hybrid perovskites visualized by ultrafast microscopy. *Science* **2017**, 356(6333), 59-62.
- (38) Xing, G.; Mathews, N.; Sun, S.; Lim, S. S.; Lam, Y. M.; Gratzel, M.; Mhaisalkar, S.; Sum, T. C. Long-Range Balanced Electron- and Hole-Transport Lengths in Organic-Inorganic $\text{CH}_3\text{NH}_3\text{PbI}_3$. *Science* **2013**, 342(6156), 344-347.
- (39) Steirer, K. X.; Schulz, P.; Teeter, G.; Stevanovic, V.; Yang, M.; Zhu, K.; Berry, J. J. Defect Tolerance in Methylammonium Lead Triiodide Perovskite. *ACS Energy Lett.* **2016**, 1(2), 360-366.
- (40) Dirin, D. N.; Protesescu, L.; Trummer, D.; Kochetygov, I. V.; Yakunin, S.; Krumeich, F.; Stadie, N. P.; Kovalenko, M. V. Harnessing Defect-Tolerance at the Nanoscale: Highly Luminescent Lead Halide Perovskite Nanocrystals in Mesoporous Silica Matrixes. *Nano Lett.* **2016**, 16(9), 5866-5874.
- (41) Brandt, R. E.; Poindexter, J. R.; Gorai, P.; Kurchin, R. C.; Hoye, R. L. Z.; Nienhaus, L.; Wilson, M. W. B.; Polizzotti, J. A.; Sereika, R.; Zaltauskas, R.; Lee, L. C.; Macmanus-Driscoll, J. L.; Bawendi, M.; Stevanović, V.; Buonassisi, T. Searching for "Defect-Tolerant" Photovoltaic Materials: Combined Theoretical and Experimental Screening. *Chem. Mater.* **2017**, 29(11), 4667-4674.
- (42) Yin, W.-J.; Yang, J.-H.; Kang, J.; Yan, Y.; Wei, S.-H. Halide perovskite materials for solar cells: a theoretical review. *J. Mater. Chem. A* **2015**, 3(17), 8926-8942.

- (43) Elumalai, N.; Mahmud, M.; Wang, D.; Uddin, A. Perovskite Solar Cells: Progress and Advancements. *Energies* **2016**, *9*(11), 861.
- (44) Wang, D.; Wright, M.; Elumalai, N. K.; Uddin, A. Stability of perovskite solar cells. *Sol. Energy Mater. Sol. Cells* **2016**, *147*, 255-275.
- (45) Saliba, M.; Matsui, T.; Seo, J.-Y.; Domanski, K.; Correa-Baena, J.-P.; Nazeeruddin, M. K.; Zakeeruddin, S. M.; Tress, W.; Abate, A.; Hagfeldt, A.; Grätzel, M. Cesium-containing triple cation perovskite solar cells: improved stability, reproducibility and high efficiency. *Energy Environ. Sci.* **2016**, *9*(6), 1989-1997.
- (46) Bai, Y.; Dong, Q.; Shao, Y.; Deng, Y.; Wang, Q.; Shen, L.; Wang, D.; Wei, W.; Huang, J. Enhancing stability and efficiency of perovskite solar cells with crosslinkable silane-functionalized and doped fullerene. *Nat. Commun.* **2016**, *7*, 12806.
- (47) Jiang, Y.; Qiu, L.; Juarez-Perez, E. J.; Ono, L. K.; Hu, Z.; Liu, Z.; Wu, Z.; Meng, L.; Wang, Q.; Qi, Y. Reduction of lead leakage from damaged lead halide perovskite solar modules using self-healing polymer-based encapsulation. *Nat. Energy* **2019**, *4*, 585-593.
- (48) Tsai, H.; Nie, W.; Blancon, J. C.; Stoumpos, C. C.; Asadpour, R.; Harutyunyan, B.; Neukirch, A. J.; Verduzco, R.; Crochet, J. J.; Tretiak, S.; Pedesseau, L.; Even, J.; Alam, M. A.; Gupta, G.; Lou, J.; Ajayan, P. M.; Bedzyk, M. J.; Kanatzidis, M. G. High-efficiency two-dimensional Ruddlesden-Popper perovskite solar cells. *Nature* **2016**, *536*, 312-316.
- (49) Even, J.; Pedesseau, L.; Katan, C. Understanding Quantum Confinement of Charge Carriers in Layered 2D Hybrid Perovskites. *ChemPhysChem* **2014**, *15*(17), 3733-3741.
- (50) Pedesseau, L.; Saporì, D.; Traore, B.; Robles, R.; Fang, H.-H.; Loi, M. A.; Tsai, H.; Nie, W.; Blancon, J.-C.; Neukirch, A.; Tretiak, S.; Mohite, A. D.; Katan, C.; Even, J.; Kepenekian, M. Advances and Promises of Layered Halide Hybrid Perovskite Semiconductors. *ACS Nano* **2016**, *10*(11), 9776-9786.
- (51) Stoumpos, C. C.; Cao, D. H.; Clark, D. J.; Young, J.; Rondinelli, J. M.; Jang, J. I.; Hupp, J. T.; Kanatzidis, M. G. Ruddlesden–Popper Hybrid Lead Iodide Perovskite 2D Homologous Semiconductors. *Chem. Mater.* **2016**, *28*(8), 2852-2867.
- (52) Li, X.; Ke, W.; Traoré, B.; Guo, P.; Hadar, I.; Kepenekian, M.; Even, J.; Katan, C.; Stoumpos, C. C.; Schaller, R. D.; Kanatzidis, M. G. Two-Dimensional Dion–Jacobson Hybrid Lead Iodide Perovskites with Aromatic Diammonium Cations. *J. Am. Chem. Soc.* **2019**, *141*(32), 12880-12890.
- (53) Ghosh, D.; Acharya, D.; Pedesseau, L.; Katan, C.; Even, J.; Tretiak, S.; Neukirch, A. J. Charge carrier dynamics in two-dimensional hybrid perovskites: Dion–Jacobson vs. Ruddlesden–Popper phases. *J. Mater. Chem. A* **2020**, *8*(42), 22009-22022.
- (54) Smith, I. C.; Hoke, E. T.; Solis-Ibarra, D.; McGehee, M. D.; Karunadasa, H. I. A Layered Hybrid Perovskite Solar-Cell Absorber with Enhanced Moisture Stability. *Angew. Chem. Int. Ed.* **2014**, *53*(42), 11232-11235.
- (55) Shao, M.; Bie, T.; Yang, L.; Gao, Y.; Jin, X.; He, F.; Zheng, N.; Yu, Y.; Zhang, X. Over 21% Efficiency Stable 2D Perovskite Solar Cells. *Adv. Mater.* **2022**, *34*(1), 2107211.

- (56) Zhang, F.; Lu, H.; Tong, J.; Berry, J. J.; Beard, M. C.; Zhu, K. Advances in two-dimensional organic–inorganic hybrid perovskites. *Energy Environ. Sci.* **2020**, *13*(4), 1154-1186.
- (57) Yuan, M.; Quan, L. N.; Comin, R.; Walters, G.; Sabatini, R.; Voznyy, O.; Hoogland, S.; Zhao, Y.; Beauregard, E. M.; Kanjanaboos, P.; Lu, Z.; Kim, D. H.; Sargent, E. H. Perovskite energy funnels for efficient light-emitting diodes. *Nat. Nanotechnol.* **2016**, *11*, 872-877.
- (58) Liang, M.; Lin, W.; Lan, Z.; Meng, J.; Zhao, Q.; Zou, X.; Castelli, I. E.; Pullerits, T.; Canton, S. E.; Zheng, K. Electronic Structure and Trap States of Two-Dimensional Ruddlesden–Popper Perovskites with the Relaxed Goldschmidt Tolerance Factor. *ACS Appl. Electron. Mater.* **2020**, *2*(5), 1402-1412.
- (59) König, D.; Casalenuovo, K.; Takeda, Y.; Conibeer, G.; Guillemoles, J. F.; Patterson, R.; Huang, L. M.; Green, M. A. Hot carrier solar cells: Principles, materials and design. *Physica E* **2010**, *42*(10), 2862-2866.
- (60) Williams, F.; Nozik, A. J. Solid-state perspectives of the photoelectrochemistry of semiconductor-electrolyte junctions. *Nature* **1984**, *312*, 21-27.
- (61) Nozik, A. J. Photoelectrochemical cells. *Philos. Trans. R. Soc. London. Ser. A* **1980**, *295*(1414), 453-470.
- (62) Landsberg, P. T.; Nussbaumer, H.; Willeke, G. Band-band impact ionization and solar cell efficiency. *J. Appl. Phys.* **1993**, *74*(2), 1451-1452.
- (63) Kolodinski, S.; Werner, J. H.; Wittchen, T.; Queisser, H. J. Quantum efficiencies exceeding unity due to impact ionization in silicon solar cells. *Appl. Phys. Lett.* **1993**, *63*(17), 2405-2407.
- (64) Zhu, H.; Miyata, K.; Fu, Y.; Wang, J.; Joshi, P. P.; Niesner, D.; Williams, K. W.; Jin, S.; Zhu, X.-Y. Screening in crystalline liquids protects energetic carriers in hybrid perovskites. *Science* **2016**, *353*(6306), 1409-1413.
- (65) Niesner, D.; Zhu, H.; Miyata, K.; Joshi, P. P.; Evans, T. J.; Kudisch, B. J.; Trinh, M. T.; Marks, M.; Zhu, X. Y. Persistent Energetic Electrons in Methylammonium Lead Iodide Perovskite Thin Films. *J. Am. Chem. Soc.* **2016**, *138*(48), 15717-15726.
- (66) Nozik, A. J. Spectroscopy and hot electron relaxation dynamics In semiconductor quantum wells and quantum dots. *Annu. Rev. Phys. Chem.* **2001**, *52*, 193-231.
- (67) Elkins, M. H.; Pensack, R.; Proppe, A. H.; Voznyy, O.; Quan, L. N.; Kelley, S. O.; Sargent, E. H.; Scholes, G. D. Biexciton Resonances Reveal Exciton Localization in Stacked Perovskite Quantum Wells. *J. Phys. Chem. Lett.* **2017**, *8*(16), 3895-3901.
- (68) March, S. A.; Riley, D. B.; Clegg, C.; Webber, D.; Liu, X.; Dobrowolska, M.; Furdyna, J. K.; Hill, I. G.; Hall, K. C. Four-Wave Mixing in Perovskite Photovoltaic Materials Reveals Long Dephasing Times and Weaker Many-Body Interactions than GaAs. *ACS Photonics* **2017**, *4*(6), 1515-1521.
- (69) Richter, J. M.; Branchi, F.; Valduga de Almeida Camargo, F.; Zhao, B.; Friend, R. H.; Cerullo, G.; Deschler, F. Ultrafast carrier thermalization in lead iodide perovskite probed with two-dimensional electronic spectroscopy. *Nat. Commun.* **2017**, *8*, 376.
- (70) Lin, Q.; Armin, A.; Nagiri, R. C. R.; Burn, P. L.; Meredith, P. Electro-optics of perovskite solar cells. *Nat. Photonics* **2015**, *9*, 106-112.

- (71) Hirasawa, M.; Ishihara, T.; Goto, T.; Uchida, K.; Miura, N. Magnetoabsorption of the lowest exciton in perovskite-type compound (CH₃NH₃)PbI₃. *Physica B* **1994**, *201*, 427-430.
- (72) Sinba, S. K. Phonons in semiconductors. *CRC crit. rev. solid state mater. sci.* **1973**, *3*(3), 273-334.
- (73) Zhang, X. B.; Taliercio, T.; Kolliakos, S.; Lefebvre, P. Influence of electron-phonon interaction on the optical properties of III nitride semiconductors. *J. Phys. Condens. Matter* **2001**, *13*, 7053.
- (74) Zheng, F.; Wang, L.-W. Large polaron formation and its effect on electron transport in hybrid perovskites. *Energy Environ. Sci.* **2019**, *12*(4), 1219-1230.
- (75) Iaru, C. M.; Brodu, A.; Van Hoof, N. J. J.; Ter Huurne, S. E. T.; Buhot, J.; Montanarella, F.; Buhbut, S.; Christianen, P. C. M.; Vanmaekelbergh, D.; De Mello Donega, C.; Rivas, J. G.; Koenraad, P. M.; Silov, A. Y. Fröhlich interaction dominated by a single phonon mode in CsPbBr₃. *Nat. Commun.* **2021**, *12*, 5844.
- (76) Klemens, P. G. Anharmonic Decay of Optical Phonons. *Phys. Rev.* **1966**, *148*(2), 845-848.
- (77) Ridley, B. K. Electron scattering by confined LO polar phonons in a quantum well. *Phys. Rev. B* **1989**, *39*(8), 5282-5286.
- (78) Pérez-Osorio, M. A.; Milot, R. L.; Filip, M. R.; Patel, J. B.; Herz, L. M.; Johnston, M. B.; Giustino, F. Vibrational Properties of the Organic-Inorganic Halide Perovskite CH₃NH₃PbI₃ from Theory and Experiment: Factor Group Analysis, First-Principles Calculations, and Low-Temperature Infrared Spectra. *J. Phys. Chem. C* **2015**, *119*(46), 25703-25718.
- (79) Vallée, F.; Bogani, F. Coherent time-resolved investigation of LO-phonon dynamics in GaAs. *Phys. Rev. B* **1991**, *43*(14), 12049-12052.
- (80) Barman, S.; Srivastava, G. P. Long-wavelength nonequilibrium optical phonon dynamics in cubic and hexagonal semiconductors. *Phys. Rev. B* **2004**, *69*(23), 235208.
- (81) Ecsedy, D. J.; Klemens, P. G. Thermal resistivity of dielectric crystals due to four-phonon processes and optical modes. *Phys. Rev. B* **1977**, *15*(12), 5957-5962.
- (82) Srivastava, G. P. Origin of the hot phonon effect in group-III nitrides. *Phys. Rev. B* **2008**, *77*(15), 155205.
- (83) Wang, R.; Zobeiri, H.; Xie, Y.; Wang, X.; Zhang, X.; Yue, Y. Distinguishing Optical and Acoustic Phonon Temperatures and Their Energy Coupling Factor under Photon Excitation in nm 2D Materials. *Adv. Sci.* **2020**, *7*(13), 2000097.
- (84) Yang, C. H.; Carlson-Swindle, J. M.; Lyon, S. A.; Worlock, J. M. Hot-Electron Relaxation in GaAs Quantum Wells. *Phys. Rev. Lett.* **1985**, *55*(21), 2359-2361.
- (85) Yang, J.; Wen, X.; Xia, H.; Sheng, R.; Ma, Q.; Kim, J.; Tapping, P.; Harada, T.; Kee, T. W.; Huang, F.; Cheng, Y. B.; Green, M.; Ho-Baillie, A.; Huang, S.; Shrestha, S.; Patterson, R.; Conibeer, G. Acoustic-optical phonon up-conversion and hot-phonon bottleneck in lead-halide perovskites. *Nat. Commun.* **2017**, *8*, 14120.

- (86) Wright, A. D.; Verdi, C.; Milot, R. L.; Eperon, G. E.; Perez-Osorio, M. A.; Snaith, H. J.; Giustino, F.; Johnston, M. B.; Herz, L. M. Electron-phonon coupling in hybrid lead halide perovskites. *Nat. Commun.* **2016**, *7*, 11755.
- (87) Kawai, H.; Giorgi, G.; Marini, A.; Yamashita, K. The mechanism of slow hot-hole cooling in lead-iodide perovskite: first-principles calculation on carrier lifetime from electron-phonon interaction. *Nano Lett.* **2015**, *15*(5), 3103-3108.
- (88) Yang, Y.; Ostrowski, D. P.; France, R. M.; Zhu, K.; van de Lagemaat, J.; Luther, J. M.; Beard, M. C. Observation of a hot-phonon bottleneck in lead-iodide perovskites. *Nat. Photonics* **2015**, *10*, 53-59.
- (89) Fu, J.; Xu, Q.; Han, G.; Wu, B.; Huan, C. H. A.; Leek, M. L.; Sum, T. C. Hot carrier cooling mechanisms in halide perovskites. *Nat. Commun.* **2017**, *8*, 1300.
- (90) van Hest, J.; Blab, G. A.; Gerritsen, H. C.; de Mello Donega, C.; Meijerink, A. The Role of a Phonon Bottleneck in Relaxation Processes for Ln-Doped NaYF₄ Nanocrystals. *J. Phys. Chem. C* **2018**, *122*(7), 3985-3993.
- (91) Efros, A. L.; Rosen, M. The Electronic Structure of Semiconductor Nanocrystals. *Annu. Rev. Mater. Sci.* **2000**, *30*, 475-521.
- (92) Inoshita, T.; Sakaki, H. Electron-phonon interaction and the so-called phonon bottleneck effect in semiconductor quantum dots. *Physica B* **1996**, *227*(1-4), 373-377.
- (93) Schaller, R. D.; Pietryga, J. M.; Goupalov, S. V.; Petruska, M. A.; Ivanov, S. A.; Klimov, V. I. Breaking the Phonon Bottleneck in Semiconductor Nanocrystals via Multiphonon Emission Induced by Intrinsic Nonadiabatic Interactions. *Phys. Rev. Lett.* **2005**, *95*(19), 196401.
- (94) Cooney, R. R.; Sewall, S. L.; Dias, E. A.; Sagar, D. M.; Anderson, K. E. H.; Kambhampati, P. Unified picture of electron and hole relaxation pathways in semiconductor quantum dots. *Phys. Rev. B* **2007**, *75*(24), 245311.
- (95) Wang, L.; Chen, Z.; Liang, G.; Li, Y.; Lai, R.; Ding, T.; Wu, K. Observation of a phonon bottleneck in copper-doped colloidal quantum dots. *Nat. Commun.* **2019**, *10*, 4532.
- (96) Efros, A. L.; Kharchenko, V. A.; Rosen, M. Breaking the phonon bottleneck in nanometer quantum dots: Role of Auger-like processes. *Solid State Commun.* **1995**, *93*(4), 281-284.
- (97) Guyot-Sionnest, P.; Shim, M.; Matranga, C.; Hines, M. Intraband relaxation in CdSe quantum dots. *Phys. Rev. B* **1999**, *60*(4), R2181-R2184.
- (98) Sercel, P. C. Multiphonon-assisted tunneling through deep levels: A rapid energy-relaxation mechanism in nonideal quantum-dot heterostructures. *Phys. Rev. B* **1995**, *51*(20), 14532-14541.
- (99) Inoshita, T.; Sakaki, H. Density of states and phonon-induced relaxation of electrons in semiconductor quantum dots. *Phys. Rev. B* **1997**, *56*(8), R4355-R4358.
- (100) Inoshita, T.; Sakaki, H. Electron relaxation in a quantum dot: Significance of multiphonon processes. *Phys. Rev. B* **1992**, *46*(11), 7260-7263.

- (101) Prezhdo, O. V. Multiple excitons and the electron–phonon bottleneck in semiconductor quantum dots: An ab initio perspective. *Chem. Phys. Lett.* **2008**, *460*(1-3), 1-9.
- (102) Prabhu, S. S.; Vengurlekar, A. S.; Roy, S. K.; Shah, J. Nonequilibrium dynamics of hot carriers and hot phonons in CdSe and GaAs. *Phys. Rev. B* **1995**, *51*(20), 14233-14246.
- (103) Chatzakis, I.; Yan, H.; Song, D.; Berciaud, S.; Heinz, T. F. Temperature dependence of the anharmonic decay of optical phonons in carbon nanotubes and graphite. *Phys. Rev. B* **2011**, *83*(20), 205411.
- (104) Li, M.; Bhaumik, S.; Goh, T. W.; Kumar, M. S.; Yantara, N.; Gratzel, M.; Mhaisalkar, S.; Mathews, N.; Sum, T. C. Slow cooling and highly efficient extraction of hot carriers in colloidal perovskite nanocrystals. *Nat. Commun.* **2017**, *8*, 14350.
- (105) Klimov, V.; Haring Bolivar, P.; Kurz, H. Hot-phonon effects in femtosecond luminescence spectra of electron-hole plasmas in CdS. *Phys. Rev. B* **1995**, *52*(7), 4728-4731.
- (106) Bockelmann, U.; Bastard, G. Phonon scattering and energy relaxation in two-, one-, and zero-dimensional electron gases. *Phys. Rev. B* **1990**, *42*(14), 8947-8951.
- (107) Clady, R.; Tayebjee, M. J. Y.; Aliberti, P.; König, D.; Ekins-Daukes, N. J.; Conibeer, G. J.; Schmidt, T. W.; Green, M. A. Interplay between the hot phonon effect and intervalley scattering on the cooling rate of hot carriers in GaAs and InP. *Prog. Photovolt.* **2012**, *20*(1), 82-92.
- (108) Monahan, D. M.; Guo, L.; Lin, J.; Dou, L.; Yang, P.; Fleming, G. R. Room-Temperature Coherent Optical Phonon in 2D Electronic Spectra of CH₃NH₃PbI₃ Perovskite as a Possible Cooling Bottleneck. *J. Phys. Chem. Lett.* **2017**, *8*(14), 3211-3215.
- (109) Esmailpour, H.; Whiteside, V. R.; Piyathilaka, H. P.; Vijayaragunathan, S.; Wang, B.; Adcock-Smith, E.; Roberts, K. P.; Mishima, T. D.; Santos, M. B.; Bristow, A. D.; Sellers, I. R. Enhanced hot electron lifetimes in quantum wells with inhibited phonon coupling. *Sci. Rep.* **2018**, *8*, 12473.
- (110) Rosenwaks, Y.; Hanna, M. C.; Levi, D. H.; Szmyd, D. M.; Ahrenkiel, R. K.; Nozik, A. J. Hot-carrier cooling in GaAs: Quantum wells versus bulk. *Phys. Rev. B* **1993**, *48*(19), 14675-14678.
- (111) Sondhaus, P.; Larsson, J.; Harbst, M.; Naylor, G. A.; Plech, A.; Scheidt, K.; Synnergren, O.; Wulff, M.; Wark, J. S. Picosecond X-Ray Studies of Coherent Folded Acoustic Phonons in a Multiple Quantum Well. *Phys. Rev. Lett.* **2005**, *94*(12), 125509.
- (112) Özgür, Ü.; Lee, C.-W.; Everitt, H. O. Control of Coherent Acoustic Phonons. *Opt. Photonics News* **2001**, *12*(12), 66.
- (113) Achermann, M.; Bartko, A. P.; Hollingsworth, J. A.; Klimov, V. I. The effect of Auger heating on intraband carrier relaxation in semiconductor quantum rods. *Nat. Phys.* **2006**, *2*, 557-561.
- (114) Klimov, V. I.; McBranch, D. W. Femtosecond 1P-to-1S Electron Relaxation in Strongly Confined Semiconductor Nanocrystals. *Phys. Rev. Lett.* **1998**, *80*(18), 4028-4031.

- (115) Anusca, I.; Balčiūnas, S.; Gemeiner, P.; Svirskas, Š.; Sanlialp, M.; Lackner, G.; Fetzkenhauer, C.; Belovickis, J.; Samulionis, V.; Ivanov, M.; Dkhil, B.; Banyš, J.; Shvartsman, V. V.; Lupascu, D. C. Dielectric Response: Answer to Many Questions in the Methylammonium Lead Halide Solar Cell Absorbers. *Adv. Energy Mater.* **2017**, 7(19), 1700600.
- (116) Miyata, K.; Meggiolaro, D.; Trinh, M. T.; Joshi, P. P.; Mosconi, E.; Jones, S. C.; De Angelis, F.; Zhu, X. Y. Large polarons in lead halide perovskites. *Sci. Adv.* **2017**, 3(8), e1701217.
- (117) Landau, L. D. The Movement of Electrons in the Crystal Lattice. *Phys. Z. Sowjetunion* **1933**, 3, 644-645.
- (118) Franchini, C.; Reticcioli, M.; Setvin, M.; Diebold, U. Polarons in materials. *Nat. Rev. Mater.* **2021**, 6, 560-586.
- (119) Emin, D., *Polarons*. Cambridge University Press: 2012.
- (120) Zhu, X. Y.; Podzorov, V. Charge Carriers in Hybrid Organic-Inorganic Lead Halide Perovskites Might Be Protected as Large Polarons. *J. Phys. Chem. Lett.* **2015**, 6(23), 4758-4761.
- (121) Brivio, F.; Walker, A. B.; Walsh, A. Structural and electronic properties of hybrid perovskites for high-efficiency thin-film photovoltaics from first-principles. *APL Mater.* **2013**, 1(4), 042111.
- (122) Even, J.; Carignano, M.; Katan, C. Molecular disorder and translation/rotation coupling in the plastic crystal phase of hybrid perovskites. *Nanoscale* **2016**, 8(12), 6222-6236.
- (123) Ma, J.; Wang, L.-W. Nanoscale Charge Localization Induced by Random Orientations of Organic Molecules in Hybrid Perovskite $\text{CH}_3\text{NH}_3\text{PbI}_3$. *Nano Lett.* **2015**, 15(1), 248-253.
- (124) Berdiyrov, G. R.; Kachmar, A.; El-Mellouhi, F.; Carignano, M. A.; El-Amine Madjet, M. Role of Cations on the Electronic Transport and Optical Properties of Lead-Iodide Perovskites. *J. Phys. Chem. C* **2016**, 120(30), 16259-16270.
- (125) Zhu, H.; Trinh, M. T.; Wang, J.; Fu, Y.; Joshi, P. P.; Miyata, K.; Jin, S.; Zhu, X. Y. Organic Cations Might Not Be Essential to the Remarkable Properties of Band Edge Carriers in Lead Halide Perovskites. *Adv. Mater.* **2017**, 29(1), 1603072.
- (126) Cinquanta, E.; Meggiolaro, D.; Motti, S. G.; Gandini, M.; Alcocer, M. J. P.; Akkerman, Q. A.; Vozzi, C.; Manna, L.; De Angelis, F.; Petrozza, A.; Stagira, S. Ultrafast THz Probe of Photoinduced Polarons in Lead-Halide Perovskites. *Phys. Rev. Lett.* **2019**, 122(16), 166601.
- (127) Marronnier, A.; Lee, H.; Geffroy, B.; Even, J.; Bonnassieux, Y.; Roma, G. Structural Instabilities Related to Highly Anharmonic Phonons in Halide Perovskites. *J. Phys. Chem. Lett.* **2017**, 8(12), 2659-2665.
- (128) Katan, C.; Mohite, A. D.; Even, J. Entropy in halide perovskites. *Nat. Mater.* **2018**, 17, 377-379.
- (129) Létoublon, A.; Paofai, S.; Rufflé, B.; Bourges, P.; Hehlen, B.; Michel, T.; Ecolivet, C.; Durand, O.; Cordier, S.; Katan, C.; Even, J. Elastic Constants, Optical Phonons, and Molecular Relaxations in the High Temperature Plastic Phase of the $\text{CH}_3\text{NH}_3\text{PbBr}_3$ Hybrid Perovskite. *J. Phys. Chem. Lett.* **2016**, 7(19), 3776-3784.

- (130) Quarti, C.; Grancini, G.; Mosconi, E.; Bruno, P.; Ball, J. M.; Lee, M. M.; Snaith, H. J.; Petrozza, A.; Angelis, F. D. The Raman Spectrum of the $\text{CH}_3\text{NH}_3\text{PbI}_3$ Hybrid Perovskite: Interplay of Theory and Experiment. *J. Phys. Chem. Lett.* **2014**, *5*(2), 279-284.
- (131) Munson, K. T.; Kennehan, E. R.; Doucette, G. S.; Asbury, J. B. Dynamic Disorder Dominates Delocalization, Transport, and Recombination in Halide Perovskites. *Chem* **2018**, *4*(12), 2826-2843.
- (132) Kang, J.; Wang, L.-W. Dynamic Disorder and Potential Fluctuation in Two-Dimensional Perovskite. *J. Phys. Chem. Lett.* **2017**, *8*(16), 3875-3880.
- (133) Ambrosio, F.; Wiktor, J.; De Angelis, F.; Pasquarello, A. Origin of low electron-hole recombination rate in metal halide perovskites. *Energy Environ. Sci.* **2018**, *11*(1), 101-105.
- (134) Ma, J.; Wang, L.-W. The Nature of Electron Mobility in Hybrid Perovskite $\text{CH}_3\text{NH}_3\text{PbI}_3$. *Nano Lett.* **2017**, *17*(6), 3646-3654.
- (135) Quarti, C.; Mosconi, E.; De Angelis, F. Structural and electronic properties of organo-halide hybrid perovskites from ab initio molecular dynamics. *Phys. Chem. Chem. Phys.* **2015**, *17*(14), 9394-9409.
- (136) Carignano, M. A.; Kachmar, A.; Hutter, J. Thermal Effects on $\text{CH}_3\text{NH}_3\text{PbI}_3$ Perovskite from Ab Initio Molecular Dynamics Simulations. *J. Phys. Chem. C* **2015**, *119*(17), 8991-8997.
- (137) Bakulin, A. A.; Selig, O.; Bakker, H. J.; Rezus, Y. L.; Muller, C.; Glaser, T.; Lovrincic, R.; Sun, Z.; Chen, Z.; Walsh, A.; Frost, J. M.; Jansen, T. L. Real-Time Observation of Organic Cation Reorientation in Methylammonium Lead Iodide Perovskites. *J. Phys. Chem. Lett.* **2015**, *6*(18), 3663-3669.
- (138) Walsh, A. Principles of Chemical Bonding and Band Gap Engineering in Hybrid Organic-Inorganic Halide Perovskites. *J. Phys. Chem. C* **2015**, *119*(11), 5755-5760.
- (139) Frost, J. M.; Whalley, L. D.; Walsh, A. Slow Cooling of Hot Polarons in Halide Perovskite Solar Cells. *ACS Energy Lett.* **2017**, *2*(12), 2647-2652.
- (140) Price, M. B.; Butkus, J.; Jellicoe, T. C.; Sadhanala, A.; Briane, A.; Halpert, J. E.; Broch, K.; Hodgkiss, J. M.; Friend, R. H.; Deschler, F. Hot-carrier cooling and photoinduced refractive index changes in organic-inorganic lead halide perovskites. *Nat. Commun.* **2015**, *6*, 8420.
- (141) Chen, K.; Barker, A. J.; Morgan, F. L.; Halpert, J. E.; Hodgkiss, J. M. Effect of Carrier Thermalization Dynamics on Light Emission and Amplification in Organometal Halide Perovskites. *J. Phys. Chem. Lett.* **2015**, *6*(1), 153-158.
- (142) Chan, C. C. S.; Fan, K.; Wang, H.; Huang, Z.; Novko, D.; Yan, K.; Xu, J.; Choy, W. C. H.; Lončarić, I.; Wong, K. S. Uncovering the Electron-Phonon Interplay and Dynamical Energy-Dissipation Mechanisms of Hot Carriers in Hybrid Lead Halide Perovskites. *Adv. Energy Mater.* **2021**, *11*(9), 2003071.
- (143) Berera, R.; Van Grondelle, R.; Kennis, J. T. M. Ultrafast transient absorption spectroscopy: principles and application to photosynthetic systems. *Photosynth. Res.* **2009**, *101*, 105-118.
- (144) Kahn, A. Fermi level, work function and vacuum level. *Mater. Horiz.* **2016**, *3*, 7-10.

- (145) Helander, M. G.; Greiner, M. T.; Wang, Z. B.; Lu, Z. H. Pitfalls in measuring work function using photoelectron spectroscopy. *Appl. Surf. Sci.* **2010**, *256*(8), 2602-2605.
- (146) Li, Z.; Yang, M.; Park, J.-S.; Wei, S.-H.; Berry, J. J.; Zhu, K. Stabilizing Perovskite Structures by Tuning Tolerance Factor: Formation of Formamidinium and Cesium Lead Iodide Solid-State Alloys. *Chem. Mater.* **2016**, *28*(1), 284-292.
- (147) Fu, Y.; Hautzinger, M. P.; Luo, Z.; Wang, F.; Pan, D.; Aristov, M. M.; Guzei, I. A.; Pan, A.; Zhu, X.; Jin, S. Incorporating Large A Cations into Lead Iodide Perovskite Cages: Relaxed Goldschmidt Tolerance Factor and Impact on Exciton-Phonon Interaction. *ACS Cent. Sci.* **2019**, *5*(8), 1377-1386.
- (148) Zhu, Q.; Zheng, K.; Abdellah, M.; Generalov, A.; Haase, D.; Carlson, S.; Niu, Y.; Heimdal, J.; Engdahl, A.; Messing, M. E.; Pullerits, T.; Canton, S. E. Correlating structure and electronic band-edge properties in organolead halide perovskites nanoparticles. *Phys. Chem. Chem. Phys.* **2016**, *18*(22), 14933-14940.
- (149) Payne, D. J.; Egdell, R. G.; Walsh, A.; Watson, G. W.; Guo, J.; Glans, P. A.; Learmonth, T.; Smith, K. E. Electronic Origins of Structural Distortions in Post-Transition Metal Oxides: Experimental and Theoretical Evidence for a Revision of the Lone Pair Model. *Phys. Rev. Lett.* **2006**, *96*(15), 157403.
- (150) Waghmare, U. V.; Spaldin, N. A.; Kandpal, H. C.; Seshadri, R. First-principles indicators of metallicity and cation off-centricity in the IV-VI rocksalt chalcogenides of divalent Ge, Sn, and Pb. *Phys. Rev. B* **2003**, *67*(12), 125111.
- (151) Stranks, S. D.; Burlakov, V. M.; Leijtens, T.; Ball, J. M.; Goriely, A.; Snaith, H. J. Recombination Kinetics in Organic-Inorganic Perovskites: Excitons, Free Charge, and Subgap States. *Phys. Rev. Appl.* **2014**, *2*(3), 034007.
- (152) Zheng, K.; Židek, K.; Abdellah, M.; Chen, J.; Chábera, P.; Zhang, W.; Al-Marri, M. J.; Pullerits, T. High Excitation Intensity Opens a New Trapping Channel in Organic-Inorganic Hybrid Perovskite Nanoparticles. *ACS Energy Lett.* **2016**, *1*(6), 1154-1161.
- (153) Zheng, K.; Židek, K.; Abdellah, M.; Messing, M. E.; Al-Marri, M. J.; Pullerits, T. Trap States and Their Dynamics in Organometal Halide Perovskite Nanoparticles and Bulk Crystals. *J. Phys. Chem. C* **2016**, *120*(5), 3077-3084.
- (154) Chen, Y.; Sun, Y.; Peng, J.; Tang, J.; Zheng, K.; Liang, Z. 2D Ruddlesden-Popper Perovskites for Optoelectronics. *Adv. Mater.* **2018**, *30*(2), 1703487.
- (155) Blancon, J. C.; Tsai, H.; Nie, W.; Stoumpos, C. C.; Pedesseau, L.; Katan, C.; Kepenekian, M.; Soe, C. M.; Appavoo, K.; Sfeir, M. Y.; Tretiak, S.; Ajayan, P. M.; Kanatzidis, M. G.; Even, J.; Crochet, J. J.; Mohite, A. D. Extremely efficient internal exciton dissociation through edge states in layered 2D perovskites. *Science* **2017**, *355*(6331), 1288-1292.
- (156) Kahmann, S.; Tekelenburg, E. K.; Duim, H.; Kamminga, M. E.; Loi, M. A. Extrinsic nature of the broad photoluminescence in lead iodide-based Ruddlesden-Popper perovskites. *Nat. Commun.* **2020**, *11*, 2344.
- (157) Kepenekian, M.; Traore, B.; Blancon, J. C.; Pedesseau, L.; Tsai, H.; Nie, W.; Stoumpos, C. C.; Kanatzidis, M. G.; Even, J.; Mohite, A. D.; Tretiak, S.; Katan, C. Concept of Lattice Mismatch and Emergence of Surface States in Two-dimensional Hybrid Perovskite Quantum Wells. *Nano Lett.* **2018**, *18*(9), 5603-5609.

- (158) Wang, K.; Wu, C.; Jiang, Y.; Yang, D.; Wang, K.; Priya, S. Distinct conducting layer edge states in two-dimensional (2D) halide perovskite. *Sci. Adv.* **2019**, *5*(7), eaau3241.
- (159) Li, S.; Luo, J.; Liu, J.; Tang, J. Self-Trapped Excitons in All-Inorganic Halide Perovskites: Fundamentals, Status, and Potential Applications. *J. Phys. Chem. Lett.* **2019**, *10*(8), 1999-2007.
- (160) Blancon, J. C.; Stier, A. V.; Tsai, H.; Nie, W.; Stoumpos, C. C.; Traore, B.; Pedesseau, L.; Kepenekian, M.; Katsutani, F.; Noe, G. T.; Kono, J.; Tretiak, S.; Crooker, S. A.; Katan, C.; Kanatzidis, M. G.; Crochet, J. J.; Even, J.; Mohite, A. D. Scaling law for excitons in 2D perovskite quantum wells. *Nat. Commun.* **2018**, *9*, 2254.
- (161) Jaffe, A.; Lin, Y.; Beavers, C. M.; Voss, J.; Mao, W. L.; Karunadasa, H. I. High-Pressure Single-Crystal Structures of 3D Lead-Halide Hybrid Perovskites and Pressure Effects on their Electronic and Optical Properties. *ACS Cent. Sci.* **2016**, *2*(4), 201-209.
- (162) Silva, G. G.; Da Cunha, W. F.; De Sousa Junior, R. T.; Almeida Fonseca, A. L.; Ribeiro Júnior, L. A.; E Silva, G. M. Influence of quasi-particle density over polaron mobility in armchair graphene nanoribbons. *Phys. Chem. Chem. Phys.* **2018**, *20*(24), 16712-16718.
- (163) Seitz, M.; Magdaleno, A. J.; Alcazar-Cano, N.; Melendez, M.; Lubbers, T. J.; Walraven, S. W.; Pakdel, S.; Prada, E.; Delgado-Buscalioni, R.; Prins, F. Exciton diffusion in two-dimensional metal-halide perovskites. *Nat. Commun.* **2020**, *11*, 2035.
- (164) Coehoorn, R.; Zhang, L.; Bobbert, P. A.; Van Eersel, H. Effect of polaron diffusion on exciton-polaron quenching in disordered organic semiconductors. *Phys. Rev. B* **2017**, *95*(13), 134202.
- (165) Mao, L.; Stoumpos, C. C.; Kanatzidis, M. G. Two-Dimensional Hybrid Halide Perovskites: Principles and Promises. *J. Am. Chem. Soc.* **2019**, *141*(3), 1171-1190.
- (166) Zhang, Z.; Fang, W.-H.; Long, R.; Prezhd, O. V. Exciton Dissociation and Suppressed Charge Recombination at 2D Perovskite Edges: Key Roles of Unsaturated Halide Bonds and Thermal Disorder. *J. Am. Chem. Soc.* **2019**, *141*(39), 15557-15566.
- (167) Bao, J.; Hadjiev, V. G. Origin of Luminescent Centers and Edge States in Low-Dimensional Lead Halide Perovskites: Controversies, Challenges and Instructive Approaches. *Nano-Micro Lett.* **2019**, *11*, 26.
- (168) Shi, E.; Deng, S.; Yuan, B.; Gao, Y.; Akriti; Yuan, L.; Davis, C. S.; Zemlyanov, D.; Yu, Y.; Huang, L.; Dou, L. Extrinsic and Dynamic Edge States of Two-Dimensional Lead Halide Perovskites. *ACS Nano* **2019**, *13*(2), 1635-1644.
- (169) Zhao, C.; Tian, W.; Sun, Q.; Yin, Z.; Leng, J.; Wang, S.; Liu, J.; Wu, K.; Jin, S. Trap-Enabled Long-Distance Carrier Transport in Perovskite Quantum Wells. *J. Am. Chem. Soc.* **2020**, *142*(35), 15091-15097.
- (170) Cao, D. H.; Stoumpos, C. C.; Farha, O. K.; Hupp, J. T.; Kanatzidis, M. G. 2D Homologous Perovskites as Light-Absorbing Materials for Solar Cell Applications. *J. Am. Chem. Soc.* **2015**, *137*(24), 7843-7850.

- (171) Guo, P.; Stoumpos, C. C.; Mao, L.; Sadasivam, S.; Ketterson, J. B.; Darancet, P.; Kanatzidis, M. G.; Schaller, R. D. Cross-plane coherent acoustic phonons in two-dimensional organic-inorganic hybrid perovskites. *Nat. Commun.* **2018**, *9*, 2019.
- (172) Lim, J. W. M.; Giovanni, D.; Righetto, M.; Feng, M.; Mhaisalkar, S. G.; Mathews, N.; Sum, T. C. Hot Carriers in Halide Perovskites: How Hot Truly? *J. Phys. Chem. Lett.* **2020**, *11*(7), 2743-2750.
- (173) Chen, J.; Messing, M. E.; Zheng, K.; Pullerits, T. Cation-Dependent Hot Carrier Cooling in Halide Perovskite Nanocrystals. *J. Am. Chem. Soc.* **2019**, *141*(8), 3532-3540.
- (174) Seah, M. P.; Dench, W. A. Quantitative electron spectroscopy of surfaces: A standard data base for electron inelastic mean free paths in solids. *Surf. Interface Anal.* **1979**, *1*(1), 2-11.
- (175) Shao, Y.; Gao, W.; Yan, H.; Li, R.; Abdelwahab, I.; Chi, X.; Rogée, L.; Zhuang, L.; Fu, W.; Lau, S. P.; Yu, S. F.; Cai, Y.; Loh, K. P.; Leng, K. Unlocking surface octahedral tilt in two-dimensional Ruddlesden-Popper perovskites. *Nat. Commun.* **2022**, *13*, 138.
- (176) Liang, M.; Lin, W.; Zhao, Q.; Zou, X.; Lan, Z.; Meng, J.; Shi, Q.; Castelli, I. E.; Canton, S. E.; Pullerits, T.; Zheng, K. Free Carriers versus Self-Trapped Excitons at Different Facets of Ruddlesden-Popper Two-Dimensional Lead Halide Perovskite Single Crystals. *J. Phys. Chem. Lett.* **2021**, *12*(20), 4965-4971.
- (177) Duan, H. G.; Tiwari, V.; Jha, A.; Berdiyurov, G. R.; Akimov, A.; Vendrell, O.; Nayak, P. K.; Snaith, H. J.; Thorwart, M.; Li, Z.; Madjet, M. E.; Miller, R. J. D. Photoinduced Vibrations Drive Ultrafast Structural Distortion in Lead Halide Perovskite. *J. Am. Chem. Soc.* **2020**, *142*(39), 16569-16578.
- (178) Zhang, Z.; Fang, W. H.; Tokina, M. V.; Long, R.; Prezhdo, O. V. Rapid Decoherence Suppresses Charge Recombination in Multi-Layer 2D Halide Perovskites: Time-Domain Ab Initio Analysis. *Nano Lett.* **2018**, *18*(4), 2459-2466.
- (179) Zhang, Y.; Wang, R.; Li, Y.; Wang, Z.; Hu, S.; Yan, X.; Zhai, Y.; Zhang, C.; Sheng, C. Optical Properties of Two-Dimensional Perovskite Films of $(\text{C}_6\text{H}_5\text{C}_2\text{H}_4\text{NH}_3)_2[\text{PbI}_4]$ and $(\text{C}_6\text{H}_5\text{C}_2\text{H}_4\text{NH}_3)_2(\text{CH}_3\text{NH}_3)_2[\text{Pb}_3\text{I}_{10}]$. *J. Phys. Chem. Lett.* **2019**, *10*(1), 13-19.
- (180) Sarma, S. D.; Jain, J. K.; Jalabert, R. Many-body theory of energy relaxation in an excited-electron gas via optical-phonon emission. *Phys. Rev. B* **1990**, *41*(6), 3561-3571.
- (181) Fang, H.-H.; Adjokatse, S.; Shao, S.; Even, J.; Loi, M. A. Long-lived hot-carrier light emission and large blue shift in formamidinium tin triiodide perovskites. *Nat. Commun.* **2018**, *9*, 243.
- (182) Zhou, Y.; Chen, J.; Bakr, O. M.; Sun, H.-T. Metal-Doped Lead Halide Perovskites: Synthesis, Properties, and Optoelectronic Applications. *Chem. Mater.* **2018**, *30*(19), 6589-6613.
- (183) Liu, W.; Lin, Q.; Li, H.; Wu, K.; Robel, I.; Pietryga, J. M.; Klimov, V. I. Mn^{2+} -Doped Lead Halide Perovskite Nanocrystals with Dual-Color Emission Controlled by Halide Content. *J. Am. Chem. Soc.* **2016**, *138*(45), 14954-14961.

- (184) Akkerman, Q. A.; Meggiolaro, D.; Dang, Z.; De Angelis, F.; Manna, L. Fluorescent Alloy $\text{CsPb}_x\text{Mn}_{1-x}\text{I}_3$ Perovskite Nanocrystals with High Structural and Optical Stability. *ACS Energy Lett.* **2017**, *2*(9), 2183-2186.
- (185) Guria, A. K.; Dutta, S. K.; Adhikari, S. D.; Pradhan, N. Doping Mn^{2+} in Lead Halide Perovskite Nanocrystals: Successes and Challenges. *ACS Energy Lett.* **2017**, *2*(5), 1014-1021.
- (186) Ji, S.; Yuan, X.; Cao, S.; Ji, W.; Zhang, H.; Wang, Y.; Li, H.; Zhao, J.; Zou, B. Near-Unity Red Mn^{2+} Photoluminescence Quantum Yield of Doped CsPbCl_3 Nanocrystals with Cd Incorporation. *J. Phys. Chem. Lett.* **2020**, *11*(6), 2142-2149.
- (187) Kahmann, S.; Loi, M. A. Hot carrier solar cells and the potential of perovskites for breaking the Shockley–Queisser limit. *J. Mater. Chem. C* **2019**, *7*(9), 2471-2486.
- (188) Shafique, A.; Shin, Y.-H. Strain engineering of phonon thermal transport properties in monolayer 2H-MoTe_2 . *Phys. Chem. Chem. Phys.* **2017**, *19*(47), 32072-32078.

Paper I



Combining Two-Photon Photoemission and Transient Absorption Spectroscopy to Resolve Hot Carrier Cooling in 2D Perovskite Single Crystals: the Effect of Surface Layer

Weihua Lin^{1, *}, Mingli Liang^{1,2, *}, Yuran Niu³, Zhesheng Chen⁴, Marie Cherasse^{4,5}, Jie Meng^{1,2}, Xianshao Zou¹, Qian Zhao², Huifang Geng⁶, Evangelos Papalazarou⁷, Marino Marsi⁷, Luca Perfetti⁴, Sophie E. Canton^{8,*}, Kaibo Zheng^{1,2,*}, Tönu Pullerits^{1,*}

1. Chemical Physics and NanoLund, Lund University, Box 124, 22100 Lund, Sweden
2. Department of Chemistry, Technical University of Denmark, DK-2800 Kongens Lyngby, Denmark
3. MAX IV Laboratory, Lund University, P.O. Box 118, 22100 Lund, Sweden
4. Laboratoire des Solides Irradiés, CEA/DRF/IRAMIS, CNRS, Ecole polytechnique, Institut Polytechnique de Paris, 91120 Palaiseau, France
5. Fritz-Haber-Institut der Max-Planck-Gesellschaft, Faradayweg 4-6, 14195 Berlin, Germany
6. Ultrafast Electron Microscopy Laboratory, The MOE Key Laboratory of Weak-Light Nonlinear Photonics, School of Physics, Nankai University, Tianjin 300071, China
7. Laboratoire de Physique des Solides, CNRS, Université Paris Saclay, Orsay 91405, France
8. European XFEL, Holzkoppel 4, 22869 Schenefeld, Germany

ABSTRACT

We investigate hot carrier (HC) cooling in two-dimensional (2D) perovskite single crystals by applying two complementary ultrafast spectroscopy techniques – transient absorption (TA) and time-resolved two-photon photoemission (TR-2PPE) spectroscopies. TR-2PPE directly maps the hot electron distribution and its dynamics in the conduction band to the detected photoelectron distribution. While TR-2PPE selectively probes the upper layer of the material, TA provides information on the whole bulk. Two cooling regimes are resolved in both techniques. The fast timescale of 100-200 fs is related to the electron scattering by longitudinal optical (LO) phonons and the slow timescale of 3-4 ps corresponds to the LO phonon relaxation. The HC cooling dynamic of TA measurement has faster initial stage and higher starting temperature for the slower stage than in TR-2PPE measurements. Conclusions about spatial sensitivity of the cooling dynamics across the 2D perovskite single crystals constitute valuable information that can guide the future development of HC solar cells and thermoelectric applications based on 2D perovskites.

KEYWORDS

perovskites, two-dimensional materials, hot carrier, materials science, time-resolved spectroscopy

INTRODUCTION

Organic-inorganic hybrid perovskites have numerous photo-physical properties, which make them promising for optoelectronic and thermoelectric applications.¹⁻³ They are particularly famous as active materials for solar cells achieving power conversion efficiencies (PCE) exceeding 25%.⁴ ⁶ This value is not so far from the Shockley-Queisser limit of the conventional single-junction photovoltaic devices,⁷ and further improvements need a principally different methodology. One approach is to establish a tandem cell structure combining the photoactive layers of alternating spectral coverage.⁸ Another very promising but not yet practically demonstrated concept is the hot carrier solar cell (HCSC) with theoretical maximum efficiency of 66% under one sun illumination.⁹ In HCSC,¹⁰⁻¹² the inhibited cooling of the photo-generated hot carriers (HC) elevates the equilibrium carrier temperature collected by the electrodes, thus reducing the heat loss during the light-to-electricity conversion process. Recently the potential of three-dimensional (3D) hybrid perovskites in the application of HCSC has attracted increasing attention.¹³⁻¹⁶ Firstly, the small effective mass of the charge carriers leads to slower HC relaxation by diminishing the possible intraband Auger-type energy transfer that promotes energy losses.^{17, 18} Secondly, the large phonon bandgap between longitudinal optical (LO) and longitudinal acoustic (LA) phonon branches of halide perovskite suppresses the pathways in the phonon decay, thereby enhancing the hot phonon bottleneck effect.^{18, 19} Thirdly, polarons are generated due to the strong polar Fröhlich interactions between the charge carriers and the LO phonons. Such strongly-coupled polarons further decelerate the cooling of the HC *via* screening the Coulomb interaction responsible for the carrier scattering with the LO phonons.²⁰ Long-lived HCs with lifetime reaching 100 picoseconds in hybrid halide perovskites have been reported by several groups based on spectroscopic techniques,^{20, 21} such as ultrafast transient absorption microscopy and time-resolved

photoluminescence spectroscopy. However, the standard analyses method based on the assumption of the exponential high energy tail of the spectrum due to the Boltzmann distribution, is sometimes problematic. For example, the resulting HC cooling temperatures significantly depend on the energy range chosen for the analyses.²² Clearly, a technique is needed where the hot carrier energies in conduction band could be directly observed and compared for different samples.

The emerging two-dimensional (2D) derivatives of the organic-inorganic hybrid perovskites are expected to be even more promising building blocks for realizing the HCSCs due to their unique electronic and phononic structures that could further hinder the HC cooling process and promote a long-lived hot quasi-equilibrium state. The 2D lead halide perovskites are denoted as $(B)_2(A)_{n-1}Pb_nX_{3n+1}$, where n inorganic octahedra layers are sandwiched between two long-chain organic spacing cation (B-site) layers, while the small cations (A-site) fill the inorganic perovskite cages. On one hand, the soft and long-chain spacing cations can significantly reduce the group velocity and propagation length of the acoustic phonons slowing down the heat dissipation.²³ Furthermore, the natural multiple-quantum-well (MQW) structure might stimulate hot phonon bottleneck effects similar to what can occur in traditional semiconductor quantum well superlattices (QWSL).^{24, 25} QW structure may hinder the diffusion of HCs and propagation of acoustic phonons at the interface. The emitted zone-centre LO phonons might be reflected by the barrier. Furthermore, a phononic bandgap between LO phonons and acoustic phonons might be opened up due to MQW structure.^{26, 27} All these effects can increase the hot phonon bottleneck effect and significantly slow down the HC cooling process. Earlier studies based on transient reflectance experiments have reported a HC cooling within sub-ps timescale in 2D perovskites.²⁸ However, the fundamental photophysical mechanism of the cooling is yet to be clarified. In particular, the QW layers in the 2D perovskites are isolated by the organic spacing cations that

modify the vibrational modes in both optical and acoustic branches. Such additional phonon modes might influence the HC cooling dynamics.

In order to elucidate the possible causal connection between the structure of the 2D perovskite and the cooling dynamics, a highly ordered single-crystal sample is preferable compared to the films with numerous grain boundaries and long-range disorder. In this article, we target the HC cooling dynamics on exfoliated $(\text{BA})_2(\text{MA})_2\text{Pb}_3\text{I}_{10}$ single-crystal flakes (BA = Butylammonium; $\text{CH}_3(\text{CH}_2)_3\text{NH}_3^+$, MA = Methylammonium; CH_3NH_3^+). To obtain a clear insight on the cooling mechanisms in the 2D perovskite crystalline flake, we compare the HC cooling dynamics monitored by transient absorption (TA) and time-resolved two-photon photoemission (TR-2PPE) spectroscopies. With the TA technique, the HC temperature is extracted by fitting the high-energy tail of photobleaching signals using the Boltzmann distribution function.^{29, 30} The uncertainties of the fitting procedure are reduced by simultaneous analyses of many excitation intensities and by exploring multiple fitting models as described below. The other used method, TR-2PPE, enables direct mapping of the distribution of the measured kinetic energies of the emitted photoelectrons into the electron energy distribution in the conduction band (CB). Therefore, in this technique the HC temperature (energy) is directly available as a function of the probe delay time allowing to follow the cooling dynamics (relaxation). All in all, combining the straightforward interpretation of the TR-2PPE analysis with TA results, allows a more comprehensive study on HC cooling in 2D perovskites.

Since the photoelectrons in TR-2PPE originate only from the top layer of the sample whereas TA probes the whole bulk, we can relate the differences in the cooling dynamics to the details of the material properties at the surface and in the bulk of the crystal.

In general, the HC cooling dynamics extracted from these two techniques exhibit two stages, where the fast one (Stage I) is caused by the efficient electron - LO phonon (e-ph) scattering after which a thermal quasi-equilibration between hot electrons and LO phonons is reached.^{31, 32} The following slower dynamics (Stage II) corresponds to the LO phonon relaxation due to the coupling to the acoustic phonons.^{18, 33, 34} We found that the dynamics obtained from TA measurement has faster cooling in Stage I and higher initial temperature of Stage II than in TR-2PPE measurements. There are three main possible explanations for this result.

First, the deviation in HC cooling dynamics can be attributed to the different probing depth of the two techniques – while the TA probes the whole sample, the photoelectrons in the TR-2PPE experiments are emitted only from the outermost layer. Thereby, the different local structure at the surface and in the bulk can cause the observed differences of the dynamics. In particular, the strain accumulation is released on the surface layer by both the in-plane and out-of-plane tilting which can lead to the weakened carrier-phonon coupling.³⁵ In addition, the tilting of the octahedra at the surface of the exfoliated sample can modify the phononic features that HCs couple to.³⁶ The spacing cation on the exfoliated surface sheet is softer, which could possibly decrease the e-ph coupling and slow down the cooling in Stage I.^{23, 37} Second, the environmental temperature in these two measurements is different, which will cause the different LO phonon population which affects the cooling efficiency in the first stage. Third, only the electrons are probed in TR-2PPE measurements,^{18, 38} while both excited electrons and holes contribute to the TA signals. The performed TA analyses provide an averaged effective cooling rate which is faster than the result for the electrons only. However, because the Fröhlich coupling strength is proportional to the square root of effective mass which is not so different for the electron and hole, it is unlikely to be the main source for the faster cooling in Stage I in the TA analysis. In Stage II, the obtained HC

cooling dynamics share similar rate from two techniques, but the higher starting temperature in TA measurement indicates stronger hot phonon bottleneck effect in the bulk compared to the surface.³⁹ Our findings reveal that the HC cooling dynamics on the crystal surface and in the bulk are different. The results suggest that the spacing cations have a significant role in the details of the cooling processes in 2D perovskites.

RESULTS AND DISCUSSION

2D perovskite single-crystal thin flakes with a diameter of around 100 μm were prepared by the mechanical exfoliation with Scotch tape from a bulk single crystal in the glove box.⁴⁰ Such a procedure can provide flakes with a pure phase and an atomically flat surface (for the experimental details, see Methods and Supporting Information S1). The steady state absorption spectrum of 2D perovskite $(\text{BA})_2(\text{MA})_2\text{Pb}_3\text{I}_{10}$ single crystal bulk is shown in Figure S1a, where the optical microscope image in the inset shows a 2D perovskite flake. The thickness of the flake is characterized in SEM measurement to be around 100 nm, see Figure S1b. Figure 1a shows a typical TA spectrogram of 2D perovskite flake excited with 3.1eV photon (i.e. 400 nm) at an intensity of 30 $\mu\text{J}/\text{cm}^2$ per pulse, which corresponds to an initial carrier density $n_0 = 6 \times 10^{18} \text{ cm}^{-3}$. A single ground state bleach (GSB) signal ($\Delta A < 0$) due to the filling of band-edge states appears at around 2 eV and is consistent with the ground state absorption band-edge position in Figure S1a, as well as with the excitonic absorption peak of the similar samples in earlier study.⁴¹ In addition, there is an evolution of photo-induced absorption (PIA) signal ($\Delta A > 0$) at the red-side of the band-edge (1.95 eV in Figure 1a) into a photobleaching signal since the lowest-energy states at the band edge are quickly (~ 0.1 ps) populated by the cooled carriers.⁴² We point out that the 2D perovskite phases with other n -value (i.e. $(\text{BA})_2\text{PbI}_4$ as $n = 1$ or $(\text{BA})_2(\text{MA})\text{Pb}_2\text{I}_7$ as $n = 2$ in Figure S1c), which are

unavoidable in film samples, are not present here, demonstrating the high purity of (BA)₂(MA)₂Pb₃I₁₀ single-crystal flakes.

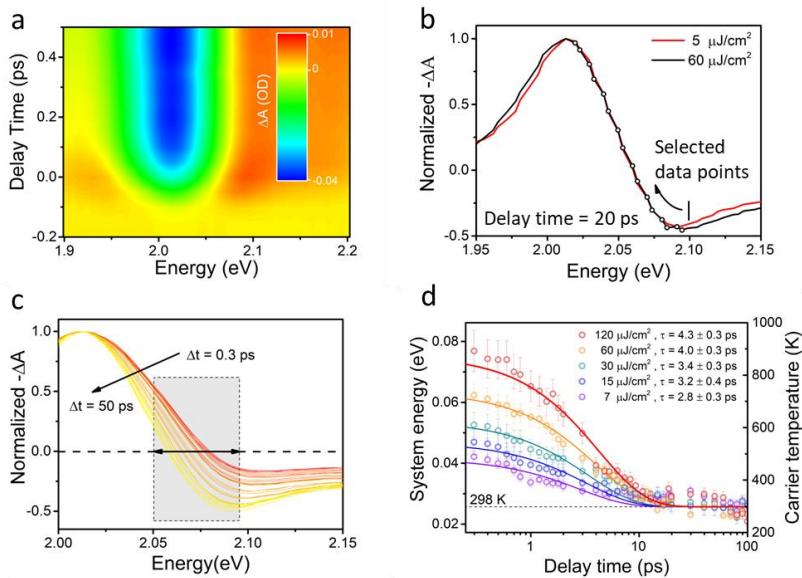


Figure 1. TA spectra and HC cooling dynamics of a 2D perovskite flake. (a) Pseudo-color representative TA spectrogram of the flake excited at 3.1 eV (400 nm) with excitation intensity of 30 $\mu\text{J}/\text{cm}^2$. (b) TA spectra of flake with excitation intensity of 5 and 60 $\mu\text{J}/\text{cm}^2$, the inserted line represents end point (~ 2.10 eV) of the fitting range. (c) Normalized TA spectra extracted from (a) with the time delay range from 0.3 to 50 ps. The shaded rectangle with a two-headed black arrow marks the fitting range of the high energy tails of the ground state bleach used for obtaining the hot carrier temperature. (d) photo-generated hot carrier temperature decay kinetics with 400nm excitation at different excitation intensities ($I_1 = 120$ $\mu\text{J}/\text{cm}^2$, $I_2 = 60$ $\mu\text{J}/\text{cm}^2$, $I_3 = 30$ $\mu\text{J}/\text{cm}^2$, $I_4 = 15$ $\mu\text{J}/\text{cm}^2$, $I_5 = 7$ $\mu\text{J}/\text{cm}^2$, corresponding to initial carrier density $n_0 = 2.4 \times 10^{19}$, 1.2×10^{19} , 6×10^{18} , 3×10^{18} , 1.4×10^{18} cm^{-3} respectively, see Supporting Information S2 and S3). The temperature decays are individually fitted with single exponential function.

First we analyze time-dependent carrier temperature based on the analysis of the TA spectra. As the ΔA reflects the population of excited carriers, we can fit the high energy tail of GSB signal by the Boltzmann distribution of HCs to extract the temperature. The approach has been widely reported in literature.^{18, 29, 43} The details of the implementation vary from study to study. Our procedure starts from verifying that the long-time line-shapes of the spectra under different excitation intensities are the same thereby showing consistency with the expected asymptotic approach to the ambient conditions. As shown in Figure 1b, the TA spectra under more than an order of magnitude different excitation intensities coincide, showing that the hot carriers have cooled to the same level within 20 ps reaching equilibrium with the environment. Based on this, we choose spectra at 100 ps under the lowest excitation intensity and assumed the ambient (298 K) carrier temperature.

Clearly, the TA spectra as in Fig. 1. cannot be directly fitted by an exponential Boltzmann distribution since the curves cross zero and resemble exponential only in a limited region. Therefore, the spectra need to be shifted up by an offset and we have to establish a way to determine which part of the spectrum should be used for the fitting.

The TA spectrum as shown in Fig 1 changes the sign because of the contributions with opposite signs to the spectrum. In the chosen representation the bleach signal is positive and the excited state absorption negative. This is chosen for visual convenience to recognize the exponential tail of the bleach while the usual convention in TA spectroscopy is opposite to this. Not much is known about the spectral shape of the excited state absorption. In semiconductors it should be largely determined by the density of states and since the latter is constant for the 2D materials, we have chosen constant offset in our analyses. We used the following expression to fit the exponential tail of the spectrum:

$$\frac{\Delta T}{T} = A_1 + A_2 \exp\left(-\frac{E-E_f}{k_B T_c}\right) \quad (1)$$

Considering the similar effective masses of electrons ($0.097 \times m_0$) and hole ($0.141 \times m_0$),^{38, 44} their contributions to the TA signals are similar. Therefore, T_c should represent the average temperature of both hot electrons and holes. We have tested also the square root dependent offset (density of states in 3D)⁴⁵ leading only to minor changes in the outcome, see Supporting Information S4.

In Fig. 1b we see that at about 2.1 eV the spectrum turns upwards and clearly does not follow the exponent. This sets the end point for the fitting range. To find the appropriate starting point, we gradually increased the number of the points used for the fitting and evaluated R-square and the sum of the absolute values of residuals (see Figure S4a). The R-square reaches a relatively flat plateau when including 8-9 points while the sum of the absolute value of residuals starts rapidly increasing after including 12 points. We plot the TA spectra with Y-axis in log scale in Figure S4c and from this we establish the optimal number of data points as 10. In order to find appropriate offset we fixed the long-time temperature as 298 K and found the offset level which gave the best fit. The range of the fitted high-energy tails of the GSB signals is marked in Figure 1c. After the photoexcitation, the initially highly non-equilibrated HCs undergo a rapid energy redistribution reaching a quasi-thermal distribution. The HC temperature is a valid measure only after such distribution has been established. Since the TA analyses in terms of HC temperature relies on the thermal distribution of the carriers, the question rises, when can we start assigning temperature to the HCs based on the TA spectra. Here we analyzed the line-shapes of TR-2PPE spectra and concluded that at 0.3 ps the quasi-thermal distribution is achieved. For the details we refer to the Supporting Information S5.

Visual inspection of the TA spectra shown in Supporting Information S6, reveals qualitative trends of the cooling dynamics. The slope of the high-energy tail increases with the time until tens

of picoseconds, indicating the decay of the HC temperature. The slope of the tail at an early timescale (up to about 0.5 ps) becomes smaller with increasing excitation intensity in Figure S6a, which represents higher HC temperature. In addition, the larger slope changes at high excitation intensity indicate longer HC cooling time towards its final temperature. Figure 1d shows the time dependence of the carrier temperature at various excitation densities. The cooling process is well described by a single exponential function. At higher excitation intensity, the HC cooling is slowed down. After a rapid relaxation, the HCs cool to reach room temperature with a lifetime of a few ps (lifetime summarized in Figure 1d). These cooling times are within the same order of magnitude as the ones reported for 3D perovskite (for a detailed comparison, see Supporting Information table S6a).^{18, 29, 30, 43, 46} To confirm reproducibility of the method, we measured another sample with similar thickness and the analysis gives comparable dynamics, as shown in Supporting Information S7.

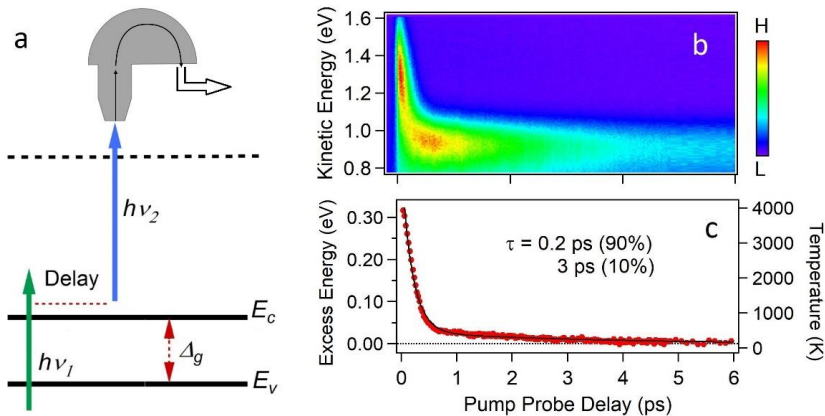


Figure 2. (a) Scheme of the TR-2PPE measurements. (b) Pseudocolor TR-2PPE spectrogram where the sample is pumped with 3.1 eV at $100 \mu\text{J}/\text{cm}^2$ and probed at 4.65 eV of incident MUV photon energy. (c) Average excess energy decay of hot electrons in TR-2PPE measurements based on eq 1. Sample is kept at close to the 135K with liquid nitrogen during the measurement.

In the following we use TR-2PPE, which directly probes electron distribution in the conduction band.^{47, 48, 49} The technique is demanding and has not been used as frequently as TA for the studies of hot carrier cooling. The pump pulse in the two experiments is very similar exciting the electrons into high energy states in the CB. In TR-2PPE, after a certain time delay, the electrons are excited from the CB to vacuum (i.e. photo-emitted) by the middle ultraviolet (MUV) probe pulse. The emitted photoelectrons are collected and analyzed in terms of both energy and momentum. Figure 2a illustrates the detailed configuration of the TR-2PPE measurement of our 2D perovskite single-crystal flake, which is cleaved under a high vacuum to generate an atomically flat surface. Figure 2b shows a TR-2PPE spectrogram of a 2D perovskite flake that displays the intensity of the photoelectron signal as a function of their kinetic energy as well as time. The detailed energy distribution curves (EDC) at representative time delays are shown in Figure S8b. At early delays the probe pulse creates an intense distribution of photoexcited electrons with kinetic energy peaking around 1.30 eV and mapping out the corresponding early hot electron distribution in the CB created by the pump pulse. Later a broader band peaked around 0.95 eV appears, indicating that the energy of initial excited hot electrons is redistributed to a pool of quasi-thermalized electrons with lower energy. The detailed fitting and discussion on dynamics at different excess energy states can be found in Supporting Information S8.

In the next step, we calculate the average excess energy $E_x(t)$ as a function of time delay by integrating the overall excess energy distribution of the HCs as⁵⁰

$$E_x(t) = \frac{\int E[I(E,t) - I(E,-)]dE}{\int [I(E,t) - I(E,-)]dE} \quad (2)$$

where the $I(E, t)$ is the spectrum at delay time t and $I(E, -)$ represents the background spectrum measured at a negative time delay. The excess energy is shown in Figure 2c. The energy can trivially be converted to carrier temperature allowing direct comparison with TA results. The description about how to obtain the excess energy can be found in Supporting Information S9.

To have a meaningful discussion on the sub-picosecond dynamics of the TA and TR-2PPE measurements, as shown in Figure 3, we use the term ‘system energy’ instead of carrier temperature since the temperature of carriers can only be evaluated after thermalization but the energy is there all the time.

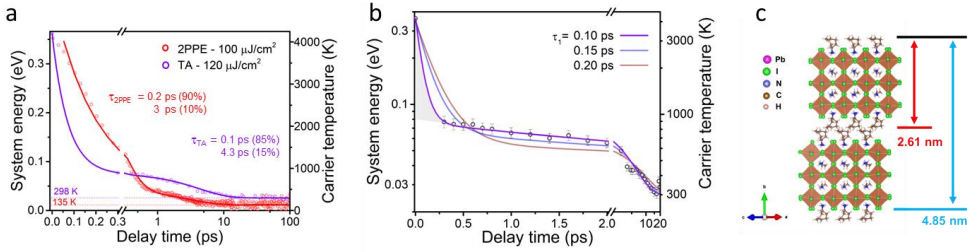


Figure 3. (a) Time dependence of HC temperature extracted from both TA measurements and average excess energy of TR-2PPE. (b) Time dependence of HC temperature extracted from TA measurements with the initial system energy adopted from TR-2PPE measurement. The temperature curve is fitted with bi-exponential function, where the fast component is fixed to be 0.1, 0.15 and 0.2 ps. (c) Schematic structure of a 2D perovskite unit. The thickness of an inorganic layer sandwiched by two spacing cations is 2.61 nm, and the distance from the surface to the bottom of the second inorganic layer is 4.85 nm. The hot phonon bottleneck temperature is 900 K in TA measurement and 480 K in 2PPE measurement.

As shown in Figure 3a, the HC cooling dynamics from TR-2PPE can be fitted by bi-exponential decay function with lifetimes of 0.2 and 3 ps. The long component is the result of the hot phonon bottleneck. The fast component matches well with the short lifetime of hot electrons in Figure S8c. TR-2PPE measurements can directly monitor the hot electron distributions, which reflects system energy straightforwardly as excess energy. This is not the case in TA analysis. TA results contain abundant information of the system in a more general way with less experimental demands than TR-2PPE, but the high energy tail of bleaching signal needs to be fitted to obtain the system energy. It means that TA cannot quantify the system energy before the measured bleach tail follows the Boltzmann distribution. We confirm the timescale of this limitation (~ 0.3 ps) by fitting the TR-2PPE spectra with Boltzmann distribution at different delays in Figure S5b.

We cannot consistently use the first 0.3 ps of the TA data for analyzing the cooling dynamics. This is why in Figure 1d a single exponential fit starting at 0.3 ps was used, but we know that the initial excitation in two experiments is the same. Thus, we can adopt the initial system energy value from TR-2PPE as the starting point in TA analysis. The adopted value is close to the initial excess energy of hot carriers (~ 4200 K) with thermal motion in 3D. This corresponds to a physical picture where the carriers can efficiently jump from layer to layer. More detailed discussion about determining the initial system energy can be found in Supporting information S10.

With this 'starting temperature', we can obtain a glance on the cooling dynamics, or relaxation, before the carrier temperature can be evaluated (< 0.3 ps). The two time constants of the HC cooling based on the TA data are ≤ 0.1 ps and 4.3 ps – the first cooling stage is significantly faster than in TR-2PPE while the second stage has a comparable rate. At the same time the second cooling stage in TA has a higher amplitude. In Figure 3b we demonstrate that the longer initial

decay times severely deviate from the data points, meaning that the 0.1 ps has to be taken as the upper limit for the fast decay component.

The reason why there are two stages of the carrier cooling is the so called hot phonon bottleneck – the hot carriers warm up the LO phonons and reach equilibrium where the energy flow from hot carriers to LO phonons is equal to the backwards flow. Once the equilibrium is reached, the further cooling corresponds to the energy flow from LO phonons to the acoustic phonons. Apparently this stage has own bottleneck behavior revealed by the slowing down at higher excitation intensities, see Fig. 1d. This behavior has been earlier reported in other studies and also called the hot phonon bottleneck.^{17, 29} However, there are subtle differences between these two bottleneck behaviors – the equilibrium at the first case is between the hot carriers and the LO phonons while in the second case the effect is more likely between the LO and acoustic phonons. The possible explanation of the latter can be the low thermal conductivity of the sample caused by the hindered acoustic phonon propagation.⁴⁶

Let us now compare the HC cooling in Stage I in the two measurements. An important difference between the TA and TR-2PPE is the probing depth of the photo-generated species. Noteworthy, the samples are both pumped with 400 nm laser with similar fluence, meaning that the excitation concentrations are comparable in the two experiments. The mean escape depth of the photoelectrons due to the photon energy used in TR-2PPE is about 3 nm.⁵¹ This means that the signal in the TR-2PPE measurement is predominantly contributed by the first inorganic Pb-I octahedral layer plus the attached long-chain spacing cation with a thickness of 2.61 nm according to the lattice structure shown in Figure 3c. On the other hand, the optical density (O.D.) of the single crystal flake in the TA measurement is 0.07, which ensures the transmittance of 86% of the incident light through the whole 2D perovskite flake containing 40 inorganic layers with a

thickness of 100 nm. This means that the HC dynamics measured in TA, with the probing depth significantly longer than the flake thickness, contain information about the bulk.

The initial HC relaxation is driven by the carrier-LO phonon coupling. In this context, the faster cooling rate may mean stronger coupling strength or the larger density of LO phonon states in the bulk. The Pb-I stretching mode of the octahedral cage provides the most important contribution to the LO phonons that cause the HC cooling in the 3D perovskite.^{31,32} If the Pb-I bond vibration on the surface of the 2D perovskite flake would be different from the analogous nuclear motions in the inner bulk, that could be a source of the differences in the cooling process in the two experiments. From the low-energy electron diffraction (LEED) measurements as seen in Figure 4a, we found the distance between neighboring Pb atoms at the 2D perovskite surface (6.2 Å) to be very close to the value in the bulk (6.3 Å) as shown in Figure 4b. The detailed calculation based on LEED pattern is discussed in Supporting Information S11. The similar bond configuration suggests that the surface layer structure does not change much, and the spacer still exists on the very surface. Recently, surface octahedral tilting in the exfoliated 2D perovskite was reported based on a scanning tunneling microscopy (STM) study,³⁶ indicating that surface lattice distortion is different from the bulk area. Our previous study revealed that the e-ph coupling strength of a 2D perovskite single crystal varies significantly between in-plane facet and facet perpendicular to the 2D layers.³⁵ The e-ph coupling is enhanced in the strain-accumulated area at perpendicular facets while weakened in the strain-relaxed area at in-plane facet, which is the target facet in our measurements. This suggests that in our case the e-ph coupling is weakened in the surface layer where the steric hindrance is relaxed. In addition, the STM work shows that the spacing cation on the surface sheet is more flexible and softened by exfoliation (which is visualized *via* the increased octahedral tilting angle). Therefore, less ‘regular’ phonon modes may appear. In other words, there

will be fewer decay channels for HC to be coupled to, which will reduce the efficiency of HC cooling on the surface layer in the first cooling stage.

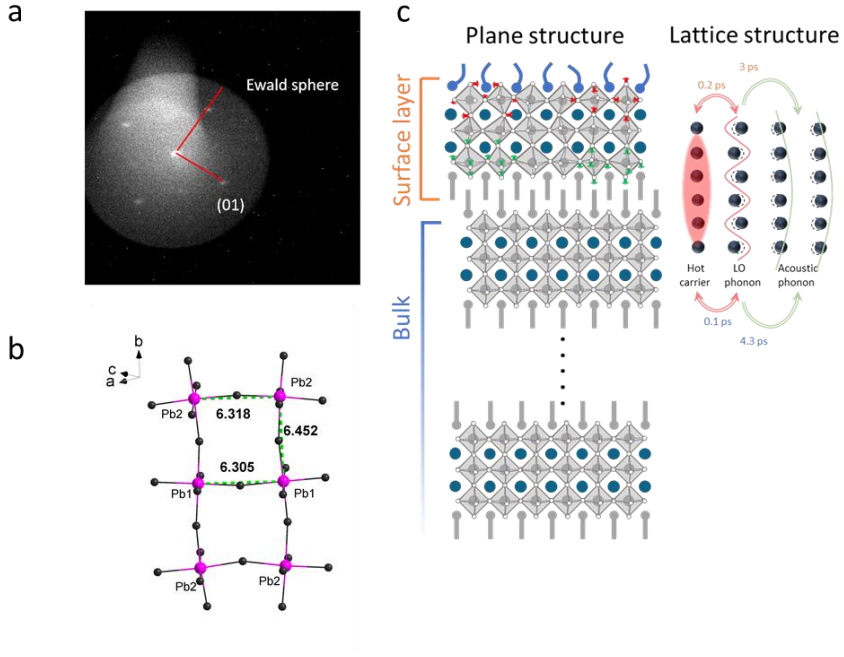


Figure 4. (a) LEED measurements with 9.86 eV of electron kinetic energy. (b) Diagram of plane structure of 2D perovskite single crystal. (c) Schematic of the HC cooling pathways. After the photoexcitation and possible carrier-carrier scattering, the HC decays *via* the coupling with LO phonon in the early time stage (Stage I). In Stage II, the LO phonon further decays to an acoustic phonon, and eventually the energy will be lost to the environment. The red oscillators represent optical phonon modes, while the green oscillators represent acoustic phonons.

Based on the above discussion, we propose that the e-ph coupling strength and amount of available LO phonons at the surface and bulk area are different due to the release of strain at

exfoliated surface layer explaining the differences in the initial carrier relaxation dynamics at the surface and in the bulk.

Another difference between the two experiments is the environmental temperature – while the TA experiments were carried out at room temperature, in the TR-2PPE measurements were conducted at cryogenic conditions with temperature of the sample about 135 K. Can the faster HC cooling at higher environmental temperature be due to the increased population of acoustic phonons and leads to a more efficient phonon-phonon scattering? ⁵² The interpretation fits our observation, but the associated timescale is much longer than our target since the phonon decay is involved.

A more likely explanation involves thermal population of LO phonons. In the Fröhlich model of electron-phonon interaction, the charge carriers are Coulomb coupled to the macroscopic electric field induced by the collective counter phase LO phonon motion of the oppositely charged ions. This coupling leads to hot electron dynamics *via* emitting or absorbing a LO phonon. The corresponding downwards (phonon emission) and upwards (phonon absorption) rates W_{em} and W_{ab} can be expressed as:^{53, 54}

$$W_{em} \sim \alpha [N(\omega_{LO}) + 1] \rho(\omega_{LO}) \quad (3)$$

$$W_{ab} \sim \alpha N(\omega_{LO}) \rho(\omega_{LO}) \quad (4)$$

Here $\rho(\omega_{LO})$ is LO phonon density of states, $N(\omega_{LO})$ is the Bose-Einstein distribution

$$N(\omega_{LO}) = \frac{1}{\exp(\hbar\omega_{LO}/k_B T_L) - 1} \quad (5)$$

giving the average number of the LO phonons at the corresponding lattice temperature T_L . α is dimensionless Fröhlich coupling constant:

$$\alpha = \frac{e^2}{\hbar\omega_{LO}} \left(\frac{1}{\epsilon_\infty} - \frac{1}{\epsilon_0} \right) \sqrt{\frac{m\omega_{LO}}{2\hbar}} \quad (6)$$

where m is the effective mass of the electrons in the band, ϵ_∞ and ϵ_0 are the high frequency and static dielectric constant. The difference of the two terms in the brackets eliminates the fast electronic polarizability leaving only the nuclear contribution.

The LO phonon here mostly corresponds to the stretching motion of the $[\text{PbI}_3]^-$ network having frequency of about 100 cm^{-1} (corresponding to 12.4 meV or $k_B \times 145 \text{ K}$).⁵⁵ This means that the LO phonon population at room temperature is much higher than at 135 K . The calculation based on eq. 4 gives values for the downwards relaxation “stimulation” factors $N(\omega_{LO}) + 1$ at room temperature and at 135 K as 2.6 and 1.5, respectively. The ratio

$$\Delta_N = \frac{N_{298K}(\omega_{LO}) + 1}{N_{135K}(\omega_{LO}) + 1} \quad (7)$$

is 1.7 and can be a source of the differences in the initial fast cooling rate in the two experiments, since the more populated LO phonons lead to higher cooling efficiency. The above energy of LO phonons is based on experiments and calculations on 3D perovskite (MAPbI_3). However, the spacing cation can modify the vibrational frequencies by mixing motions of the organic cation with the vibrations of the inorganic cage.^{56, 57} Therefore, the more abundant ligand environment in 2D perovskite can substantially affect the optical phonon properties compared to the 3D perovskite,⁵⁸ and a clear conclusion about the significance of environmental temperature on HC cooling rate cannot be drawn due to the uncertainty in LO phonon energy. For example, the ratio Δ_N will decrease to 1.34 and 1.15 for LO phonon energy of 30 meV and 50 meV , which have been reported for the 2D perovskites.^{59, 60}

The other possible reason for observing different HC cooling dynamics with TR-2PPE and TA is that the former can only probe the population of hot electrons, while the latter detects both hot electrons and holes. Taking the energy of LO phonon and the initial energy of the HC (i.e. directly after carrier excitation and before any energy transfer processes) as constants, the power loss rate

is proportional to the Fröhlich coupling constant α and thereby further to the square root of the effective mass m of carriers, as shown in eq 5.^{53, 54} The effective mass of electrons is lighter than the effective mass of holes in 2D perovskite.³⁸ Therefore the hot electrons should exhibit a lower power loss rate due to the e-ph coupling. However, the difference of the effective masses is small,^{38, 44} and the square root further reduces the corresponding difference in the Fröhlich constant. Therefore, effective mass, should not be a dominating reason for the faster cooling rate in TA measurements. Though, the polaron formation can influence the electron and hole effective masses differently,^{61, 62} we do not extend this discussion further.

As the result of the differences in two experiments, the hot electron temperature at the surface layer in the TR-2PPE measurements cools slower (0.2 ps) than the temperature in the whole bulk volume in the TA measurements (0.1 ps).

As for Stage II (thermal equilibration between LO phonons and acoustic phonons), the cooling time of the surface layer extracted from TR-2PPE data is 3 ps, while for bulk area extracted TA data it is 4.3 ps. These times are comparable. However, what is clear is that the initial temperature of the second stage, the hot phonon bottleneck temperature, is higher in TA measurement than TR-2PPE measurement. This difference is larger than the ambient temperature difference in the two experiments. We can speculate that if the density of states of LO phonons is higher in the surface area, the LO phonons could accommodate more energy and the hot phonon bottleneck would occur at lower temperature than in the bulk area. However, more work is needed before the explanation can be put forward with certainty.

CONCLUSION

We have studied photo-induced HC cooling dynamics in 2D perovskite single crystal flakes using TA and TR-2PPE spectroscopies. In the TA analysis, the high-energy tails of the bleaching signals are fitted by Boltzmann distribution. The analyses are applicable starting from 0.3 ps when the electron distribution has reached the quasi-equilibrium. The carrier temperature obtained from TA analysis strongly depends on the offset and the fitting range. The uncertainty is minimized by statistical analyses of the results and assuming long-time convergence of the temperature supported by direct line shape comparison of the spectra measured with wide range of intensities. By adopting the initial system energy from the TR-2PPE, the bi-exponential analysis of the TA temperature decay provides two lifetimes, ≤ 0.1 ps (upper limit for the fast component) and 4.3 ps. In the TR-2PPE analysis, we convert the average excess energy to system energy and fit it with a bi-exponential decay function (0.2 and 3 ps). All in all, compared to the TA results the cooling rates observed in TR-2PPE are slower in the first stage and the initial temperature in the second stage is lower. There are several possible origins of the differences in the two experiments. First of all, the probing depth is drastically different – TR-2PPE only “sees” the upper layer of the sample while the TA probes the whole. We also discuss the different temperatures of the environment and the contribution of the hole signal as the possible sources of the differences.

The different probing depths speak for the influence of local structure on the HC cooling mechanisms. On the surface sheet, the local lattice structure is more distorted, and the attached spacing cations are more flexible and softer, which can modify the phononic features and decrease the e-ph coupling efficiency. Based on the temperature dependence of LO phonon population, the difference in the fast initial relaxation can partially be explained by different phonon populations. We also point out that only the electrons can be detected in TR-2PPE, and the lighter effective

mass will lead to slower carrier temperature decay than what the holes have. However, the expected dependence is small and the effective mass difference alone cannot be the explanation. We conclude that the modification of the LO-phonon structure possibly combined with the other two factors, temperature difference and insensitivity to the holes, is responsible for the prolonged HC lifetime in Stage I observed in the TR-2PPE measurements. As for the lower initial temperature of Stage II in TR-2PPE measurement, possibly the hot phonon bottleneck effect is weakened due to the higher density of states of LO phonons. More investigations on the spatial profile of phonons are needed for the clearer understanding and identification of involved mechanisms.

Our work indicates a spatial dependency of the cooling process in 2D crystals. It also rationalizes the origins of HC cooling in 2D perovskites, which may benefit the future applications of hot carriers. In addition, we show the TR-2PPE technique is a powerful tool for investigating the HC properties allowing clear visualization of the cooling stages.

ASSOCIATED CONTENT

Supporting Information

The following files are available free of charge.

Characterization of 2D perovskite single crystals; Absorption coefficient and carrier density calculations of 2D perovskite flake; Absorption coefficient of 2D perovskite thin film; Determination of energy window and offset for TA analysis; Quasi-equilibrium timescale; Excitation dependent TA spectra and time dependent HC temperature; Comparison to other flakes; Time dependent energy distribution curve (EDC) of TR-2PPE measurements; Calculation of excess energy from TR-2PPE spectrogram; Initial system energy and fast component analysis for TA results; Low-energy electron diffraction (LEED) measurements; 2D perovskite flake preparation and position-selective TA measurements; Estimation of lattice temperature and hot

phonon bottleneck temperature; Calculation of binding energy based on temperature dependent photoluminescence measurements (PDF)

AUTHOR INFORMATION

Corresponding Author

*tonu.pullerits@chemphys.lu.se

*kaibo.zheng@chemphys.lu.se

*sophie.canton@xfel.eu

Funding Sources

China Scholarship Council, Swedish Research Council (VR), KAW foundation, Swedish Energy Agency, ANR project 2D-Hype (Nr. ANR-21-CE30-0059-01)

Conflicts of interest

The authors declare no competing financial interest.

ACKNOWLEDGMENT

We acknowledge financial support from Swedish Research Council, Swedish Energy Agency, the Knut and Alice Wallenberg Foundation (Project 2016.0089), the ANR project 2D-Hype (Nr. ANR-21-CE30-0059-01). This work was supported by Chinese Scholarship Council for the PhD scholarship to W. L., M. L., J. M., X. Z., Q. Z, and the DAAD Scholarship for the PhD Scholarship of M.C.

REFERENCES

- 1 H. J. Snaith, *J. Phys. Chem. Lett.*, 2013, **4**, 3623-3630.
- 2 Y. Fang, Q. Dong, Y. Shao, Y. Yuan and J. Huang, *Nat. Photonics*, 2015, **9**, 679-686.
- 3 M. Yuan, L. N. Quan, R. Comin, G. Walters, R. Sabatini, O. Voznyy, S. Hoogland, Y. Zhao, E. M. Beauregard, P. Kanjanaboos, Z. Lu, D. H. Kim and E. H. Sargent, *Nat. Nanotechnol.*, 2016, **11**, 872-877.

- 4 L. Dou, A. B. Wong, Y. Yu, M. Lai, N. Kornienko, S. W. Eaton, A. Fu, C. G. Bischak, J. Ma, T. Ding, N. S. Ginsberg, L.-W. Wang, A. P. Alivisatos and P. Yang, *Science*, 2015, **349**, 1518-1521.
- 5 M. Saliba, T. Matsui, J.-Y. Seo, K. Domanski, J.-P. Correa-Baena, M. K. Nazeeruddin, S. M. Zakeeruddin, W. Tress, A. Abate, A. Hagfeldt and M. Grätzel, *Energy Environ. Sci.*, 2016, **9**, 1989-1997.
- 6 J. Burschka, N. Pellet, S.-J. Moon, R. Humphry-Baker, P. Gao, M. K. Nazeeruddin and M. Grätzel, *Nature*, 2013, **499**, 316-319.
- 7 W. Shockley and H. J. Queisser, *J. Appl. Phys.*, 1961, **32**, 510-519.
- 8 A. Rajagopal, Z. Yang, S. B. Jo, I. L. Braly, P. W. Liang, H. W. Hillhouse and A. K. Y. Jen, *Adv. Mater.*, 2017, **29**, 1702140.
- 9 R. T. Ross and A. J. Nozik, *J. Appl. Phys.*, 1982, **53**, 3813-3818.
- 10 G. Conibeer, N. Ekins-Daukes, J.-F. Guillemoles, D. König, E.-C. Cho, C.-W. Jiang, S. Shrestha and M. Green, *Sol. Energy Mater. Sol. Cells*, 2009, **93**, 713-719.
- 11 Y. Takeda, T. Motohiro, D. König, P. Aliberti, Y. Feng, S. Shrestha and G. Conibeer, *Appl. Phys. Express*, 2010, **3**, 104301.
- 12 A. J. Nozik, *Nat. Energy*, 2018, **3**, 170-171.
- 13 Z. Nie, X. Gao, Y. Ren, S. Xia, Y. Wang, Y. Shi, J. Zhao and Y. Wang, *Nano Lett.*, 2020, **20**, 4610-4617.
- 14 Q. Sun, J. Gong, X. Yan, Y. Wu, R. Cui, W. Tian, S. Jin and Y. Wang, *Nano Lett.*, 2022, **22**, 2995-3002.
- 15 J. Meng, Z. Lan, W. Lin, M. Liang, X. Zou, Q. Zhao, H. Geng, I. E. Castelli, S. E. Canton, T. Pullerits and K. Zheng, *Chem. Sci.*, 2022, **13**, 1734-1745.
- 16 J. M. Frost, L. D. Whalley and A. Walsh, *ACS Energy Lett.*, 2017, **2**, 2647-2652.
- 17 M. Li, S. Bhaumik, T. W. Goh, M. S. Kumar, N. Yantara, M. Gratzel, S. Mhaisalkar, N. Mathews and T. C. Sum, *Nat. Commun.*, 2017, **8**, 14350.
- 18 J. Fu, Q. Xu, G. Han, B. Wu, C. H. A. Huan, M. L. Leek and T. C. Sum, *Nat. Commun.*, 2017, **8**, 1300.
- 19 G. Ghosh, R. K. Biswas, K. Marjit, S. Ghosh, A. Ghosh, S. K. Pati and A. Patra, *Adv. Opt. Mater.*, 2022, **10**, 2200030.
- 20 H. Zhu, K. Miyata, Y. Fu, J. Wang, P. P. Joshi, D. Niesner, K. W. Williams, S. Jin and X.-Y. Zhu, *Science*, 2016, **353**, 1409-1413.
- 21 Z. Guo, Y. Wan, M. Yang, J. Snaider, K. Zhu and L. Huang, *Science*, 2017, **356**, 59-62.
- 22 J. W. M. Lim, D. Giovanni, M. Righetto, M. Feng, S. G. Mhaisalkar, N. Mathews and T. C. Sum, *J. Phys. Chem. Lett.*, 2020, **11**, 2743-2750.
- 23 P. Guo, C. C. Stoumpos, L. Mao, S. Sadasivam, J. B. Ketterson, P. Darancet, M. G. Kanatzidis and R. D. Schaller, *Nat. Commun.*, 2018, **9**, 2019.
- 24 M. Liang, W. Lin, Z. Lan, J. Meng, Q. Zhao, X. Zou, I. E. Castelli, T. Pullerits, S. E. Canton and K. Zheng, *ACS Appl. Electron. Mater.*, 2020, **2**, 1402-1412.
- 25 G. Conibeer, S. Shrestha, S. Huang, R. Patterson, H. Xia, Y. Feng, P. Zhang, N. Gupta, M. Tayebjee, S. Smyth, Y. Liao, S. Lin, P. Wang, X. Dai and S. Chung, *Sol. Energy Mater. Sol. Cells*, 2015, **135**, 124-129.
- 26 L. Brillouin, *Wave Propagation In Periodic Structures*, Mcgraw-hil Book Company, Inc., New York, 1946.
- 27 V. Narayanamurti, H. L. Störmer, M. A. Chin, A. C. Gossard and W. Wiegmann, *Phys. Rev. Lett.*, 1979, **43**, 2012-2016.

- 28 J. Yin, P. Maity, R. Naphade, B. Cheng, J.-H. He, O. M. Bakr, J.-L. Brédas and O. F. Mohammed, *ACS Nano*, 2019, **13**, 12621-12629.
- 29 Y. Yang, D. P. Ostrowski, R. M. France, K. Zhu, J. van de Lagemaat, J. M. Luther and M. C. Beard, *Nat. Photonics*, 2015, **10**, 53-59.
- 30 M. B. Price, J. Butkus, T. C. Jellicoe, A. Sadhanala, A. Briane, J. E. Halpert, K. Broch, J. M. Hodgkiss, R. H. Friend and F. Deschler, *Nat. Commun.*, 2015, **6**, 8420.
- 31 K. Miyata, D. Meggiolaro, M. T. Trinh, P. P. Joshi, E. Mosconi, S. C. Jones, F. De Angelis and X. Y. Zhu, *Sci. Adv.*, 2017, **3**, e1701217.
- 32 X. Lao, Z. Yang, Z. Su, Y. Bao, J. Zhang, X. Wang, X. Cui, M. Wang, X. Yao and S. Xu, *J. Phys. Chem. C*, 2019, **123**, 5128-5135.
- 33 S. Kahmann and M. A. Loi, *J. Mater. Chem. C*, 2019, **7**, 2471-2486.
- 34 P. G. Klemens, *Phys. Rev.*, 1966, **148**, 845-848.
- 35 M. Liang, W. Lin, Q. Zhao, X. Zou, Z. Lan, J. Meng, Q. Shi, I. E. Castelli, S. E. Canton, T. Pullerits and K. Zheng, *J. Phys. Chem. Lett.*, 2021, **12**, 4965-4971.
- 36 Y. Shao, W. Gao, H. Yan, R. Li, I. Abdelwahab, X. Chi, L. Rogée, L. Zhuang, W. Fu, S. P. Lau, S. F. Yu, Y. Cai, K. P. Loh and K. Leng, *Nat. Commun.*, 2022, **13**, 138.
- 37 P. Maity, J. Yin, B. Cheng, J.-H. He, O. M. Bakr and O. F. Mohammed, *J. Phys. Chem. Lett.*, 2019, **10**, 5259-5264.
- 38 C. C. Stoumpos, D. H. Cao, D. J. Clark, J. Young, J. M. Rondinelli, J. I. Jang, J. T. Hupp and M. G. Kanatzidis, *Chem. Mater.*, 2016, **28**, 2852-2867.
- 39 N. S. Dahod, A. France-Lanord, W. Paritmongkol, J. C. Grossman and W. A. Tisdale, *J. Chem. Phys.*, 2020, **153**, 044710.
- 40 K. S. Novoselov, A. K. Geim, S. V. Morozov, D. Jiang, Y. Zhang, S. V. Dubonos, I. V. Grigorieva and A. A. Firsov, *Science*, 2004, **306**, 666-669.
- 41 J. C. Blancon, A. V. Stier, H. Tsai, W. Nie, C. C. Stoumpos, B. Traore, L. Pedesseau, M. Kepenekian, F. Katsutani, G. T. Noe, J. Kono, S. Tretiak, S. A. Crooker, C. Katan, M. G. Kanatzidis, J. J. Crochet, J. Even and A. D. Mohite, *Nat. Commun.*, 2018, **9**, 2254.
- 42 H. Chung, S. I. Jung, H. J. Kim, W. Cha, E. Sim, D. Kim, W. K. Koh and J. Kim, *Angew. Chem.*, 2017, **56**, 4160-4164.
- 43 J. Chen, M. E. Messing, K. Zheng and T. Pullerits, *J. Am. Chem. Soc.*, 2019, **141**, 3532-3540.
- 44 M. Dyksik, H. Duim, X. Zhu, Z. Yang, M. Gen, Y. Kohama, S. Adjokatse, D. K. Maude, M. A. Loi, D. A. Egger, M. Baranowski and P. Plochocka, *ACS Energy Lett.*, 2020, **5**, 3609-3616.
- 45 S. D. Verma, Q. Gu, A. Sadhanala, V. Venugopalan and A. Rao, *ACS Energy Lett.*, 2019, **4**, 736-740.
- 46 J. Yang, X. Wen, H. Xia, R. Sheng, Q. Ma, J. Kim, P. Tapping, T. Harada, T. W. Kee, F. Huang, Y. B. Cheng, M. Green, A. Ho-Baillie, S. Huang, S. Shrestha, R. Patterson and G. Conibeer, *Nat. Commun.*, 2017, **8**, 14120.
- 47 B. Lv, T. Qian and H. Ding, *Nat. Rev. Phys.*, 2019, **1**, 609-626.
- 48 D. Niesner, H. Zhu, K. Miyata, P. P. Joshi, T. J. Evans, B. J. Kudisch, M. T. Trinh, M. Marks and X. Y. Zhu, *J. Am. Chem. Soc.*, 2016, **138**, 15717-15726.
- 49 E. Jung, K. Budzinauskas, S. Öz, F. Ünlü, H. Kuhn, J. Wagner, D. Grabowski, B. Klingebiel, M. Cherasse, J. Dong, P. Aversa, P. Vivo, T. Kirchartz, T. Miyasaka, P. H. M. Van Loosdrecht, L. Perfetti and S. Mathur, *ACS Energy Lett.*, 2020, **5**, 785-792.

- 50 Z. Chen, J. Sjakste, J. Dong, A. Taleb-Ibrahimi, J. P. Rueff, A. Shukla, J. Peretti, E. Papalazarou, M. Marsi and L. Perfetti, *Proc. Natl. Acad. Sci. U.S.A.*, 2020, **117**, 21962-21967.
- 51 M. P. Seah and W. A. Dench, *Surf. Interface Anal.*, 1979, **1**, 2-11.
- 52 I. Chatzakis, H. Yan, D. Song, S. Berciaud and T. F. Heinz, *Phys. Rev. B*, 2011, **83**, 205411.
- 53 S. Das Sarma, J. K. Jain and R. Jalabert, *Phys. Rev. B*, 1988, **37**, 6290-6296.
- 54 S. D. Sarma, J. K. Jain and R. Jalabert, *Phys. Rev. B*, 1990, **41**, 3561-3571.
- 55 M. A. Pérez-Osorio, Q. Lin, R. T. Phillips, R. L. Milot, L. M. Herz, M. B. Johnston and F. Giustino, *J. Phys. Chem. C*, 2018, **122**, 21703-21717.
- 56 F. Brivio, J. M. Frost, J. M. Skelton, A. J. Jackson, O. J. Weber, M. T. Weller, A. R. Goñi, A. M. A. Leguy, P. R. F. Barnes and A. Walsh, *Phys. Rev. B*, 2015, **92**, 144308
- 57 H. G. Duan, V. Tiwari, A. Jha, G. R. Berdiyrov, A. Akimov, O. Vendrell, P. K. Nayak, H. J. Snaith, M. Thorwart, Z. Li, M. E. Madjet and R. J. D. Miller, *J. Am. Chem. Soc.*, 2020, **142**, 16569-16578.
- 58 L. N. Quan, Y. Park, P. Guo, M. Gao, J. Jin, J. Huang, J. K. Copper, A. Schwartzberg, R. Schaller, D. T. Limmer and P. Yang, *Proc. Natl. Acad. Sci. U.S.A.*, 2021, **118**, e2104425118.
- 59 Y. Zhang, R. Wang, Y. Li, Z. Wang, S. Hu, X. Yan, Y. Zhai, C. Zhang and C. Sheng, *J. Phys. Chem. Lett.*, 2019, **10**, 13-19.
- 60 Z. Zhang, W. H. Fang, M. V. Tokina, R. Long and O. V. Prezhdo, *Nano Lett.*, 2018, **18**, 2459-2466.
- 61 M. Sendner, P. K. Nayak, D. A. Egger, S. Beck, C. Müller, B. Epding, W. Kowalsky, L. Kronik, H. J. Snaith, A. Pucci and R. Lovrinčić, *Mater. Horiz.*, 2016, **3**, 613-620.
- 62 C. Liu, H. Tsai, W. Nie, D. J. Gosztola and X. Zhang, *J. Phys. Chem. Lett.*, 2020, **11**, 6256-6261.

Supporting Information

Combining Two-Photon Photoemission and Transient Absorption Spectroscopy to Resolve Hot Carrier Cooling in 2D Perovskite Single Crystals: the Effect of Surface Layer

Weihua Lin^{1, *}, Mingli Liang^{1,2, *}, Yuran Niu³, Zhesheng Chen⁴, Marie Cherasse^{4,5}, Jie Meng², Xianshao Zou¹, Qian Zhao², Huifang Geng⁶, Evangelos Papalazarou⁷, Marino Marsi⁷, Luca Perfetti⁴, Sophie E. Canton^{8, *}, Kaibo Zheng^{1,2, *}, Tõnu Pullerits^{1, *}

Abstract: We investigate hot carrier (HC) cooling in two-dimensional (2D) perovskite single crystals by applying two complementary ultrafast spectroscopy techniques – transient absorption (TA) and time-resolved two-photon photoemission (TR-2PPE) spectroscopies. TR-2PPE directly maps the hot electron distribution and its dynamics in the conduction band to the detected photoelectron distribution. While TR-2PPE selectively probes the upper layer of the material, TA provides information on the whole bulk. Two cooling regimes are resolved in both techniques. The fast timescale of 100-200 fs is related to the electron scattering by longitudinal optical (LO) phonons and the slow timescale of 3-4 ps corresponds to the LO phonon relaxation. The HC cooling dynamic of TA measurement has faster initial stage and higher starting temperature for the slower stage than in TR-2PPE measurements. Conclusions about spatial sensitivity of the cooling dynamics across the 2D perovskite single crystals constitute valuable information that can guide the future development of HC solar cells and thermoelectric applications based on 2D perovskites.

DOI: 10.1002/anie.2021XXXXX

Table of Contents

- S1. Characterization of 2D perovskite single crystals
- S2. Absorption coefficient and carrier density calculations of 2D perovskite flake
- S3. Absorption coefficient of 2D perovskite thin film
- S4. Determination of energy window and offset for TA analysis
- S5. Quasi-equilibrium timescale
- S6. Excitation dependent TA spectra and time dependent HC temperature
- S7. Comparison to other flakes
- S8. Time dependent energy distribution curve (EDC) of TR-2PPE measurements
- S9. Calculation of excess energy from TR-2PPE spectrogram
- S10. Initial system energy and fast component analysis for TA results
- S11. Low-energy electron diffraction (LEED) measurements
- S12. 2D perovskite flake preparation and position-selective TA measurements
- S13. Estimation of lattice temperature and hot phonon bottleneck temperature
- S14. Calculation of binding energy based on temperature dependent photoluminescence measurements

Experimental Procedures

Synthesis of 2D Perovskite Single Crystals. The bulk single crystal of $(\text{BA})_2(\text{MA})_{n-1}\text{Pb}_{n13n+1}$ ($n = 1, 2, 3$) were obtained by the temperature gradient growth method, which is similar to our previous work.¹ First, PbI_2 (99 %), methanamine hydriodide (98 %, MAI),

butylammonium iodide (98 %, BAI), hypophosphorous acid solution (50 % in water; 5 ml) and hydroiodic acid (57 % in water; 0.25 ml) were initially formulated as the precursor solutions in 20 ml glass bottles (all the chemicals were supplied by Sigma-Aldrich). For the three samples ($n = 1, 2$ and 3), the $\text{PbI}_2/\text{MAI}/\text{BAI}$ contents are 1.5 mmol/0 mmol/2.0 mmol, 1.5 mmol/1.5 mmol/2.0 mmol, and 1.5 mmol/2.5 mmol/2.0 mmol, respectively. Then, such precursor solutions were sealed and stirred at room temperature for 30 mins. After that, they were heated at 80 °C until solutions become completely clear. The bulk single crystals were grown from the clear solutions at a cooling rate of 0.5 °C/day starting from 55 °C. The obtained crystals and their ball-stick model of the structure are shown in Figure S1d. In order to facilitate the measurements of our transient spectra, these bulk single crystals are separated into thin flakes using Scotch tape in a glove box. Later, these 2D perovskite flakes are sealed between the two quartz glasses with liquid optical clear adhesive (without touching samples, see Supporting Information S12) to prevent them from being damaged by moisture or oxidation after being taken out of the glove box.

Position-Selective Transient Absorption (TA) Measurements. The transient absorption (TA) spectra are collected in a transmission configuration with 400 nm pump beam and white light as probe beam. A pulsed laser of 800 nm wavelength, 80 fs pulse duration and 1kHz repetition frequency is generated by injecting the seed laser (Mai Tai, Spectra Physics) into a regenerative amplifier (Spitfire XP Pro, Spectra Physics). The output fundamental laser is split by a beam splitter for generating pump and probe beams. The pump is produced by second harmonic generation of 800nm incident beam *via* a BBO crystal. The probe beam is generated by focusing the 1350nm laser, which is obtained from the 800nm fundamental laser *via* a collinear optical parametric amplifier (TOPAS-C, Light Conversion), on a thin CaF_2 plate that mounted on a moving stage to avoid heat damage. The pump and probe beams are not parallel but is set to spatially overlap on flake sample which is monitored by digital microscope during TA measurements, see Supporting Information S12. The polarization between pump and probe beams is set to the magic angle (54.7°) by using the Berek compensator in the path of pump beam. A circular graduated neutral density filter is also placed in the pump path for the excitation intensity-dependent measurements. The time delay between pump and probe is controlled by a delay stage placed in the path of probe beam. After transmitting through sample, the probe beam is eventually passing the prism and dispersed on the photodiode array. To gain better signal-to-noise, the intensity of the scattering of pump beam is monitored and a gate is set to discard the useless data affected by laser fluctuation. A limit is set how different the scan results can be to alert for the possible degradation-related changes. If the signal (transmitted pulse intensity) differs from the average by more than 10 %, the measurement is stopped and the sample is carefully inspected. The optical microscope figure can be considered as a position reference for locating the suitable flake under digital microscope, where the neighboring bulky crystals work as marks. During the TA measurements, the position of probe light on sample was fixed and it was confirmed by the real-time digital microscope measurements.

Time-Resolved Two-Photon Photoemission (TR-2PPE) Spectroscopy. The TR-2PPE spectra were measured with angle-resolved photoemission spectroscopy (ARPES) in FEMTOARPES lab at SOLEIL synchrotron facility in France.² The fundamental laser beam (1.55 eV, 250 kHz repetition rate, 6 μJ intensity) is generated from a Ti:Sapphire laser system (Light conversion). The output fundamental laser is split by a beam splitter for generating pump and probe beams. The pump we applied in this study is the second harmonic generation (3.1 eV with maximum power density of 0.5 mJ/cm^2) of the fundamental one. The probe beams are the third harmonic beam (4.65 eV) in Figure 2 and fourth harmonic beam (6.2 eV) as shown in Figure S8a. The probe geometry is set to have a 45° incident angle on the sample. The emitted photo-electrons are collected and analyzed by an electrostatic analyzer in kinetic energy with a resolution of 50 meV. Note that the investigation of electron emission angle is not included in this study. A delay stage is applied to control the time delay between pump and probe with temporal resolution better than 100 fs considering the pulse duration.

The single crystals of 2D perovskite are first exfoliated by a scotch tape to produce to remove the surface residuals. After exfoliated crystal is then pressed onto the copper post in the sample plate, with the other side of crystal is glued on a ceramic post. After being loaded on the sample holder in the manipulator, the crystal is further cleaved by knocking down the ceramic post to have a flat atomic surface free from the moisture or oxygen invasion. The degradation test is carried out on sample using more intense pump beam than what is used in the real experiment. At the highest intensities the signal started to decrease after long time exposure. The experiments shown in the article were carried out at lower intensities and the exposer times were shorter warranting negligible degradation during the measurements.

Low-energy Electron Diffraction (LEED) Measurements. The LEED pattern was measured in a spectroscopic photoemission and low energy electron microscope (SPELEEM III, Elmitec) in MAXPEEM beamline at MAX-IV laboratory in Lund, Sweden. The instrument has a single digit nanometer spatial resolution. Before being placed in the loadlock of the microscope, the surface of the 2D perovskite single crystal was attached on a tape, while the other end of the tape is fixed on the surface of the loadlock. After pumping down the loadlock, the sample holder was taken out from the loadlock by a transfer arm, the tape was then automatically removed from the sample surface. At the same time, a few layers of the sample were peeled off and trashed. By using this method, a cleaved clean surface was obtained. Finally, the sample was transferred quickly into the main chamber that has a base pressure better than 1×10^{-10} torr for further analysis.

Results and Discussion

S1. Characterization of 2D perovskite single crystals

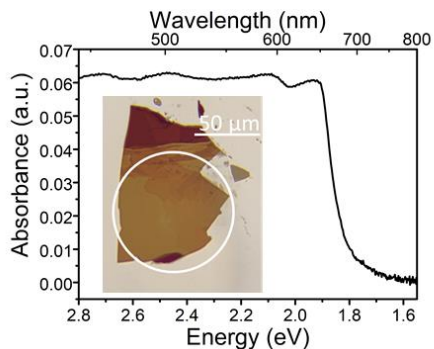


Figure S1a. Steady-state absorption spectrum of 2D perovskite bulk crystal and the optical microscope image of 2D perovskite flake on quartz with the thickness around 100 nm.

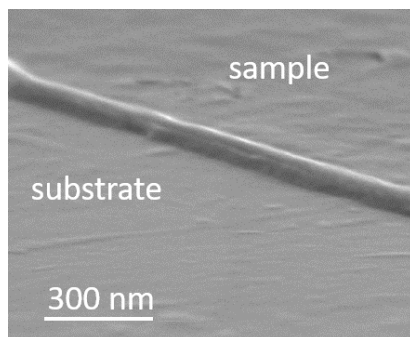


Figure S1b. Tilted scanning electron microscope (SEM) measurements of 2D perovskite flake which shares similar contrast in optical microscope measurements (*i.e.*, similar thickness) to the analyzed samples.

Since the purity plays an important role in the advance spectroscopy measurements, as the flake for transient absorption (TA) measurements has only few hundred nanometers thickness and x-ray measurements are surface-sensitive, we conduct the TA measurements on other 2D perovskite flakes that have different n -value as common impurities in single phase 2D perovskite films. By comparing the signal positions in Figure S1c, we can confirm the high purity of the 2D perovskite flakes and that the flake fabrication method is suitable for providing clean samples with suitable thickness. In the meantime, it indicates the feasibility of fitting temperature of HC based on transient absorption spectra of 2D perovskite flakes, as the signal from sample can be clearly assigned without being affected by other phases.

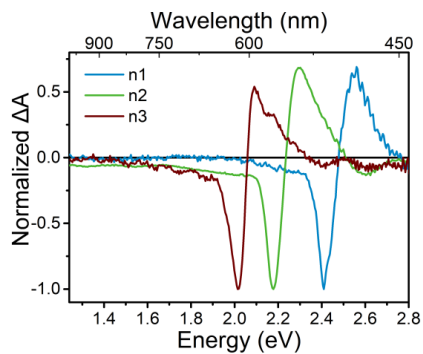


Figure S1c. TA spectra of 2D perovskite with different n-value in $(\text{BA})_2(\text{MA})_{n-1}\text{Pb}_n\text{I}_{3n+1}$ ($n = 1, 2$ and 3) at 1 ps time delay, pumped with 400 nm excitation with medium intensity (around 15 uJ/cm^2 per pulse).

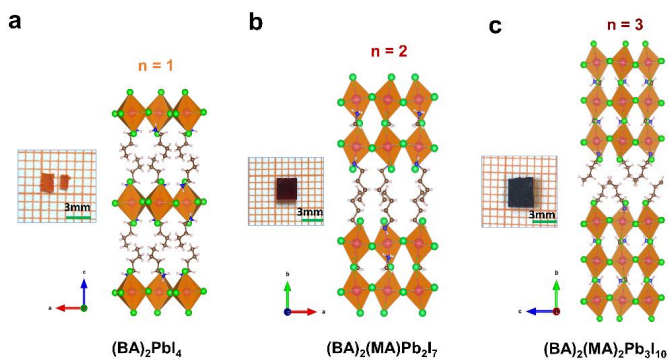


Figure S1d. The bulk single crystals and their ball-stick model of (a) $(\text{BA})_2\text{PbI}_4$ ($n1$), (b) $(\text{BA})_2(\text{MA})\text{Pb}_2\text{I}_7$ ($n2$), and (c) $(\text{BA})_2(\text{MA})_2\text{Pb}_3\text{I}_{10}$ ($n3$).

S2. Absorption coefficient and carrier density calculations of 2D perovskite flake

The 2D perovskite single crystal thick flake (not the thin flake that we investigated hot carrier cooling dynamics in) was first fabricated on the quartz, as shown in Figure S2 using the same method described in S1. The optical density (OD) at 400 nm is 1.2, obtained by measuring the remaining percentage of transmitted light. The area size difference between the sample ($2.7 \times 10^4 \text{ um}^2$) and the white light beam ($1.125 \times 10^5 \text{ um}^2$) was considered in the calculation. The influence of scattering and reflectance from sample are corrected by calculating the loss of transmittance at 1000 nm, as 83% of beam can be collected *via* this bulk sample at the same detection angle, comparing to the incident light intensity.

$$A = \log_{10}(I_0/I) \quad (1)$$

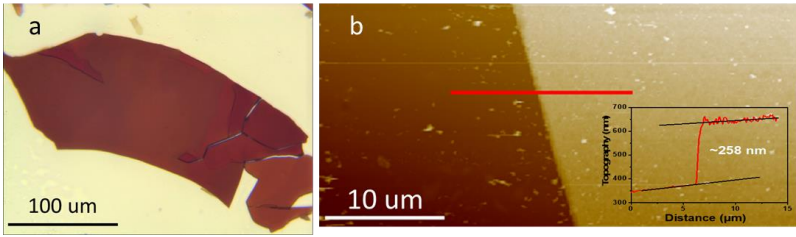


Figure S2. (a) Optical microscope image of a 2D perovskite thick flake on quartz and (b) atomic force microscope (AFM) measurement on it where the red line indicates the measured path on sample.

We can obtain the absorption coefficient $\varepsilon \sim 1.0 \times 10^5 \text{ cm}^{-1}$, where the d is the length of light path inside the crystal and is equal to the thickness of the thick flake as 258 nm, see Figure S2 (b).

$$\varepsilon = 2.303 \times A/d \quad (2)$$

The excitation density n can be calculated as $n = f \times \varepsilon$, where the f is the photon flux in photons per cm^2 . The excitation intensities used in the TA measurements are summarized as Table S1.

Table S1. Excitation density at different photon flux per pulse

Energy density I ($\mu\text{J}/\text{cm}^2/\text{pulse}$)	Photons flux f ($\text{ph}/\text{cm}^2/\text{pulse}$)	Excitation density n ($\text{ph}/\text{cm}^3/\text{pulse}$)
7	1.4×10^{13}	1.4×10^{18}
15	3.0×10^{13}	3.0×10^{18}
30	6.0×10^{13}	6.0×10^{18}
60	1.2×10^{14}	1.2×10^{19}
120	2.4×10^{14}	2.4×10^{19}

S3. Absorption coefficient of 2D perovskite thin film

To confirm the absorption coefficient of 2D perovskite, the thin film has also been measured. As for the absorption in 700 nm region, it is due to the 2D perovskite with higher n -value which have narrower band gap. The other n -value 2D perovskite in film sample is so-far unavoidable. This is one of the reasons why we use in our experiments flakes from a single crystal with well-defined n as is confirmed in the Figure S1c. The absorbance of 2D perovskite film at 400 nm is measured as 1.72, as shown in Figure S3. The absorption coefficient is calculated as $\epsilon = 2.08 \times 10^5 \text{ cm}^{-1}$, where the length of light path inside the thin film is 190 nm measured with profilometer. The calculated absorption coefficient of thin film is on the same order of the single crystal thick flake and prove the validity of calculation in S2.

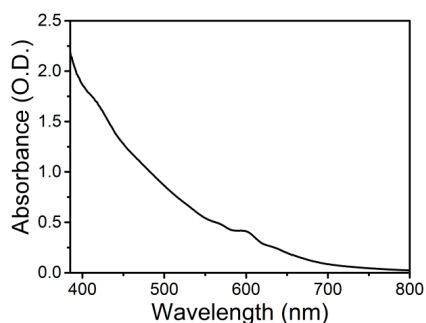


Figure S3. Steady state absorption spectrum of 2D perovskite thin film.

S4. Determination of energy window and offset for TA analysis

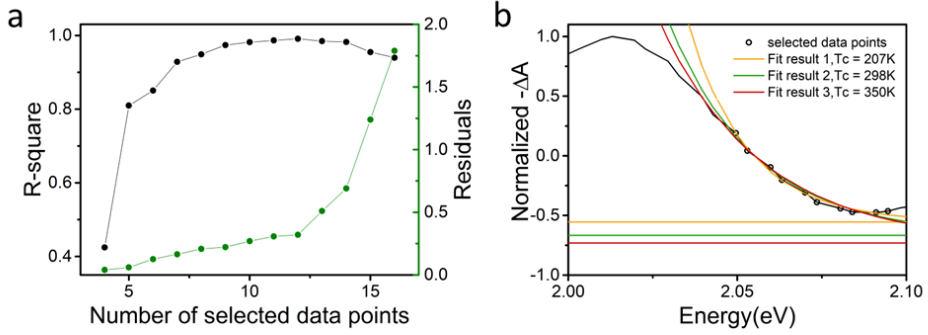


Figure S4a. (a) R-square and the sum of absolute value of residuals for spectra fitting with different energy range with equation shown as below. (b) The hot carrier temperature with different offset with 10 data points selected, where result 1 is obtained without restriction while offset is fixed for obtaining result 2 and 3.

The equation used in Figure S4a is

$$\frac{\Delta T}{T} = A_1 + A_2 \exp\left(-\frac{E-E_f}{k_B T_c}\right) \quad (3)$$

where the offset is a constant as used in main body.

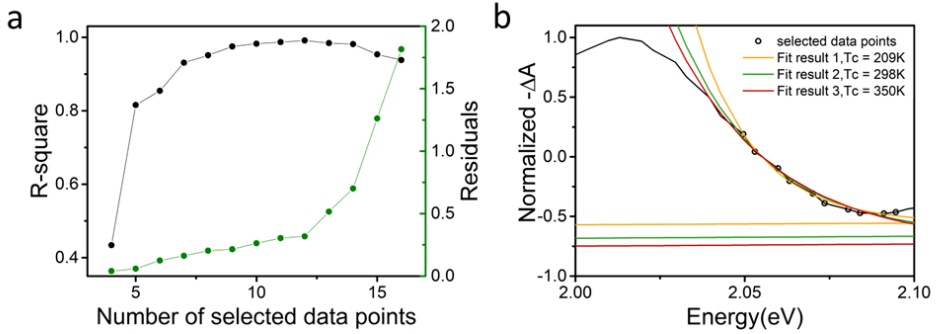


Figure S4b. (a) R-square and the sum of absolute value of residuals for spectra fitting with different energy range with equation shown as below. (b) The hot carrier temperature with different offset with 10 data points selected, where result 1 is obtained without restriction while offset is fixed for obtaining result 2 and 3.

The equation used in Figure S4b is

$$\frac{\Delta T}{T} = A_1 E^{-\frac{1}{2}} + A_2 \exp\left(-\frac{E-E_f}{k_B T_c}\right) \quad (4)$$

where the parabolic approximation is considered in the first term.

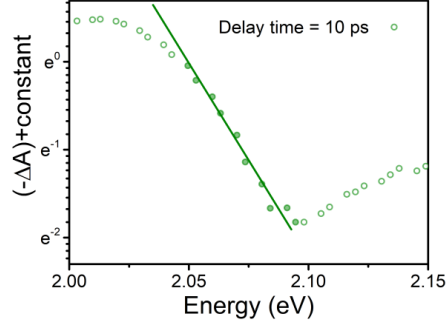


Figure S4c. Transient absorption spectrum of 2D perovskite with excitation intensity of $30 \mu\text{J}/\text{cm}^2$ at 10 ps delay time. The constant is chosen to make the plot has positive value for log-scale Y-axis. The solid dots are the selected data points for fitting the carrier temperature.

The Y-axis is in the log scale and the deviated data points from the line are not suitable for exponential fitting. In TA analysis, the carrier temperature is obtained by fitting the high energy tail with the Boltzmann distribution $\exp(-E/k_B \cdot T)$, therefore the energy window is selected as the solid dot regime.

S5. Quasi-equilibrium timescale

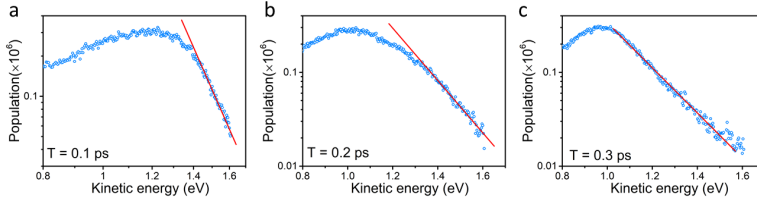


Figure S5a. Time-resolved two-photon photoemission (TR-2PPE) spectra at (a) 0.1 ps, (b) 0.2 ps and (c) 0.3 ps, where the pump is 3.1 eV and the probe is 4.65 eV. The Y-axis is in log-scale for clearly showing the high energy tail can be fitted with one exponential component at 0.3 ps.

Figure S5a shows that the population of photoelectrons start to exhibit Boltzmann distribution (*i.e.*, the high energy tail can be fitted with single exponential function) after 0.3 ps.

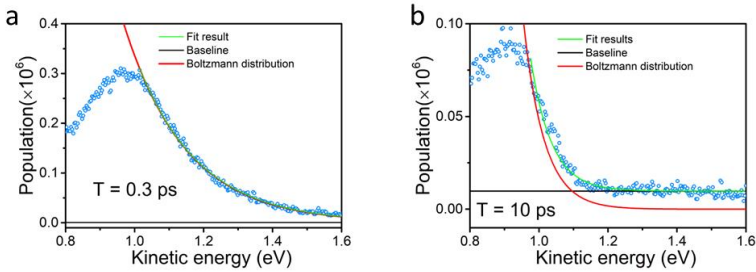


Figure S5b. Fitting the TR-2PPE spectra with Boltzmann distribution at (a) 0.3 ps and (b) 10 ps, where the pump is 3.1 eV and the probe is 4.65 eV.

Figure S5b shows that the high energy tail of TR-2PPE spectra can be fitted with Boltzmann distribution. The analysis shows that if we set the hot electron temperature at 10 ps to be 135 K, then at 0.3 ps the temperature of hot electrons is around 1530 K, which is comparable to the result we obtained from average excess energy analysis.

S6. Excitation dependent TA spectra and time dependent HC temperature

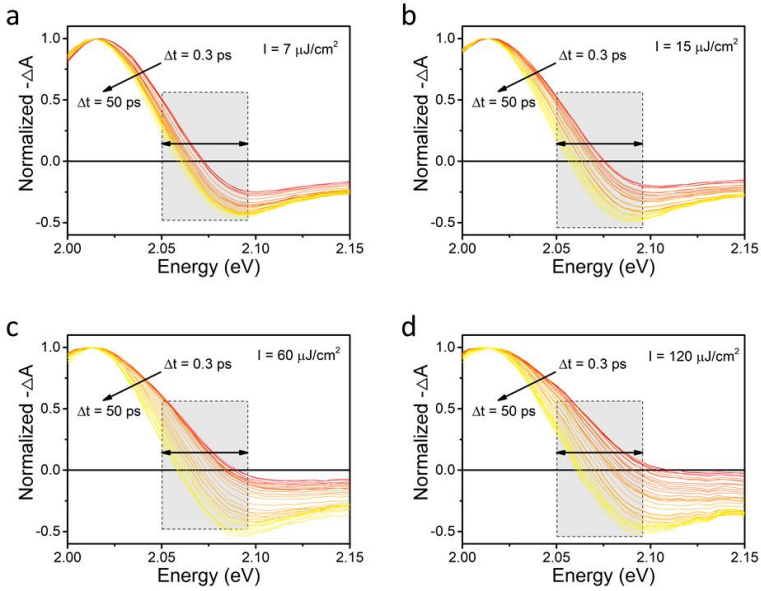


Figure S6a. TA spectra of 2D perovskite flake with 400 nm at different intensity of (a) $7 \mu\text{J}/\text{cm}^2$, (b) $15 \mu\text{J}/\text{cm}^2$, (c) $60 \mu\text{J}/\text{cm}^2$ and (d) $120 \mu\text{J}/\text{cm}^2$, respectively.

Table S6a. Comparison of time delays from initial HC temperature cooled to 600 K in 3D perovskite and our result in 2D perovskite.

Ref	Excess energy (eV)	Carrier density ($\times 10^{19}$)	Initial carrier temperature (K)	Time until 600 K (ps)
Fu et al. ³	≈ 0.8	≈ 1.02	≈ 900	≈ 0.8
Yang et al. ⁴	≈ 1.45	≈ 1.2	≈ 920	≈ 2
Our result	≈ 1.1	≈ 1.2	≈ 722	≈ 1.5

S7. Comparison to other flakes

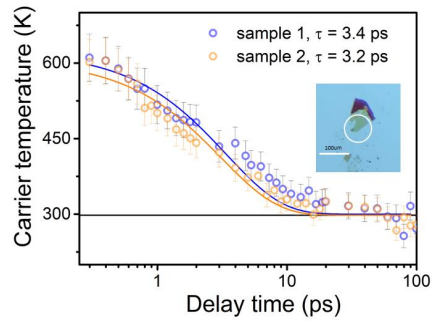


Figure S7a. Comparison in HC cooling dynamics with another flake sample (sample 2) under 3.1 eV (400 nm) excitation at intensity of $30 \mu\text{J}/\text{cm}^2$.

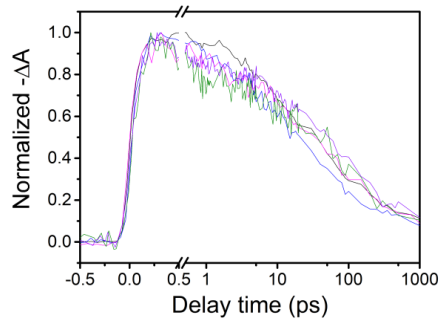


Figure S7b. Normalized GSB dynamics (around 610 nm) of 5 different flakes with similar thickness under 3.1 eV (400 nm) excitation at intensity around $15 \mu\text{J}/\text{cm}^2$.

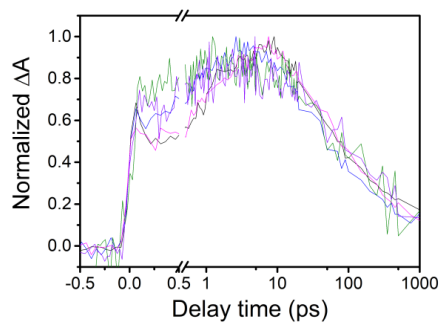


Figure S7c. Normalized PIA dynamics (around 590 nm) of 5 different flakes with similar thickness under 3.1 eV (400 nm) excitation at intensity around $15 \mu\text{J}/\text{cm}^2$.

S8. Time dependent energy distribution curve (EDC) of TR-2PPE measurements

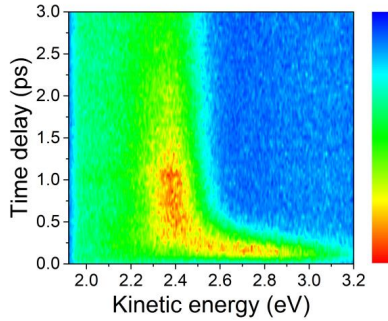


Figure S8a. Time-dependent EDC pumped with 3.1 eV of $160 \mu\text{J}/\text{cm}^2$ and probed with 6.2 eV. Before measurements, the sample was cooled with liquid N_2 in the main chamber at $4.6 \text{ E-}11$ mbar for slowing the heat damage on samples.

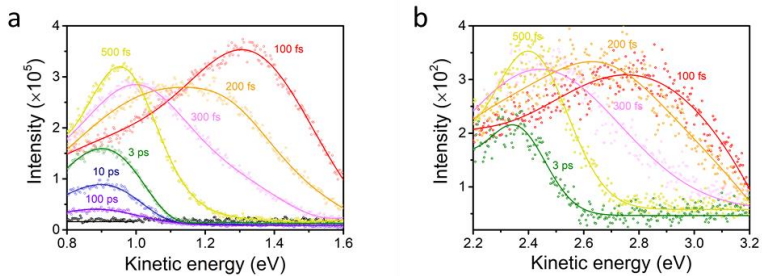


Figure S8b. TR-2PPE spectra at selected time delay, where the pump is 3.1 eV and the probe is (a) 4.65 eV or (b) 6.2 eV, respectively. The black line in (a) represents the spectrum at a negative time delay.

In both measurements, the hot electron population at the high excess energy states peak around 100 fs, and then the peak shift to lower excess energy and peak around 3 ps. The similarity indicates the probe energy has not significantly affected the intrinsic hot electron relaxation.

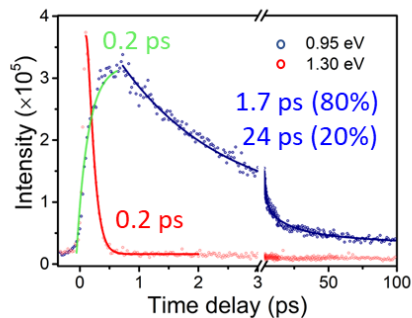


Figure S8c. Exponential fitting on the dynamics at different excess energy states (1.30 eV as excess energy state E_1^* and 0.95 eV as excess energy state E_2^*) in TR-2PPE measurement.

At early delays the probe pulse creates an intense distribution of hot electrons with excess energy E_1^* peaked at 1.30 eV. After an instantaneous rise to the maximum intensity (Figure S8c, red curve), the kinetics of electrons at E_1^* can be fitted by a single-exponential decay with a lifetime of 0.2 ± 0.1 ps. Simultaneously, a broader band with lower excess energy E_2^* peaked around 0.95 eV appears with the rising time (0.2 ± 0.1 ps) matching well with the decay of the E_1^* band. This indicates that the energy of initial photoexcited electrons (E_1^* band) is redistributed to a pool of quasi-thermalized electrons with decreased energy (E_2^* band). The depopulation kinetics of electrons at E_2^* can be fitted by bi-exponential decay function with lifetimes of $1.7 (\pm 0.1)$ ps and $24 (\pm 2)$ ps. Different cooling rates of hot electrons at these two excess energy states indicate different cooling dynamic stages.

S9. Calculation of excess energy from TR-2PPE spectrogram

After the complete cooling (both of electrons and optical phonons) at long delay time, the electrons accumulate to the 1S exciton state. The photoelectrons extracted from this state have kinetic energy of roughly 0.95 eV. Therefore, the excess energy equals to kinetic energy minus 0.95 eV. For example, when the average kinetic energy is 1.25 eV, the average excess energy is 0.3 eV.

S10. Initial system energy and fast component analysis for TA results

We can evaluate from the initial excess energy of hot carriers (i.e. 1.1 eV larger than the bandgap under 3.1 eV excitation) what would be the corresponding carrier temperature at time zero. If we assume that the energy is equally distributed between electron and hole, the initial thermal energy of the excited electrons is $E = 1.5 k_B T = 0.55$ eV giving $T = \sim 4200$ K, which is close to the value adopted from TR-2PPE results as shown in Figure 2c, 3a and 3b.

Using this value and doing the exponential fitting on the HC cooling dynamic for TA analysis, we obtain the upper limit value for the fast component is around 0.1 ps.

In the above discussion, the carriers are assumed can move to other layer (quasi two-dimensional structure). To further confirm the upper limit of fast component in two-dimensional structure (carriers can't move between layers), the carrier temperature can be calculated from initial thermal energy $E = k_B T = 0.55$ eV giving $T = \sim 6400$ K.

$$E_{carrier} = 0.55 \text{ eV} = k_B \times T \quad (5)$$

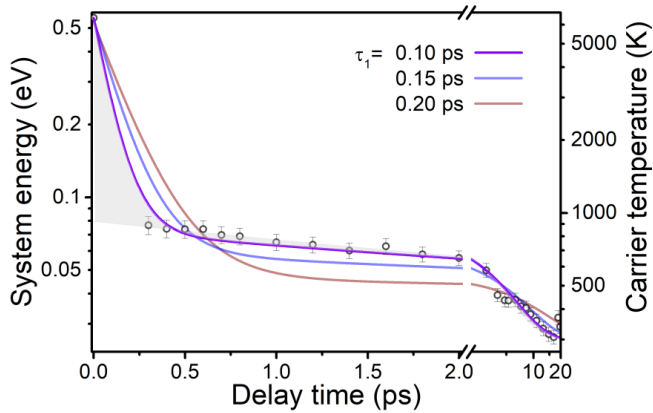


Figure S10. HC temperature kinetic extracted from TA measurements with the initial carrier temperature is assumed to be 6400 K. The kinetic is fitted with bi-exponential function, where the fast component is fixed to be 0.1, 0.15 and 0.2 ps.

Then, we use the 6400 K as the initial data point in Figure S10 and place the bi-exponential fitting on it. It clearly shows that under this circumstance the fast component has shorter timescale than the case in main text. Therefore, the conclusion that 0.1 ps is the upper limit for the fast component in TA analysis is valid.

S11. Low-energy electron diffraction (LEED) measurements

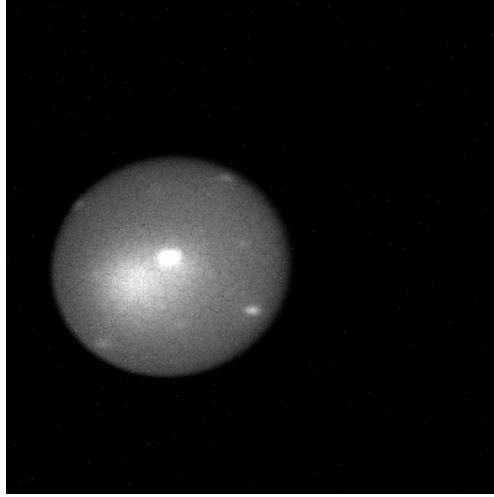


Figure S11. LEED measurements with 4.86 eV of electron kinetic energy.

To have a clearer insight on the mechanism of fast decay within 1 ps in TR-2PPE measurement, the LEED measurement was taken placed to investigate the structure of exposed first layer. The LEED pattern was taken at start voltage of 5 and 10 eV respectively for Figure 4(a) and Figure S11. The kinetic energy was corrected to be 4.86 and 9.86 eV with a small difference of 0.14 eV due to the relation between sample's work function and electron gun's. In Figure 4(a), one can measure the distances from (00) to four (10) spots and the average distance is 212.5 pixels. The average distance from (00) to the Ewald sphere edge (along the same directions from (00) to (01) is 236.5 pixels. As the wavelength of 4.86 eV electron beam is 5.56 Å and then the wave vector from (00) to (01) is $2\pi / (6.188 \text{ Å})$, by considering the ratio between (00) to Ewald sphere edge and (00) to (01).^c It means the lattice of the surface atoms that make this LEED should have the lattice vector is $6.188 \pm 0.2 \text{ Å}$, where the error is considered based on the possible 7 pixels error in the measurements.

^c Calculation of wave vector:
$$k = \frac{2\pi}{5.56\text{Å} \times 212.5 / 236.5} = \frac{2\pi}{6.188\text{Å}}$$

The distance between Pb atoms is 6.305 Å based on structure stimulation, namely between two Octahedron's centers. The value is the closest one to the number from the LEED measurements and is also consistent with the physical reality that there is no clear inorganic layer distortion on the surface layer.

S12. 2D perovskite flake preparation and position-selective TA measurements

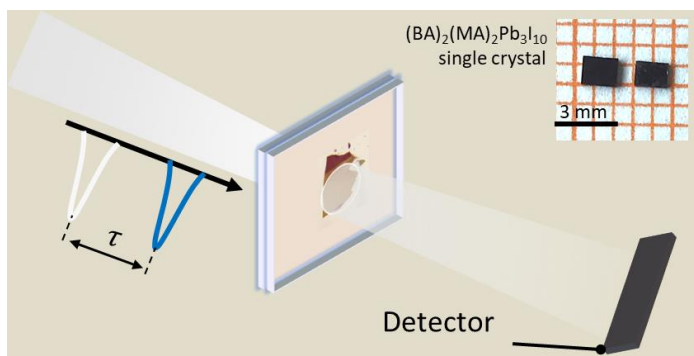


Figure S12a. Schematic of encapsulated 2D perovskite flake during TA measurements.

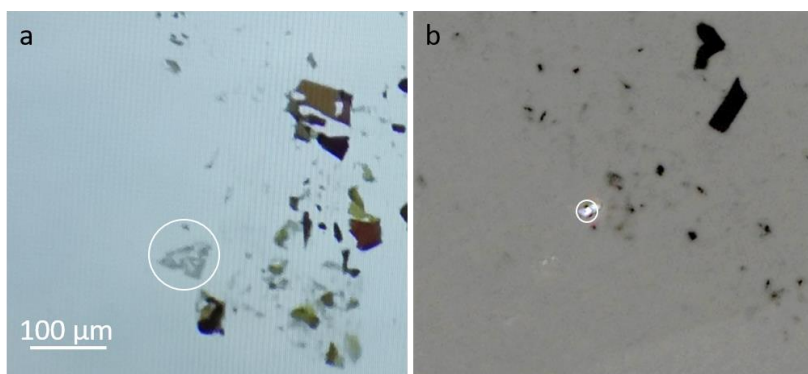


Figure S12b. (a) Optical microscope image of flake. (b) Digital microscope image during TA measurements. The white circles represent the probe beam in TA measurements.

S13. Estimation of lattice temperature and hot phonon bottleneck temperature

Under the 3.1 eV excitation, the initial excess energy of the hot carriers is 1.1 eV, by considering the bandgap of 2D perovskite is around 2 eV. When applying $120 \mu\text{J}/\text{cm}^2$ per pulse intensity which is used in TA measurements, the carrier density is $2.4 \times 10^{19} \text{ cm}^{-3}$. The volume of the chosen unit for 2D perovskite is around 1.1 nm^3 . By multiplying with the carrier density, the result turns out that we have 2.64×10^{-2} carrier per unit cell. Therefore, the total energy contained in one unit cell will be 0.029 eV. Considering the formula of 2D perovskite as $(\text{BA})_2(\text{MA})_2\text{Pb}_3\text{I}_{10}$, there are 17 parts (two BA, two MA, three Pb atom and ten I atom) in one unit cell. The number of degrees of freedom is 17×3 . Assuming that all energy is transferred to the lattice, the total increase of the lattice temperature is 6 K based on eq 3.

The calculation implies that after the final equilibration the lattice is unlikely to achieve high temperature in our study.

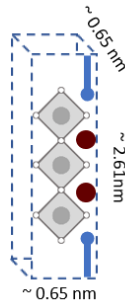


Figure S13. Volume estimation of one $(\text{BA})_2(\text{MA})_2\text{Pb}_3\text{I}_{10}$ crystal unit, where the blue parts represent the spacing cation, red parts represent MA cation, and the grey parts represent the inorganic octahedra.

$$\varepsilon = 2.303 \times A/d \quad (6)$$

In the envisioned cooling process initially the electron energy would be given to a single degree of freedom of the unit cell corresponding to the LO phonon. This allows to estimate the hot phonon bottleneck temperature as ambient temperature plus the temperature rise from photoexcitation ($0.029 \text{ eV} = k_B \times 340 \text{ K}$). The calculation gives hot phonon bottleneck temperature as 640 K in TA measurement and 475 K in TR-2PPE measurement, which agree with the experimental results as 900 K in TA measurement and 480 K in TR-2PPE measurement shown in Figure 3a. More work is needed for drawing further conclusions regarding the cooling details.

S14. Calculation of binding energy based on temperature dependent photoluminescence measurements

The temperature dependent PL spectra were measured on 2D perovskite sample in a cryostat cooled with liquid nitrogen under an excitation wavelength of 375 nm.

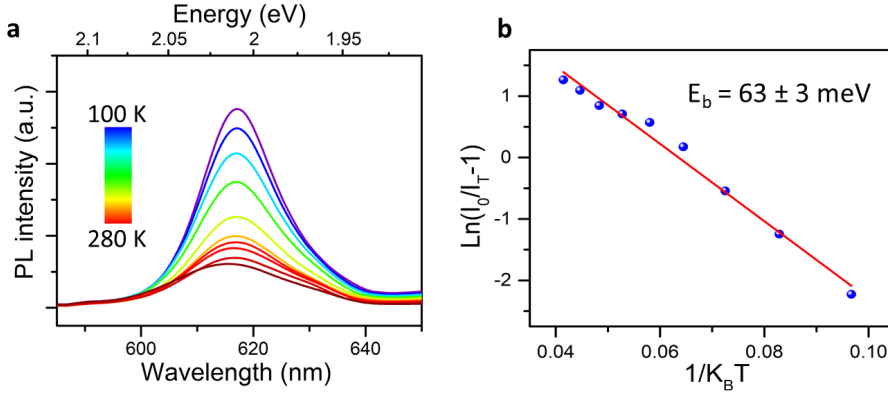


Figure S14. (a) The temperature dependent PL spectra of 2D perovskite at temperature from 100 to 280 K and (b) $\ln(I_0/I(T)-1)$ vs $1/k_B T$ plot of temperature dependent PL spectra.

Since the PL intensity decreases with temperature increasing due to the thermal dissociation of excitons at high temperatures, the temperature dependence trend of PL intensity $I(T)$ can be fitted with

$$I(T) = \frac{I_0}{1 + Ae^{(-E_b/k_B T)}} \quad (7)$$

where the I_0 is the PL intensity at low temperature and E_b is the binding energy. By fitting the $\ln(I_0/I(T)-1)$ vs $1/k_B T$ plot with linear function, the value of binding energy (around 60 meV) can be obtained as the slope.

References

- 1 M. Liang, W. Lin, Q. Zhao, X. Zou, Z. Lan, J. Meng, Q. Shi, I. E. Castelli, S. E. Canton, T. Pullerits and K. Zheng, *J. Phys. Chem. Lett.*, 2021, **12**, 4965-4971.
- 2 J. Faure, J. Mauchain, E. Papalazarou, W. Yan, J. Pinon, M. Marsi and L. Perfetti, *Rev. Sci. Instrum.*, 2012, **83**, 043109.
- 3 J. Fu, Q. Xu, G. Han, B. Wu, C. H. A. Huan, M. L. Leek and T. C. Sum, *Nat. Commun.*, 2017, **8**, 1300.
- 4 J. Yang, X. Wen, H. Xia, R. Sheng, Q. Ma, J. Kim, P. Tapping, T. Harada, T. W. Kee, F. Huang, Y. B. Cheng, M. Green, A. Ho-Baillie, S. Huang, S. Shrestha, R. Patterson and G. Conibeer, *Nat. Commun.*, 2017, **8**, 14120.

Author Contributions

T. P., K. Z. and S. C. conceived and supervised the whole project. W. L. and M. L. implemented the sample preparation, performed the experiments and analyzed the data. Y. N. performed the LEED measurements and analyzed the data. W. L., M. L., Z. C. and M. C. performed the TR-2PPE measurements under the supervision of E. P., L. P. and M. M. J. M., X. Z. and Q. Z. helped with optical measurements. J. M. and H. G. helped with TA data analyses. W. L. and L. P. performed TR-2PPE fitting. W. L. wrote the manuscript. M. L., Y. N., Z. C., M. M., L. P., S. C., K. Z. and T. P. provided revisions to the manuscript. All authors commented the manuscript and gave approval to the final submitted version of the manuscript. +W. L. and M. L. contributed equally to this work.

Paper II



Electronic Structure and Trap States of Two-Dimensional Ruddlesden–Popper Perovskites with the Relaxed Goldschmidt Tolerance Factor

Mingli Liang,[†] Weihua Lin,[†] Zhenyun Lan, Jie Meng, Qian Zhao, Xianshao Zou, Ivano E. Castelli, Tõnu Pullerits, Sophie E. Canton,^{*} and Kaibo Zheng^{*}



Cite This: *ACS Appl. Electron. Mater.* 2020, 2, 1402–1412



Read Online

ACCESS |



Metrics & More



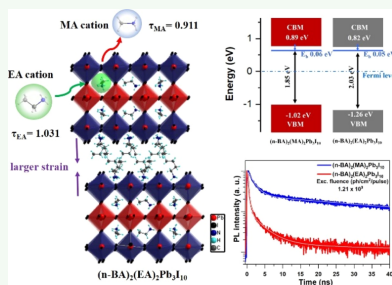
Article Recommendations



Supporting Information

ABSTRACT: Two-dimensional Ruddlesden–Popper perovskites (2D RPPs) have been considered as promising building blocks for optoelectronic applications owing to optical properties comparable to the ones of 3D perovskites, together with superior stability. In addition, the more flexible structure adopted by such perovskites leads to a relaxation of the Goldschmidt tolerance factor (τ) requirement. Herein, we compare the crystalline and electronic structures, as well as the photophysics of two 2D perovskite single crystals $(n\text{-BA})_2(\text{MA})_2\text{Pb}_3\text{I}_{10}$ (BMAPI) and $(n\text{-BA})_2(\text{EA})_2\text{Pb}_3\text{I}_{10}$ (BEAPI) ($n\text{-BA} = n\text{-butylamine}$) containing small A-cations (MA, methylammonium) and large A-cations (EA, ethylammonium), respectively. The latter presents a relaxed τ ($\tau_{\text{EA}} > 1$) compared with the requirement of a stable phase in 3D perovskites ($\tau < 1$). Such relaxed τ is beneficial from the structural flexibility of the long organic cation bilayer and the pronounced lattice distortions in the 2D perovskite structures. We further elucidate how the greater lattice distortions concurrently modulate the electronic structure as well as trap densities in these 2D RPPs. The electronic band gap (E_g) of BEAPI (2.08 ± 0.03 eV) is ~ 0.17 eV larger than the one of BMAPI (1.91 ± 0.03 eV). This is mainly because of a shift in the valence band maximum associated with the expansion of the Pb–I bond length in BEAPI. In addition, the overall trap state densities for BMAPI and BEAPI are calculated to be $\sim 2.18 \times 10^{16}$ and $\sim 3.76 \times 10^{16}$ cm^{-3} , respectively, as extracted from the time-resolved photoluminescence studies. The larger trap density in BEAPI can be attributed to the stronger interfacial lattice distortion that sets in when large EA cations are contained into the inorganic crystal lattice.

KEYWORDS: two-dimensional Ruddlesden–Popper perovskites, Goldschmidt tolerance factor, lattice distortions, electronic structure, trap densities



INTRODUCTION

Over the past decade, metal halide perovskite materials have occurred as a forefront kind of innovative materials suited for the next generation of cost-efficient optoelectronic devices. This is due to their advantageous physical properties, such as strong light absorption, slow charge carrier recombination rate, and high carrier mobility.^{1–8} The certified efficiencies of the perovskite photovoltaic devices have been improved from 3.8 to 25.2% within the past 10 years.^{9,10} In addition, these materials also show good prospects for advanced applications, such as light-emitting diodes, photodetectors for various wavelength regions as well as lasing devices.^{11–22} However, the conventional three-dimensional (3D) lead halide perovskites holding the chemical formula of APbX_3 (here A refers to a cation, X refers a halide) suffer from structural instability triggered by exposure to moisture. This problem can be potentially solved by utilizing 2D Ruddlesden–Popper perovskite (RPP) derivatives, with generic formula of

$(\text{B})_2(\text{A})_{n-1}\text{Pb}_n\text{X}_{3n+1}$ (where A refers to the same small cation, B refers a long chain organic spacing cation, n is the number of lead halide octahedra layers).^{23–26} 2D RPPs are constructed by repeating inorganic perovskite layers and organic spacing cations, so that they exhibit an enhanced structural flexibility compared with 3D perovskites.^{27–29} Their electronic band gap (E_g) is determined by the thickness of the inorganic perovskite layers (i.e., the value of n), thereby extending greatly the diversity of their properties and possible applications.

In general, the formation of 3D APbX_3 perovskites is governed by the Goldschmidt tolerance factor (τ), a

Received: March 5, 2020

Accepted: April 23, 2020

Published: April 23, 2020



geometrical parameter related to the ionic radii of the elemental constituents, defined as follows

$$\tau = \frac{r_A + r_X}{\sqrt{2}(r_{\text{Pb}} + r_X)} \quad (1)$$

where r_A , r_{Pb} , and r_X are the effective radii of the A-cations, the Pb^{2+} , and the halogen X ions, respectively. In principle, τ needs to fall into the range from 0.8 to 1.0 for the stable cubic or distorted 3D perovskite structures to be formed.^{30,31} In this scenario, only a limited number of small A-cations, such as the cesium cation (Cs^+), the methylammonium (MA), and the formamidinium (FA) cations could be employed to realize the Pb-based perovskite lattice.³² However, it has been recently realized that the strong restriction of the τ range can be relaxed in 2D RPPs, which allows larger A-cations, such as ethylammonium (EA) and guanidinium (GA) to fill the inorganic $[\text{PbI}_3]^-$ cages. The 2D RPPs that have been reported so far include $\text{EA}_2\text{Pb}_3\text{X}_{10}$ ($\text{X} = \text{Cl}, \text{Br}, \text{or I}$),^{33,34} $(n\text{-BA})_2(\text{EA})_2\text{Pb}_3\text{I}_{10}$ ($n\text{-BA} = n\text{-butylamine}$),³⁵ $(n\text{-PA})_2(\text{GA})\text{Pb}_2\text{I}_7$ ($n\text{-PA} = n\text{-pentylamine}$),³⁶ and $(n\text{-HA})_2(\text{GA})\text{Pb}_2\text{I}_7$ ($n\text{-HA} = n\text{-hexylammonium}$).³⁷ Compared to the 2D RPPs using the usual A cations (i.e., Cs^+ , MA, or FA), they all exhibit greater structural distortions identified through elongated Pb–X bond lengths and tilted X–Pb–X bond angles in the $[\text{PbX}_6]^{4-}$ octahedron motif.

In this paper, we systematically study the effect of the lattice distortions on the electronic structure and photo-physical properties of 2D RPPs as a function of the relaxed tolerance factor. We target two benchmark single crystals with similar molecular composition, namely, $(n\text{-BA})_2(\text{MA})_2\text{Pb}_3\text{I}_{10}$ (BMAPI) and $(n\text{-BA})_2(\text{EA})_2\text{Pb}_3\text{I}_{10}$ (BEAPI). We confirmed a relaxed τ in BEAPI. The larger electronic band gap (E_g) of BEAPI compared to the one of BMAPI has been rationalized by the elongated Pb–I bond length. In addition, time-resolved photoluminescence (TRPL) studies of the two compounds reveal long-lived trap states in both of them. We observe dynamic trap filling under repetitive laser pulse excitation. By modeling the trap filling process, we can evaluate the trap state density of these two compounds to be $\sim 3.76 \times 10^{16} \text{ cm}^{-3}$ for BEAPI and $\sim 2.18 \times 10^{16} \text{ cm}^{-3}$ for BMAPI. The larger trap density in the EA-based 2D RPP can be attributed to the more severe lattice distortion. These results provide robust references for the intrinsic properties of new type of 2D perovskites with relaxed tolerance factor toward materials engineering and for further implementations into improved devices.

MATERIAL AND METHODS

PbI_2 (99%), methanamine hydroiodide (98%, MAI), ethylamine hydroiodide (98%, EAI), n -butylammonium iodide (98%, n -BAI), hypophosphorous acid solution (50%, in water), and hydroiodic acid (57%, in water) have been utilized without further treatment. All of the chemicals were supplied by Sigma-Aldrich.

Synthesis of BMAPI and BEAPI Single Crystals. The single crystals of the two compounds BMAPI and BEAPI were prepared by the temperature lowering method of PbI_2 , MAI/EAI, and n -BAI in 5 mL hydroiodic acid. The precursor solution contained PbI_2 (1.5 mmol, 0.691 g), EAI (3.0 mmol, 0.519 g), and n -BAI (2.0 mmol, 0.402 g) for BEAPI; PbI_2 (1.5 mmol, 0.691 g), MAI (2.5 mmol, 0.395 g), and n -BAI (2.0 mmol, 0.402 g) for BMAPI. The mixtures were placed into glass bottles (20 mL), and 0.25 mL of hypophosphorous acid was added to prevent the hydroiodic acid from being oxidized. Afterward, the glass bottles were sealed and stirred at room temperature to induce the formation of red colored precipitates. Completely clear solutions were obtained after reaction for few

minutes at 80 °C as precursor. Bulk single crystals were grown from such solution at a cooling rate of 0.5 °C/day starting from 55 °C. The schematic diagram of the synthesis process and the obtained crystals are shown in Figure S1. The purity of these two crystals was characterized by powder X-ray diffraction (XRD) studies (Figure S2).

Single Crystal Crystallography. Crystallographic data for these two single crystals were collected on SuperNova Dual Wavelength CCD diffractometer (Agilent Technologies) equipped with a graphite-monochromatic Mo $K\alpha$ radiation ($\lambda = 0.71073 \text{ \AA}$) at the room temperature ($\sim 298 \text{ K}$) with the detailed procedures and following data treatment identical to our previous work.³⁸ The detailed crystallographic data with structural refinement parameters for these two compounds are provided in Table S1 with the final crystallographic data in CIF and checked CIF results also given (in the Supporting Information). The Pb–I bond lengths and I–Pb–I angles are listed in Tables S2 and S3, respectively.

Spectroscopy Studies. The absorption spectra were measured by a UV–vis–NIR absorption spectrophotometer (PerkinElmer, Lambda 1050). Powder XRD patterns were measured on a Rigaku MiniFlex II diffractometer using Mo $K\alpha$ radiation ($\lambda = 1.5406 \text{ \AA}$). The Raman measurements (InduRAM, HORIBA Jobin Yvon) were performed with excitation at around 795 nm. X-ray photoelectron spectroscopy (XPS) (Thermo Scientific) was employed to study the elemental composition and the electronic structure of the compounds, with an X-ray photon energy of 1486 eV (Al $K\alpha$ X-ray source). The steady-state PL spectra were acquired on a spectrometer (Avantes AvaSpec-2048) under an excitation wavelength of 405 nm. The TRPL measurements were performed by time-correlated single photon counting (PicoHarp) using a pulsed diode laser (Wavelength: 438 nm; Frequency: 2.5 MHz; Pulse duration: 40 ps; A long-pass filter from 450 nm) and a fast avalanche photodiode. It is important to note that during all photophysical measurements the bulk crystals were exfoliated with scotch tapes in order to expose fresh surfaces.

Computational Method. All calculations were implemented in the framework of density functional theory (DFT), using the Atomistic Simulation Environment (ASE), Vienna ab initio simulation package (VASP), and GPAW codes.^{39–42} The structures were optimized using VASP and the generalized gradient approximation PBEsol exchange–correlation functional.⁴³ The electronic wave functions were calculated by using projected augmented wave (PAW).⁴⁴ The cutoff energy for the plane-wave basis was set to be 500 eV. The Brillouin zone samplings were carried out with a Γ -center $5 \times 1 \times 5$ k -point mesh. The atomic forces were relaxed to be less than 0.01 \AA^{-1} . Because of the well-known issue with the underestimation of the band gap, the GLLB-SC exchange–correlation functional has been used to calculate the electronic properties.⁴⁵ Thanks to the explicit calculation of the derivative discontinuity, it has been shown that this functional gives a very good estimation of the band gap at a reasonable computational cost.^{46,47} The Brillouin zone samplings were carried out using a Γ -center point mesh, with density of 8 k -point/ \AA . Spin–orbit coupling (SOC) corrections were included.

RESULTS AND DISCUSSION

Relaxed Tolerance Factor and Intraoctahedral Distortions in the 2D RPPs. In general, the 3D APbX_3 perovskites are stable only when their τ -value falls between 0.8 and 1.0.^{30,31,48} For instance, MA with an effective radius of 217 pm has a τ -value of 0.911; thus, MAPbI_3 is easy to crystallize in the stable perovskite phase. However, EAPbI_3 tends to crystallize in an orthorhombic space group $Pna2_1$ (no. 33) at room temperature and cannot form a traditional continuous 3D perovskite lattice (Figure S3).⁴⁹ This is due to the larger effective radius of EA ($r_{\text{EA}} = 274 \text{ pm}$), which leads to a τ -value of 1.031. Interestingly, BEAPI can exist at room temperature. This indicates that the conventional τ -value threshold can be relaxed if the target compound is expected to adopt a 2D structure rather than a 3D structure. Fu, et al.

attributed this phenomenon to the fact that the strain accumulation caused by larger A-cations is compensated by the separating flexible organic layers.³⁷ The organic spacing cations act as “buffers” to the compression imposed on the rigid inorganic layers. The large strain accumulation is directly reflected by the increased distortion of the $[\text{PbI}_6]^{4-}$ octahedron that form the inorganic layers. To get detailed insight into the lattice distortion, the $[\text{PbI}_6]^{4-}$ octahedral structures in BMAPI and BEAPI were systematically compared.

In order to ensure the accuracy of the structural comparisons and exclude the impact from nonstructural factors, we have collected their single crystal data at room temperature (~ 298 K). BMAPI crystallizes in the orthorhombic space groups $Aba2$ (no. 41), while BEAPI crystallizes in the orthorhombic space groups $Cmc2_1$ (no. 36). Despite the different space groups, they both belong to the homologous series of 2D RPPs phases $(\text{B})_2(\text{A})_{n-1}\text{Pb}_n\text{X}_{3n+1}$ with $n = 3$ and identical periodic layered structure (Figure 1a,b). In their lattices, the organic cations are

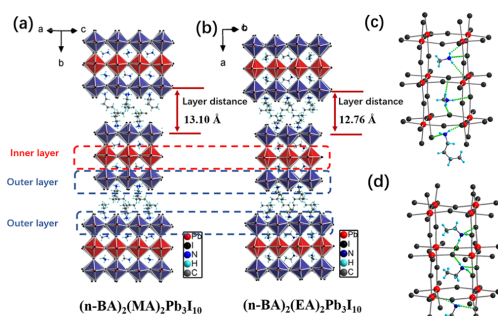


Figure 1. Detailed structure of (a) BMAPI and (b) BEAPI, where the inner layers (red) consist of “slightly distorted” while the outer layers (blue) consist of “largely distorted” octahedra; strong hydrogen bonding in (c) BMAPI and (d) BEAPI is indicated in green.

intercalated into the 2D octahedron layered quantum wells through the inorganic units via N–H...I hydrogen bonds.⁵⁰ The green dashed lines in Figure 1c,d represent the strong N–H...I hydrogen bonds. The corresponding bond lengths and angles are shown in Table S4. The three inorganic monolayers in the 2D quantum wells can be classified into an inner layer (red) and two outer layers (blue).

It is clear that all of the $[\text{PbI}_6]^{4-}$ octahedra in BMAPI and BEAPI are distorted. The characteristic Pb–I bond lengths present in the two compounds are indicated in Figure 2a. For BMAPI, the longest and shortest Pb–I bond lengths are 3.3040(12) and 3.0521(15) Å, respectively, with a difference of ~ 0.25 Å. For BEAPI, the longest and shortest Pb–I bonds are [3.457(2) Å, red dotted lines] and [3.010(2) Å] so that the difference now reaches ~ 0.45 Å (Table S1). Furthermore, their I–Pb–I bond angles are also tilted. The minimum I–Pb–I trans-angles of BMAPI and BEAPI are only 175.72(5) $^\circ$ and 167.94(4) $^\circ$, respectively, which are both far from 180 $^\circ$ (Table S2). A quantitative comparison of the lattice distortion in the two compounds can be performed by evaluating the intra-octahedral distortions parameters,^{51,52} consisting of the average metal–halide (Pb–I) the bond distance parameter ($\langle D \rangle$), distance distortion parameter (ζ), tilting distortion parameter

(Δ), torsional distortion parameter (Θ), and angle distortion parameter (Σ) which are defined as follows

$$\langle D \rangle = \left(\sum_{i=1}^6 d_i \right) / 6 \quad (2)$$

$$\zeta = \sum_{i=1}^6 |d_i - \langle D \rangle| \quad (3)$$

$$\Delta = \sum_{i=1}^6 \left(\frac{d_i - \langle D \rangle}{\langle D \rangle} \right)^2 \quad (4)$$

$$\Theta = \sum_{i=1}^{24} |60 - \theta_i| \quad (5)$$

$$\Sigma = \sum_{i=1}^{12} |90 - \phi_i| \quad (6)$$

The d_i are the individual Pb–I bond distances in the $[\text{PbI}_6]^{4-}$ octahedron. θ_i are the angles of the 24 unique projections of the I–Pb–I angles to the triangular faces of the $[\text{PbI}_6]^{4-}$ octahedron along its pseudo-3-fold axis. ϕ_i are the 12 cis-angles of I–Pb–I around the Pb atom. Among these five parameters, $\langle D \rangle$, ζ , and Δ are related to the distortions of Pb–I bond length. Θ represents the distortion of the $[\text{PbI}_6]^{4-}$ geometry from perfectly octahedral symmetry (O_h) to trigonal prismatic symmetry (D_{3h}), a process known as the Bailor trigonal twist.⁵² Σ is the sum of the $|90 - \phi_i|$, which a general measure of the deviation from an ideal octahedron. In principle, the larger values of these parameters indicate the greater degree of $[\text{PbI}_6]^{4-}$ intra-octahedral distortions, shown in Figure 2b–f with specific values listed in Table S5. Comparing the values of the five parameters provides a global overview into the $[\text{PbI}_6]^{4-}$ octahedra distortions. As expected, the values of the five parameters are identical for the $[\text{PbI}_6]^{4-}$ octahedra from the two outer layers for both complexes because they are in the same chemical coordination environment.

First, as shown in Figure 2b, the $\langle D \rangle$ values of BEAPI are much larger than those of BMAPI. This is due to the large EA cations filling the $[\text{PbI}_3]^-$ cages, which increases the strain accumulation of the inorganic layers, thereby elongating the Pb–I bonds. Moreover, the $\langle D \rangle$ value of the outer layers is higher than that of the inner layers in BMAPI. The reverse holds in BEAPI. This is mainly due to a very short Pb2–I6 bond of only 3.010(2) Å. The two parameters ζ and Δ describe the uniformity of the six Pb–I bond lengths in a $[\text{PbI}_6]^{4-}$ octahedron. As seen in Figure 2c,d, the ζ and Δ values of the outer layers are much larger than those of the inner layer. It is attributed to the strain relaxation occurring at the $[\text{PbI}_6]^{4-}$ octahedra in the outer layer, due to lower geometric constraint, aided by the structural flexibility of the long organic spacing cations outside the cages that accommodate the $[\text{PbI}_6]^{4-}$ octahedral distortions. The same situation is also reflected by the two angle-dependent Θ and Σ parameters. Figure 2e,f shows a greater trigonal angular distortion of the $[\text{PbI}_6]^{4-}$ octahedra in BEAPI. Overall, the five parameters are all larger for BEAPI than for compared to BMAPI. This is in line with the distance between the two inorganic layers being ~ 13.10 Å for BMAPI and ~ 12.76 Å for BEAPI as a sign of compression in the latter (Figure 1a,b).

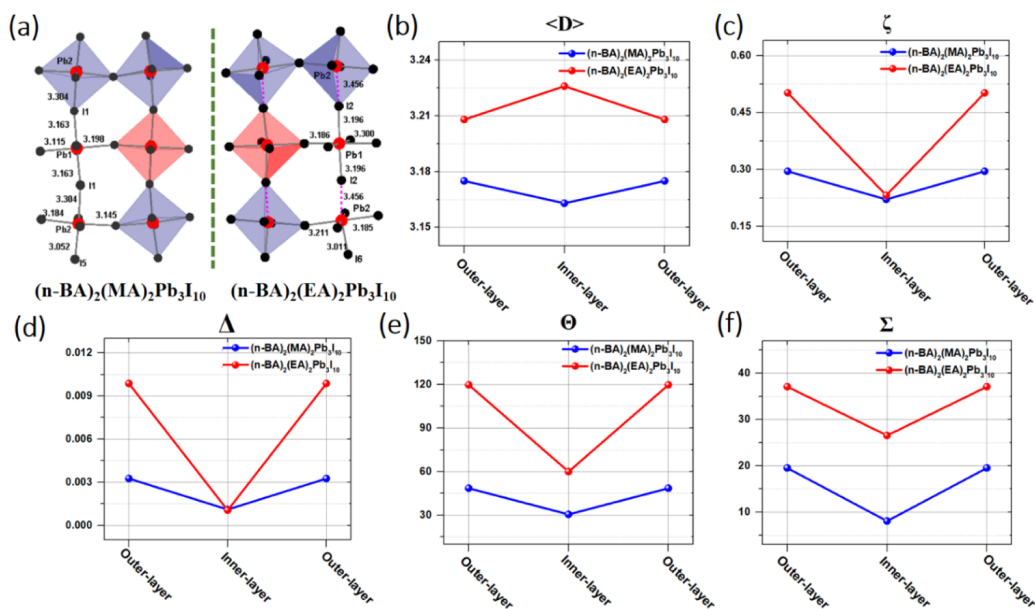


Figure 2. (a) Inorganic lattice and the $[\text{PbI}_6]^{4-}$ octahedral distortions in BMAPI and BEAPI; the magnitude of $[\text{PbI}_6]^{4-}$ octahedral distortion parameters: (b) bond distance parameter ($\langle D \rangle$), (c) distance distortion parameter (ζ), (d) tilting distortion parameter (Δ), (e) torsional distortion parameter (Θ), and (f) angle distortion parameter (Σ).

To summarize, we find both an increase in $[\text{PbI}_6]^{4-}$ octahedral distortions and an increase in compression for organic layers in BEAPI, which all account for the stable accommodation of larger EA cations in the $[\text{PbI}_3]^-$ cages. However, we found that 2D RPP (*n*-BA as the spacing cation) with even larger A-cations like GA (with a τ -value of 1.039) is not stable any more.

Vibrational Modes of the MA and EA Cations in the $[\text{PbI}_3]^-$ Cages. In order to compare the vibrational modes of the MA and EA cations in the $[\text{PbI}_3]^-$ cages of the two compounds, we measured the Raman spectra of the crystals with an excitation around 795 nm, which was chosen to avoid strong background photoluminescence. The measurement range was determined such that the internal vibrations of the organic cations dominated over the mixed modes involving the organic cations and inorganic units.⁵³ To clearly identify the vibrational modes of the EA cation, we also compared our experimental results with the theoretical calculations performed for the isolated cation (Figure S4). As shown in Figures 3 and S5, the peaks observed at 1468.0 cm^{-1} for BMAPI and 1467.2 cm^{-1} for BEAPI can be assigned to the symmetric NH_3 deformation. The peaks at 1571.6 cm^{-1} for BMAPI and 1568.3 cm^{-1} for BEAPI are attributed to the asymmetric NH_3 deformation.^{53,54} Only a small red shift of these peaks can be noted between the two compounds, a finding which complies with their similar average bond lengths of N–H...I hydrogen bonds (Table S4). The average N–H...I hydrogen bond distance in BEAPI [2.934(10) Å] is only slightly smaller than that in BMAPI [3.092(10) Å]. This implies that the NH_3 unit in BEAPI interacts slightly more with the $[\text{PbI}_3]^-$ cages. The peak of BMAPI at 960 cm^{-1} can be assigned to the MA rocking mode. In contrast, the EA rocking peak appears at

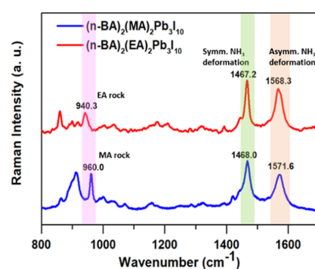


Figure 3. Raman spectrum of BMAPI and BEAPI.

940.3 cm^{-1} , with a large red shift of $\sim 20 \text{ cm}^{-1}$. This suggests that the rocking degree of freedom of the EA cations in $[\text{PbI}_3]^-$ cages is limited due to their larger sizes.⁵⁵

Impact of the Relaxed Tolerance Factor on the Electronic Band-Edge Properties. In general, the changes in the lattice structure induce an alteration of the physical properties in semiconductors, especially the electronic band-edge properties. We first measured the optical band gaps (E_{opt}) of both BMAPI and BEAPI. The UV–vis absorption spectra of BEAPI (Figure 4a) show the absorption band edge at $\sim 611 \text{ nm}$, which is blue-shifted by $\sim 59 \text{ nm}$ compared with BMAPI (located at $\sim 670 \text{ nm}$). This difference refers to a widening of E_{opt} from 1.85 ± 0.01 to $2.03 \pm 0.01 \text{ eV}$ according to the Tauc plots, respectively (inset of the Figure 4a). It is well known that the electronic band gap E_g of the semiconductors is actually the sum of E_{opt} and the exciton binding energy (E_b).⁵⁶ Therefore, we measured the E_b of the 2D RPP using temperature-dependent PL (for details of E_b calculation see S5). The

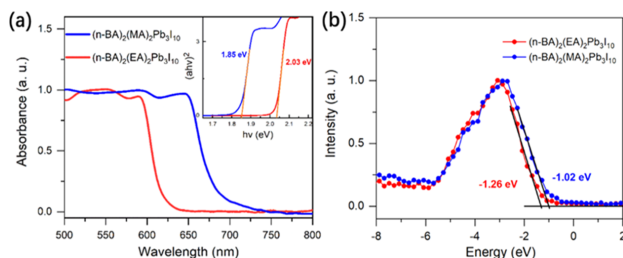


Figure 4. (a) Steady-state absorption spectrum. Insert: Tauc plot representing the band gap of BMAPI and BEAPI, respectively. (b) XPS valence band spectra for the BMAPI and BEAPI.

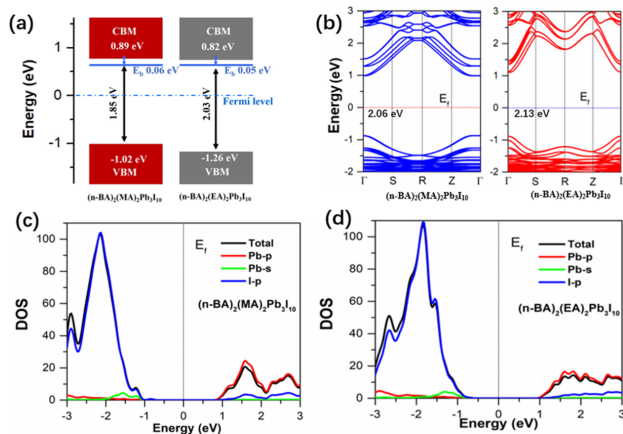


Figure 5. (a) Band alignment between BMAPI and BEAPI, the zero energy level corresponds to the Fermi level; (b) band structure of two compounds with SOC calculated from the experimental crystallographic structure; the PDOS diagrams of (c) BMAPI and (d) BEAPI. The Fermi energy is set to zero; MA/EA and *n*-BA mainly interact with the inorganic framework via hydrogen bonding and are not shown in the figure for clarity.

calculated E_b of BMAPI and BEAPI are 65.8 ± 10 and 46.4 ± 10 meV, respectively. Therefore, the final E_g -values are 1.91 ± 0.03 and 2.08 ± 0.03 eV for BMAPI and BEAPI, respectively. We note that the calculated E_b values are smaller than the results obtained with other methods, which is probably due to the minor contribution of the shallow traps on the dissociation of the excitons.^{58,59} However, the present relative comparison between the two samples should be still valid.

The energy positions of the valence band maximum (VBM) with respect to the Fermi level (zero energy) are then established from the XPS spectra displayed in Figure 4b. A clear up-shift of the VBM in BEAPI (-1.26 ± 0.03 eV) by ~ 0.24 eV is observed in comparison with BMAPI (-1.02 ± 0.03 eV). It should be noted that it is very close to the difference of E_{opt} . As the definition of electronic band gap E_g is the difference between the energies of the conduction band minimum (CBM) and VBM [that is, $E_g = E(\text{CBM}) - E(\text{VBM})$], we can now locate the CBM levels of two compounds as shown in Figure 5a.

In order to elucidate the nature of the band gap and the correlation between the electronic and geometric structures in these two materials, the DFT band structures, including SOC corrections, were calculated based on the crystal structures determined experimentally, as shown in Figure 5b. The lowest

energy of the CBs and highest energy of the VBs of BMAPI and BEAPI are all located at the Γ points, meaning the direct band gap character of these semiconductors. These bands are mostly composed of I p, Pb p, and Pb 6s states, respectively, as previously shown for other hybrid perovskite materials.^{27,60} We found consistency between the experimental and computational values of the gap: the calculated gaps are 2.06 and 2.13 eV for BMAPI and BEAPI, respectively, while the experimental values are 1.91 and 2.08 eV. The projections of the density of states (PDOS) on the different constituent atoms indicate that the VBMs for both compounds are mainly due to the I 5p and Pb 6s orbitals, whereas the CBMs mainly originate from the I 5p and Pb 6p orbitals (Figure 5c,d).

From the XPS spectra shown in Figure 6a, we can clearly see that the binding energy of the Pb 4f core levels is lower in BMAPI than in BEAPI (with a shift ~ 0.2 eV). This means that the electronic density at the Pb center is higher in BMAPI than in BEAPI, owing to the more pronounced delocalization of the outer charges caused by a shorter Pb–I distance. On the other hand, the XPS spectra of the I 3d core level are identical in two compounds (Figure 6b) indicating similar chemical environments around the I atoms. A possible reason could be the contribution of N–H \cdots I hydrogen bonding between N and I

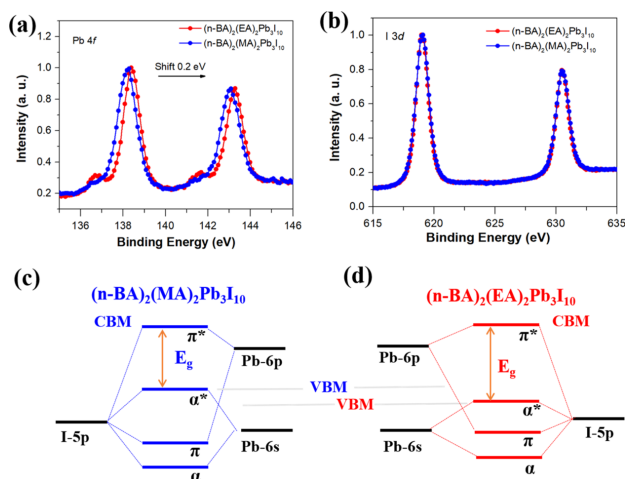


Figure 6. XPS core level emission of (a) Pb 4f doublet and (b) I 3d doublet; and the lone-pair model with stereochemical activity of the s^2 electrons in the (c) BMAPI and (d) BEAPI.

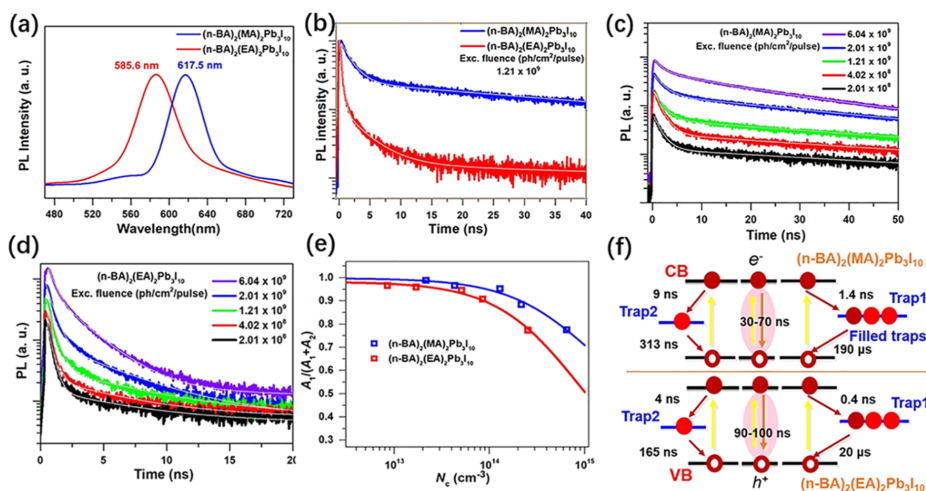


Figure 7. (a) Steady-state PL and (b) transient PL of BMAPI and BEAPI crystals. PL decay kinetics with different excitation fluence for (c) BMAPI and (d) BEAPI. (e) Amplitude ratios $A_1/(A_1 + A_2)$ extracted from the multiexponential fitting of the decays vs the initial charge carrier densities N_c for two compounds. (f) Illustration of the trap-mediated charge recombination in the two compounds.

that could balance the charge reorganization within the Pb–I covalent bond.

Based on the DOS calculations for BMAPI and BEAPI and other published results, the VBM of lead iodide perovskites mainly consists of the anti-bonding combination between the Pb 6s and I 5p orbitals, while their CBM consists of the slightly anti-bonding combination of the Pb 6p and I 5p orbitals.⁶¹ In other words, the electronic band edges of these two compounds are determined by the bonding in the $[\text{PbI}_6]^{4-}$ octahedral unit. The orbitals of the organic molecules are either too deep in the VB or too high in the CB, so that they do not participate to the electronic band edges.^{27,61} The

electronic band edge models of EA and MA materials are illustrated in Figure 6a,b. We notice that the 6s and 6p orbitals from Pb^{2+} are mixed despite the fact that, in a perfect metal octahedron MX_6 , this should not happen based on stringent selection rules associated with symmetry upon inversion. However, as a lone-pair metal cation, Pb^{2+} possesses a pair of $6s^2$ electrons in its valence shell. This ion is usually observed to be off-centered within the X6 cage,^{62,63} which is quantified through the distortion parameters of the $[\text{PbI}_6]^{4-}$ octahedron discussed above. A well-accepted explanation for the off-centering of Pb^{2+} distortion is that the lone-pair is stereochemically active. The resulting covalent hybridization of the

6s and 6p orbitals of Pb^{2+} causes a nonspherical electronic distribution.⁶¹

Structurally, the Pb–I bond distance ($\langle D \rangle$ parameter) of BMAPI is shorter than that for BEAPI. This reflects a stronger interaction, hence a larger degree of charge delocalization over the I 5p and Pb 6s orbitals. As such, the energy difference between the bonding orbitals (σ) and anti-bonding orbitals (σ^*) increases. Therefore, the VBM position of BMAPI is higher than that of BEAPI. In contrast, unlike the hybridization mode between I 5p and Pb 6s orbitals, I 5p and Pb 6p orbitals are hybridized into bonding orbitals (π) and anti-bonding orbitals (π^*), with the CBM being less affected by Pb–I bond distance. Hence, in Figure 6a,b the CBM positions of BMAPI and BEAPI are almost identical.

Impact of the Relaxed Tolerance Factor on the Trap-Mediated Charge Recombination. The different lattice distortions associated with the relaxed tolerance factor are also expected to affect the photo-physical properties of the two compounds, as shown in Figure 7. First, the steady-state PL spectrum of BEAPI (585.6 nm) is clearly blue-shifted compared to the one of BMAPI (617.5 nm) (Figure 7a). This is mainly ascribed to the differences in their E_g . Moreover, we find that the PL lifetime of BEAPI is much shorter than the one of BMAPI (Figure 7b). Under the same excitation fluence (1.21×10^9 ph/cm²/pulse), the average PL lifetime of BMAPI ($t_{\text{average}} = 5.86$ ns) is approximately 6.5-fold longer than that of BEAPI ($t_{\text{average}} = 0.90$ ns) (Tables S6 and S7). Here, it should be noted that in order to avoid the effect of edge emission of the crystal on the PL kinetics during the TRPL measurements, we focused the laser spot only on the flat bulk area of the crystal flakes (Figure S7). We can fit adequately the PL decays using triexponential decays including a fast component (t_1), medium component (t_2), and slow component (t_3). It should be first noted that owing to the low exciton binding energy of our 2D perovskite crystals and the low excitation concentration during the TRPL measurement, the majority of the photo-generated species should be free carriers (see the calculation in S7 and S8). In this scenario, we can associate the slow component to the intrinsic bimolecular recombination. The other two faster components, although very often assigned to nonradiative trap-mediated recombination, can have various origins, such as Auger process, photo-chemically induced reaction, internal energy/charge transfer, or charge carrier recombination induced by different phases or impurities in the samples.^{64–67} First, because the samples are uniform fresh crystal flakes and have excellent powder XRD patterns, the existence of additional phase or impurities can be excluded. Second, the low excitation fluence applied in the experiment guarantee the absence of any Auger recombination process. Third, photo-induced chemical reactions are also unlikely in these stable 2D perovskites.

The PL kinetics exhibit very notable on the excitation intensity (Figure 7c,d). We can clearly observe a prolongation of the PL lifetime with the increment of excitation intensity for both compounds. This behavior is a well-known fingerprint of trap filling/accumulation seen in most perovskite materials. This process occurs when the lifetime of traps is longer than the laser pulse interval time so that some of traps constantly remain filled.⁶⁸ We can globally fit the different PL decays by three exponential components with the same set of lifetimes (t_1 , t_2 and t_3) but with different amplitudes (A_1 , A_2 , and A_3) that are allowed to vary with the laser intensities. As seen in Tables S6 and S7, the ratios $[A_1/(A_1 + A_2)]$ are becoming

smaller with increasing intensity. Such a phenomenon has already been observed in our previous study on 3D perovskite bulk crystals, where the dynamics were extensively rationalized by considering the parallel charge carrier trapping processes by two different types of trap states in the crystal.⁶⁴ One type of traps possessed a long lifetime, which could cause trap filling depending on the excitation condition, while the other type of traps was immune to trap filling due to its faster depopulation time. Here, we use the same model to simulate the PL dynamics in the 2D perovskite crystals. Briefly, the ratio A_1/A_2 can reflect the fraction between photogenerated charge carriers that undergo trapping by two different traps. It should be equal to the initial ratio between unfilled density of traps 1 (n_{uncT1}) and traps 2 (n_{uncT2}): $n_{\text{uncT1}}/n_{\text{uncT2}}$, where such unoccupied traps refer to the equilibrium condition between photo-induced trap filling and trap recovery within two excitation pulse. We can then obtain the density of the filled traps n_T under a certain excitation density (N_c) and a total trap densities (N_T) using the following equations that have been outlined in the previous paper (for the details of the calculation model see S9), where the equilibrium between free carriers and excitons after photoexcitation is calculated by the Saha equation.^{64,68}

$$n_T = -\frac{1}{2}\alpha + \frac{1}{2}\sqrt{\alpha^2 + 4\beta N_T} \quad (7)$$

$$\alpha = \frac{[A + R(A - N_T)]}{\left(1 + \frac{1}{K} + R\right)} \quad (8)$$

$$\beta = \frac{RA}{\left(1 + \frac{1}{K} + R\right)} \quad (9)$$

$$K = \frac{1}{\gamma_0 t_0} \ln \left[1 + \frac{AN_c}{N_T(A + N_T)} \right] \quad (10)$$

$$A = \frac{\nu_s}{\nu_e \nu_h} e^{-E_b/k_B T} \quad (11)$$

Here, R indicates the ratio between the trap population and depopulation rates; γ_0 is the total electronic decay rate except for any trapping processes; t_0 is laser pulse interval time; λ_i refers to the thermal wavelength of each quasiparticles i (free electrons e , holes h and excitons x), and $\nu_i = \lambda_i^3$. We can further obtain the concentration of n_{uncT1} and n_{uncT2} as

$$n_{\text{uncT1}} = N_{T1} - n_{T1} = N_{T1} + \frac{1}{2}\alpha - \frac{1}{2}\sqrt{\alpha^2 + 4\beta N_{T1}} \quad (12)$$

$$n_{\text{uncT2}} = N_{T2} - n_{T1} = N_{T2} + \frac{1}{2}\alpha - \frac{1}{2}\sqrt{\alpha^2 + 4\beta N_{T2}} \quad (13)$$

$$A_1/(A_1 + A_2) = n_{\text{uncT1}}/(n_{\text{uncT1}} + n_{\text{uncT2}}) \quad (14)$$

where N_{T1} , N_{T2} are the initial densities of two type of traps, respectively. The $A_1/(A_1 + A_2)$ ratios versus N_c can then be depicted and fitted using the model within the eqs 12–14. The four fitting parameters are (N_{T1} , N_{T2}), R_1 , and R_2 . From the analysis, we calculated that the depopulation time of traps 2 in BMAPI and BEAPI are about ~ 313 and ~ 165 ns, respectively, which are close to t_0 (250 ns). Therefore, there should be no significant trap filling occurring in their traps 2 because the

depopulation rate is quite fast. The model is then modified for the case where the trap filling occurs only in trap 1 as follows

$$A_1/(A_1 + A_2) = n_{\text{nucT1}}/(n_{\text{nucT1}} + N_{\text{T2}}) \quad (15)$$

Here, the $A_1/(A_1 + A_2)$ ratio equals the ratio between n_{nucT1} and N_{T2} . This model provides an excellent fit for both compounds as shown in Figure 7e. Defining R as the ratio between trap population and depopulation rates, we can calculate that the depopulation time of traps 1 of BMAPI (trapping time ≈ 1.4 ns) and of BEAPI (trapping time ≈ 0.4 ns) are ~ 190 and ~ 20 μs , respectively. The illustrations of the trap-mediated charge recombination are given in Figure 7f. Table 1 summarizes the fitted trap densities of two types of

Table 1. Trap Densities Calculated From the Fitting Shown in Figure 7e

	N_{T1} (10^{15} cm^{-3})	N_{T2} (10^{15} cm^{-3})
$(n\text{-BA})_2(\text{MA})_2\text{Pb}_3\text{I}_{10}$	21.8	0.11
$(n\text{-BA})_2(\text{EA})_2\text{Pb}_3\text{I}_{10}$	37.6	0.59

traps. Compared to N_{T1} , N_{T2} are small and can be neglected. Therefore, the trap-mediated recombination should be dominated by the traps 1 at low excitation density. The N_{T1} values for BMAPI and BEAPI are $\sim 2.18 \times 10^{16}$ and $\sim 3.76 \times 10^{16} \text{ cm}^{-3}$, respectively. They are of the same order of magnitude as the ones reported for 3D perovskites ($2.5 \times 10^{16} \text{ cm}^{-3}$, at 300 K) using identical analysis method.⁶⁸ In general, because of the presence of long organic bilayer and larger lattice distortions in 2D RPPs, the trap densities would be expected to be larger than that of 3D perovskites. However, their similarities could be due to the absence of grain boundaries in the fresh single crystal compared to the film samples. In addition, the N_{T1} of BEAPI is 1.7 times higher than that of BMAPI. Considering the similar single-crystal growth conditions, we believe that such a difference in trap density reflects the larger degree of interfacial lattice distortion in BEAPI where the larger EA cations fill the crystal lattice. As noted above, this is also the main reason for the overall shorter PL lifetime in the EA-based 2D RPPs. In addition, both fast trapping and detrapping times in BEAPI indicate much shallower trap states compared to the MA based 2D RPPs. Globally, the combination of shallower traps together with larger trap density should be the main reason for the overall shorter PL lifetime in the EA-based 2D RPPs. Finally, our previous studies on 3D perovskite crystals suggest the origins of the traps 1 and traps 2 to be the volume traps and surface traps, respectively, due to their different trapping times (i.e., it takes generally longer time for photogenerated carriers to migrate to the surface of the crystals).⁶⁴ However, the defect structures in 2D perovskites should be more complicated owing to the existence of large organic cations, as aspect which requires further exploration.

CONCLUSIONS

In this work, we have successfully synthesized the single crystals of two lead iodide 2D RPPs, BMAPI, and BEAPI. The detailed structural comparison shows that BEAPI with large-size A cations and relaxed τ exhibit increased inorganic layer distortions and compression by long organic bilayers. The larger lattice distortions, especially the increase in the Pb–I bond lengths, further widen the band gap by mainly lowering the position of the VBM, which can be rationalized by the

orbital hybridization theory. In addition, from the TRPL studies, we revealed ultra-long-lived trap states in both two compounds with trap densities of $\sim 2.18 \times 10^{16}$ and $\sim 3.76 \times 10^{16} \text{ cm}^{-3}$ for BMAPI and BEAPI, respectively. We believe that the higher trap densities of BEAPI is due to the more severe lattice distortion leading to a much shorter PL lifetime compared to BMAPI. However, the shorter detrapping time of BEAPI may diminish the trapping process in the sample. The present findings can provide robust reference for future materials engineering and device application based on such 2D RPPs.

ASSOCIATED CONTENT

Supporting Information

The Supporting Information is available free of charge at <https://pubs.acs.org/doi/10.1021/acsaelm.0c00179>.

Crystal data and structure determinations of the samples, values of Pb–I bond distances and I–Pb–I bond angles, schematic diagram of the growth of bulk single crystals, powder XRD data of the samples, the values of five distortion parameters, multiexponential fitting parameters for TRPL kinetics for the samples, details about calculation of E_b using the temperature-dependent photoluminescence method, details about calculations of the absorption coefficients and excitation density of the samples, and detailed model of trap filling and fitting process (PDF)

Crystallographic data of C10H36I10N4Pb3 and C12H40N4Pb3I10 (CIF)

checkCIF/PLATON report and datablock: C10H36I10N4Pb3 and C12H40N4Pb3I10 (PDF)

AUTHOR INFORMATION

Corresponding Authors

Sophie E. Canton – ELI-ALPS, ELI-HU Non-Profit, Ltd., 6720 Szeged, Hungary; scanton@eli-alps.hu; orcid.org/0000-0003-4337-8129; Email: Sophie.Canton@eli-alps.hu

Kaibo Zheng – Department of Chemistry, Technical University of Denmark, DK-2800 Kongens Lyngby, Denmark; Chemical Physics and NanoLund, Lund University, 22100 Lund, Sweden; orcid.org/0000-0002-7236-1070; Email: kzheng@kemi.dtu.dk

Authors

Mingli Liang – Department of Chemistry, Technical University of Denmark, DK-2800 Kongens Lyngby, Denmark; orcid.org/0000-0002-1854-7026

Weihua Lin – Chemical Physics and NanoLund, Lund University, 22100 Lund, Sweden

Zhenyun Lan – Department of Energy Conversion and Storage, Technical University of Denmark, DK-2800 Kongens Lyngby, Denmark; orcid.org/0000-0001-7943-5936

Jie Meng – Department of Chemistry, Technical University of Denmark, DK-2800 Kongens Lyngby, Denmark; orcid.org/0000-0002-3813-5221

Qian Zhao – Department of Chemistry, Technical University of Denmark, DK-2800 Kongens Lyngby, Denmark

Xianshao Zou – Chemical Physics and NanoLund, Lund University, 22100 Lund, Sweden

Ivano E. Castelli – Department of Energy Conversion and Storage, Technical University of Denmark, DK-2800 Kongens Lyngby, Denmark; orcid.org/0000-0001-5880-5045

Tõnu Pullerits – Chemical Physics and NanoLund, Lund University, 22100 Lund, Sweden; orcid.org/0000-0003-1428-5564

Complete contact information is available at:
<https://pubs.acs.org/10.1021/acsaelm.0c00179>

Author Contributions

[†]M.L. and W.L. contributed equally to this work.

Notes

The authors declare no competing financial interest.

ACKNOWLEDGMENTS

This work was supported by the Independent Research Fund Denmark-Sapere Aude starting grant (no. 7026-00037A) and Swedish Research Council VR starting grant (no. 2017-05337), Swedish Energy Agency and the Chinese Scholarship Council for the PhD scholarship to M.L., W.L., Z.L., M. J., and Q.Z. The ELI-ALPS project (GINOP-2.3.6-15-2015-00001) is supported by the European Union and co-financed by the European Regional Development Fund.

REFERENCES

- Lee, M. M.; Teuscher, J.; Miyasaka, T.; Murakami, T. N.; Snaith, H. J. Efficient Hybrid Solar Cells Based on Meso-Structured Organometal Halide Perovskites. *Science* **2012**, *338*, 643–647.
- Etgar, L.; Gao, P.; Xue, Z.; Peng, Q.; Chandiran, A. K.; Liu, B.; Nazeeruddin, M. K.; Grätzel, M. Mesoscopic $\text{CH}_3\text{NH}_3\text{PbI}_3/\text{TiO}_2$ Heterojunction Solar Cells. *J. Am. Chem. Soc.* **2012**, *134*, 17396–17399.
- Bai, S.; Da, P.; Li, C.; Wang, Z.; Yuan, Z.; Fu, F.; Kaweckii, M.; Liu, X.; Sakai, N.; Wang, J. T.-W.; Huettner, S.; Buecheler, S.; Fahlman, M.; Gao, F.; Snaith, H. J. Planar Perovskite Solar Cells with Long-Term Stability Using Ionic Liquid Additives. *Nature* **2019**, *571*, 245–250.
- Wu, Z.; Bai, S.; Xiang, J.; Yuan, Z.; Yang, Y.; Cui, W.; Gao, X.; Liu, Z.; Jin, Y.; Sun, B. Efficient Planar Heterojunction Perovskite Solar Cells Employing Graphene Oxide as Hole Conductor. *Nanoscale* **2014**, *6*, 10505–10510.
- Ponseca, C. S.; Savenije, T. J.; Abdellah, M.; Zheng, K.; Yartsev, A.; Pascher, T.; Harlang, T.; Chabera, P.; Pullerits, T.; Stepanov, A.; Wolf, J.-P.; Sundström, V. Organometal Halide Perovskite Solar Cell Materials Rationalized: Ultrafast Charge Generation, High and Microsecond-Long Balanced Mobilities, and Slow Recombination. *J. Am. Chem. Soc.* **2014**, *136*, 5189–5192.
- Burschka, J.; Pellet, N.; Moon, S.-J.; Humphry-Baker, R.; Gao, P.; Nazeeruddin, M. K.; Grätzel, M. Sequential Deposition as a Route to High-Performance Perovskite-Sensitized Solar Cells. *Nature* **2013**, *499*, 316–319.
- Brenner, T. M.; Egger, D. A.; Kronik, L.; Hodes, G.; Cahen, D. Hybrid Organic - Inorganic Perovskites: Low-Cost Semiconductors with Intriguing Charge-Transport Properties. *Nat. Rev. Mater.* **2016**, *1*, 15007.
- Zhao, Y.; Zhu, K. Organic-Inorganic Hybrid Lead Halide Perovskites for Optoelectronic and Electronic Applications. *Chem. Soc. Rev.* **2016**, *45*, 655–689.
- Kojima, A.; Teshima, K.; Shirai, Y.; Miyasaka, T. Organometal Halide Perovskites as Visible-Light Sensitizers for Photovoltaic Cells. *J. Am. Chem. Soc.* **2009**, *131*, 6050–6051.
- National Renewable Energy Laboratory. Best Research-Cell Efficiencies. http://www.nrel.gov/pv/assets/images/efficiency_chart.jpg (accessed Jan 13, 2020).
- Ha, S.-T.; Su, R.; Xing, J.; Zhang, Q.; Xiong, Q. Metal Halide Perovskite Nanomaterials: Synthesis and Applications. *Chem. Sci.* **2017**, *8*, 2522–2536.
- Di, X.; Shen, L.; Jiang, J.; He, M.; Cheng, Y.; Zhou, L.; Liang, X.; Xiang, W. Efficient White LEDs with Bright Green-Emitting

CsPbBr₃ Perovskite Nanocrystal in Mesoporous Silica Nanoparticles. *J. Alloys Compd.* **2017**, *729*, 526–532.

- Yao, J.-S.; Ge, J.; Han, B.-N.; Wang, K.-H.; Yao, H.-B.; Yu, H.-L.; Li, J.-H.; Zhu, B.-S.; Song, J.-Z.; Chen, C.; Zhang, Q.; Zeng, H.-B.; Luo, Y.; Yu, S.-H. Ce^{3+} -Doping to Modulate Photoluminescence Kinetics for Efficient CsPbBr₃ Nanocrystals Based Light-Emitting Diodes. *J. Am. Chem. Soc.* **2018**, *140*, 3626–3634.
- Dai, S.-W.; Hsu, B.-W.; Chen, C.-Y.; Lee, C.-A.; Liu, H.-Y.; Wang, H.-F.; Huang, Y.-C.; Wu, T.-L.; Manikandan, A.; Ho, R.-M.; Tsao, C.-S.; Cheng, C.-H.; Chueh, Y.-L.; Lin, H.-W. Perovskite Quantum Dots with Near Unity Solution and Neat-Film Photoluminescent Quantum Yield by Novel Spray Synthesis. *Adv. Mater.* **2018**, *30*, 1705532.
- Yang, B.; Chen, J.; Yang, S.; Hong, F.; Sun, L.; Han, P.; Pullerits, T.; Deng, W.; Han, K. Lead-Free Silver-Bismuth Halide Double Perovskite Nanocrystals. *Angew. Chem., Int. Ed.* **2018**, *57*, 5359–5363.
- Saidaminov, M. I.; Adinolfi, V.; Comin, R.; Abdelhady, A. L.; Peng, W.; Dursun, I.; Yuan, M.; Hoogland, S.; Sargent, E. H.; Bakr, O. M. Planar-Integrated Single-Crystalline Perovskite Photodetectors. *Nat. Commun.* **2015**, *6*, 8724.
- Zhuo, S.; Zhang, J.; Shi, Y.; Huang, Y.; Zhang, B. Self-Template-Directed Synthesis of Porous Perovskite Nanowires at Room Temperature for High-Performance Visible-Light Photodetectors. *Angew. Chem., Int. Ed.* **2015**, *54*, 5693–5696.
- Zhang, F.; Yang, B.; Zheng, K.; Yang, S.; Li, Y.; Deng, W.; He, R. Formamidinium Lead Bromide (FAPbBr₃) Perovskite Microcrystals for Sensitive and Fast Photodetectors. *Nano-Micro Lett.* **2018**, *10*, 43.
- Yang, B.; Zhang, F.; Chen, J.; Yang, S.; Xia, X.; Pullerits, T.; Deng, W.; Han, K. Ultrasensitive and Fast All-Inorganic Perovskite-Based Photodetector via Fast Carrier Diffusion. *Adv. Mater.* **2017**, *29*, 1703758.
- Pan, W.; Wu, H.; Luo, J.; Deng, Z.; Ge, C.; Chen, C.; Jiang, X.; Yin, W.-J.; Niu, G.; Zhu, L.; Yin, L.; Zhou, Y.; Xie, Q.; Ke, X.; Sui, M.; Tang, J. Cs₂AgBiBr₆ Single-Crystal X-Ray Detectors with a Low Detection Limit. *Nat. Photonics* **2017**, *11*, 726–732.
- Yin, L.; Wu, H.; Pan, W.; Yang, B.; Li, P.; Luo, J.; Niu, G.; Tang, J. Controlled Cooling for Synthesis of Cs₂AgBiBr₆ Single Crystals and Its Application for X-Ray Detection. *Adv. Opt. Mater.* **2019**, *7*, 1900491.
- Cegielski, P. J.; Giesecke, A. L.; Neutzner, S.; Porschais, C.; Gandini, M.; Schall, D.; Perini, C. A. R.; Bolten, J.; Suckow, S.; Kataria, S.; Chmielak, B.; Wahlbrink, T.; Petrozza, A.; Lemme, M. C. Monolithically Integrated Perovskite Semiconductor Lasers on Silicon Photonic Chips by Scalable Top-Down Fabrication. *Nano Lett.* **2018**, *18*, 6915–6923.
- Raghavan, C. M.; Chen, T.-P.; Li, S.-S.; Chen, W.-L.; Lo, C.-Y.; Liao, Y.-M.; Haider, G.; Lin, C.-C.; Chen, C.-C.; Sankar, R.; Chang, Y.-M.; Chou, F.-C.; Chen, C.-W. Low-Threshold Lasing from 2D Homologous Organic-Inorganic Hybrid Ruddlesden-Popper Perovskite Single Crystals. *Nano Lett.* **2018**, *18*, 3221–3228.
- Chen, Y.; Sun, Y.; Peng, J.; Zhang, W.; Su, X.; Zheng, K.; Pullerits, T.; Liang, Z. Tailoring Organic Cation of 2D Air-Stable Organometal Halide Perovskites for Highly Efficient Planar Solar Cells. *Adv. Energy Mater.* **2017**, *7*, 1700162.
- Tsai, H.; Nie, W.; Blancon, J.-C.; Stoumpos, C. C.; Asadpour, R.; Harutyunyan, B.; Neukirch, A. J.; Verduzco, R.; Crochet, J. J.; Tretyak, S.; Pedesseau, L.; Even, J.; Alam, M. A.; Gupta, G.; Lou, J.; Ajayan, P. M.; Bedzyk, M. J.; Kanatzidis, M. G.; Mohite, A. D. High-Efficiency Two-Dimensional Ruddlesden-Popper Perovskite Solar Cells. *Nature* **2016**, *536*, 312–316.
- Yang, S.; Wu, D.; Gong, W.; Huang, Q.; Zhen, H.; Ling, Q.; Lin, Z. Highly Efficient Room-Temperature Phosphorescence and Afterglow Luminescence from Common Organic Fluorophores in 2D Hybrid Perovskites. *Chem. Sci.* **2018**, *9*, 8975–8981.
- Stoumpos, C. C.; Soe, C. M. M.; Tsai, H.; Nie, W.; Blancon, J.-C.; Cao, D. H.; Liu, F.; Traoré, B.; Katan, C.; Even, J.; Mohite, A. D.; Kanatzidis, M. G. High Members of the 2D Ruddlesden-Popper

Halide Perovskites: Synthesis, Optical Properties, and Solar Cells of $(\text{CH}_3(\text{CH}_2)_2\text{NH}_3)_2(\text{CH}_3\text{NH}_3)_4\text{Pb}_6\text{I}_{16}$. *Chem* **2017**, *2*, 427–440.

(28) Saparov, B.; Mitzi, D. B. Organic-Inorganic Perovskites: Structural Versatility for Functional Materials Design. *Chem. Rev.* **2016**, *116*, 4558–4596.

(29) Blancon, J.-C.; Tsai, H.; Nie, W.; Stoumpos, C. C.; Pedesseau, L.; Katan, C.; Kepenekian, M.; Soe, C. M. M.; Appavoo, K.; Sfeir, M. Y.; Tretiak, S.; Ajayan, P. M.; Kanatzidis, M. G.; Even, J.; Crochet, J. J.; Mohite, A. D. Extremely Efficient Internal Exciton Dissociation through Edge States in Layered 2D Perovskites. *Science* **2017**, *355*, 1288–1292.

(30) Charles, B.; Dillon, J.; Weber, O. J.; Islam, M. S.; Weller, M. T. Understanding the Stability of Mixed A-Cation Lead Iodide Perovskites. *J. Mater. Chem. A* **2017**, *5*, 22495–22499.

(31) Li, Z.; Yang, M.; Park, J.-S.; Wei, S.-H.; Berry, J. J.; Zhu, K. Stabilizing Perovskite Structures by Tuning Tolerance Factor: Formation of Formamimidium and Cesium Lead Iodide Solid-State Alloys. *Chem. Mater.* **2016**, *28*, 284–292.

(32) Han, G.; Hadi, H. D.; Bruno, A.; Kulkarni, S. A.; Koh, T. M.; Wong, L. H.; Soci, C.; Mathews, N.; Zhang, S.; Mhaisalkar, S. G. Additive Selection Strategy for High Performance Perovskite Photovoltaics. *J. Phys. Chem. C* **2018**, *122*, 13884–13893.

(33) Mao, L.; Wu, Y.; Stoumpos, C. C.; Traore, B.; Katan, C.; Even, J.; Wasielewski, M. R.; Kanatzidis, M. G. Tunable White-Light Emission in Single-Cation-Templated Three-Layered 2D Perovskites $(\text{CH}_3\text{CH}_2\text{NH}_3)_4\text{Pb}_3\text{Br}_{10}\text{XCl}_x$. *J. Am. Chem. Soc.* **2017**, *139*, 11956–11963.

(34) Wang, S.; Liu, X.; Li, L.; Ji, C.; Sun, Z.; Wu, Z.; Hong, M.; Luo, J. An Unprecedented Biaxial Trilayered Hybrid Perovskite Ferroelectric with Directionally Tunable Photovoltaic Effects. *J. Am. Chem. Soc.* **2019**, *141*, 7693–7697.

(35) Han, S.; Liu, X.; Liu, Y.; Xu, Z.; Li, Y.; Hong, M.; Luo, J.; Sun, Z. High-Temperature Antiferroelectric of Lead Iodide Hybrid Perovskites. *J. Am. Chem. Soc.* **2019**, *141*, 12470–12474.

(36) Xu, Z.; Li, Y.; Liu, X.; Ji, C.; Chen, H.; Li, L.; Han, S.; Hong, M.; Luo, J.; Sun, Z. Highly Sensitive and Ultrafast Responding Array Photodetector Based on a Newly Tailored 2D Lead Iodide Perovskite Crystal. *Adv. Opt. Mater.* **2019**, *7*, 1900308.

(37) Fu, Y.; Hautzinger, M. P.; Luo, Z.; Wang, F.; Pan, D.; Aristov, M. M.; Guzei, I. A.; Pan, A.; Zhu, X.; Jin, S. Incorporating Large A Cations into Lead Iodide Perovskite Cages: Relaxed Goldschmidt Tolerance Factor and Impact on Exciton-Phonon Interaction. *ACS Cent. Sci.* **2019**, *5*, 1377–1386.

(38) Liang, M.-L.; Ma, Y.-X.; Hu, C.-L.; Kong, F.; Mao, J.-G. $\text{A}(\text{VO}_2\text{F})(\text{SeO}_3)$ (A = Sr, Ba) and $\text{Ba}(\text{MOF}_2)(\text{TeO}_4)$ (M = Mo, W): first examples of alkali-earth selenites/tellurites with a fluorinated d0-TM octahedron. *Dalton Trans.* **2018**, *47*, 1513–1519.

(39) Larsen, A. H.; Mortensen, J. J.; Blomqvist, J.; Castelli, I. E.; Christensen, R.; Dulak, M.; Friis, J.; Groves, M. N.; Hammer, B.; Hargus, C.; Hermes, E. D.; Jennings, P. C.; Jensen, P. B.; Kermode, J.; Kitchin, J. R.; Kolsbjerg, E. L.; Kubal, J.; Kaasbjerg, K.; Lysgaard, S.; Maronsson, J. B.; Maxson, T.; Olsen, T.; Pastewka, L.; Peterson, A.; Rostgaard, C.; Schiøtz, J.; Schütt, O.; Strange, M.; Thygesen, K. S.; Vegge, T.; Vilhelmsen, L.; Walter, M.; Zeng, Z.; Jacobsen, K. W. The Atomic Simulation Environment—A Python Library for Working with Atoms. *J. Phys.: Condens. Matter* **2017**, *29*, 273002.

(40) Kresse, G.; Hafner, J. Ab Initio Molecular Dynamics for Liquid Metals. *Phys. Rev. B: Condens. Matter Mater. Phys.* **1993**, *47*, 558–561.

(41) Mortensen, J. J.; Hansen, L. B.; Jacobsen, K. W. Real-Space Grid Implementation of the Projector Augmented Wave Method. *Phys. Rev. B: Condens. Matter Mater. Phys.* **2005**, *71*, 035109.

(42) Enkovaara, J.; Rostgaard, C.; Mortensen, J. J.; Chen, J.; Dulak, M.; Ferrighi, L.; Gavnholt, J.; Glinvad, C.; Haikola, V.; Hansen, H. A.; Kristoffersen, H. H.; Kuisma, M.; Larsen, A. H.; Lehtovaara, L.; Ljungberg, M.; Lopez-Acevedo, O.; Moses, P. G.; Ojanen, J.; Olsen, T.; Petzold, V.; Romero, N. A.; Stausholm-Møller, J.; Strange, M.; Tritsarolis, G. A.; Vanin, M.; Walter, M.; Hammer, B.; Häkkinen, H.; Madsen, G. K. H.; Nieminen, R. M.; Nørskov, J. K.; Puska, M.; Rantala, T. T.; Schiøtz, J.; Thygesen, K. S.; Jacobsen, K. W. Electronic

Structure Calculations with GPAW: A Real-Space Implementation of the Projector Augmented-Wave Method. *J. Phys.: Condens. Matter* **2010**, *22*, 253202.

(43) Perdew, J. P.; Ruzsinszky, A.; Csonka, G. I.; Vydrov, O. A.; Scuseria, G. E.; Constantin, L. A.; Zhou, X.; Burke, K. Restoring the Density-Gradient Expansion for Exchange in Solids and Surfaces. *Phys. Rev. Lett.* **2008**, *100*, 136406.

(44) Blöchl, P. E. Projector Augmented-Wave Method. *Phys. Rev. B: Condens. Matter Mater. Phys.* **1994**, *50*, 17953–17979.

(45) Kuisma, M.; Ojanen, J.; Enkovaara, J.; Rantala, T. T. Kohn-Sham Potential with Discontinuity for Band Gap Materials. *Phys. Rev. B: Condens. Matter Mater. Phys.* **2010**, *82*, 115106.

(46) Castelli, I. E.; Hüser, F.; Pandey, M.; Li, H.; Thygesen, K. S.; Seger, B.; Jain, A.; Persson, K. A.; Ceder, G.; Jacobsen, K. W. New light-harvesting materials using accurate and efficient bandgap calculations. *Adv. Energy Mater.* **2015**, *5*, 1400915.

(47) Castelli, I. E.; Garcia-Lastra, J. M.; Thygesen, K. S.; Jacobsen, K. W. Bandgap Calculations and Trends of Organometal Halide Perovskites. *APL Mater.* **2014**, *2*, 081514.

(48) Becker, M.; Klüner, T.; Wark, M. Formation of Hybrid ABX_3 Perovskite Compounds for Solar Cell Application: First-Principles Calculations of Effective Ionic Radii and Determination of Tolerance Factors. *Dalton Trans.* **2017**, *46*, 3500–3509.

(49) Gao, P.; Bin Mohd Yusoff, A. R.; Nazeeruddin, M. K. Dimensionality Engineering of Hybrid Halide Perovskite Light Absorbers. *Nat. Commun.* **2018**, *9*, 5028.

(50) Varadwaj, P. R.; Varadwaj, A.; Marques, H. M.; Yamashita, K. Significance of Hydrogen Bonding and Other Noncovalent Interactions in Determining Octahedral Tilting in the $\text{CH}_3\text{NH}_3\text{PbI}_3$ Hybrid Organic-Inorganic Halide Perovskite Solar Cell Semiconductor. *Sci. Rep.* **2019**, *9*, 50.

(51) Lufaso, M. W.; Woodward, P. M. Jahn-Teller Distortions, Cation Ordering and Octahedral Tilting in Perovskites. *Acta Crystallogr., Sect. B: Struct. Sci.* **2004**, *60*, 10–20.

(52) Alvarez, S. Distortion Pathways of Transition Metal Coordination Polyhedra Induced by Chelating Topology. *Chem. Rev.* **2015**, *115*, 13447–13483.

(53) Pérez-Osorio, M. A.; Lin, Q.; Phillips, R. T.; Milot, R. L.; Herz, L. M.; Johnston, M. B.; Giustino, F. Raman Spectrum of the Organic-Inorganic Halide Perovskite $\text{CH}_3\text{NH}_3\text{PbI}_3$ from First Principles and High-Resolution Low-Temperature Raman Measurements. *J. Phys. Chem. C* **2018**, *122*, 21703–21717.

(54) Quarti, C.; Grancini, G.; Mosconi, E.; Bruno, P.; Ball, J. M.; Lee, M. M.; Snaith, H. J.; Petrozza, A.; De Angelis, F. The Raman Spectrum of the $\text{CH}_3\text{NH}_3\text{PbI}_3$ Hybrid Perovskite: Interplay of Theory and Experiment. *J. Phys. Chem. Lett.* **2014**, *5*, 279–284.

(55) Xie, L.-Q.; Zhang, T.-Y.; Chen, L.; Guo, N.; Wang, Y.; Liu, G.-K.; Wang, J.-R.; Zhou, J.-Z.; Yan, J.-W.; Zhao, Y.-X.; Mao, B.-W.; Tian, Z.-Q. Organic-Inorganic Interactions of Single Crystalline Organolead Halide Perovskites Studied by Raman Spectroscopy. *Phys. Chem. Chem. Phys.* **2016**, *18*, 18112–18118.

(56) Zheng, K.; Zhu, Q.; Abdellah, M.; Messing, M. E.; Zhang, W.; Generalov, A.; Niu, Y.; Ribaud, L.; Canton, S. E.; Pullerits, T. Exciton Binding Energy and the Nature of Emissive States in Organometal Halide Perovskites. *J. Phys. Chem. Lett.* **2015**, *6*, 2969–2975.

(57) Chen, Z.; Yu, C.; Shum, K.; Wang, J. J.; Pfenniger, W.; Vockic, N.; Midgley, J.; Kenney, J. T. Photoluminescence Study of Polycrystalline CsSnI_3 Thin Films: Determination of Exciton Binding Energy. *J. Lumin.* **2012**, *132*, 345–349.

(58) Blancon, J.-C.; Stier, A. V.; Tsai, H.; Nie, W.; Stoumpos, C. C.; Traoré, B.; Pedesseau, L.; Kepenekian, M.; Katsutani, F.; Noe, G. T.; Kono, J.; Tretiak, S.; Crooker, A. A.; Katan, C.; Kanatzidis, M. G.; Crochet, J. J.; Even, J.; Mohite, A. D. Scaling law for excitons in 2D perovskite quantum wells. *Nat. Commun.* **2018**, *9*, 2254.

(59) Baranowski, M.; Plochocka, P. Excitons in Metal-Halide Perovskites. *Adv. Energy Mater.* **2020**, 1903659.

(60) Katan, C.; Pedesseau, L.; Kepenekian, M.; Rolland, A.; Even, J. Interplay of Spin-Orbit Coupling and Lattice Distortion in Metal

Substituted 3D Tri-Chloride Hybrid Perovskites. *J. Mater. Chem. A* **2015**, *3*, 9232–9240.

(61) Zhu, Q.; Zheng, K.; Abdellah, M.; Generalov, A.; Haase, D.; Carlson, S.; Niu, Y.; Heimdal, J.; Engdahl, A.; Messing, M. E.; Pullerits, T.; Canton, S. E. Correlating Structure and Electronic Band-Edge Properties in Organolead Halide Perovskites Nanoparticles. *Phys. Chem. Chem. Phys.* **2016**, *18*, 14933–14940.

(62) Waghmare, U. V.; Spaldin, N. A.; Kandpal, H. C.; Seshadri, R. First-Principles Indicators of Metallicity and Cation off-Centricity in the IV-VI Rocksalt Chalcogenides of Divalent Ge, Sn, and Pb. *Phys. Rev. B: Condens. Matter Mater. Phys.* **2003**, *67*, 125111.

(63) Payne, D. J.; Egdell, R. G.; Walsh, A.; Watson, G. W.; Guo, J.; Glans, P. A.; Learmonth, T.; Smith, K. E. Electronic Origins of Structural Distortions in Post-Transition Metal Oxides: Experimental and Theoretical Evidence for a Revision of the Lone Pair Model. *Phys. Rev. Lett.* **2006**, *96*, 157403.

(64) Zheng, K.; Židek, K.; Abdellah, M.; Messing, M. E.; Al-Marri, M. J.; Pullerits, T. Trap States and Their Dynamics in Organometal Halide Perovskite Nanoparticles and Bulk Crystals. *J. Phys. Chem. C* **2016**, *120*, 3077–3084.

(65) Zheng, K.; Židek, K.; Abdellah, M.; Chen, J.; Chábera, P.; Zhang, W.; Al-Marri, M. J.; Pullerits, T. High Excitation Intensity Opens a New Trapping Channel in Organic-Inorganic Hybrid Perovskite Nanoparticles. *ACS Energy Lett.* **2016**, *1*, 1154–1161.

(66) de Quilettes, D. W.; Vorpahl, S. M.; Stranks, S. D.; Nagaoka, H.; Eperon, G. E.; Ziffer, M. E.; Snaith, H. J.; Ginger, D. S. Impact of Microstructure on Local Carrier Lifetime in Perovskite Solar Cells. *Science* **2015**, *348*, 683–686.

(67) Abdellah, M.; Židek, K.; Zheng, K.; Chábera, P.; Messing, M. E.; Pullerits, T. Balancing Electron Transfer and Surface Passivation in Gradient CdSe/ZnS Core-Shell Quantum Dots Attached to ZnO. *J. Phys. Chem. Lett.* **2013**, *4*, 1760–1765.

(68) Stranks, S. D.; Burlakov, V. M.; Leijtens, T.; Ball, J. M.; Goriely, A.; Snaith, H. J. Recombination Kinetics in Organic-Inorganic Perovskites: Excitons, Free Charge, and Subgap States. *Phys. Rev. Appl.* **2014**, *2*, 034007.

Supporting Information

Electronic Structure and Trap-States of Two-Dimensional Ruddlesden-Popper Perovskites with Relaxed Goldschmidt Tolerance Factor

Mingli Liang^{†,1}, Weihua Lin^{‡,1}, Zhenyun Lan[#], Jie Meng[†], Qian Zhao[†], Xianshao Zou[‡], Ivano E. Castelli[#], Tönu Pullerits[‡], Sophie E. Canton^{*,^} and Kaibo Zheng^{*,†,‡}

[†]*Department of Chemistry, Technical University of Denmark, DK-2800 Kongens Lyngby, Denmark;*

[‡]*Chemical Physics and NanoLund, Lund University, Box 124, 22100 Lund, Sweden;*

[#]*Department of Energy Conversion and Storage, Technical University of Denmark, DK-2800 Kongens Lyngby, Denmark;*

[^]*ELI-ALPS, ELI-HU Non-Profit, Ltd., Dugonics ter 13, Szeged 6720, Hungary;*

*Sophie E. Canton, Sophie.Canton@eli-alps.hu

*Kaibo Zheng, kzheng@kemi.dtu.dk

Table S1. Crystal data and structure determinations of the BMAPI and BEAPI.

Table S2. Bond distances (Angstroms) of Pb-I for the BMAPI and BEAPI.

Table S3. I-Pb-I angles (deg) for the BMAPI and BEAPI.

Table S4. Selected strong N-H \cdots I hydrogen bond distances (H \cdots I, Angstroms) angles (deg) for the BMAPI and BEAPI.

Table S5. The values of five distortion parameters of BMAPI and BEAPI.

Table S6. Multi-exponential fitting parameters for TRPL kinetics of BMAPI.

Table S7. Multi-exponential fitting parameters for TRPL kinetics of BEAPI.

Table S8. Excitation density of BMAPI and BEAPI with different laser photon flux.

Table S9. The calculated values of ratio of the free carriers x .

Table S10. Trap densities obtained from the fitting.

Figure S1. A schematic diagram of the growth of the bulk single crystals, and the resulting two title single crystals.

Figure S2. The powder XRD spectra of (a) BMAPI and (b) BEAPI.

Figure S3. A diagram for the formation processes of perovskite phase MAPbI_3 and non-perovskite phase EAPbI_3 .

Figure S4. Comparison between experimental Raman spectra of BEAPI and the calculation of isolated EA cation.

Figure S5. The vibration modes of MA and EA in BMAPI and BEAPI.

S5. Calculation of E_b using temperature dependent photoluminescence method.

Figure S6. The temperature dependent PL spectra of (a) BMAPI and (c) BEAPI; $\ln(I_0/I(T)-1)$ vs. $1/k_bT$ plot of temperature dependent PL of (b) BMAPI and (d) BEAPI.

S7. Calculations of the absorption coefficients and excitation density of two compounds.

Figure S7. The fresh crystal flakes of (a) BMAPI and (b) BEAPI were used for PL kinetics measurements.

S8. Calculation of the free carrier ratio after photo-excitation.

S9. Detailed model of trap filling and fitting process.

Table S1. Crystal data and structure determinations of the BMAPI and BEAPI.

Formula	BMAPI	BEAPI
Formula Weight	2103.00	2131.05
Space group	<i>Aba2</i>	<i>Cmc2₁</i>
<i>a</i> (Å)	8.9365(10)	52.098(5)
<i>b</i> (Å)	51.969(5)	8.9769(9)
<i>c</i> (Å)	8.8754(9)	8.9902(9)
α (deg)	90	90
β (deg)	90	90
γ (deg)	90	90
<i>V</i> (Å ³)	4121.9(7)	4204.5(7)
<i>Z</i>	4	4
μ (Mo <i>Ka</i>) (mm ⁻¹)	19.721	19.366
GOF on <i>F</i> ²	1.029	1.066
<i>R</i> ₁ , <i>wR</i> ₂ [<i>I</i> >2 σ (<i>I</i>)] ^a	0.0711, 0.1262	0.0856, 0.1990
<i>R</i> ₁ , <i>wR</i> ₂ (all data) ^a	0.1595, 0.1600	0.1632, 0.2611

$$^a R_1 = \sum ||F_o| - |F_c|| / \sum |F_o|, wR_2 = \{ \sum w[(F_o)^2 - (F_c)^2]^2 / \sum w[(F_o)^2] \}^{1/2}$$

Table S2. Bond distances (Angstroms) of Pb-I for the BMAPI and BEAPI.

BMAPI			
Pb(1)-I(4)#1	3.115(5)	Pb(2)-I(3)#4	3.145(3)
Pb(1)-I(4)	3.115(5)	Pb(2)-I(2)#2	3.159(3)
Pb(1)-I(1)#1	3.1633(11)	Pb(2)-I(3)	3.184(3)
Pb(1)-I(1)	3.1634(11)	Pb(2)-I(2)	3.185(3)
Pb(1)-I(4)#2	3.199(5)	Pb(2)-I(1)	3.3040(12)
Pb(1)-I(4)#3	3.199(5)	Pb(2)-I(5)	3.0521(15)
BEAPI			
Pb(1)-I(5)#1	3.186(4)	Pb(2)-I(6)	3.010(2)
Pb(1)-I(2)	3.1950(16)	Pb(2)-I(3)	3.183(3)

Pb(1)-I(2)#2	3.1950(16)	Pb(2)-I(1)	3.184(3)
Pb(1)-I(5)	3.213(4)	Pb(2)-I(1)#4	3.202(3)
Pb(1)-I(4)	3.270(3)	Pb(2)-I(3)#5	3.211(3)
Pb(1)-I(4)#3	3.299(4)	Pb(2)-I(2)	3.457(2)

Symmetry transformations used to generate equivalent atoms:

For BMAPI: #1 -x+1, -y, z; #2 -x+3/2, y, z+1/2; #3 x-1/2, -y, z+1/2; #4 -x+1/2, y, z+1/2.

For BEAPI: #1 -x+2, -y+1, z-1/2; #2 -x+2, y, z; #3 -x+2, -y+2, z+1/2; #4 x, -y+2, z-1/2; #5 x, -y+1, z-1/2.

Table S3. I-Pb-I angles (deg) for the BMAPI and BEAPI.

BMAPI			
I(4)#1-Pb(1)-I(4)	90.1(3)	I(5)-Pb(2)-I(3)#4	92.71(10)
I(4)#1-Pb(1)-I(1)#1	90.57(9)	I(5)-Pb(2)-I(2)#2	90.54(10)
I(4)-Pb(1)-I(1)#1	91.00(8)	I(3)#4-Pb(2)-I(2)#2	89.50(10)
I(4)#1-Pb(1)-I(1)	91.00(8)	I(5)-Pb(2)-I(3)	93.84(9)
I(4)-Pb(1)-I(1)	90.57(9)	I(3)#4-Pb(2)-I(3)	89.17(2)
I(1)#1-Pb(1)-I(1)	177.8(2)	I(2)#2-Pb(2)-I(3)	175.48(6)
I(4)#1-Pb(1)-I(4)#2	179.4(3)	I(5)-Pb(2)-I(2)	91.23(9)
I(4)-Pb(1)-I(4)#2	89.331(10)	I(3)#4-Pb(2)-I(2)	175.72(5)
I(1)#1-Pb(1)-I(4)#2	89.29(9)	I(2)#2-Pb(2)-I(2)	88.78(2)
I(1)-Pb(1)-I(4)#2	89.16(8)	I(3)-Pb(2)-I(2)	92.25(10)
I(4)#1-Pb(1)-I(4)#3	89.331(10)	I(5)-Pb(2)-I(1)	175.69(6)
I(4)-Pb(1)-I(4)#3	179.4(3)	I(3)#4-Pb(2)-I(1)	90.21(8)
I(1)#1-Pb(1)-I(4)#3	89.16(8)	I(2)#2-Pb(2)-I(1)	86.31(8)
I(1)-Pb(1)-I(4)#3	89.29(9)	I(3)-Pb(2)-I(1)	89.37(8)
I(4)#2-Pb(1)-I(4)#3	91.2(3)	I(2)-Pb(2)-I(1)	85.77(8)
BEAPI			
I(5)#1-Pb(1)-I(2)	90.15(9)	I(1)-Pb(2)-I(2)	82.28(7)
I(5)#1-Pb(1)-I(2)#2	90.15(9)	I(6)-Pb(2)-I(3)	89.84(9)
I(2)-Pb(1)-I(2)#2	172.06(13)	I(6)-Pb(2)-I(1)	87.89(9)
I(5)#1-Pb(1)-I(5)	92.26(5)	I(3)-Pb(2)-I(1)	91.81(9)
I(2)-Pb(1)-I(5)	93.96(7)	I(6)-Pb(2)-I(1)#4	90.00(9)
I(2)#2-Pb(1)-I(5)	93.96(7)	I(3)-Pb(2)-I(1)#4	178.70(9)
I(5)#1-Pb(1)-I(4)	87.27(10)	I(1)-Pb(2)-I(1)#4	89.47(3)
I(2)-Pb(1)-I(4)	86.05(7)	I(6)-Pb(2)-I(3)#5	91.73(9)
I(2)#2-Pb(1)-I(4)	86.05(7)	I(3)-Pb(2)-I(3)#5	89.35(3)

I(5)-Pb(1)-I(4)	179.53(12)	I(1)-Pb(2)-I(3)#5	178.77(9)
I(5)#1-Pb(1)-I(4)#3	175.27(10)	I(1)#4-Pb(2)-I(3)#5	89.37(9)
I(2)-Pb(1)-I(4)#3	89.52(8)	I(2)-Pb(2)-I(3)	97.40(7)
I(2)#2-Pb(1)-I(4)#3	89.52(8)	I(2)-Pb(2)-I(6)	167.94(4)
I(5)-Pb(1)-I(4)#3	92.47(11)	I(2)-Pb(2)-I(1)#4	82.98(7)
I(4)-Pb(1)-I(4)#3	88.00(4)	I(2)-Pb(2)-I(3)#5	97.96(7)

Symmetry transformations used to generate equivalent atoms:

For BMAPI: #1 -x+1, -y, z; #2 -x+3/2, y, z+1/2; #3 x-1/2, -y, z+1/2; #4 -x+1/2, y, z+1/2.

For BEAPI: #1 -x+2, -y+1, z-1/2; #2 -x+2, y, z; #3 -x+2, -y+2, z+1/2; #4 x, -y+2, z-1/2; #5 x, -y+1, z-1/2; #5 x, -y+1, z-1/2.

Table S4. Selected strong N-H \cdots I hydrogen bond distances (H \cdots I, Angstroms) angles (deg) for the BMAPI and BEAPI.

BMAPI		
N(1)-H(1A)-I(2)	3.065(10) (Å)	132.19(7) (°)
N(1)-H(1B)-I(1)	2.985(10)	164.43(7)
N(1)-H(1C)-I(5)	3.002(10)	142.74(7)
N(2)-H(2A)-I(4)	3.234(10)	144.16(7)
N(2)-H(2B)-I(3)	3.147(10)	149.52(7)
N(2)-H(2C)-I(2)	3.120(10)	133.45(7)
Average	3.092(10)	
BEAPI		
N(1)-H(1B)-I(6)	2.988(10)	146.94(7)
N(1)-H(1C)-I(3)	2.924(10)	154.89(7)
N(7)-H(7A)-I(5)	2.857(10)	157.12(7)
N(7)-H(7B)-I(2)	3.039(10)	142.56(7)
N(7)-H(7C)-I(2)	2.862(10)	136.91(7)
Average	2.934(10)	

Table S5 The values of five distortion parameters of BMAPI and BEAPI.

BMAPI	$\langle D \rangle$	ζ	Δ	Θ	Σ
Outer layer	3.18	0.29	3.3×10^{-3}	48.5	19.5
Inner layer	3.16	0.22	1.1×10^{-3}	30.5	8.1
Outer layer	3.18	0.29	3.3×10^{-3}	48.5	19.5
BEAPI	$\langle D \rangle$	ζ	Δ	Θ	Σ
Outer layer	3.21	0.50	9.9×10^{-3}	119.7	37.1
Inner layer	3.23	0.23	1.1×10^{-3}	60.1	26.5
Outer layer	3.21	0.50	9.9×10^{-3}	119.7	37.1

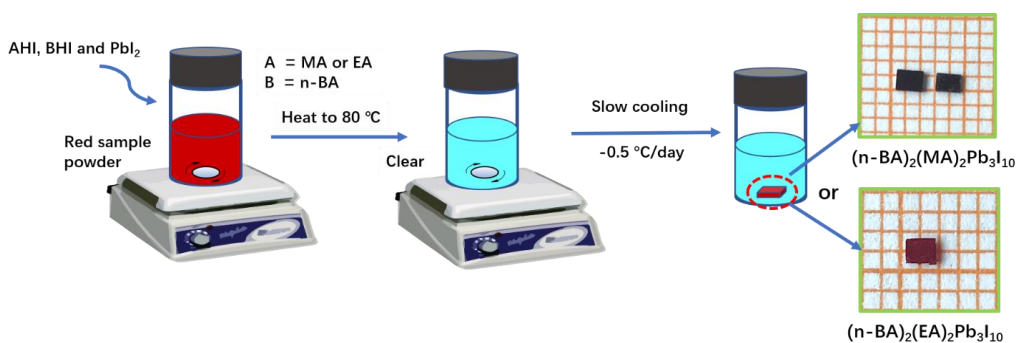


Figure S1. A schematic diagram of the growth of the bulk single crystals, and the resulting the two title single crystals (~1.5 - 2.0 mm).

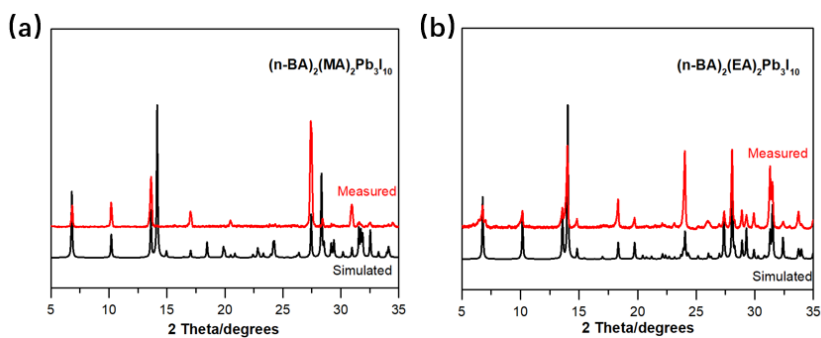


Figure S2. The powder XRD spectra of (a) BMAPI and (b) BEAPI.

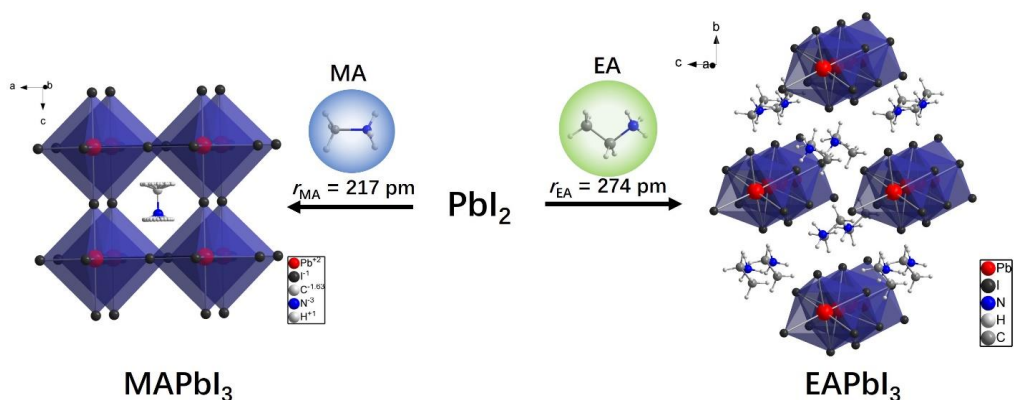


Figure S3. A diagram for the formation processes of perovskite phase MAPbI_3 (Reproduced with permission from ref 1, Copyright 2018 American Chemical Society) and non-perovskite phase EAPbI_3 (Reproduced with permission from ref 2, Copyright 2015 Royal Society of Chemistry).

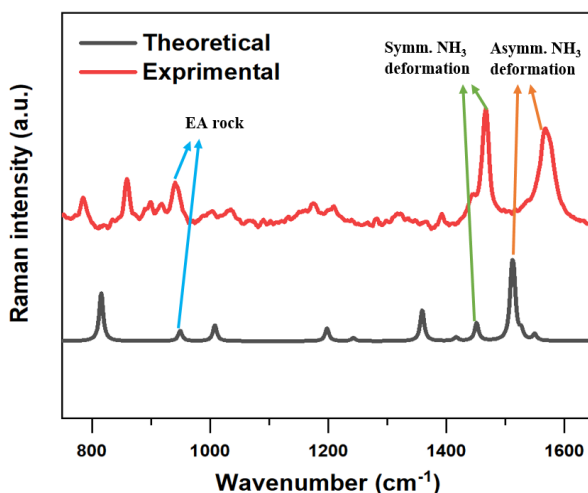


Figure S4. Comparison between experimental Raman spectra of BEAPI and the calculation of isolated EA cation. The experimental peaks of EA cation at 943, 1467 and 1560 cm^{-1} could be assigned to the vibrational modes of EA rock, symmetric NH_3 deformation and asymmetric NH_3 deformation. The stronger electron static correlation between the surface states and adsorbed molecules in our sample could lead to stronger Van Der Waals interactions, which changes the force constant of the adsorbed molecules and further results in Raman peak shifts.

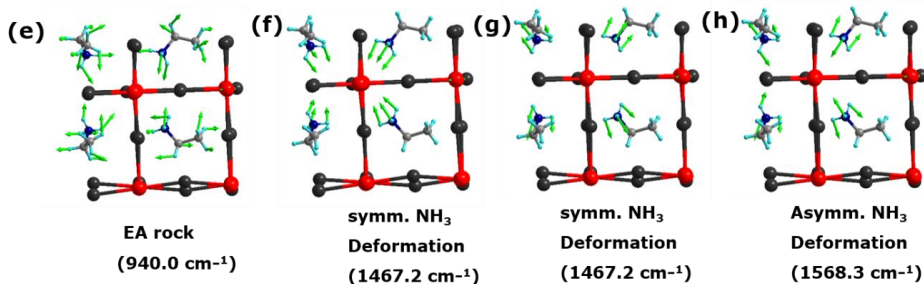
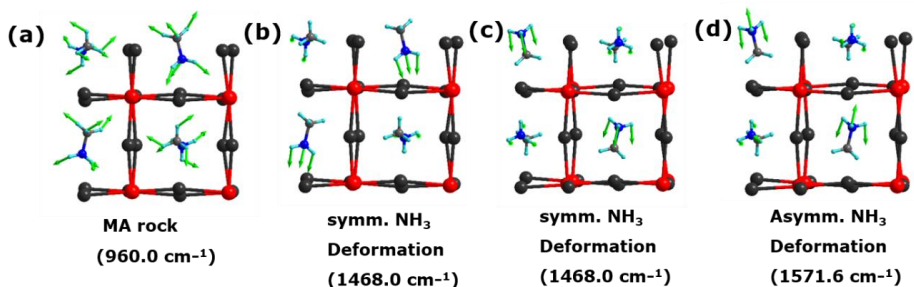


Figure S5. The vibration modes of MA and EA in BMAPI and BEAPI.

S5. Calculation of E_b using temperature dependent photoluminescence method.

PL spectra of these two fresh title compounds were measured at temperatures ranging 100-260 K in a cryostat, liquid nitrogen as the coolant, and the integrated PL intensities $I(T)$ were calculated (Figure s5a, s5c). Here, the PL intensity decreased with increased temperatures due to the thermal dissociation of excitons at higher temperatures, the temperature dependent PL intensity can be expressed as follows:

$$I(T) = \frac{I_0}{1 + Ae^{(-E_b/k_B T)}} \quad (6)$$

In which, I_0 is the PL intensity at low temperature, and k_B is the Boltzmann constant. From the linear fitting of $\ln(I_0/I(T)-1)$ and $1/k_B T$ plot, we can obtain their E_b as the slopes.³ The E_b of BMAPI and BEAPI are 65.8 ± 10 meV and 46.4 ± 10 meV, respectively (Figure s5b, s5d). In general, the PL peaks of two samples both exhibit blue shifts over the increasing temperature range, which

should be due to the dominating effect from the lattice expansion. There also remain some impurity emission peaks as background, which should come from the substrate and do not affect the E_b calculation.

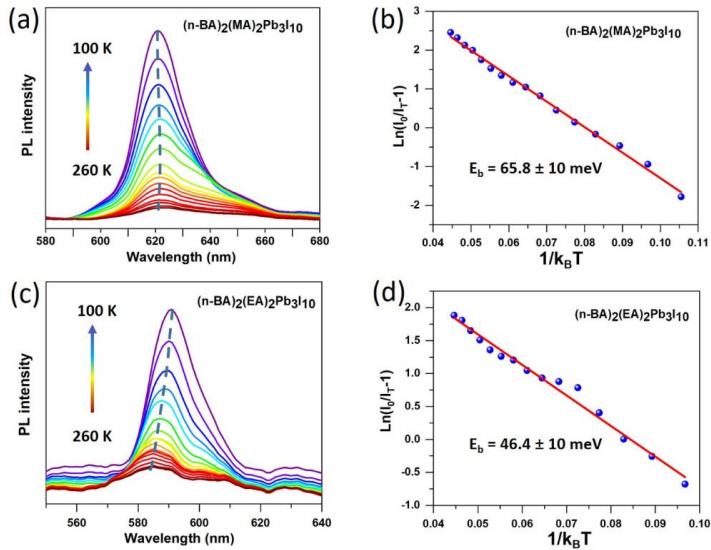


Figure S6. The temperature dependent PL spectra of (a) BMAPI and (c) BEAPI at temperature from 100-260 K; $\ln(I_0/I(T)-1)$ vs. $1/k_B T$ plot of temperature dependent PL of (b) BMAPI and (d) BEAPI.

Table S6. Multi-exponential fitting parameters for TRPL kinetics of BMAPI.

Excitation Fluence (photon/pulse/cm ²)	A ₁ (%)	t ₁ (ns)	A ₂ (%)	t ₂ (ns)	A ₃ (%)	t ₃ (ns)	t _{average} (ns)
6.04×10 ⁹	56.1	1.64 (±0.01)	16.2	10.29 (±0.12)	27.7	34.61 (±0.08)	12.17
2.01×10 ⁹	72.2	1.53 (±0.01)	9.4	10.53 (±0.18)	18.4	49.85 (±0.11)	11.27
1.21×10 ⁹	89.3	1.35 (±0.01)	4.4	9.52 (±0.20)	6.3	67.16 (±0.19)	5.86
4.02×10 ⁸	93.3	1.23(±0.01)	3.2	8.71 (±0.36)	3.5	76.42 (±0.49)	4.10

2.01×10⁸ 94.3 1.28 (±0.01) 1.0 6.37 (±0.15) 4.7 70.67 (±0.27) 4.59

Table S7. Multi-exponential fitting parameters for TRPL kinetics of BEAPI.

Excitation Fluence (photon/pulse/cm ²)	A ₁ (%)	t ₁ (ns)	A ₂ (%)	t ₂ (ns)	A ₃ (%)	t ₃ (ns)	t _{average} (ns)
6.04×10 ⁹	77.2	0.496 (±0.002)	22.5	2.44 (±0.01)	0.3	86.7 (±1.2)	1.19
2.01×10 ⁹	90.4	0.426 (±0.001)	9.2	3.41 (±0.03)	0.4	96.1 (±2.3)	1.08
1.21×10 ⁹	94.3	0.390 (±0.001)	5.4	4.20 (± 0.06)	0.3	101.5 (±2.9)	0.90
4.02×10 ⁸	95.8	0.369 (±0.002)	3.9	4.53 (±0.10)	0.3	100.2 (±5.2)	0.83
2.01×10 ⁸	96.2	0.367 (±0.002)	3.4	4.89 (± 0.16)	0.4	93.4 (±5.6)	0.89

S7. Calculations of the absorption coefficients and excitation density of two compounds.

To calculate the excitation density of the two samples, we first measured their absorption coefficients using the laser. The perovskite crystals were torn into thin flakes that were placed on a quartz substrate and used for measurements (Figure S7). From Scanning Electron Microscope (SEM) measurement, the section thicknesses of BMAPI and BEAPI are approximately 680 and 600 nm, respectively. The absorbance (A) can be calculated by the following formula:

$$A = \log(I_0/I_1) \quad (1)$$

Here, I_0 is incident light intensity and I_1 is the transmitted light intensity. The A values of BMAPI and BEAPI are 0.73 and 0.25, respectively. The absorption coefficient $\varepsilon = A/l$, where l is the path length of the light, which is equal to the thickness of the crystal. So, we obtain $\varepsilon = 1.07 \times 10^5$ and $4.2 \times 10^4 \text{ cm}^{-1}$ for BMAPI and BEAPI, respectively. The excitation density n can be calculated as photon flux f in photons/cm² multiplied by absorption coefficient ε : $n = f\varepsilon$, Table S8 summarizes the corresponding excitation density at different laser photon flux in the TRPL measurements:

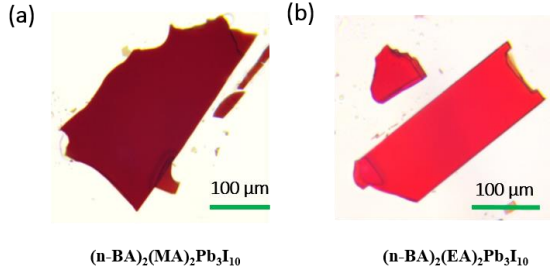


Figure S7. The fresh crystal flakes of (a) BMAPI and (b) BEAPI were used for TRPL kinetics measurements. The laser spot was focused on a bulk area during the measurements.

Table S8 Excitation density of BMAPI and BEAPI with different laser photon flux.

Excitation Fluence (photon/pulse/cm ²)	Excitation Intensity (cm ⁻³) of BMAPI	Excitation Intensity (cm ⁻³) of BEAPI
6.04×10^9	6.46×10^{14}	2.54×10^{14}
2.01×10^9	2.15×10^{14}	8.44×10^{13}
1.21×10^9	1.29×10^{14}	5.08×10^{13}
4.02×10^8	4.30×10^{13}	1.69×10^{13}
2.01×10^8	2.15×10^{13}	8.44×10^{12}

S8 Calculation of the free carrier ratio after photo-excitation

After photoexcitation by the laser pulse, the free carriers and weak coupled excitons actually coexist in the crystal under a thermodynamics equilibrium. The ratio between these two species is a fixed term resembling the ion-electron balance in a hot plasma, which depends strongly on the exciton binding energy as well as the excitation concentration. Therefore, we can use a classic Saha-Langmuir theory to calculate approximately the ratio of the free carriers X (i.e. fraction of the free carriers among all the excited species) in the system:

$$\frac{x^2}{1-x} = \frac{1}{n} \left(\frac{2\pi m k_B T}{h^2} \right)^{1.5} e^{-\frac{E_b}{k_B T}} \quad (12)$$

where E_b refers to the exciton binding energy, m is the exciton effective mass, T is the temperature

and n is the excitation concentration. The following table summarizes the calculated x ratio of the two samples under the excitation condition of the PL decay measurements. Apparently, during our measurement, the majority of the excited species in the 2D perovskite crystals are free carriers and the contribution of the exciton can be mostly neglected.

Table S9. The calculated values of ratio of the free carriers x .

Excitation Intensity (cm^{-3}) of BMAPI	x	Excitation Intensity (cm^{-3}) of BEAPI	x
6.46×10^{14}	0.949	2.54×10^{14}	0.994
2.15×10^{14}	0.982	8.44×10^{13}	0.998
1.29×10^{14}	0.989	5.08×10^{13}	0.999
4.30×10^{13}	0.996	1.69×10^{13}	0.999
2.15×10^{13}	0.998	8.44×10^{12}	0.999

S9. Detailed model of trap filling and fitting process.

The detailed calculation procedures of the model have been described in the reference⁴. In brief, the equilibrium between free carriers and excitons can be described using the Saha equation. When photodoping (i.e accumulated trap filling) is present, the Saha equation can be generalized as the following equation expressing the concentrations of electrons (n_e), holes (n_h) and excitons (n_x) corresponding to the overall untrapped photogenerated species density N :

$$n_h = -\frac{(A - n_T)}{2} + \frac{1}{2}\sqrt{(A + N_T)^2 + 4AN} \quad (2)$$

$$n_e = n_h - n_T \quad (3)$$

where $A = v_x/(v_h v_e) \exp[-E_b/(k_B T)]$, λ_i is the thermal wavelength of the species i and $v_i = \lambda_i^{-3}$, n_T is concentration of filled traps and N_T is the concentration of total traps.

Here, we assume that n_T varies little and is only dependent on the average concentration of electrons $\overline{n_e(t)} = \frac{1}{t_0} \int_0^{t_0} n_e(t) dt$ during the PL recording time t_0 between the repetition pulses. Then, we get the following rate equations:

$$\frac{dn_T}{dt} = R_{pop}(N_T - n_T)\overline{n_e(t)} - R_{dep}(N_T^2 + n_T\overline{n_e(t)}) = 0 \quad (4)$$

where R_{pop} and R_{dep} are the recombination rates of trap population and depopulation, respectively. Taking equations (2) and (3) we can obtain the average concentration of electrons as:

$$\overline{n_e(t)} = \frac{1}{t_0} \int_0^{t_0} n_e(t) dt \approx K(A + n_T), K = \frac{1}{\gamma_0 t_0} \ln \left[1 + \frac{AN(0)}{N_T(A + N_T)} \right] \quad (5)$$

Here $N(0)$ can be simplified as the initial excitation density N_c . γ_0 is the total rate of electronic decay not involving the traps. Substitution of equation (5) into (4) gives:

$$n_T = -\frac{1}{2}\alpha + \frac{1}{2}\sqrt{\alpha^2 + 4\beta N_T} \quad (6)$$

$$\alpha = \frac{[A + R(A - N_T)]}{\left(1 + \frac{1}{K} + R\right)} \quad (7)$$

$$\beta = \frac{RA}{\left(1 + \frac{1}{K} + R\right)} \quad (8)$$

$$K = \frac{1}{\gamma_0 t_0} \ln \left[1 + \frac{AN_c}{N_T(A + N_T)} \right], R = R_{pop}/R_{dep} \quad (9)$$

which are the equations 7~10 in the main text.

During the fitting of the trapping model, we first assume that both traps exhibit filling but due to different trap population and depopulation rates, the ratio of unoccupied trap densities between two type of traps varies with different excitation intensity. Therefore we can plot $A_1/(A_1+A_2) \sim N_c$ data and fit with the expression combination equation 12-14 in the main text.

$$\frac{A_1}{A_1+A_2} = \frac{n_{uncT1}}{n_{uncT1}+n_{uncT2}} = \frac{N_{T1} + \frac{1}{2}\alpha_1 - \frac{1}{2}\sqrt{\alpha_1^2 + 4\beta_1 N_{T1}}}{(N_{T1} + \frac{1}{2}\alpha_1 - \frac{1}{2}\sqrt{\alpha_1^2 + 4\beta_1 N_{T1}}) + (N_{T2} + \frac{1}{2}\alpha_2 - \frac{1}{2}\sqrt{\alpha_2^2 + 4\beta_2 N_{T2}})} \quad (10)$$

Here, n_{uncT1} and n_{uncT2} are the concentrations of filled traps 1 and 2, respectively. N_{T1} and N_{T2} are the original concentrations of trap 1 and trap 2, respectively. In this work, A of BMAPI and BEAPI were calculated as $1.42 \times 10^{15} \text{ cm}^{-3}$ and $5.10 \times 10^{15} \text{ cm}^{-3}$, respectively, the PL recording time t_0 was $2.5 \times 10^{-7} \text{ s}$, and γ_0 was taken as the rate of the charge recombination not contributing to the trap filling process (i.e. the slow component in the PL kinetics, as shown in Table S6 and S7). We first set all the four fitting parameters (N_{T1} , N_{T2} , R_1 , and R_2) while analyzing these two compounds. The best fitting results are shown in Table S9. In this table, R_2 of BMAPI and BEAPI are 34.8 and 41.1, respectively. Considering that R is the ratio between trap population and

depopulation rates, we can then estimate the depopulation time of their traps 2 using the trap population time obtained in the PL kinetics (from the lifetime of the second component ~9 and ~4 ns, respectively) to be ~313 and ~165 ns, respectively. These depopulation time of traps 2 are not much different from the interval between the pulses in our measurement (250 ns). Therefore we conclude that no considerable trap filling should occur in their traps 2 since the depopulation rate is too fast.⁵ The model is then modified for the case where trap filling occurs only in trap1 as follows:

$$\frac{A_1}{A_1+A_2} = \frac{n_{\text{uncT1}}}{n_{\text{uncT1}}+N_{\text{T2}}} = \frac{N_{\text{T1}} + \frac{1}{2}\alpha_1 - \frac{1}{2}\sqrt{\alpha_1^2+4\beta_1N_{\text{T1}}}}{(N_{\text{T1}} + \frac{1}{2}\alpha_1 - \frac{1}{2}\sqrt{\alpha_1^2+4\beta_1N_{\text{T1}}}) + N_{\text{T2}}} \quad (11)$$

Here the $A_1/(A_1+A_2)$ represents the ratio between the unoccupied density of trap 1 and the original density of trap 2. We first set all the three fitting parameters (N_{T1} , N_{T2} , and R) free for the values from the equation (10) as shown in Table S9. Then, we fit the equation (11) to get the new parameters (Table S9).

Table S10. Trap densities obtained from the fitting.

Model	Compounds	R ₁	R ₂	N_{T1} (10 ¹⁵ cm ⁻³)	N_{T2} (10 ¹⁵ cm ⁻³)
				³⁾	
$\frac{A_1}{A_1+A_2} = \frac{n_{\text{uncT1}}}{n_{\text{uncT1}}+n_{\text{uncT2}}}$	BMAPI	1.4×10^5	34.8	6.0	0.08
	BEAPI	5.3×10^4	41.1	7.4	0.18
$\frac{A_1}{A_1+A_2} = \frac{n_{\text{uncT1}}}{n_{\text{uncT1}}+N_{\text{T2}}}$	BMAPI	1.4×10^5	/	21.8	0.11
	BEAPI	5.1×10^4	/	37.6	0.59

Reference

- (1) Spanopoulos, I.; Ke, Wei.; Stoumpos, C. C.; Schueller, E. C.; Kontsevoi, O. Y.; Seshadri, R.; Kanatzidis, M. G. Unraveling the chemical nature of the 3D "hollow" hybrid halide perovskites. *J. Am. Chem. Soc.* **2018**, *140*, 5728–5742.

- (2) Safdari, M.; Fischer, A.; Xu, B.; Kloo, L.; Gardner, J. M. Structure and function relationships in alkylammonium lead(ii) iodide solar cells. *J. Mater. Chem. A* **2015**, *3*, 9201–9207.
- (3) Chen, Z.; Yu, C.; Shum, K.; Wang, J. J.; Pfenninger, W.; Vockic, N.; Midgley, J.; Kenney, J. T. Photoluminescence Study of Polycrystalline CsSnI₃ Thin Films: Determination of Exciton Binding Energy. *J. Lumin.* **2012**, *132*, 345–349.
- (4) Stranks, S. D.; Burlakov, V. M.; Leijtens, T.; Ball, J. M.; Goriely, A.; Snaith, H. J. Recombination Kinetics in Organic-Inorganic Perovskites: Excitons, Free Charge, and Subgap States. *Phys. Rev. Appl.* **2014**, *2*, 034007.
- (5) Zheng, K.; Židek, K.; Abdellah, M.; Messing, M. E.; Al-Marri, M. J.; Pullerits, T. Trap States and Their Dynamics in Organometal Halide Perovskite Nanoparticles and Bulk Crystals. *J. Phys. Chem. C* **2016**, *120*, 3077–3084.

Paper III



Free Carriers versus Self-Trapped Excitons at Different Facets of Ruddlesden–Popper Two-Dimensional Lead Halide Perovskite Single Crystals

Mingli Liang, Weihua Lin, Qian Zhao, Xianshao Zou, Zhenyun Lan, Jie Meng, Qi Shi, Ivano E. Castelli, Sophie E. Canton, Tõnu Pullerits, and Kaibo Zheng*



Cite This: *J. Phys. Chem. Lett.* 2021, 12, 4965–4971



Read Online

ACCESS |



Metrics & More

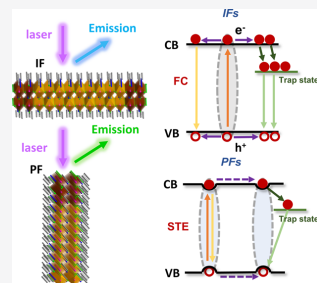


Article Recommendations



Supporting Information

ABSTRACT: The physical origin of sub-band gap photoluminescence in Ruddlesden–Poppers two-dimensional (2D) lead halide perovskites (LHPs) is still under debate. In this paper, we studied the photoluminescence features from two different facets of 2D LHP single crystals: the in-plane facet (IF) containing the 2D inorganic layers and the facet perpendicular to the 2D layers (PF). At the IF, the free carriers (FCs) dominate due to the weak electron–phonon coupling in a symmetric lattice. At the PF, the strain accumulation along the 2D layers enhances the electron–phonon coupling and facilitates self-trapped exciton (STE) formation. The time-resolved PL studies indicate that free carriers (FCs) at the IF can move freely and display the trapping by the intrinsic defects. The STEs at the PF are not likely trapped by the defects due to the reduced mobility. However, with increasing STE density, the STE transport is promoted, enabling the trapping of STE by the intrinsic defects.



In Ruddlesden–Poppers (RP) two-dimensional lead halide perovskites (2D LHPs) $(B)_2(A)_{n-1}Pb_nX_{3n+1}$ (A = small amine cation, B = long chain organic amine cation, X = halides, n = number of octahedral layers), inorganic semiconductor quantum wells (QWs) with a certain thickness (n) are isolated periodically by organic spacing layers. Such a unique microscopic structure induces properties that differ from their 3D counterparts.^{1–6} Currently, one essential topic is to identify the nature of elementary photoexcitations. Wannier excitons are believed to be generated in semiconductor 2D quantum wells due to the dielectric confinement.⁷ 2D perovskites, on the other hand, possess a much softer lattice and more complex vibrational structures due to the intercalation of the organic spacing cations.⁸ Consequently, photoinduced local lattice distortion can occur due to strong electron–phonon coupling leading to the formation of self-trapped excitons (STEs).^{9–12} One fingerprint of such an STE is a broad sub-bandgap emission with a large Stokes shift.¹³ However, such emissions depend on the sample parameters such as n values and molecular composition.¹⁴ A recent photoluminescence (PL) microscopic study on single 2D perovskite flakes even disagrees with the assignment of the broad emission to STE.¹⁵ The photophysics in the 2D perovskites have also been reported as modulated by the local structures. Low-energy emission was observed specifically from the edge of single-crystal (SC) flakes interpreted by the formation of low energy edge states (LES).¹⁶ DFT calculations indicate that the formation of such LES is induced by the asymmetric relaxation of the interface strain that triggers the

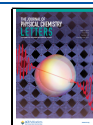
surface reorganization.^{17,18} In this regard, the photogenerated species in the bulk volume and at the edge area can be different due to the difference in local electronic structures. Therefore, identifying the photogenerated species and clarifying the corresponding dynamics within various local structures is essential to characterize the actual photophysics in 2D perovskite materials.

In this paper, we investigate the emissive state dynamics to identify the photogenerated species at two different surface facets of 2D RP lead bromide perovskite corresponding to in-plane facets (IFs) and perpendicular facets (PFs) to the 2D inorganic lattice layers, respectively. Single crystals with three spacing cations [i.e., iso-butylamine (iso-BA), *n*-butylamine (*n*-BA), and *n*-pentylamine (*n*-PA)] have been studied. The temperature-dependent PL measurements indicate that STEs are dominant at the PF while free carriers (FC) are generated at the IF. The STE formation is strongly affected by the spacing cations. Furthermore, the time-resolved PL study reveals that the STEs at the PFs are less mobile than the FCs at the IFs and exempt from the intrinsic defect state trapping. However, when the excitation density is increased, the large

Received: April 10, 2021

Accepted: May 18, 2021

Published: May 20, 2021



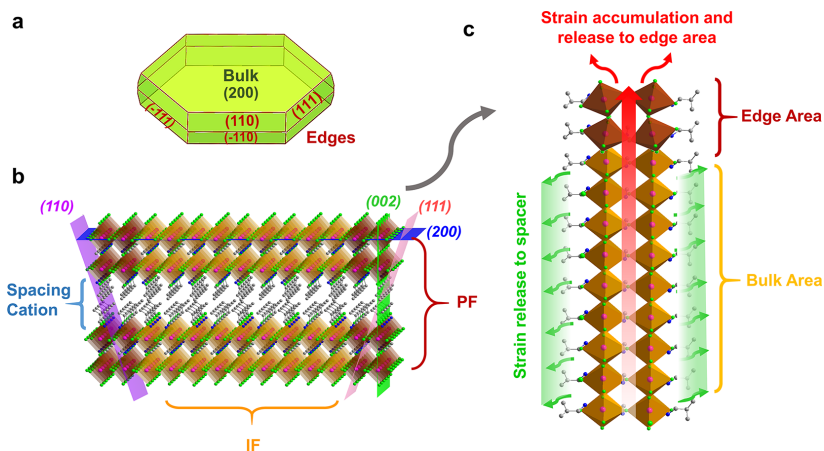


Figure 1. Macroscopic morphology of a 2D RP perovskite crystal (a), which is simulated by Mercury based on our structural data in the Supporting Information; schematics showing the definition of IF and PF (b) and the directions of strain accumulation and release (c).

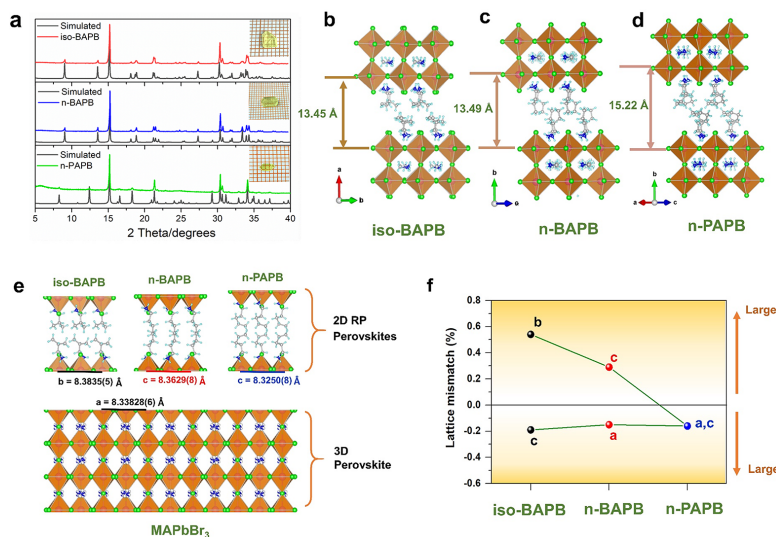


Figure 2. Powder XRD patterns of iso-BAPB, *n*-BAPB, and *n*-PAPB SCs (inset: optical pictures of the three SCs with the size of each red grid in the background being 1 mm × 1 mm) (a); 2D layered structures of iso-BAPB (b), *n*-BAPB (c), and *n*-PAPB (d); the changes of the lattice constants on the 2D layered facets compared to that of 3D MAPbBr₃ (*I4/mcm*) (e); lattice mismatch between the three 2D RP perovskites and the 3D MAPbBr₃ lattice; and the two points of each sample representing two directions on the 2D layered facets (f).

STE concentration facilitates the STE transport. The STEs are therefore more likely to be captured by the intrinsic trap states. Our results confirmed the photogenerated species strongly depend on the local structures in 2D perovskites which leads to distinct photophysical behaviors.

According to the DFT calculation, the LES in 2D RP perovskites are mainly induced by the relaxation of the interface strain along the 2D inorganic layer nucleating the surface reorganization, while such strain along the direction perpendicular to the 2D layer can be released by the spacing

cations.¹⁷ Here, as demonstrated by an example structure of as-obtained (B)₂(A)_{*n*-1}Pb_{*n*}X_{3*n*+1} (*n* = 2) (Figure 1), the PbX₆ octahedra are extended by the cocorner links along the (200) facet forming the largest crystal facet in the macroscopic crystal. The crystals grow slowly along the (002), (110), and (111) facets due to the superimposed organic spacing layers and the inorganic QWs leading to small crystal facets (Figure 1a,b). The lattice strain along the direction vertical to the (200) facet can be released into the organic spacing cations (Figure 1c). Thus, we can consider the (200) surface facet

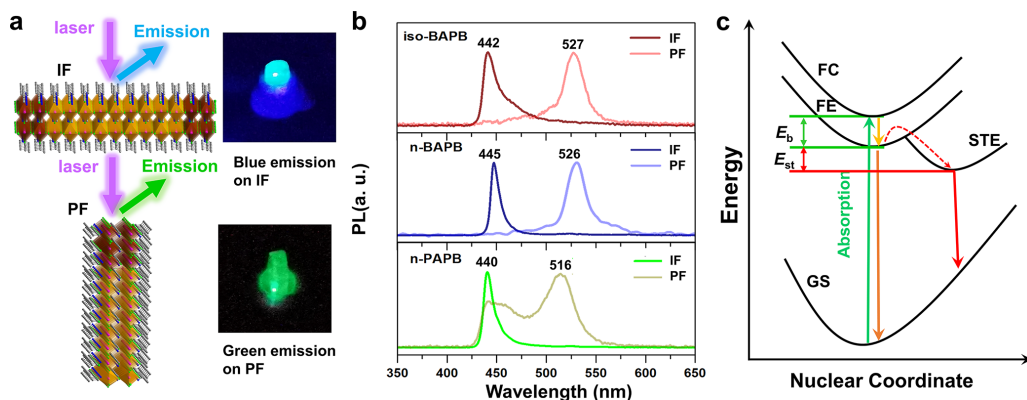


Figure 3. Schematics of PL measurements and the pictures of blue emission on IF and green emission on PF of the SC (a); PL spectra of PF and IF of the three SCs (b) and the schematic of the energy level structure of STE (c) (FC is the free carrier state; FE is the free exciton state; GS is the ground state; E_{st} is self-trapping energy).

identical to a bulk-like structure. On the other hand, the lattice strain continuously accumulates along the (002), (110), and (111) directions and releases at the surface boundary. Therefore, the surface lattice structure along these directions should be different from the inner bulk structure, resulting in the so-called edge area where LES are found (Figure 1c).¹⁶

Since the LES formation is induced by the accumulation and relaxation of strain-related elastic energy, spacing cations are expected to play a critical role in modulating the LES.^{19,20} Therefore, by changing the spacing cations, we can expect to facilitate or diminish the LES formation. In this work, we have synthesized three 2D perovskites SCs with various spacing cations, (iso-BA)₂(MA)Pb₂Br₇ (iso-BAPB), (n-BA)₂(MA)Pb₂Br₇ (n-BAPB), and (n-PA)₂(MA)Pb₂Br₇ (n-PAPB) (for experimental details and characterizations, see Supporting Information Section S1). They all belong to the typical 2D RP phase perovskites (B)₂(A)_{n-1}Pb_nX_{3n+1} with $n = 2$. The powder XRD patterns of the crystal in Figure 2a all exhibited perfect 2D layered structure as illustrated in Figure 2b–d. Crystallographic analysis shows that the lattice of n-BAPB is the least distorted while storing the strain-related elastic energy to the largest extent, whereas that of n-PAPB is the most distorted when relaxing the interface lattice strain (for the details of the structural analysis, see Supporting Information Section S2). In order to evaluate the strain accumulation along the 2D layered facets for three SCs, we calculated the internal lattice mismatch by simplifying the 2D structures as the bulk 3D lattice connected to a 2D LHP layer at the interface of the quantum wells (Figure 2e, for the details of mismatch calculation, see Supporting Information Section S3).^{21,22} As shown in Figure 2f, the internal lattice mismatch of n-PAPB is much smaller than those of the other two samples, leading to a smaller elastic energy and consequently less pronounced LES formation on the PFs.

Afterward, we measure the steady-state PL spectra at both PF and IF of the three SCs as discussed above (Figure 3a). The configuration of the PL measurement ensures the signals are solely contributed by the incident beam area at the surface of each facet (for the details of the method, see Supporting Information Sections S1 and S4). As shown in Figure 3b, the emissions from different facets in iso-BAPB and n-BAPB

exhibit clear single bands, but the PL at the PF drastically red shifts compared to that of the IF by 85 nm (~ 0.45 eV) and 82 nm (~ 0.43 eV), respectively. In n-PAPB, two emission peaks occur at the PF, while the low-energy emission is less red-shifted (75 nm, ~ 0.41 eV) compared with the other two samples.

The difference in the PL emissions at the two facets cannot be merely explained by static lattice distortion since the energy shift (i.e., 0.4–0.45 eV) is much larger than what the octahedral distortion-induced bandgap modification can provide.²³ The origin of the low-energy emission in 2D RP LHPs which is especially pronounced at the “edge” of the grains or crystals has been frequently debated in recent years. We can first exclude the formation of the 3D phase claimed in some recent studies since no 3D phase can be observed in the powder XRD characterization of the ground crystals (Figure S1).^{24,25} In the following, we will also exhibit that the photophysics at the PFs are different from that in conventional bulk 3D perovskites. The red-shifted emission is usually assigned to STEs. Figure 3c is a schematic of the energy level structure of STE, in which, once electrons and holes are photogenerated, they will quickly self-trap from a mobile state to a more stable self-trapped state. Here the self-trapping energy (E_{st}) is defined as the energy loss of exciton in this process.¹² However, recent PL microscopy studies argued that the low-energy emission in 2D RP LHPs should be more related to the mid-band gap trap states trapping the diffusing FEs (free excitons).¹⁵

In order to clarify the physical process, we conducted temperature-dependent PL measurements at the IFs and PFs with temperatures from 100 to 280 K for three samples (Figure S7). For n-PAPB, the PL intensity of the IF decreases with increasing temperature due to the dissociation of the excitons into free charges. On the other hand, the dual emission peaks occur all over the temperature region at the PF, whereas the respective fraction of high-energy PL becomes more dominant at low temperature. This phenomenon is against the traditional exciton trapping mechanism where the emissions from the trap state and band-edge exciton states are competing and modulated by the thermal equilibrium between the trapping and detrapping of the excited carriers. Therefore, we believe

the emission at the PF should be attributed to STEs formed by Fröhlich interaction as shown in Figure 3c, which decreases at low temperature.²⁶ On the other hand, at lower temperature the energy barrier between the FE and the STE states will hinder the self-trapping and promote the band-edge emission (Figure 3c). The PL spectra at PF of *n*-BAPB and iso-BAPB only contain the low-energy emission with the absence of band-edge emission regardless of the temperature, indicating no deactivation from STE to FE in those samples (i.e., larger E_{st}).

In order to further verify our argument, we calculate the electron–phonon coupling strength from the fwhm's of the temperature-dependent PL spectra using the model in refs 26 and 27, and the line width parameters are shown in Table 1

Table 1. Extracted Line Width Parameters from the Temperature Dependent PL Measurement

IFs	Γ_0 (meV)	γ_{LO} (meV)	E_{LO} (meV)
iso-BAPB	69.1	251.5	49.5
<i>n</i> -BAPB	61.3	359.9	45.1
<i>n</i> -PAPB	56.1	218.3	50.3
PFs	Γ_0 (meV)	γ_{LO} (meV)	E_{LO} (meV)
iso-BAPB	94.8	452.5	63.1
<i>n</i> -BAPB	101.1	434.1	60.3
<i>n</i> -PAPB	127.5	233.4	49.6

(for the details of the analysis, see Supporting Information Section S5). The fitted values of energy representative of the frequency for the weakly dispersive LO phonon branch (E_{LO}) are much larger than those of the vibration mode of Pb–Br stretching (18 meV), which is believed to dominate the Fröhlich interaction in 3D perovskites.^{26,28} In 2D RP perovskites, however, E_{LO} only provides an effective value, which should not be associated with specific phonon modes due to the complex vibrational structure.^{29–31} The vibrational modes of tens of millielectronvolts usually correspond to the rotation or bending of large molecular moieties (e.g., NH_4^+).⁹ More importantly, the coupling strength γ_{LO} at the PFs are larger than those at the IFs in three samples except for *n*-PAPB. The stronger PF electron–phonon (e–ph) coupling drives the formation of STE in our 2D perovskite SCs. In addition, the relatively weaker coupling of excitons or charge carriers with lattice deformation at the PF of *n*-PAPB explains the less stabilized STE as mentioned above. We noticed that the bandwidth of such STE emission is still much narrower than conventional observation in 2D perovskites or other polaronic semiconductors.^{32,33} The narrowing of the STE emission here can be due to two factors: (1) relative weaker e–ph coupling at the PF of our SCs compared with traditional polaronic materials and/or (2) that the vibration energy of the above-mentioned large molecular moieties that contributes to the e–ph coupling should be less varied by the surrounding coordination compared with Pb–Br stretching vibration.

In order to further distinguish the photophysics at the IFs and PFs, we studied the PL dynamics at the two facets of the three samples (Figure 4a–f) with the corresponding excited state dynamic demonstrated in Figure 4g–i. Figure 4a shows the PL lifetime at the PF is longer than at the IF (for detailed fitting analysis of the PL decays, see Supporting Information Section S6). In addition, the PL lifetimes of the in-plane state increase with the excitation intensity as illustrated in Figure 4b. This behavior has been explained by trap filling/accumulation

(Figure 4g), which is widely observed in 2D and 3D perovskite single and microcrystals.^{34,35} We can obtain trap density of the IFs to be $2.9 \times 10^{16} \text{ cm}^{-3}$ by globally fitting the intensity-dependent PL kinetics using a dynamic trap-filling model (for the details of the model, see Supporting Information Section S7).³⁶ More importantly, such behavior indicates that the initial photogenerated species at the IFs are free carriers moving along the perovskite lattices until filling a trap. In fact, we can estimate the fraction of free carriers in the photogenerated species using the Saha–Langmuir theory between 84% to 99% at the IFs of our samples (for details, see Supporting Information Section S8). On the contrary, the PL decay becomes faster with the increasing excitation intensity at the PFs, indicating a different charge recombination process (Figure 4c). We can first exclude the occurrence of any high order recombination because the intensity of the PL decay at time zero (PL_0) exhibits a linear dependence on the excitation intensity, as shown in the inset pictures of Figure 4d–f. As PL_0 reflected the population of all the spontaneous emission before any trapping or the Auger process, such linearity manifests the monomolecular recombination mode of the photoexcited species.³⁷ The deviation of the intensity-dependent PL kinetics at the PF can be well interpreted by the STE model. Unlike in 3D perovskite or IFs in 2D perovskite where the electron–phonon coupling generates mainly a large polaron, a larger degree of lattice distortion at the PFs of 2D perovskites tends to form small polarons that move through site-to-site hopping.^{36,38} The intrinsic trap density of the *n*-BAPB SCs calculated above provides a mean interval distance among the trap states to be 32 nm. It is difficult for the STE at the PFs to transport to the trap state at low excitation density and undergo a trapping process due to the reduced mobility after self-trapping. Therefore, the dominant excited state depopulation pathway is the STE radiative recombination as shown in Figure 4h. With the increase of the excitation intensity, the relative PL_{QY} at the PFs also decreases, indicating that extra carrier trapping has been introduced at a high excitation density (Table S8 and Figure S10). We believe it can be attributed to the enhanced motion of the STEs to be trapped by the defect states as illustrated in Figure 4i. Two possible interpretations can be provided: (1) The stability of the STE can be decreased by the increasing density.³⁹ Therefore, more STEs can be dissociated into FEs or free carriers. (2) A larger STE density may increase the carrier mobility due to the collective polaron behavior, which is widely observed in OPV materials and graphene.^{40,41} In iso-BAPB, however, the PL decay remains independent of excitation intensity. One possible reason is the larger trap density in iso-BAPB SCs (for a detailed calculation, see Supporting Information Section S7). In addition, we noticed the efficient exciton dissociation has been reported at the edge area for *n*-BA based 2D RP iodide perovskites,^{6,9,42} which deviates from our conclusion. We believe this is due to the higher bulk modulus and larger lattice polarity of the Br-based perovskites that enhanced the local strain accumulation and phonon coupling, respectively (for detailed analysis, see Supporting Information Section S9). Both factors facilitate the STE formation.

In conclusion, we investigated the local structure and PL dynamics at different surface facets (IF and PF) of 2D RP lead bromide perovskite SCs with three spacing cations (i.e., *n*-BA, iso-BA, and *n*-PA). The PL spectra at the IF of three SCs exhibit typical pure band-edge emission bands, while the

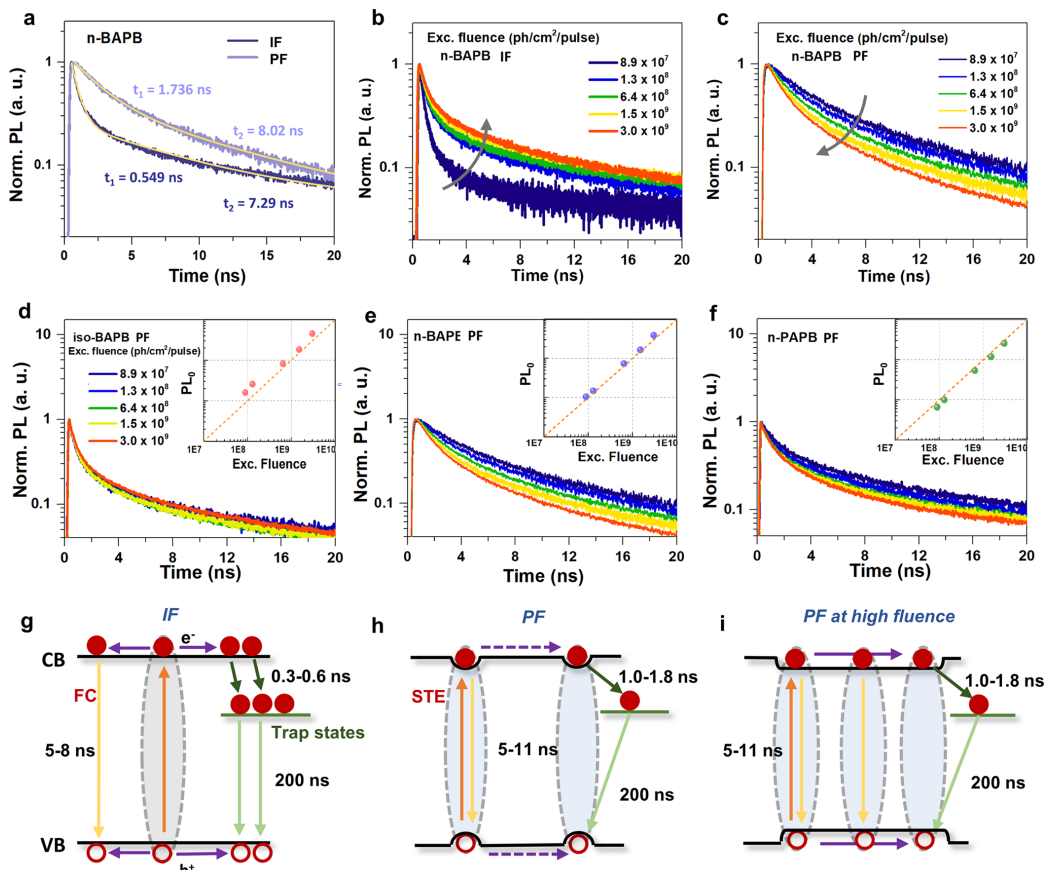


Figure 4. TRPL kinetics of IFs and PFs of *n*-BAPB (a–c) and TRPL kinetics with different excitation fluences for the PFs of these three SCs (d–f). Insets: initial PL intensity change with fluence. Illustrations of the charge recombination processes in these three SCs (g–i).

emission at the PF is drastically red-shifted. In addition, at the PF of *n*-PAPB, the band edge emission and the red-shifted emission occur concurrently. The temperature-dependent PL study at two facets indicates that the low-energy emission at PF should be attributed to the STE due to larger electron–LO phonon coupling strength compared with IFs. The dual emission bands in *n*-PAPB can be explained by the lower self-trapping energy, which is consistent with the structural analysis. In addition, we find the PL decays become slower with the increasing excitation density at the IFs with opposite behavior at PFs. This can be well interpreted by the different photophysics of photogenerated FCs at the IF and STEs at the PF. Our findings confirmed the origin of the LES in 2D RP perovskites to be the STE. The STE formation is also strongly influenced by the spacing cations in the 2D lattice. That conclusion can guide materials engineering and device applications in the future.

■ ASSOCIATED CONTENT

Supporting Information

The Supporting Information is available free of charge at <https://pubs.acs.org/doi/10.1021/acs.jpcllett.1c01148>.

Experimental details and characterizations, crystallographic data, values of Pb–Br bond distances and Br–Pb–Br bond angles, TRPL kinetic study, details about calculations of lattice distortion parameters, lattice mismatch, penetration depths, electron–phonon coupling strength, and trap densities (PDF)

Crystallographic information file for iso-BAPB (CIF)

Crystallographic information file for *n*-BAPB (CIF)

Crystallographic information file for *n*-PAPB (CIF)

■ AUTHOR INFORMATION

Corresponding Author

Kaibo Zheng – Department of Chemistry, Technical University of Denmark, DK-2800 Kongens Lyngby, Denmark; Chemical Physics and NanoLund, Lund

University, 22100 Lund, Sweden; orcid.org/0000-0002-7236-1070; Email: kzheng@kemi.dtu.dk

Authors

- Mingli Liang** – Department of Chemistry, Technical University of Denmark, DK-2800 Kongens Lyngby, Denmark; orcid.org/0000-0002-1854-7026
- Weihua Lin** – Chemical Physics and NanoLund, Lund University, 22100 Lund, Sweden
- Qian Zhao** – Department of Chemistry, Technical University of Denmark, DK-2800 Kongens Lyngby, Denmark
- Xianshao Zou** – Chemical Physics and NanoLund, Lund University, 22100 Lund, Sweden
- Zhenyun Lan** – Department of Energy Conversion and Storage, Technical University of Denmark, DK-2800 Kongens Lyngby, Denmark; orcid.org/0000-0001-7943-5936
- Jie Meng** – Department of Chemistry, Technical University of Denmark, DK-2800 Kongens Lyngby, Denmark; orcid.org/0000-0002-3813-5221
- Qi Shi** – Chemical Physics and NanoLund, Lund University, 22100 Lund, Sweden
- Ivano E. Castelli** – Department of Energy Conversion and Storage, Technical University of Denmark, DK-2800 Kongens Lyngby, Denmark; orcid.org/0000-0001-5880-5045
- Sophie E. Canton** – European XFEL, 22869 Schenefeld, Germany; orcid.org/0000-0003-4337-8129
- Tõnu Pullerits** – Chemical Physics and NanoLund, Lund University, 22100 Lund, Sweden; orcid.org/0000-0003-1428-5564

Complete contact information is available at: <https://pubs.acs.org/10.1021/acs.jpclett.1c01148>

Notes

The authors declare no competing financial interest.

ACKNOWLEDGMENTS

This work was supported by the Independent Research Fund Denmark-Sapere Aude starting grant (No. 7026-00037A), Swedish Research Council VR starting grant (No. 201705337), Crafood foundation (No. 20200522), Swedish Energy Agency research grant, Research Fund for International Young Scientists from NSFC, China (No. 21950410515), and the Chinese Scholarship Council for the Ph.D. scholarship to M.L., W.L., Q.Z., Z.L., and J.M.

REFERENCES

- (1) Chen, Y.; Sun, Y.; Peng, J.; Tang, J.; Zheng, K.; Liang, Z. 2D Ruddlesden-Popper Perovskites for Optoelectronics. *Adv. Mater.* **2018**, *30* (2), 1703487.
- (2) Savenije, T. J.; Ponceca, C. S., Jr.; Kunneman, L.; Abdellah, M.; Zheng, K.; Tian, Y.; Zhu, Q.; Canton, S. E.; Scheblykin, I. G.; Pullerits, T.; et al. Thermally Activated Exciton Dissociation and Recombination Control the Carrier Dynamics in Organometal Halide Perovskite. *J. Phys. Chem. Lett.* **2014**, *5* (13), 2189–94.
- (3) Stoumpos, C. C.; Cao, D. H.; Clark, D. J.; Young, J.; Rondinelli, J. M.; Jang, J. I.; Hupp, J. T.; Kanatzidis, M. G. Ruddlesden-Popper Hybrid Lead Iodide Perovskite 2D Homologous Semiconductors. *Chem. Mater.* **2016**, *28* (8), 2852–2867.
- (4) Zheng, K.; Pullerits, T. Two Dimensions Are Better for Perovskites. *J. Phys. Chem. Lett.* **2019**, *10* (19), 5881–5885.
- (5) Mao, L.; Stoumpos, C. C.; Kanatzidis, M. G. Two-Dimensional Hybrid Halide Perovskites: Principles and Promises. *J. Am. Chem. Soc.* **2019**, *141* (3), 1171–1190.

- (6) Tsai, H.; Nie, W.; Blancon, J. C.; Stoumpos, C. C.; Asadpour, R.; Harutyunyan, B.; Neukirch, A. J.; Verduzco, R.; Crochet, J. J.; Tretiak, S.; et al. High-Efficiency Two-Dimensional Ruddlesden-Popper Perovskite Solar Cells. *Nature* **2016**, *536* (7616), 312–316.
- (7) Blancon, J. C.; Stier, A. V.; Tsai, H.; Nie, W.; Stoumpos, C. C.; Traore, B.; Pedesseau, L.; Kepenekian, M.; Katsutani, F.; Nae, G. T.; et al. Scaling Law for Excitons in 2D Perovskite Quantum Wells. *Nat. Commun.* **2018**, *9* (1), 2254.
- (8) Straus, D. B.; Kagan, C. R. Electrons, Excitons, and Phonons in Two-Dimensional Hybrid Perovskites: Connecting Structural, Optical, and Electronic Properties. *J. Phys. Chem. Lett.* **2018**, *9* (6), 1434–1447.
- (9) Straus, D. B.; Hurtado Parra, S.; Iotov, N.; Gebhardt, J.; Rappe, A. M.; Subotnik, J. E.; Kikkawa, J. M.; Kagan, C. R. Direct Observation of Electron-Phonon Coupling and Slow Vibrational Relaxation in Organic-Inorganic Hybrid Perovskites. *J. Am. Chem. Soc.* **2016**, *138* (42), 13798–13801.
- (10) Srimath Kandada, A. R.; Silva, C. Exciton Polarons in Two-Dimensional Hybrid Metal-Halide Perovskites. *J. Phys. Chem. Lett.* **2020**, *11* (9), 3173–3184.
- (11) Guo, Z.; Wu, X.; Zhu, T.; Zhu, X.; Huang, L. Electron-Phonon Scattering in Atomically Thin 2D Perovskites. *ACS Nano* **2016**, *10* (11), 9992–9998.
- (12) Li, S.; Luo, J.; Liu, J.; Tang, J. Self-Trapped Excitons in All-Inorganic Halide Perovskites: Fundamentals, Status, and Potential Applications. *J. Phys. Chem. Lett.* **2019**, *10* (8), 1999–2007.
- (13) Smith, M. D.; Karunadasa, H. I. White-Light Emission from Layered Halide Perovskites. *Acc. Chem. Res.* **2018**, *51* (3), 619–627.
- (14) Cortecchia, D.; Neutzner, S.; Srimath Kandada, A. R.; Mosconi, E.; Meggiolaro, D.; De Angelis, F.; Soci, C.; Petrozza, A. Broadband Emission in Two-Dimensional Hybrid Perovskites: The Role of Structural Deformation. *J. Am. Chem. Soc.* **2017**, *139* (1), 39–42.
- (15) Kahmann, S.; Tekelenburg, E. K.; Duim, H.; Kammberg, M. E.; Loi, M. A. Extrinsic Nature of The Broad Photoluminescence in Lead Iodide-Based Ruddlesden-Popper Perovskites. *Nat. Commun.* **2020**, *11* (1), 2344.
- (16) Blancon, J.-C.; Tsai, H.; Nie, W.; Stoumpos, C. C.; Pedesseau, L.; Katan, C.; Kepenekian, M.; Soe, C. M. M.; Appavoo, K.; Sfeir, M. Y.; Tretiak, S.; et al. Extremely Efficient Internal Exciton Dissociation through Edge States in Layered 2D Perovskites. *Science* **2017**, *355*, 1288–1292.
- (17) Kepenekian, M.; Traore, B.; Blancon, J. C.; Pedesseau, L.; Tsai, H.; Nie, W.; Stoumpos, C. C.; Kanatzidis, M. G.; Even, J.; Mohite, A. D.; et al. Concept of Lattice Mismatch and Emergence of Surface States in Two-dimensional Hybrid Perovskite Quantum Wells. *Nano Lett.* **2018**, *18* (9), 5603–5609.
- (18) Wang, K.; Wu, C.; Jiang, Y.; Yang, D.; Wang, K.; Priya, S. Distinct Conducting Layer Edge States in Two-Dimensional (2D) Halide Perovskite. *Sci. Adv.* **2019**, *5*, eaau3241.
- (19) Fu, Y.; Hautzinger, M. P.; Luo, Z.; Wang, F.; Pan, D.; Aristov, M. M.; Guzei, I. A.; Pan, A.; Zhu, X.; Jin, S. Incorporating Large A Cations into Lead Iodide Perovskite Cages: Relaxed Goldschmidt Tolerance Factor and Impact on Exciton-Phonon Interaction. *ACS Cent. Sci.* **2019**, *5* (8), 1377–1386.
- (20) Liang, M.; Lin, W.; Lan, Z.; Meng, J.; Zhao, Q.; Zou, X.; Castelli, I. E.; Pullerits, T.; Canton, S. E.; Zheng, K. Electronic Structure and Trap States of Two-Dimensional Ruddlesden-Popper Perovskites with the Relaxed Goldschmidt Tolerance Factor. *ACS Appl. Elect. Mater.* **2020**, *2* (5), 1402–1412.
- (21) Stiff-Roberts, A. D. Quantum-Dot Infrared Photodetector. *Materials Science and Materials Engineering* **2011**, *6*, 452–485.
- (22) López, C. A.; Martínez-Huerta, V. M.; Alvarez-Galván, M. C.; Kayser, P.; Gant, P.; Castellanos-Gomez, A.; Fernández-Díaz, M. T.; Fauth, F.; Alonso, J. A. Elucidating the Methylammonium (MA) Conformation in MAPbBr₃ Perovskite with Application in Solar Cells. *Inorg. Chem.* **2017**, *56* (22), 14214–14219.
- (23) Jaffe, A.; Lin, Y.; Beavers, C. M.; Voss, J.; Mao, W. L.; Karunadasa, H. I. High-Pressure Single-Crystal Structures of 3D Lead-

Halide Hybrid Perovskites and Pressure Effects on their Electronic and Optical Properties. *ACS Cent. Sci.* **2016**, *2* (4), 201–209.

(24) Qin, Z.; Dai, S.; Gajjala, C. C.; Wang, C.; Hadjiev, V. G.; Yang, G.; Li, J.; Zhong, X.; Tang, Z.; Yao, Yan.; et al. Spontaneous Formation of 2D/3D Heterostructures on the Edges of 2D Ruddlesden–Popper Hybrid Perovskite Crystals. *Chem. Mater.* **2020**, *32* (12), 5009–5015.

(25) Wang, C.; Wang, Y.; Su, X.; Hadjiev, V. G.; Dai, S.; Qin, Z.; Calderon Benavides, H. A.; Ni, Y.; Li, Q.; Jian, J.; et al. Extrinsic Green Photoluminescence from the Edges of 2D Cesium Lead Halides. *Adv. Mater.* **2019**, *31*, 1902492.

(26) Wright, A. D.; Verdi, C.; Milot, R. L.; Eperon, G. E.; Perez-Osorio, M. A.; Snaith, H. J.; Giustino, F.; Johnston, M. B.; Herz, L. M. Electron-Phonon Coupling in Hybrid Lead Halide Perovskites. *Nat. Commun.* **2016**, *7*, 11755.

(27) Shi, Q.; Ghosh, S.; Kumar, P.; Folkers, L. C.; Pal, S. K.; Pullerits, T.; Karki, K. J. Variations in the Composition of the Phases Lead to the Differences in the Optoelectronic Properties of MAPbBr₃ Thin Films and Crystals. *J. Phys. Chem. C* **2018**, *122* (38), 21817–21823.

(28) Lao, X.; Yang, Z.; Su, Z.; Bao, Y.; Zhang, J.; Wang, X.; Cui, X.; Wang, M.; Yao, X.; Xu, S. Anomalous Temperature-Dependent Exciton–Phonon Coupling in Cesium Lead Bromide Perovskite Nanosheets. *J. Phys. Chem. C* **2019**, *123* (8), 5128–5135.

(29) Ziegler, J. D.; Zipfel, J.; Meisinger, B.; Menahem, M.; Zhu, X.; Taniguchi, T.; Watanabe, K.; Yaffe, O.; Egger, D. A.; Chernikov, A. Fast and Anomalous Exciton Diffusion in Two-Dimensional Hybrid Perovskites. *Nano Lett.* **2020**, *20* (9), 6674–6681.

(30) Urban, J. M.; Chehade, G.; Dyksik, M.; Menahem, M.; Surrente, A.; Trippé-Allard, G.; Maude, D. K.; Garrot, D.; Yaffe, O.; Deleporte, E.; et al. Revealing Excitonic Phonon Coupling in (PEA)₂(MA)_{n-1}Pb_nI_{3n+1} 2D Layered Perovskites. *J. Phys. Chem. Lett.* **2020**, *11* (15), 5830–5835.

(31) Feldstein, D.; Perea-Causin, R.; Wang, S.; Dyksik, M.; Watanabe, K.; Taniguchi, T.; Plochocka, P.; Malic, E. Microscopic Picture of Electron-Phonon Interaction in Two-Dimensional Halide Perovskites. *J. Phys. Chem. Lett.* **2020**, *11* (23), 9975–9982.

(32) Dohner, E. R.; Hoke, E. T.; Karunadasa, H. I. Self-Assembly of Broadband White-Light Emitters. *J. Am. Chem. Soc.* **2014**, *136* (5), 1718–21.

(33) Thirumal, K.; Chong, W. K.; Xie, W.; Ganguly, R.; Muduli, S. K.; Sherburne, M.; Asta, M.; Mhaisalkar, S.; Sum, T. C.; Soo, H. S.; et al. Morphology-Independent Stable White-Light Emission from Self-Assembled Two-Dimensional Perovskites Driven by Strong Exciton–Phonon Coupling to the Organic Framework. *Chem. Mater.* **2017**, *29* (9), 3947–3953.

(34) Zheng, K.; Zidek, K.; Abdellah, M.; Messing, M. E.; Al-Marri, M. J.; Pullerits, T. Trap States and their Dynamics in Organometal Halide Perovskite Nanoparticles and Bulk Crystals. *J. Phys. Chem. C* **2016**, *120* (5), 3077–3084.

(35) Stranks, S. D.; Burlakov, V. M.; Leijtens, T.; Ball, J. M.; Goriely, A.; Snaith, H. J. Recombination Kinetics in Organic-Inorganic Perovskites: Excitons, Free Charge, and Subgap States. *Phys. Rev. Appl.* **2014**, *2* (3), 034007.

(36) Miyata, K.; Meggiolaro, D.; Trinh, M. T.; Joshi, P. P.; Mosconi, E.; Jones, S. C.; De Angelis, F.; Zhu, X.-Y. Large Polarons in Lead Halide Perovskites. *Sci. Adv.* **2017**, *3*, No. e1701217.

(37) Zheng, K.; Zhu, Q.; Abdellah, M.; Messing, M. E.; Zhang, W.; Generalov, A.; Niu, Y.; Ribaud, L.; Canton, S. E.; Pullerits, T. Exciton Binding Energy and the Nature of Emissive States in Organometal Halide Perovskites. *J. Phys. Chem. Lett.* **2015**, *6* (15), 2969–2975.

(38) Silva, G. G.; da Cunha, W. F.; de Sousa Junior, R. T.; Almeida Fonseca, A. L.; Ribeiro Júnior, L. A.; e Silva, G. M. Influence of Quasi-Particle Density over Polaron Mobility in Armchair Graphene Nanoribbons. *Phys. Chem. Chem. Phys.* **2018**, *20* (24), 16712–16718.

(39) Seitz, M.; Magdaleno, A. J.; Alcazar-Cano, N.; Melendez, M.; Lubbers, T. J.; Walraven, S. W.; Pakdel, S.; Prada, E.; Delgado-Buscalioni, R.; Prins, F. Exciton Diffusion in Two-Dimensional Metal-Halide Perovskites. *Nat. Commun.* **2020**, *11* (1), 2035.

(40) Ribeiro Junior, L. A.; e Castro, L. L.; de Sousa, L. E.; e Silva, G. M.; de Oliveira Neto, P. H. Concentration Effects on the Thermally-Activated Transport of Polarons in Conducting Polymers. *Chem. Phys. Lett.* **2019**, *716*, 162–166.

(41) Coehoorn, R.; Zhang, L.; Bobbert, P. A.; van Eersel, H. Effect of Polaron Diffusion on Exciton-Polaron Quenching in Disordered Organic Semiconductors. *Phys. Rev. B: Condens. Matter Mater. Phys.* **2017**, *95* (13), 134202.

(42) Kingstein, E. D.; Tsai, H.; Nie, W.; Blancon, J.-C.; Yager, K. G.; Appavoo, K.; Even, J.; Kanatzidis, M. G.; Mohite, A. D.; Sfeir, M. Y. Edge States Drive Exciton Dissociation in Ruddlesden–Popper Lead Halide Perovskite Thin Films. *ACS Materials Lett.* **2020**, *2* (10), 1360–1367.

Free Carriers versus Self-Trapped Excitons at Different Facets of Ruddlesden-Popper Two-Dimensional Lead Halide Perovskite Single Crystals

Mingli Liang[†], Weihua Lin[‡], Qian Zhao[†], Xianshao Zou[‡], Zhenyun Lan[#], Jie Meng[†], Qi Shi[‡], Ivano E. Castelli[#], Sophie E. Canton[^], Tönu Pullerits[‡] and Kaibo Zheng^{*,†,‡}

[†]*Department of Chemistry, Technical University of Denmark, DK-2800 Kongens Lyngby, Denmark;*

[‡]*Chemical Physics and NanoLund, Lund University, Box 124, 22100 Lund, Sweden;*

[#]*Department of Energy Conversion and Storage, Technical University of Denmark, DK-2800 Kongens Lyngby, Denmark;*

[^]*European XFEL, Holzkoppel 4, 22869 Schenefeld, Germany*

*Corresponding Author

Kaibo Zheng: kzheng@kemi.dtu.dk

Supporting Information

S1 Experimental details and characterizations

Materials: PbBr₂ (98 %), methenamine hydrobromide (98 %, MABr), iso-butylamine (99 %, iso-BA), *n*-butylamine (99.5 %, *n*-BA), *n*-pentylamine (99.5 %, *n*-PA), ethanol (99.8%) and hydrobromic acid (HBr, 47 % in water) have been utilized without further treatment. All the chemicals were supplied by Sigma-Aldrich.

Synthesis of long-chain amine bromides: The long-chain amine bromides were manufactured by adding equal stoichiometric ratio of iso-BA, *n*-BA and *n*-PA to dilute aqueous HBr (25% in mixed ethanol and water) under vigorous stirring in an ice-water bath. The white products were acquired by rotary evaporation at 60 °C. After

that, a lot of white crystals of long-chain amine bromides (iso-BABr, *n*-BABr, and *n*-PABr) were obtained by washing three times with ethanol and vacuum drying for 24h.

Synthesis of 2D RPP SCs: (iso-BA)₂(MA)Pb₂Br₇ (iso-BAPB), (*n*-BA)₂(MA)Pb₂Br₇ (*n*-BAPB) and (*n*-PA)₂(MA)Pb₂Br₇ (*n*-PAPB) SCs obtained by the temperature lowering method of PbBr₂ (2.5 mmol), MABr (1.5 mmol), iso-BABr/ *n*-BABr/ *n*-PABr (3.0 mmol) in 5 ml HBr (47 % in water). The mixtures were placed into glass bottles (20 ml). Afterwards, the glass bottles were sealed and stirred at room temperature for 30 minutes to induce yellow precipitates. Completely clear solutions were obtained after reaction for few minutes at 80 °C as a precursor. Bulk SCs were grown from such a solution at a cooling rate of 0.5 °C/day starting from 50 °C.

Characterizations: Single-crystal XRD measurements were performed on SuperNova Dual Wavelength CCD diffractometer (Agilent Technologies, Mo-K α with $\lambda = 0.71073 \text{ \AA}$) at room temperature ($\sim 298 \text{ K}$). Further structural solves and refinements by full-matrix least-squares fitting on F^2 using SHELX-97, the details are similar to our recent work.¹ Crystallographic data and structural refinements for three samples are summarized in Table S1. The Pb-Br bond lengths and Br-Pb-Br angles are listed in Table S2 and S3, respectively. Powder XRD data were collected on a Rigaku MiniFlex 136 II diffractometer using Cu-K α radiation with $\lambda = 1.5406 \text{ \AA}$. In addition, our comparison with 3D MAPbBr₃ perovskite XRD data shows that our samples are pure phases with the absence of 3D MAPbBr₃ impurity (Figure S1). The UV-vis absorption spectra were measured on PerkinElmer (Lambda 1050) with a UV-Vis-NIR absorption spectrophotometer. Steady-state PL spectra were acquired on an Avantes AvaSpec-2048 spectrometer under an excitation wavelength of 375 nm. The time-resolved photoluminescence (TRPL) measurements were performed with time-correlated single-photon counting (TCSPC, PicoHarp) by using a pulsed diode laser (Wavelength: 375 nm; Frequency: 2.5 MHz; Pulse duration: 8 ps) and a fast avalanche photodiode; when measuring TRPL spectra of IFs and PFs, a long-pass filter from 400 nm and a long-pass filter from 470 nm are used, respectively. Figure S2 are the brief set-up schematics of the steady-state PL and the TCSPC spectroscopy. The beam size ($\sim 0.12 \text{ mm}^2$) is much smaller than the area of each faceted surface, ensuring that the PL signals are solely contributed by the incident beam area. During their measurements, we adjusted the angle of the crystal so that the laser could be incident perpendicularly to the different facets.

Table S1. Crystal data and structure determinations of the iso-BAPB, *n*-BAPB and *n*-PAPB.

Samples	iso-BAPB	<i>n</i> -BAPB	<i>n</i> -PAPB
Formula Weight	1154.11	1154.11	1199.20
Space group	<i>Cc</i>	<i>Ccc2</i>	<i>Ccc2</i>
<i>a</i> (Å)	39.173(4)	8.3262(7)	8.3250(6)
<i>b</i> (Å)	8.3835(5)	39.247(4)	42.717(4)
<i>c</i> (Å)	8.3225(5)	8.3629(8)	8.3250(8)
<i>α</i> (deg)	90	90	90
<i>β</i> (deg)	90.789(7)	90	90
<i>γ</i> (deg)	90	90	90
<i>V</i> (Å ³)	2732.9(4)	2732.8(5)	2960.5(4)
<i>Z</i>	4	4	4
<i>μ</i> (Mo <i>Kα</i>) (mm ⁻¹)	22.537	22.538	20.811
GOF on <i>F</i> ²	1.031	1.065	1.046
<i>R</i> ₁ , <i>wR</i> ₂ [<i>I</i> > 2σ(<i>I</i>)] ^a	0.0892, 0.2080	0.0789, 0.1935	0.0633, 0.1406
<i>R</i> ₁ , <i>wR</i> ₂ (all data) ^a	0.1300, 0.2587	0.1235, 0.2231	0.1241, 0.1707

$$^a R_1 = \sum ||F_o| - |F_c|| / \sum |F_o|, wR_2 = \{ \sum w[(F_o)^2 - (F_c)^2]^2 / \sum w[(F_o)^2]^2 \}^{1/2}$$

Table S2. Bond distances (Angstroms) of Pb-Br for the iso-BAPB, *n*-BAPB and *n*-PAPB.

iso-BAPB			
Pb(1)-Br(4)	2.884(5)	Pb(2)-Br(10)	2.951(5)
Pb(1)-Br(9)	2.979(3)	Pb(2)-Br(7)#1	2.981(3)
Pb(1)-Br(9)#1	2.988(3)	Pb(2)-Br(7)	2.992(3)
Pb(1)-Br(3)	3.009(3)	Pb(2)-Br(6)	3.017(3)
Pb(1)-Br(3)#2	3.016(3)	Pb(2)-Br(6)#2	3.025(3)
Pb(1)-Br(5)	3.061(9)	Pb(2)-Br(5)	3.071(9)
<i>n</i> -BAPB			
Pb(1)-Br(6)	2.908(4)	Pb(1)-Br(3)	3.002(8)
Pb(1)-Br(4)	2.968(9)	Pb(1)-Br(3)#2	3.004(6)
Pb(1)-Br(4)#1	2.980(7)	Pb(1)-Br(2)	3.0636(9)
<i>n</i> -PAPB			
Pb(1)-Br(4)	2.890(3)	Pb(1)-Br(3)#2	2.998(6)

Pb(1)-Br(3)	2.925(7)	Pb(1)-Br(5)	3.034(5)
Pb(1)-Br(5)#1	2.967(4)	Pb(1)-Br(2)	3.0697(8)

Symmetry transformations used to generate equivalent atoms:

For iso-BAPB: #1 $x, -y+1, z+1/2$; #2 $x, -y+2, z+1/2$

For n-BAPB: #1 $-x, y, z+1/2$; #2 $-x+1, y, z-1/2$

For n-PAPB: #1 $-x, y, z+1/2$; #2 $-x+1, y, z-1/2$

Table S3. Br-Pb-Br angles (deg) for the iso-BAPB, n-BAPB and n-PAPB.

iso-BAPB			
Br(4)-Pb(1)-Br(9)	90.09(13)	Br(10)-Pb(2)-Br(7)#1	89.54(12)
Br(4)-Pb(1)-Br(9)#1	93.44(13)	Br(10)-Pb(2)-Br(7)	95.31(12)
Br(9)-Pb(1)-Br(9)#1	90.29(3)	Br(7)#1-Pb(2)-Br(7)	90.46(3)
Br(4)-Pb(1)-Br(3)	86.23(12)	Br(10)-Pb(2)-Br(6)	92.08(12)
Br(9)-Pb(1)-Br(3)	89.45(9)	Br(7)#1-Pb(2)-Br(6)	177.21(12)
Br(9)#1-Pb(1)-Br(3)	179.58(13)	Br(7)-Pb(2)-Br(6)	91.65(8)
Br(4)-Pb(1)-Br(3)#2	89.41(12)	Br(10)-Pb(2)-Br(6)#2	86.53(11)
Br(9)-Pb(1)-Br(3)#2	178.21(9)	Br(7)#1-Pb(2)-Br(6)#2	89.15(8)
Br(9)#1-Pb(1)-Br(3)#2	91.45(9)	Br(7)-Pb(2)-Br(6)#2	178.11(14)
Br(3)-Pb(1)-Br(3)#2	88.81(3)	Br(6)-Pb(2)-Br(6)#2	88.68(3)
Br(4)-Pb(1)-Br(5)	174.77(9)	Br(10)-Pb(2)-Br(5)	173.14(13)
Br(9)-Pb(1)-Br(5)	92.33(16)	Br(7)#1-Pb(2)-Br(5)	89.24(16)
Br(9)#1-Pb(1)-Br(5)	91.18(13)	Br(7)-Pb(2)-Br(5)	91.45(13)
Br(3)-Pb(1)-Br(5)	89.16(12)	Br(6)-Pb(2)-Br(5)	88.88(15)
Br(3)#2-Pb(1)-Br(5)	88.03(15)	Br(6)#2-Pb(2)-Br(5)	86.70(13)
n-BAPB			
Br(6)-Pb(1)-Br(4)	91.2(3)	Br(4)#1-Pb(1)-Br(3)#2	176.2(3)
Br(6)-Pb(1)-Br(4)#1	90.4(2)	Br(3)-Pb(1)-Br(3)#2	90.12(6)
Br(4)-Pb(1)-Br(4)#1	90.36(5)	Br(6)-Pb(1)-Br(2)	179.4(6)
Br(6)-Pb(1)-Br(3)	91.2(3)	Br(4)-Pb(1)-Br(2)	89.3(3)
Br(4)-Pb(1)-Br(3)	176.3(2)	Br(4)#1-Pb(1)-Br(2)	89.2(2)
Br(4)#1-Pb(1)-Br(3)	86.9(3)	Br(3)-Pb(1)-Br(2)	88.2(3)
Br(6)-Pb(1)-Br(3)#2	92.0(2)	Br(3)#2-Pb(1)-Br(2)	88.3(2)
Br(4)-Pb(1)-Br(3)#2	92.5(3)		

<i>n</i> -PAPB			
Br(4)-Pb(1)-Br(3)	91.3(3)	Br(5)#1-Pb(1)-Br(5)	89.68(4)
Br(4)-Pb(1)-Br(5)#1	90.1(2)	Br(3)#2-Pb(1)-Br(5)	85.6(3)
Br(3)-Pb(1)-Br(5)#1	94.5(3)	Br(4)-Pb(1)-Br(2)	179.1(4)
Br(4)-Pb(1)-Br(3)#2	90.8(2)	Br(3)-Pb(1)-Br(2)	88.6(3)
Br(3)-Pb(1)-Br(3)#2	90.22(4)	Br(5)#1-Pb(1)-Br(2)	89.0(2)
Br(5)#1-Pb(1)-Br(3)#2	175.2(3)	Br(3)#2-Pb(1)-Br(2)	90.1(2)
Br(4)-Pb(1)-Br(5)	89.7(3)	Br(5)-Pb(1)-Br(2)	90.5(3)
Br(3)-Pb(1)-Br(5)	175.7(2)		

Symmetry transformations used to generate equivalent atoms:

For iso-BAPB: #1 $x, -y+1, z+1/2$; #2 $x, -y+2, z+1/2$

For n-BAPB: #1 $-x, y, z+1/2$; #2 $-x+1, y, z-1/2$

For n-PAPB: #1 $-x, y, z+1/2$; #2 $-x+1, y, z-1/2$

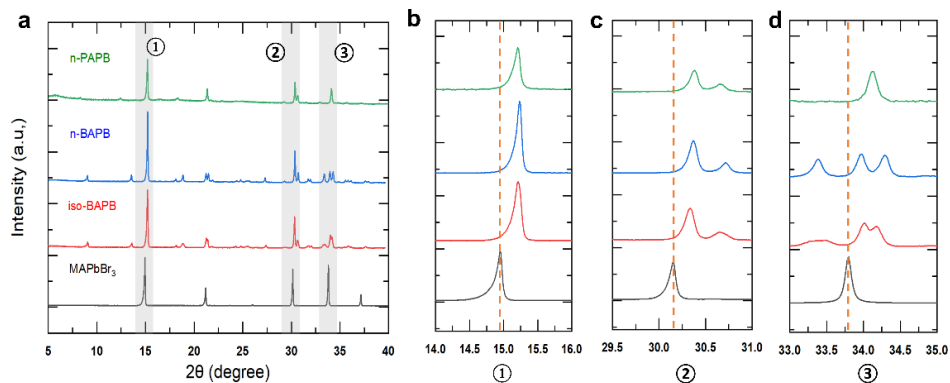


Figure S1. Comparison of powder XRD patterns of our three samples and pure MAPbBr₃ (a); the magnified area corresponding to the three strong peaks (b-d).

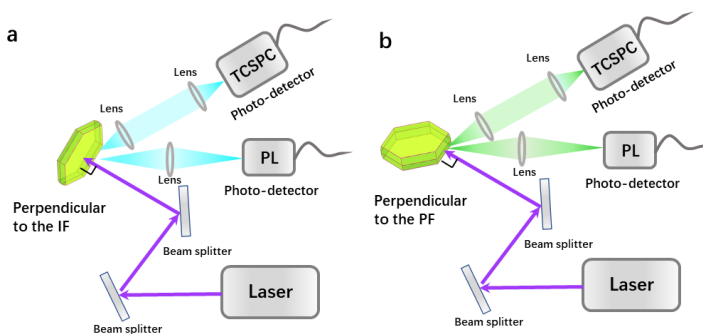


Figure S2. The set-up schematics of PL and TCSPC measurements on IF (a) and PF (b).

S2: Calculations of tilting distortion parameter (Δ), the angle distortion parameter (Σ), and the off-center distortion parameter (Δ_{od}).

When the lone-pair cations (e.g., Sn^{2+} , Pb^{2+} , Bi^{3+} , etc.) and d^0 transition metals (e.g., Nb^{5+} , V^{5+} , Mo^{6+} , etc.) form a polyhedron with oxygen or halide ions, the primary distortive cause can be attributed to second-order Jahn-Teller (SOJT) effects (electronic effects).^{2,3} For instance, Figure S3 is a PbBr_6 octahedron from the iso-BAPB sample of this work, in which the Pb^{2+} deviate from the center position where they should be.

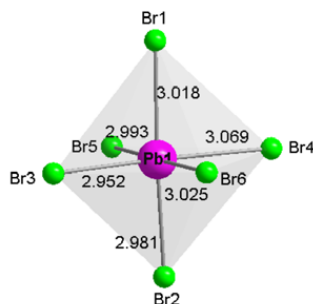


Figure S3. A distorted PbBr_6 octahedron

Herein, we can use three parameters, namely the tilting distortion parameter (Δ), the angle distortion parameter (Σ), and the off-center distortion parameter (Δ_{od}), to quantitatively compare the PbBr_6 octahedral distortions in our iso-BAPB, n-BAPB, and n-PAPB. Δ and Σ represent the distortion degree of the Pb-Br bond lengths and Br-Pb-Br cis-angles, respectively.⁴ Δ_{od} describes the degree of deviation of the Pb atom from the ideal octahedral

center.²The calculation equations for Δ and Σ are listed below (Eq. S1 and Eq. S2). And the calculation method of Δ_{od} are also given in section.

$$\Delta = \sum_{i=1}^6 \left(\frac{d_i - \langle D \rangle}{\langle D \rangle} \right)^2 \quad (S1)$$

$$\Sigma = \sum_{i=1}^{12} |90 - \varphi_i| \quad (S2)$$

where the d_i are the individual Pb-Br bond distances in a the PbBr_6 octahedron. $\langle D \rangle$ is the average Pb-Br bond length, The φ_i are the twelve cis-angles of Br-Pb-Br around the Pb atom.

For the calculation of Δ_{od} , we can first define three trans-bond angles based on Figure S3 as follows: $\theta_1 = \angle \text{Br1-Pb1-Br2}$, $\theta_2 = \angle \text{Br3-Pb1-Br4}$, $\theta_3 = \angle \text{Br5-Pb1-Br6}$. Then, taking the difference in the associated bond lengths and dividing by the cosine of each angle results in the magnitude of the Δ_{od} :²

$$\Delta_{od} = [|(Pb1-Br1) - (Pb2-Br2)| \div |\cos \theta_1|] + [|(Pb1-Br3) - (Pb1-Br4)| \div |\cos \theta_2|] + [|(Pb1-Br5) - (Pb-Br6)| \div |\cos \theta_3|] \quad (S3)$$

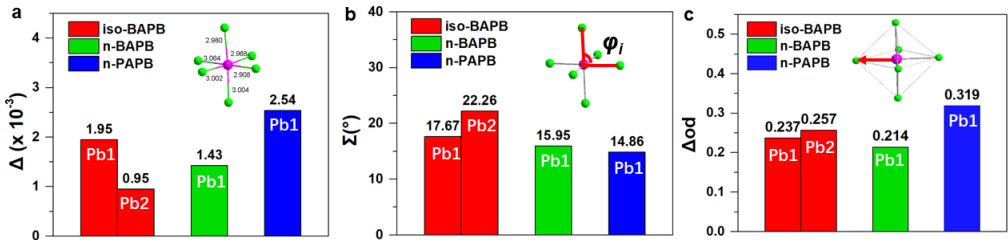


Figure S4 The distorted parameters of PbBr_6 octahedrons, tilting distortion parameter (Δ) (a), the angle distortion parameter (Σ) (b), and the off-center distortion parameter (Δ_{od}) (c).

The calculation results of these three parameters are shown in the Figure S4a-c. It is worth noting that there are two types of Pb^{2+} ions in iso-BAPB (i.e., Pb1 and Pb2) since it crystallizes in a low symmetry monoclinic space group. In this work, we took their average parameter value to represent its PbBr_6 distortion. The distortion analysis revealed that the Δ and Δ_{od} values of n-PAPB are much larger than that of iso-PAPB and n-BAPB. On the other hand, the value of Σ in iso-BAPB is the largest one (19.97°), while the values of n-BAPB (15.95°) and n-PAPB (14.86°) are relatively close. Overall, we can conclude that the PbBr_6 octahedron of n-BAPB is the least distorted, whereas that of n-PAPB is distorted the strongest to relax the interface lattice strain.

S3 Calculation of the lattice mismatch between our three 2D RP perovskites.

The lattice mismatches between our 2D RP perovskites and 3D MAPbBr₃ were calculated by the following equation:⁵

$$f = \frac{(a_{2D} - a_{3D})}{a_{3D}} \times 100\% \quad (S4)$$

where the a_{2D} is the lattice constant along the 2D layered facets, which were taken from the resolved structures by us (Table S1, Figure S5); a_{3D} is the lattice constant of 3D MAPbBr₃ (*I4/mcm*) (Figure S5a).⁶ The calculation results of lattice mismatches were shown in the Figure S5e.

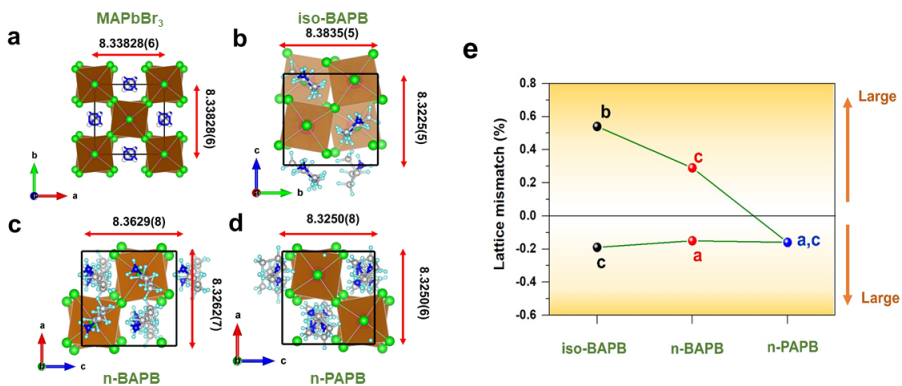


Figure S5, the lattice constants of 3D MAPbBr₃ (*I4/mcm*) (a), and the lattice constants along the 2D layered facets of iso-BAPB (b), *n*-BAPB (c), and *n*-PAPB (d); the lattice mismatch between the three 2D RP perovskites and 3D MAPbBr₃ (f).

S4 Calculations of the penetration depths and excitation density of the three compounds.

To calculate the penetration depths and excitation density of these samples, we first measured their absorption coefficients using the laser. In order to ensure that the laser spot is completely illuminated on the samples, we prepared a sufficiently large film according to the method in the literature.⁷ After the absorption measurements, we used AFM to determine the thickness of the film (Figure S6). The absorbance (*A*) can be calculated by the following formula:

$$A = \log(I_0/I_1) \quad (S5)$$

Here, I_0 is incident light intensity and I_1 is outgoing light intensity. After measuring the A values at 375 nm of the iso-BAPB, n -BAPB and n -PAPB are about 0.37, 0.39 and 0.33, respectively. The absorption coefficient $\epsilon = 2.303A/l$, where l is the path length of the light which equals to the thickness of the crystal. So, we obtain $\epsilon = 1.40 \times 10^5$, 1.38×10^5 and $1.27 \times 10^5 \text{ cm}^{-1}$ for iso-BAPB, n -BAPB and n -PAPB, respectively. The penetration depths of them at 375 nm are about 71, 73 and 79 nm, respectively ($\delta = 1/\epsilon$). The excitation density n can be calculated as photon flux f in photons/cm² multiplied by absorption coefficient ϵ : $n = f\epsilon$, Table S4 summarizes the corresponding excitation density at different laser photon flux in TRPL measurements:

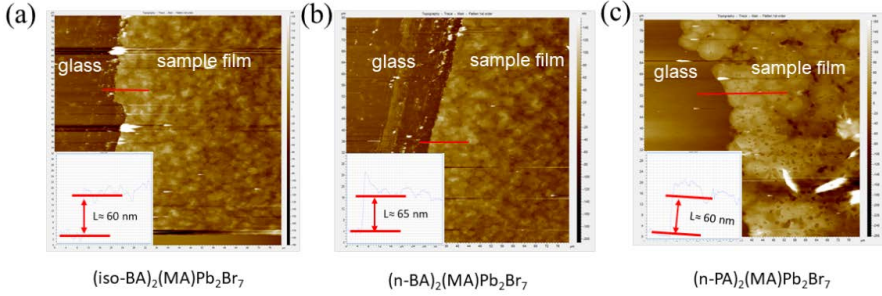


Figure S6. The AFM pictures of iso-BAPB (a), n -BAPB (b) and n -PAPB (c) films with the thickness values.

Table S4 Excitation density of iso-BAPB, n -BAPB and n -PAPB with different laser photon flux.

Excitation Fluence (photon/pulse/cm ²)	Excitation Intensity (cm ⁻³) of iso-BAPB	Excitation Intensity (cm ⁻³) of n -BAPB	Excitation Intensity (cm ⁻³) of n -PAPB
8.9×10^7	1.25×10^{13}	1.23×10^{13}	1.13×10^{13}
1.3×10^8	1.82×10^{13}	1.79×10^{13}	1.65×10^{13}
6.4×10^8	8.96×10^{13}	8.83×10^{13}	8.13×10^{13}
1.5×10^9	2.10×10^{14}	2.07×10^{14}	1.91×10^{14}
3.0×10^9	4.20×10^{14}	4.14×10^{14}	3.81×10^{14}

S5. Calculation of electron-phonon coupling strength using temperature dependent photoluminescence method.

PL spectra of these three compounds were measured at temperatures ranging 100-280 K in a cryostat (Figure S7), liquid nitrogen as the coolant. In order to verify our argumentation, we calculate the electron-phonon coupling strength from the FWHMs of the temperature-dependent PL spectra using the following model.^{8,9}

$$\Gamma(T) = \Gamma_0 + \Gamma_{ac} + \Gamma_{LO} + \Gamma_{imp} = \Gamma_0 + \gamma_{ac}T + \gamma_{LO}N_{LO}(T) + \gamma_{imp}e^{-E_b/k_B T} \quad (S7)$$

Here, Γ_0 is a temperature-independent inhomogeneous broadening that arises from scattering due to disorder and imperfections. Γ_{ac} and Γ_{LO} are homogeneous broadening terms, which result from acoustic and Fröhlich scattering, with charge-carrier phonon coupling strengths of acoustic phonon modes γ_{ac} and LO phonon modes γ_{LO} , respectively. $N_{LO}(T) = 1/(e^{E_{LO}/k_B T} - 1)$, where the E_{LO} is an energy representative of the frequency for the weakly dispersive LO phonon branch, and k_B is Boltzmann constant. Γ_{imp} is the inhomogeneous broadening due to the ionized impurities. It is worth noting that Γ_{ac} and Γ_{imp} do not contribute much to the temperature dependence at higher temperatures and they can be included to Γ_0 .⁸ Hence, we model the linewidth broadening of these three SCs using equation S8 (Figure S8).

$$\Gamma(T) = \Gamma_0 + \gamma_{LO}N_{LO}(T) \quad (S8)$$

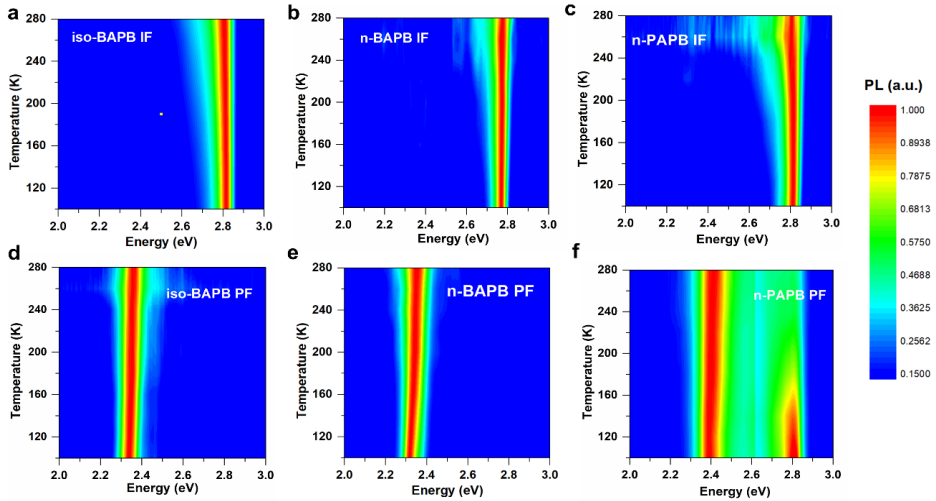


Figure S7 Temperature-dependent PL spectra of IFs and PFs of the three SCs.

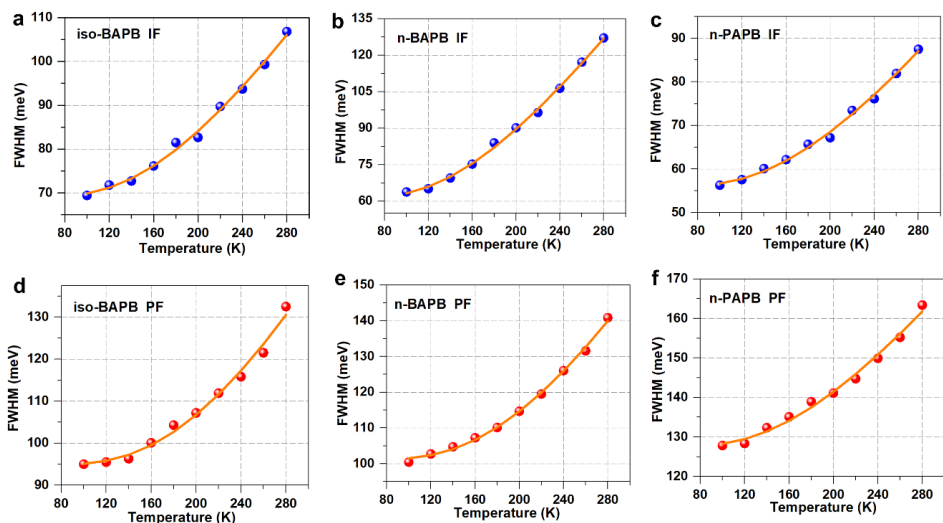


Figure S8. FWHM of the temperature-dependent PL for the IFs and PFs of the three SCs, and the solid orange lines fit equation S8 in main text.

S6. The fitting analysis of the PL decay.

We can fit the PL kinetics using triexponential decays with one fast component (t_1), a medium component (t_2), and a slow component (t_3) (Table S5). The slow components t_3 has a very small amplitude and can be neglected. Here t_1 and t_2 can be assigned to the trapping related nonradiative recombination and radiative recombination of the photoexcited charge carriers, respectively.

Table S5 Multi-exponential fitting parameters for TRPL kinetics of iso-BAPB, *n*-BAPB and *n*-PAPB under the excitation fluence of 1.3×10^8 photon/pulse/cm².

IFs	$A_1(\%)$	t_1 (ns)	$A_2(\%)$	t_2 (ns)	$A_3(\%)$	t_3 (ns)
iso-BAPB	88.4	0.398 (± 0.001)	8.2	8.15 (± 0.02)	3.4	84.4 (± 0.2)
<i>n</i> -BAPB	87.9	0.549 (± 0.001)	9.8	7.29 (± 0.03)	2.3	75.6 (± 0.2)
<i>n</i> -PAPB	93.4	0.492 (± 0.002)	5.6	5.98 (± 0.03)	1.0	76.3 (± 0.4)
PFs	$A_1(\%)$	t_1 (ns)	$A_2(\%)$	t_2 (ns)	$A_3(\%)$	t_3 (ns)
iso-BAPB	84.1	0.481 (± 0.002)	13.6	5.05 (± 0.02)	2.3	52.2 (± 0.2)

n-BAPB	68.0	1.736 (± 0.006)	48.7	8.02 (± 0.04)	3.3	50.7(± 0.2)
n-PAPB	71.9	1.123 (± 0.006)	23.7	10.24 (± 0.02)	4.4	98.9 (± 0.4)

S7. Detailed model of trap filling and fitting process.

The detailed calculation procedures of the model have been described in the reference.¹⁰ In brief, the equilibrium between free carriers and excitons can be described using the Saha equation. When photodoping (i.e. accumulated trap filling) is present, the Saha equation can be generalized as the following equation expressing the concentrations of electrons (n_e), holes (n_h) and excitons (n_x) corresponding to the overall untapped photogenerated species density N :

$$N_h = -\frac{(A - n_T)}{2} + \frac{1}{2}\sqrt{(A + N_T)^2 + 4AN} \quad (S9)$$

$$n_e = n_h - n_T \quad (S10)$$

where $A = v_d/(v_h v_e) \exp[-E_b/(k_B T)]$ and $v_i = \lambda_i^3$, λ_i is the thermal wavelength of the species i . n_T is concentration of filled traps and N_T is the concentration of total traps.

Here we assume that n_T varies little and is only dependent on average concentration of electrons $\overline{n_e(t)} = \frac{1}{t_0} \int_0^{t_0} n_e(t) dt$ during the PL recording time t_0 among the repetition pulses. Then we can get the following rate equations:

$$\frac{dn_T}{dt} = R_{pop}(N_T - n_T)\overline{n_e(t)} - R_{dep}(N_T^2 + n_T\overline{n_e(t)}) = 0 \quad (S11)$$

where R_{pop} and R_{dep} are the recombination rates of trap population and depopulation, respectively. Taking equations (S9) and (S10) we can obtain the average concentration of electrons as:

$$\overline{n_e(t)} = \frac{1}{t_0} \int_0^{t_0} n_e(t) dt \approx K(A + n_T), K = \frac{1}{\gamma_0 t_0} \ln \left[1 + \frac{AN(0)}{N_T(A + N_T)} \right] \quad (S12)$$

Here $N(0)$ can be simplified as initial excitation density N_c . γ_0 is the total rate of electronic decay not involving traps. Substitution of equation (S11) into (S12) gives:

$$n_T = -\frac{1}{2}\alpha + \frac{1}{2}\sqrt{\alpha^2 + 4\beta N_T} \quad (S13)$$

$$\alpha = \frac{[A + R(A - N_T)]}{\left(1 + \frac{1}{K} + R\right)} \quad (S14)$$

$$\beta = \frac{RA}{\left(1 + \frac{1}{K} + R\right)} \quad (S15)$$

$$K = \frac{1}{\gamma_0 t_0} \ln \left[1 + \frac{AN_c}{N_T(A + N_T)} \right], R = R_{pop}/R_{dep} \quad (S16)$$

During the fitting of the trapping model, we first assume that both traps exhibit filling but due to different trap population and depopulation rates, the ratio of unoccupied trap densities between two type of traps varies with different excitation intensity (Figure S9a-b). Therefore we can plot $A_1/(A_1+A_2) \sim N_c$ data and fit with the expression combination equations S13-S16.

$$\frac{A_1}{A_1+A_2} = \frac{n_{\text{uncT1}}}{n_{\text{uncT1}}+n_{\text{uncT2}}} = \frac{N_{T1} + \frac{1}{2}\alpha_1 - \frac{1}{2}\sqrt{\alpha_1^2+4\beta_1N_{T1}}}{(N_{T1} + \frac{1}{2}\alpha_1 - \frac{1}{2}\sqrt{\alpha_1^2+4\beta_1N_{T1}}) + (N_{T2} + \frac{1}{2}\alpha_2 - \frac{1}{2}\sqrt{\alpha_2^2+4\beta_2N_{T2}})} \quad (\text{S17})$$

Here n_{uncT1} and n_{uncT2} are the concentration of filled traps 1 and 2, respectively. N_{T1} and N_{T2} are the concentrations of original concentration of trap 1 and trap 2, respectively. In this work, A of iso-BAPB and n -BAPB were approximately equal to $0.97 \times 10^{15} \text{ cm}^{-3}$, respectively, PL recording time t_0 was $2.5 \times 10^{-7} \text{ s}$, and γ_0 was taken as the rate of the charge recombination not contributing to the trap filling process, we first set all the four fitting parameters (N_{T1} , N_{T2} , R_1 , and R_2) while analyzing these two compounds. The best fitting results as shown in Table S6. In this table, R_2 of iso-BAPB and n -BAPB are 15.5 and 36.7, respectively. Considering R is the ratio between trap population and depopulation rates, we can then roughly estimate the depopulation time of their traps 2 using the trap population time obtained in PL kinetics (lifetime of the second component 5.05 and $\sim 8.02 \text{ ns}$, respectively) to be ~ 80 and $\sim 290 \text{ ns}$, respectively. These depopulation time of traps 2 are not much different from the interval between the pulses in our measurement (250 ns). Therefore, we conclude that no considerable trap filling should occur in their traps 2 since the depopulation rate is too fast.¹¹ The model is then modified for the case that trap filling occurs only in trap1 as follows:

$$\frac{A_1}{A_1+A_2} = \frac{n_{\text{uncT1}}}{n_{\text{uncT1}}+N_{T2}} = \frac{N_{T1} + \frac{1}{2}\alpha_1 - \frac{1}{2}\sqrt{\alpha_1^2+4\beta_1N_{T1}}}{(N_{T1} + \frac{1}{2}\alpha_1 - \frac{1}{2}\sqrt{\alpha_1^2+4\beta_1N_{T1}}) + N_{T2}} \quad (\text{S18})$$

Here the $A_1/(A_1+A_2)$ represents the ratio between unoccupied density of trap 1 and original density of trap 2. We first set all the three fitting parameters (N_{T1} , N_{T2} , and R) free for the values from the equation (S17). Then, we fit the equation (S18) (Figure S9c) to get the new parameters (Table S6).

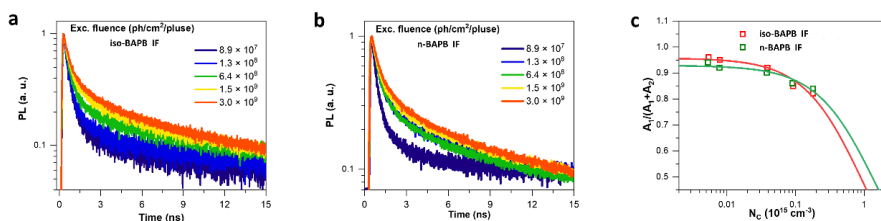


Figure S9. PL decay kinetics with different excitation fluence for the IFs of iso-BAPB (a) and *n*-BAPB (b); dependence of the amplitude ratios $A_1/(A_1 + A_2)$ in the multi-exponential fitting of the decays on the initial charge densities N_c for the IFs of iso-BAPB and *n*-BAPB (c).

Table S6. Trap Densities obtained from the fitting.

Model	IFs	R_1	R_2	N_{T1} (10^{15} cm ⁻³)	N_{T2} (10^{15} cm ⁻³)
$\frac{A_1}{A_1+A_2} = \frac{n_{uncT1}}{n_{uncT1}+n_{uncT2}}$	iso-BAPB	2.3×10^5	15.5	11.7	0.23
	<i>n</i> -BAPB	2.7×10^4	36.7	9.1	0.57
$\frac{A_1}{A_1+A_2} = \frac{n_{uncT1}}{n_{uncT1}+N_{T2}}$	iso-BAPB	1.4×10^5	/	46.9	2.08
	<i>n</i> -BAPB	5.1×10^4	/	29.1	2.19

S8. Calculation of the free carrier ratio after photo-excitation

After photoexcitation by the laser pulse, actually the free carriers and weak coupled excitons coexist in the crystal under a thermodynamics equilibrium. The ratio between two species is a fixed term resembling the ion-electron balance in a hot plasma, which depends strongly on the exciton binding energy as well as the excitation concentration. Therefore, we can use a classic Saha-Langmuir theory to roughly calculate the ratio of the free carriers X (i.e., fraction of the free carriers among all the excited species) in the system:

$$\frac{x^2}{1-x} = \frac{1}{n} \left(\frac{2\pi m k_B T}{h^2} \right)^{1.5} e^{-\frac{E_b}{k_B T}} \quad (\text{S19})$$

where E_b refers to the exciton binding energy (We obtained their E_b by fitting the temperature-dependent PL peak intensities of ~59 meV, ~93 meV, ~88 meV for iso-BAPB, *n*-BAPB, and *n*-PAPB, respectively),⁴ m is the exciton effective mass, T is the temperature and n is the excitation concentration. Previous study has shown that this equation is also applicable to 2D hybrid lead halide perovskites.¹² The following table summarized the calculated x ratio of three samples under the excitation condition in PL decay measurement (Table S7). Apparently, during our measurement, the majority of the excited species in the 2D perovskite crystals is free carriers and the contribution of the exciton can almost be negligible.

Table S7. The calculated values of ratio of the free carriers x .

Samples	Excitation Intensity (cm ⁻³)	x
iso-BAPB IF	$0.125 - 4.20 \times 10^{14}$	$0.998 - 0.946$

<i>n</i> -BAPB IF	$0.123 - 4.14 \times 10^{14}$	0.993 – 0.839
<i>n</i> -PAPB IF	$0.113 - 3.81 \times 10^{14}$	0.995 – 0.868

Table S8 Relative PLQY (%) at PFs of three samples (PL decay Aera/Exc. Fluence)

Samples Exc. Fluence	iso-BAPB PF	<i>n</i> -BAPB PF	<i>n</i> -PAPB PF
8.9×10^7	0.00167	0.03288	0.01074
1.3×10^8	0.00154	0.02422	0.00984
6.4×10^8	0.00069	0.01062	0.00705
1.5×10^9	0.00065	0.00745	0.00672
3.0×10^9	0.00069	0.00687	0.00626

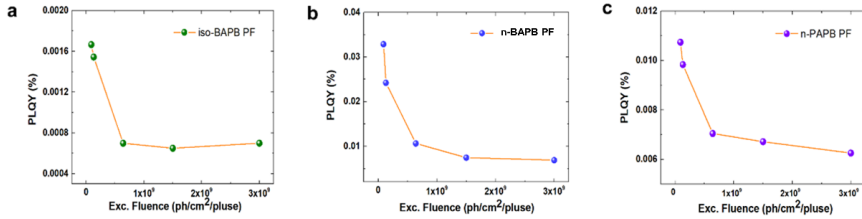


Figure S10. Relative PLQY (%) at PFs of three samples.

S9 Local strain accumulation and phonon coupling analysis of Br-based and I-based perovskites

First, the feature of the ‘edge state’ should be determined by the stiffness of the lattice. According to the theoretical calculation and the experimental measurement, the Br-based perovskites generally have a higher bulk modulus than I-based perovskites and become less prone to long-range lattice distortions.^{13,14} This can lead to two consequences: 1) stronger strain accumulation in Br-based perovskite, 2) small instead of large polaron formation in Br-based perovskites corresponding to the short-range local lattice distortion (e.g. on the surface facet). In addition, the general e-LO phonon coupling strength can be calculated by the following equation:¹⁵

$$a = \frac{e^2}{h} \frac{1}{4\pi\epsilon_0} \sqrt{\frac{m^*}{2h\omega_{LO}}} \left[\frac{1}{\epsilon_\infty} - \frac{1}{\epsilon_s} \right] \quad (\text{S20})$$

Here and ϵ_s and ϵ_∞ refers to the dielectric permittivities at static and optical frequencies, respectively. The term within the bracket evaluates the lattice polarity. The lattice polarity made by Pb-Br bonding should be higher than Pb-I due to the larger electronegativity difference between Pb and Br (0.7) compared with Pb and I (0.4). Therefore, we can expect high phonon coupling in Br-based system, which would facilitate the formation of polaron states. The above two reasons should encounter why in our Br-based 2D perovskites, the STE instead of conventional sub-gap states are formed at PFs.

Reference

- (1) Liang, M.-L.; Ma, Y.-X.; Hu, C.-L.; Kong, F.; Mao, J.-G., Ba(MoO₂F)₂(QO₃)₂ (Q = Se, Te): Partial Fluorination of MoO₆ Octahedra Enabling Two Polar Solids with Strong and Phase Matchable SHG Response. *Chem. Mater.* **2020**, *32*, 9688-9695.
- (2) Halasyamani, P. S. Asymmetric Cation Coordination in Oxide Materials: Influence of Lone-Pair Cations on the Intra-octahedral Distortion in d⁰ Transition Metals. *Chem. Mater.* **2004**, *16*, 3586-3592.
- (3) Zhu, Q.; Zheng, K.; Abdellah, M.; Generalov, A.; Haase, D.; Carlson, S.; Niu, Y.; Heimdal, J.; Engdahl, A.; Messing, M. E.; et al. Correlating Structure and Electronic Band-Edge Properties in Organolead Halide Perovskites Nanoparticles. *Phys. Chem. Chem. Phys.* **2016**, *18*, 14933-14940.
- (4) Liang, M.; Lin, W.; Lan, Z.; Meng, J.; Zhao, Q.; Zou, X.; Castelli, I. E.; Pullerits, T.; Canton, S. E.; Zheng, K., Electronic Structure and Trap States of Two-Dimensional Ruddlesden–Popper Perovskites with the Relaxed Goldschmidt Tolerance Factor. *ACS Appli. Elect. Mater.* **2020**, *2*, 1402-1412.
- (5) Stiff-Roberts, A. D. Quantum-Dot Infrared Photodetector. *Materials Science and Materials Engineering* **2011**, *6*, 452-485.
- (6) López, C. A.; Martínez-Huerta, V. M.; Alvarez-Galván, M. C.; Kayser, Paula.; Gant, Pa.; Castellanos-Gomez, A.; Fernández-Díaz, M. T.; Fauth, F.; Alonso, J. A. Elucidating the Methylammonium (MA) Conformation in MAPbBr₃ Perovskite with Application in Solar Cells. *Inorg. Chem.* **2017**, *56*, 14214–14219.
- (7) Chen, Z.; Yu, C.; Shum, K.; Wang, J. J.; Pfenninger, W.; Vockic, N.; Midgley, J.; Kenney, J. T. Photoluminescence Study of Polycrystalline CsSnI₃ Thin Films: Determination of Exciton Binding

- Energy. *J. Lumin.* **2012**, *132*, 345–349.
- (8) Wright, A. D.; Verdi, C.; Milot, R. L.; Eperon, G. E.; Perez-Osorio, M. A.; Snaith, H. J.; Giustino, F.; Johnston, M. B.; Herz, L. M., Electron-Phonon Coupling in Hybrid Lead Halide Perovskites. *Nat. Commun.* **2016**, *7*, 11755.
- (9) Shi, Q.; Ghosh, S.; Kumar, P.; Folkers, L. C.; Pal, S. K.; Pullerits, T.; Karki, K. J. Variations in the Composition of the Phases Lead to the Differences in the Optoelectronic Properties of MAPbBr₃ Thin Films and Crystals. *J. Phys. Chem. C* **2018**, *122* (38), 21817–21823.
- (10) Stranks, S. D.; Burlakov, V. M.; Leijtens, T.; Ball, J. M.; Goriely, A.; Snaith, H. J. Recombination Kinetics in Organic-Inorganic Perovskites: Excitons, Free Charge, and Subgap States. *Phys. Rev. Appl.* **2014**, *2*, 034007.
- (11) Zheng, K.; Židek, K.; Abdellah, M.; Messing, M. E.; Al-Marri, M. J.; Pullerits, T. Trap States and Their Dynamics in Organometal Halide Perovskite Nanoparticles and Bulk Crystals. *J. Phys. Chem. C* **2016**, *120*, 3077–3084.
- (12) Gelvez-Rueda, M. C.; Hutter, E. M.; Cao, D. H.; Renaud, N.; Stoumpos, C. C.; Hupp, J. T.; Savenije, T. J.; Kanatzidis, M. G.; Grozema, F. C. Interconversion between Free Charges and Bound Excitons in 2D Hybrid Lead Halide Perovskites. *J. Phys. Chem. C* **2017**, *121*, 26566–26574.
- (13) Neukirch, A. J.; Abate, I. I.; Zhou, L.; Nie, W.; Tsai, H.; Pedesseau, L.; Even, J.; Crochet, J. J.; Mohite, A. D.; Katan, C.; Tretiak S. Geometry Distortion and Small Polaron Binding Energy Changes with Ionic Substitution in Halide Perovskites. *J. Phys. Chem. Lett.* **2018**, *9*, 7130–7136.
- (14) Ferreira, A. C.; Létoublon, A.; Paofai, S.; Raymond, S.; Ecolivet, C.; Rufflé, B.; Cordier, S.; Katan, C.; Saidaminov, M. I.; Zhumekenov, A. A.; et al. Elastic Softness of Hybrid Lead Halide Perovskites. *Phys. Rev. Lett.* **2018**, *121*, 085502.
- (15) Fu, J.; Xu, Q.; Han, G.; Wu Bo.; Huan, C. H. A.; Leek, M. L.; Sum, T. C. Hot carrier cooling mechanisms in halide perovskites. *Nat. Commun.* **2017**, *8*, 1300.

Paper IV



Optimizing the quasi-equilibrium state of hot carriers in all-inorganic lead halide perovskite nanocrystals through Mn doping: fundamental dynamics and device perspectives†

Cite this: *Chem. Sci.*, 2022, 13, 1734

All publication charges for this article have been paid for by the Royal Society of Chemistry

Jie Meng,^{†a} Zhenyun Lan,^{†b} Weihua Lin,^c Mingli Liang,^a Xianshao Zou,^c Qian Zhao,^a Huifang Geng,^d Ivano E. Castelli,^b Sophie E. Canton,^e Tõnu Pullerits^c and Kaibo Zheng^{*,ac}

Hot carrier (HC) cooling accounts for the significant energy loss in lead halide perovskite (LHP) solar cells. Here, we study HC relaxation dynamics in Mn-doped LHP CsPbI₃ nanocrystals (NCs), combining transient absorption spectroscopy and density functional theory (DFT) calculations. We demonstrate that Mn²⁺ doping (1) enlarges the longitudinal optical (LO)–acoustic phonon bandgap, (2) enhances the electron–LO phonon coupling strength, and (3) adds HC relaxation pathways via Mn orbitals within the bands. The spectroscopic study shows that the HC cooling process is decelerated after doping under band-edge excitation due to the dominant phonon bandgap enlargement. When the excitation photon energy is larger than the optical bandgap and the Mn²⁺ transition gap, the doping accelerates the cooling rate owing to the dominant effect of enhanced carrier–phonon coupling and relaxation pathways. We demonstrate that such a phenomenon is optimal for the application of hot carrier solar cells. The enhanced electron–LO phonon coupling and accelerated cooling of high-temperature hot carriers efficiently establish a high-temperature thermal quasi-equilibrium where the excessive energy of the hot carriers is transferred to heat the cold carriers. On the other hand, the enlarged phononic band-gap prevents further cooling of such a quasi-equilibrium, which facilitates the energy conversion process. Our results manifest a straightforward methodology to optimize the HC dynamics for hot carrier solar cells by element doping.

Received 20th October 2021
Accepted 10th January 2022

DOI: 10.1039/d1sc05799e
rsc.li/chemical-science

Introduction

In a single-junction solar cell, the rapid cooling of the hot carrier (HC) excited by photons with energy well above the bandgap is a major energy loss channel responsible for the

Shockley–Queisser (SQ) limit.¹ The hot carrier solar cell (HCSC) is set to tackle this issue by keeping the HC in a sufficiently high energy quasi-equilibrium (*i.e.* with a mean carrier temperature > 500 K) with a subset of the thermal environment directly coupled to the electrons. In this way, the carriers can be extracted at significantly higher energy than the bandgap of the semiconductor, thereby making efficient use of the excess energy of the HC.² An ideal single-junction HCSC can reach a power conversion efficiency as high as 66%.¹ However, achieving an efficient HC extraction with all the excess energy to be harvested is highly challenging. As illustrated in Scheme 1, previous studies attributed the bottleneck to the suppression of HC extraction by faster HC cooling to the near-band-edge (Scheme 1a), and sought materials with a slow HC cooling rate to ensure the HC injection into electrodes at hot states (Scheme 1b).^{3,4} However, the excess energy of the HC in this case will still be lost in the acceptor electrodes. Utilization of an energy selective electrode (ESC) to screen the energy of the injected hot carrier can be one possible solution. However, it requires a perfect energy alignment between photoactive materials and ESCs, which is difficult to achieve. Therefore, the

^aDepartment of Chemistry, Technical University of Denmark, DK-2800 Kongens Lyngby, Denmark. E-mail: kzhang@kemi.dtu.dk; kaibo.zheng@chemphys.lu.se

^bDepartment of Energy Conversion and Storage, Technical University of Denmark, DK-2800 Kongens Lyngby, Denmark

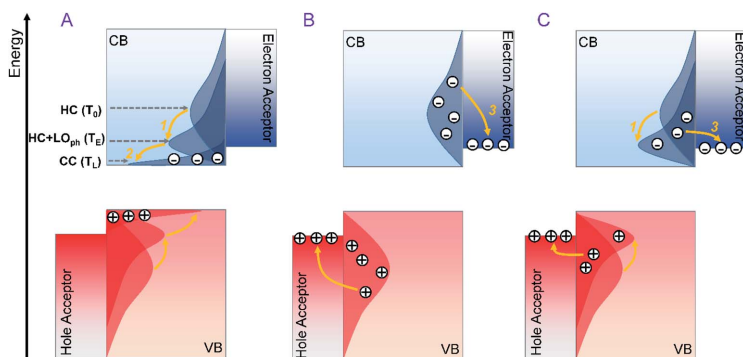
^cChemical Physics and NanoLund, Lund University, Box 124, 22100 Lund, Sweden

^dUltrafast Electron Microscopy Laboratory, The MOE Key Laboratory of Weak-Light Nonlinear Photonics, School of Physics, Nankai University, Tianjin 300071, China

^eEuropean XFEL, Holzkoppel 4, 22869 Schenefeld, Germany

† Electronic supplementary information (ESI) available: Synthesis and characterization, DFT calculations, TEM images and size distribution, pump fluence dependent TA kinetics, cross section calculations, TA spectra with different wavelengths and fluences, time-dependent carrier temperature with different excitation energies, temperature dependent PL emission, carrier temperature for samples with different doping concentration, and table for the cross section and exponential fitting of the cooling process. See DOI: 10.1039/d1sc05799e

‡ These authors contributed equally to this work.



Scheme 1 Schematic diagram of HC cooling versus HC extraction to charge acceptor electrodes in a HCSC: (a) HC cooling is so efficient that the HC cools from the initial temperature (T_0) to a thermal quasi-equilibrium (T_E) combined with emitted LO phonons (process 1) and finally all reach the cold carrier (CC) state after LO phonon decay (process 2) at a temperature of T_L . (b) HC cooling is extremely slow so that all the HCs are directly injected into acceptors (process 3) without thermalization, where the excess energy is dissipated during the injection. (c) HC undergoes efficient process 1 to establish the thermal equilibrium, and such equilibrium is long-lived to ensure the subsequent HC extraction to the acceptors.

optimal solution for HCSCs is to modify the HC cooling dynamics of photoactive materials to initiate the efficient establishment of the above-mentioned thermal quasi-equilibrium where the excess energy of the HC is converted to heat the cold carriers. Subsequently, such a quasi-equilibrium state should be long-lived to facilitate the HC extraction (Scheme 1c). In general, the lifetime of the quasi-equilibrium state should be ten times longer than the carrier injection time to acceptors (about 0.1 ps) to ensure a sufficient HC harvesting efficiency.³

In general, HC cooling in conventional semiconductors mainly involves carrier excitation, carrier-LO-phonon scattering, and LO-phonon decay.^{6,7} The competition between the phonon emission and decay in these processes determines the final HC cooling dynamics.⁸ Among them, the first two steps contribute to the establishment of the thermal quasi-equilibrium, while the last step promotes heat dissipation to dissociate such equilibrium. Therefore, the objectives of HCSC material engineering need to be revised by enhancing carrier-LO-phonon scattering and diminishing LO-phonon decay simultaneously so as to promote a stable thermal quasi-equilibrium.

The emerging lead halide perovskites (LHPs) with promising potential for solar cell applications can be the perfect target materials to evaluate the above strategy. The thermal quasi-equilibrium state is easily formed in LHPs with a long lifetime due to the large polaron screening effect,⁹ hot-phonon effect,¹⁰ and pronounced acoustical-optical phonon upconversion.⁸ Increasing attention has been focused on the HC dynamics in these materials since the first report of HC cooling in methylammonium lead iodide (MAPbI₃) polycrystalline thin films.^{11,12} Highly efficient HC extraction (up to $\approx 83\%$) could be achieved by an energy-selective electron acceptor layer from a surface-treated MAPbBr₃ LHP nanocrystal (NC) film.¹³ In

formamidinium Sn-based perovskite FASnI₃, a long HC cooling lifetime of up to a few ns was reported.¹⁴ In particular, the transport of a persistent HC over long distances (up to ≈ 600 nm)³ makes LHPs greatly promising for HCSCs.

In parallel, transition metal doping has been widely explored to impart novel optical, magnetic, and electronic properties to LHPs.¹⁵ A representative study in this regard is the Mn doping of LHP materials (*e.g.*, CsPbCl₃).^{16–18} Such doping can generate long-lived sensitized dopant luminescence and create a magnetically-coupled exciton state.¹⁹ The unique Mn²⁺ triplet emission in doped LHPs is derived from the Mn²⁺ d-d transition (⁴T₁ → ⁶A₁) after energy transfer or charge transfer from the excited state of the host LHPs.²⁰ In addition, we have previously demonstrated that partial replacement of Pb²⁺ by Mn²⁺ also causes local structural distortions and defect formation due to the difference in the cation radius between Mn²⁺ and Pb²⁺.²¹ It should be noted that the HC dynamic processes are determined by both electronic and phononic structures of the material. For instance, an enlarged phononic bandgap between optical phonon and acoustic phonon branches can efficiently suppress the channel for LO phonon decay, while a small LO phonon energy requires more phonons to be emitted for a given energy loss of a HC.²² Since both electronic states and local structures are modified by Mn²⁺ doping in LHPs, we thereby expect that it can be a robust tool to also modulate HC cooling dynamics towards enhanced carrier-LO-phonon scattering and diminished LO-phonon decay as mentioned above.

In this work, we investigated the HC cooling dynamics in Mn-doped CsPbI₃ nanocrystals (NCs) using transient absorption (TA) spectroscopy combined with theoretical and experimental characterization of the material structures. Compared to CsPbCl₃ and CsPbBr₃, CsPbI₃ has a lower optical bandgap so that the Mn d orbitals are located within the conduction band (CB) and valence band (VB), and thereby contribute to the

cooling pathways. We found that Mn doping modifies the HC cooling rate, but the trend is excitation energy-dependent. We have observed an acceleration in HC cooling at high excitation energy, but a deceleration in HC cooling at near-band-edge excitation energy. The temperature-dependent photoluminescence (PL) measurements and density functional theory (DFT) calculations confirmed the addition of in-band states and enhancement in the carrier-LO phonon coupling by Mn doping. On the other hand, Mn doping enlarged the phonon bandgap between the optical modes and the acoustic modes. We believe that the trade-off among these factors is the main reason for the excitation energy-dependent HC cooling dynamics in Mn-doped LHP NCs. The enhanced carrier-LO phonon coupling and enlarged phonon bandgap comply well with the optimal feature of HCSC materials described in Fig. 1c. This work demonstrates that HC cooling dynamics can be optimized by element doping that tailors the electronic as well as the lattice structure of the materials for the application of HCSCs.

Results and discussion

Sample characterization

Both pristine CsPbI₃ and Mn-doped CsPbI₃ NCs were synthesized by a reported hot-injection method (details are given in the Experimental section).²³ Fig. 1a schematically shows how Mn metal ions can be incorporated into perovskite lattices with homovalent B-site substitution (ionic radii: Pb²⁺: 133 pm and Mn²⁺: 97 pm).¹⁹ The transmission electron microscopy (TEM)

images show that doped NCs retain the cubic morphology of undoped NCs with an average particle size of around 17 nm (Fig. 1c, d and S1†). Subsequently, the absorption and emission spectra were measured (Fig. 1b). The absorption band-edge of all NCs is ~680 nm, corresponding to an optical bandgap (E_g) of ~1.8 eV. The introduction of Mn does not influence the absorption edge of the CsPbI₃ NCs. In addition, no dopant-related absorption/emission bands can be observed since the Mn d orbitals are not located within the bandgap of CsPbI₃.²⁴

X-ray absorption spectroscopy (XAS) measurements were then conducted at the Mn K-edge to confirm the Mn²⁺ doping into the perovskite lattice and to further characterize the local bonding environment around the Mn²⁺ ions (for experimental details, see the ESI†). Fig. 2a displays the XAS profiles of the samples containing 5% (brown), 7% (red) and 10% Mn (orange). The parameter ΔE is defined as the difference between the incident photon energy and the threshold value of Mn⁰.²⁵ The inset shows the first derivative of the XANES profiles as a function of ΔE for the 3 samples (orange, red and brown lines) and reference Mn foil (grey line). The energy position of the first inflection point correlates with the effective oxidation state of the absorbing atom. For the 3 samples, it falls between the values observed in Mn-oxides of +2, +3 and +4 valencies.^{26–28} This observation confirms that Mn is not present as metallic Mn⁰ clusters, but as Mn²⁺ ions incorporated into the perovskite lattice. The aggregation at the surface of the NCs can be ruled out based on the homogeneous atomic contrast in HR-TEM images. Fig. 2b shows a zoom of the X-ray absorption near-edge (XANES) region. The XANES profile consists of a weak

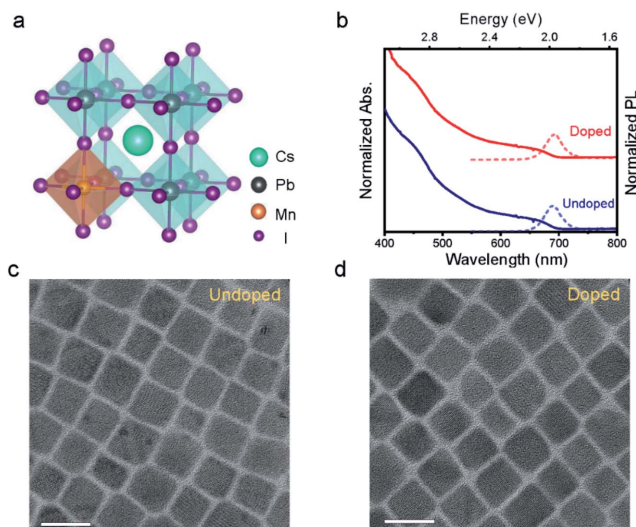


Fig. 1 (a) Schematic structure of Mn-doped CsPbI₃ NCs. The doping concentration is 5%. (b) The absorption (solid line) and PL spectra (dashed line) of undoped (bottom, black line) and Mn-doped (top, red line) CsPbI₃ NCs. TEM image of (c) undoped and (d) Mn-doped CsPbI₃ NCs. Examination of the TEM pictures shows that the Mn ions are not located at the surface of the NCs.

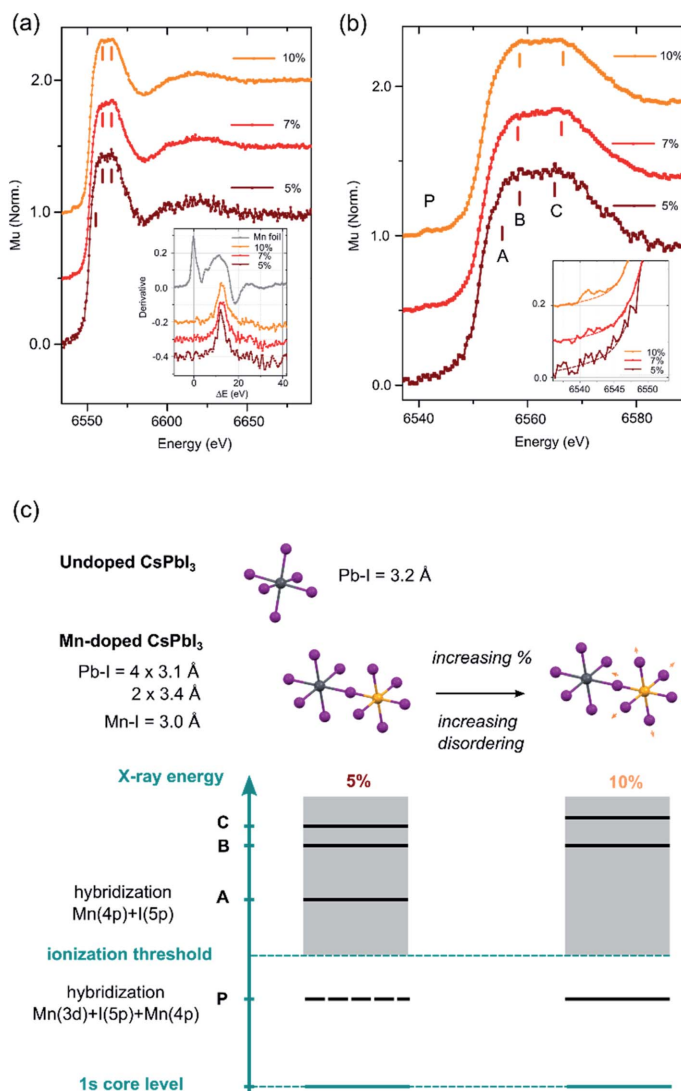


Fig. 2 (a) XANES spectra of Mn-doped NCs with various doping concentrations. The inset shows their derivatives along with the one of Mn foil, (b) magnified near edge XANES spectra at the Mn–K edge of Mn-doped NCs with various doping concentrations. The inset shows a zoom of the pre-edge region (the dotted lines are added as guides) and (c) proposed structural motif representing the octahedra in undoped and Mn-doped NCs and schematics of quasi-molecular energy levels used for interpreting the XANES spectral features.

pre-edge feature P centered around 6541 eV and a strong white line at 6560 eV. Forbidden in ideal octahedral symmetry, the pre-edge feature arises from the transition of a Mn 1s electron to the unoccupied Mn 3d levels hybridized with the ligand 4p and Mn 4p levels as a consequence of symmetry lowering and

distortions.^{29,30} This feature is observed for 7% and 10% samples (inset of Fig. 2b); but not for 5% due to the lower S/N ratio. The white line is less intense than in materials where Mn²⁺ is coordinated by low-Z elements (*i.e.* Mn oxides).²⁵ The white line of the Mn-doped NCs is attributed to the transition of

a Mn 1s electron to the molecular levels built from unoccupied 4p levels. In Mn-containing materials (particularly with perovskite structures), the fine structure of the white line is affected by the Mn 3d–4p exchange interaction,³¹ the hybridization of Mn 4p by the ligand orbitals³² and the balance between Mn 3d occupation and the Madelung constant^{33,34} and the degree of disorder.³⁵ At a low doping concentration (*i.e.*, 5%), the white line presents a distinct shoulder A which can be ascribed to the hybridization of Mn 4p, along with a clear double peak structure (B and C). As the doping concentration increases (7% and 10%), the intensity of P increases, A disappears and the double structure B–C broadens (see Fig. S0†). All these spectral features signal a more pronounced disordering around the Mn atoms, which might be accompanied by a slight elongation of the average Mn–I bond (Fig. 2c). Further work is required to explore the systematic variations of the XANES features in Mn-doped lead-based perovskites.

Next, we studied the HC cooling dynamics of the Mn-doped NCs mainly *via* transient absorption spectroscopy (TA) under various excitation energies and intensities. Fig. 3a shows a pseudo-color TA plot of Mn-doped CsPbI₃ NCs excited at 500 nm and high excitation intensity with an average number of excitons per NCs ($\langle N \rangle \approx 7.7$ corresponding to an initial average carrier density $n \approx 4.2 \times 10^{18} \text{ cm}^{-3}$ (for details of pump fluence and absorption coefficient calculations, see Fig. S2, S3 and Table S1†). All the other pseudo-color TA plots with different

excitation energies and intensities for undoped and doped NCs are summarized in Fig. S4–S9.† In general, the TA plot shows three distinct spectral features (see Fig. 3b): (1) the ground state bleach (GB) band centered at around 1.9 eV that arises from the near-band-edge state filling (B1); (2) the excited state absorption (ESA) above the bandgap (larger than 1.9 eV) that later evolved into a GB signature (A2); (3) toward the lower energy, the asymmetric derivative is the probe-induced Stark effect (A1).⁶ In addition, we can observe a red shift of the GB peak position with the delay time (Fig. 3a), which becomes more pronounced at high excitation fluences (Fig. S4–S9†). Such a GB position shift can be attributed to two effects: the Moss–Burstein effect and the bandgap renormalization at short timescales (before 2 ps).³⁶ The Moss–Burstein effect refers to the increase of the effective bandgap of a semiconductor when the lower energy states in the CB or VB have been populated or blocked.³⁷ On the other hand, bandgap renormalization is induced by the screening of Coulomb repulsion leading to a decrease in the electronic bandgap of semiconductors.³⁸ Those two effects should compensate each other near the band-edge of the LHPs, resulting in a slight shift in the observed optical band-edge.

Fig. 3b shows the normalized TA spectra $-\Delta A$ of Mn-doped CsPbI₃ NCs with a delay time between 0.3 and 3 ps extracted from the TA plot in Fig. 3a. In Mn-doped CsPbI₃ NCs, after high-energy photon excitation, the excited carriers first undergo carrier–carrier scattering within 100 fs, a process which is called

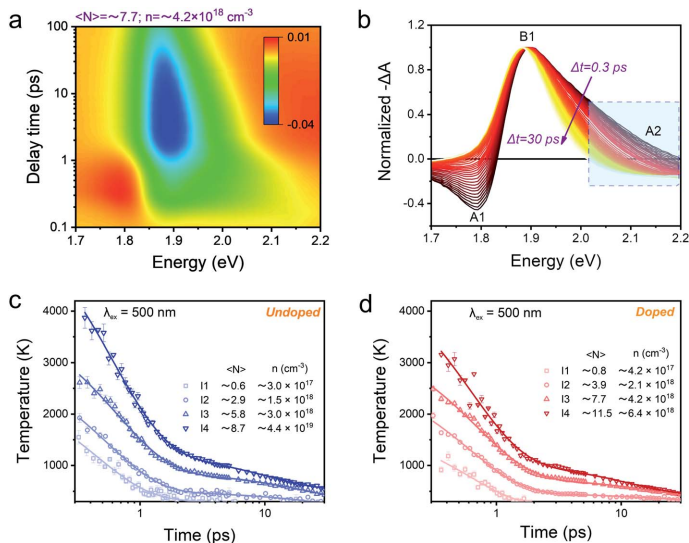


Fig. 3 (a) Pseudocolor representation of TA spectra of Mn-doped CsPbI₃ NCs for 500 nm (2.48 eV) excitation at high excitation intensity with $\langle N \rangle \approx 7.7$ (corresponding to $n \approx 4.2 \times 10^{18} \text{ cm}^{-3}$). (b) Normalized TA spectra of Mn-doped CsPbI₃ NCs for 2.48 eV excitation at high excitation intensity with $\langle N \rangle \approx 7.7$ (corresponding to $n \approx 4.2 \times 10^{18} \text{ cm}^{-3}$) with a time delay from 0.3 ps to 30 ps. The higher energy tails (between 2.02 and 2.2 eV marked by a dashed rectangle) are globally fitted to a Boltzmann distribution from which the carrier temperature is extracted. Carrier temperature decay kinetics with 2.48 eV excitation at four different excitation intensities for (c) undoped and (d) Mn-doped CsPbI₃ NCs. The solid lines are the multi-exponential fits, and fitting parameters can be seen in the ESI.†

carrier thermalization.³⁹ The HC then reaches a Fermi–Dirac distribution with a carrier temperature T_c larger than the lattice temperature T_l . Following carrier thermalization, the HC equilibrates with the lattice mainly through an inelastic carrier–phonon interaction, known as the “cooling” process. To ensure that the HCs have redistributed their energies and reached a quasi-temperature as the Boltzmann distribution, we analyzed the HC cooling dynamics after a delay of 0.3 ps, when the initial thermalization process should be finished. In order to extract the HC temperature, we fitted the high energy tail of the TA spectra (*i.e.*, between 2.02 eV and 2.20 eV) using the Maxwell–Boltzmann distribution function:³⁶

$$\frac{\Delta T}{T} \propto \exp\left(-\frac{E - E_f}{k_B T_c}\right) \quad (1)$$

where ΔT is the TA signal in the region of interest, E_f is the quasi-Fermi energy, k_B is the Boltzmann constant, and T_c is the carrier temperature. Since electrons/holes show similar effective masses based on the calculations (pure CsPbI₃: $m_e = 0.10m_0$, $m_h = 0.15m_0$; Mn-doped CsPbI₃: $m_e = 0.13m_0$, $m_h = 0.19m_0$), we expect comparable contributions from hot electrons and hot holes to the extracted HC temperatures. Fig. 3c and d shows the fitted HC cooling dynamics of undoped and doped samples with increasing carrier densities (or pump fluence), respectively. The HC cooling rates become lower with increasing carrier densities in both doped and undoped samples. The HC cooling decay can be well-fitted by bi-exponential functions with a fast component and a slow component. The fast component should be attributed to the emission of the LO phonons through carrier–phonon interactions, and the slow component should be due to the reduction of the energy loss rate by reduced decay of LO phonons.^{40,41} We then used the average time to compare the cooling rates of undoped and doped NCs. At low excitation density below 10^{18} cm^{-3} , the average decay times are 1.8 ps and 0.6 ps for undoped and doped NCs, respectively. When excitation density is higher than 10^{18} cm^{-3} , the average decay times for undoped and doped NCs reach 20.2 ps and 17.9 ps, respectively (Tables S4 and S5†). Notably, the same trend occurs in all the samples with various excitation photon energies (Fig. S10–S17 and Tables S2–S7†). The enhanced hot-phonon bottleneck can explain this general carrier density dependence of HC cooling dynamics, which is widely observed in semiconductors and LHPs.^{6,10,39,42,43} It is mainly induced by the presence of a non-equilibrium LO-phonon population in the phonon pool that reduces the net LO-phonon emission and enhances the cold carrier reheating, which consequently slows down the cooling process.^{6,39,44}

Excitation energy-dependent role of Mn doping in HC dynamics

In order to elucidate the influence of Mn doping on HC cooling, we mainly compared the cooling dynamics between undoped and Mn-doped CsPbI₃ NCs excited at different excitation energies at very low excitation intensity ($N \leq 1$) (Fig. 4). Although such excitation density is still higher than real sunlight radiation conditions, the low excitation density per NC in our system

can guarantee that the many-body effects influencing HC cooling, such as Auger reheating, are negligible.¹³

We can fit all the HC cooling decay processes by multiple exponential components as summarized in Table 1. When the samples are excited at 2.18 eV with the phonon energy close to the bandgap energy, the cooling decay of the undoped NCs can be fitted with a fast component (0.1 ps) and a slow component (0.7 ps), delivering an average lifetime of 0.3 ps (Fig. 4a). Upon Mn doping, only one exponential component can be fitted with a longer lifetime of 0.4 ps (also evidenced by the log plot of the kinetics in Fig. S22†). This manifests that HC cooling in doped NCs becomes slower with the excitation energy near the band-edge position (Fig. 4a). It should be noted that due to the limited spectral region which can be utilized for the T_c fitting under 2.18 eV excitation conditions where the GB tail is close to the scattering of the pump pulse, the fitted minimum T_c is a bit above 300 K. Nevertheless, we believe the trend of the cooling dynamics should not be influenced as the fitting parameters are kept constant for data points from each time delay.

When the sample is excited at 3.1 eV, the kinetics for the undoped NCs can be fitted by a fast component (0.2 ps) and a slow component (0.9 ps), giving an average lifetime of 0.5 ps. Upon Mn doping, the average lifetime becomes much faster (0.2 ps) (Fig. 4b). The same trend can also be seen in the excitation energy of 2.48 eV (Fig. S21†) (for detailed fitting parameters, see Table S11†). The above excitation energy-dependent comparison can be further confirmed by the increasing time of TA kinetics at the maximum GB position, which monitors the population of the band-edge states (Fig. 4c and d).

In general, HC cooling dynamics in semiconductors are related to the coupling between various thermal pools. Here the above analysis monitors the temperature of the electronic pool, which is coupled to the pool of LO phonons.¹³ Owing to the anharmonicity of the vibrations, the LO phonon pool transfers energy efficiently to the acoustic phonon pool followed by the energy dissipation to the solvent environment.⁴⁵ In order to identify the dominant steps of HC relaxation at various time delays, we have extracted the electronic energy power loss as a function of carrier temperature by using the conventional model of hot electron relaxation *via* optical-phonon emissions in Fig. 4e and f.¹³ The energy loss rate (P) of the carriers can be

derived from the equation $P = \frac{d}{dt} \left(\frac{3}{2} k_B T_c \right)$ where T_c refers to the carrier temperature. The power loss plots in Fig. 4e and f further confirm that HC cooling in doped NCs is slower under 2.18 eV excitation and faster under 3.1 eV excitation compared with undoped NCs. In addition, two distinct slopes can be observed in the plot corresponding to two power loss regimes. As shown in Fig. 4f, for the undoped NCs excited at 3.1 eV, the power loss rate slowly decreases from 1 to 0.2 eV ps⁻¹, until T_c reaches ≈ 700 K. Subsequently, as the HC temperature approaches the lattice temperature, P drops rapidly. We defined the temperature at the transition point between these two regions as transition temperature (T_t). When the samples are excited at 2.18 eV, the T_t for the undoped and doped NCs is about 410 K and 450 K, respectively (Fig. 4e). At 3.1 eV

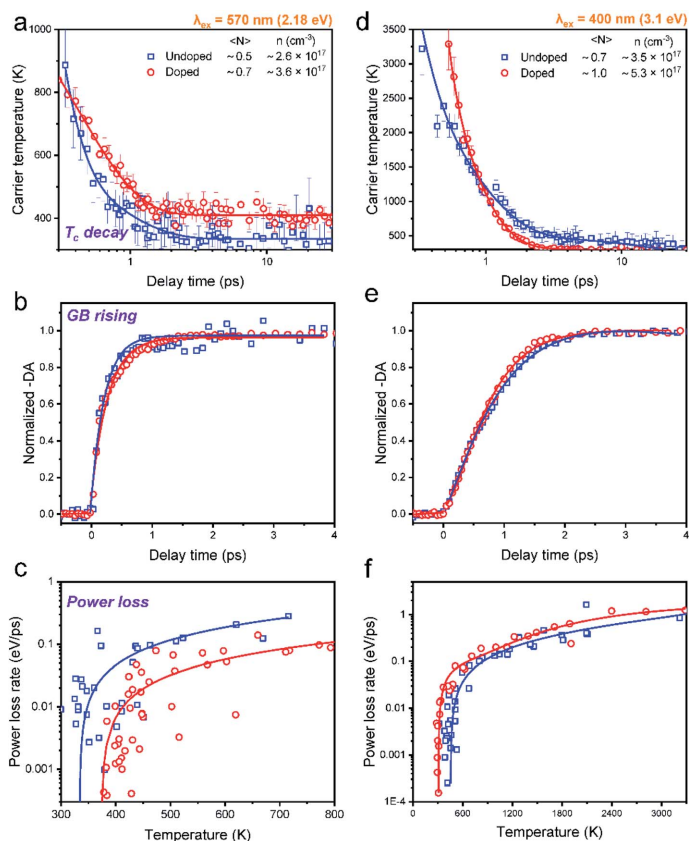


Fig. 4 Time-dependent carrier temperature for undoped and Mn-doped CsPbI₃ NCs at low excitation density ($\langle N \rangle < 1$) with (a) 2.18 eV and (b) 3.1 eV excitation energies. Normalized GB dynamics probed at the band-edge for undoped and Mn-doped CsPbI₃ NCs at low excitation intensity with (c) 2.18 eV and (d) 3.1 eV excitation energies. Power loss as a function of the carrier temperature of Mn-doped CsPbI₃ NCs and corresponding exponential fitting at low excitation intensity with (e) 2.18 eV and (f) 3.1 eV excitation energies.

Table 1 Fit parameters for carrier temperature decay kinetics of Mn-doped CsPbI₃ NCs with 3.1 eV and 2.18 eV excitations. The unit of time t is ps. The doped sample excited at 2.18 eV can be well fitted by a single exponential function, which can be justified from the $\ln T$ vs. t plot in Fig. S22

Exc. Wavelength		A_1	t_1	A_2	t_2	t_{ave}
3.1 eV	Undoped	0.85	0.2	0.15	0.9	0.5
	Doped	0.97	0.1	0.03	0.5	0.2
2.18 eV	Undoped	0.95	0.1	0.05	0.7	0.3
	Doped	1	0.4	—	—	0.4

excitation, the T_r for the undoped and doped NCs is about 780 K and 580 K (Fig. 4f), respectively. Mn doping leads to a lower T_r under 3.1 eV excitation and a higher T_r under 2.18 eV excitation. The two distinct regions of HC power loss are mainly dependent

on the electronic and phononic structures of the materials. Notably, at a low carrier density ($\sim 10^{-17} \text{ cm}^{-3}$), the power loss of the HC during the cooling process is dominated by the scattering between carriers and LO phonons. The initial rapid HC cooling (*i.e.*, the higher power loss rate) with the T_c above the T_r is due to the efficient LO phonon emission through the dominant Fröhlich interaction that dissipates the excess energy of the HC. These LO phonons decay into acoustic phonons until the T_c cools to the lattice temperature. The subsequent slower cooling of the HC closer to the near-band-edges (*i.e.*, around 300–600 K in Fig. 4e) is determined by the thermal equilibration between LO phonons and acoustic phonons.¹³ In this scenario, the T_r between the two power loss regions qualitatively reflects the impact of the hot-phonon bottleneck, which is determined by the population dynamics of non-equilibrium LO phonons in the phonon pools. At high excitation energy, the T_r values of

undoped and doped NCs are generally increased compared to low excitation energy as shown in Fig. 4e and f. This can be explained as more LO phonons are emitted due to the higher excess energy of the excited HC. On the other hand, the change of the T_r after Mn doping in NCs indicates modified phonon generation and decay dynamics.

In the following, we interpret the excitation energy-dependent role of Mn doping in the HC cooling dynamics observed in Fig. 4 from the intrinsic electronic/phononic structure of the doped NCs. We first revealed the electronic band structure of the samples *via* DFT calculations, as shown in Fig. 5a and b. The effective electron mass and hole mass of Mn-doped CsPbI₃ ($m_e = 0.13m_0$ and $m_h = 0.19m_0$) are larger than those of pure CsPbI₃ ($m_e = 0.10m_0$ and $m_h = 0.15m_0$). This is because of the perturbation in the periodicity of the Pb 6p orbitals after Mn doping which leads to the reduction of both VBM and CBM dispersion. This indicates a more localized electron and hole state in the doped NCs.⁴⁶ In the absence of the hot-phonon effect at low carrier concentrations, the energy loss rate of the HC *via* carrier–LO phonon interactions is predominantly affected by the effective mass as illustrated in eqn (2).⁶

$$P = \frac{m^{1/2}e^2}{\pi\epsilon_0\hbar^2} \left(\frac{\hbar\omega_{LO}}{2} \right)^{3/2} \left[\frac{1}{\epsilon_{opt}} - \frac{1}{\epsilon_{stat}} \right] \quad (2)$$

where ϵ_{opt} and ϵ_{stat} are the optical and static dielectric constants. Therefore, the heavier carrier effective mass in doped NCs should induce an intrinsically faster HC relaxation than in undoped NCs.

Secondly, we calculated the density of states (DOS) of pure CsPbI₃ NCs and the Mn-doped levels shown in Fig. 5a–c. For the undoped NCs, the pathways of HC cooling are mediated by states built from Pb and I orbitals. The doping adds Mn orbitals into the electronic structures of the NCs as shown in Fig. 5c. According to the previous theoretical calculations, the first excitation at every symmetry point shows high optical strength.^{47,48} As shown in Fig. 5b, when the doped samples are excited at high energy, (e.g., 3.1 eV) more channels are available for electronic relaxation of the HC. When the doped samples are excited at near band-edge energies, the excited electrons/holes possess energy lower than the majority of the Mn orbitals. Therefore, we believe that the participation of the Mn orbital in HC cooling should be negligible.

Following the discussion of the effect of electronic structure, we now examine the role of carrier–phonon coupling. For most inorganic semiconductors, coupling or scattering between charge carriers and phonons is a functional dependence of the PL linewidth $\Gamma(T)$ on temperature.⁴⁹ In order to evaluate such coupling, temperature-dependent PL spectra were acquired.

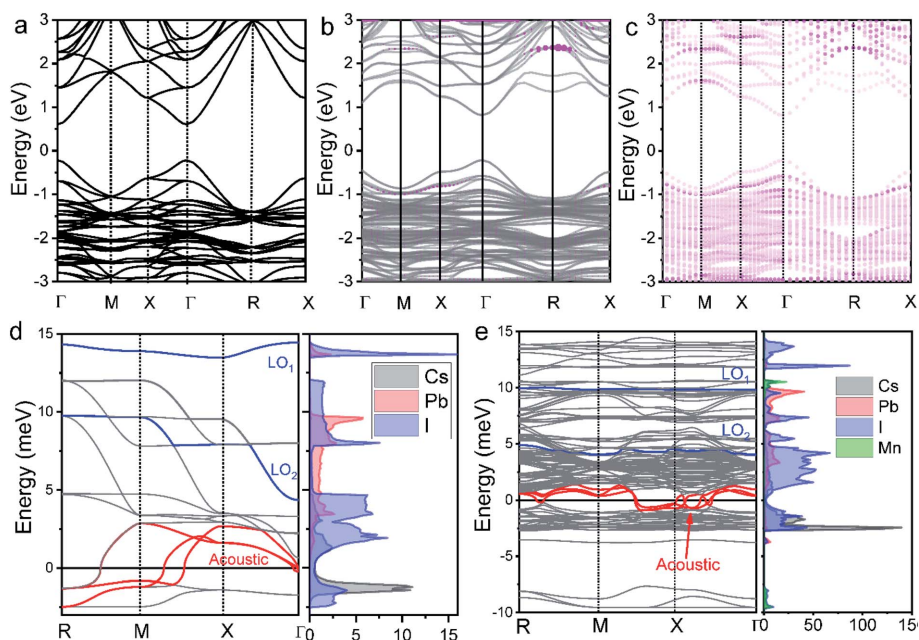


Fig. 5 Electronic band structure of (a) CsPbI₃ and (b) Mn-doped CsPbI₃ including Mn orbitals shown by pink color. (c) The contribution of Mn d orbitals in the electronic band structure of Mn-doped CsPbI₃. Phonon energy as a function of phonon momentum and density of states (DOS) of (d) undoped CsPbI₃ and (e) Mn-doped CsPbI₃. The size of these circles is proportional to the contribution of the corresponding orbitals. The two blue lines indicate the LO phonon mode. The red lines indicate the acoustic phonon mode.

Table 2 Linewidth parameters and calculated E_{LO} extracted from Fig. S18 and S19

Samples	Γ_0 /meV	γ_{LO} /meV	E_{LO} /meV (fitting)	E_{LO-min} /meV (calculated)	E_{LO-max} /meV (calculated)
Undoped	51.25	74.8	23.79	4.3	14.0
Doped	52.87	126.5	30.45	4.1	9.9

They are shown in Fig. S18 and S19.† We calculated the electron–phonon coupling strength from the FWHMs of temperature-dependent PL spectra using the following model:⁵⁰

$$\Gamma(T) = \Gamma_0 + \Gamma_{ac} + \Gamma_{LO} + \Gamma_{imp} = \Gamma_0 + \gamma_{ac}T + \gamma_{LO}N_{LO}(T) + \gamma_{imp}e^{-E_i/k_B T} \quad (3)$$

where Γ_0 is a temperature-independent inhomogeneous broadening that arises from scattering due to disorder and imperfections. Γ_{ac} is the contribution from acoustic-phonon scattering and γ_{ac} is the corresponding phonon-coupling strength. Γ_{LO} corresponds to the homogeneous broadening that results from LO-phonon scattering with a coupling strength γ_{LO} . In $N_{LO}(T) = 1/(e^{E_{LO}/k_B T} - 1)$, E_{LO} is an energy representative of the frequency for the weakly dispersive LO phonon branch, and k_B is the Boltzmann constant. Γ_{imp} is the inhomogeneous broadening due to the ionized impurities. Γ_{ac} and Γ_{imp} do not contribute much to the temperature dependence at higher temperatures (>100 K) so that they can be treated as constant and merged into Γ_0 . Hence, we model the

linewidth broadening of the samples using eqn (4) (Fig. S19†), and the linewidth parameters are shown in Table 2.

$$\Gamma(T) = \Gamma_0 + \gamma_{LO}N_{LO}(T) \quad (4)$$

Specifically, the LO phonon term in eqn (4) accounts for the Fröhlich interaction between LO phonons and carriers. The difference between fitted and calculated E_{LO} is within the experimental error range. The fitted γ_{LO} for undoped NCs (74.8 meV) is 1.7 times smaller than that of doped NCs (126.5 meV). This demonstrates the strengthened electron–LO phonon coupling by Mn doping.

The last critical factor for determining HC cooling dynamics is the phonon band structures that dominate the pathways of LO-phonon decay and energy transfer to the acoustic phonons. We performed first-principles calculations of phonon dispersion spectra to uncover the possible phonon decay dynamics (for detailed calculations, see the ESI†). The projected DOS on each atom is also given in Fig. 5d and e to show the detailed contributions from each atom. As well accepted, the most efficient pathway for LO phonon decay to acoustic phonons is the Klemens channel, where one optical phonon decays into two acoustic phonons with symmetric momentum.⁵¹ However, the Klemens decay requires that the phononic bandgap between LO and acoustic phonons ($\hbar\omega_{LO-min} - \hbar\omega_{LA-max}$) is lower than the maximum $\hbar\omega_{LA}$ ($\hbar\omega_{LA-max}$) energy (i.e., $\hbar\omega_{LO-min} - \hbar\omega_{LA-max} < \hbar\omega_{LA-max}$).⁵² Otherwise, the large phononic bandgap hinders the LO phonon decay and hence leads to the formation of a non-

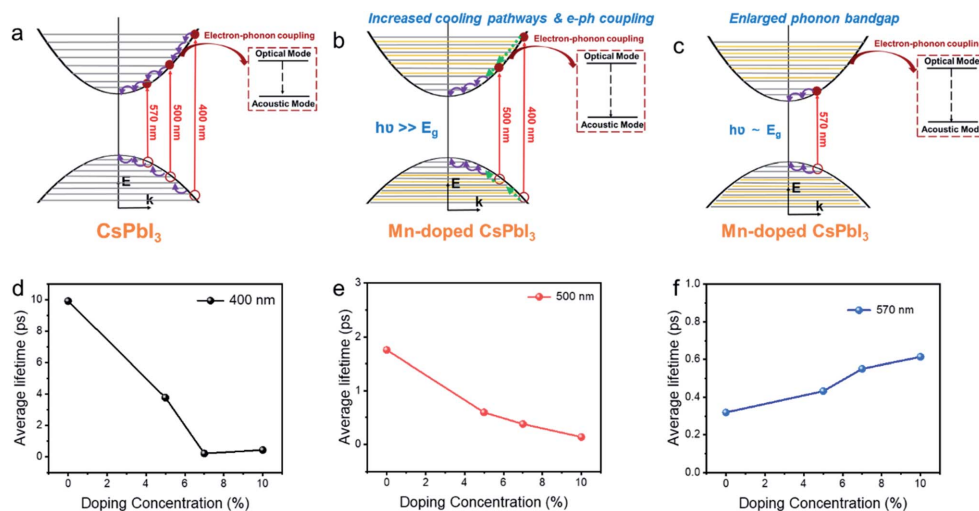


Fig. 6 Schematic mechanism diagram of hot carrier cooling for Mn-doped CsPbI₃ with (a) undoped CsPbI₃ NCs, (b) Mn-doped CsPbI₃ with high energy excitation, (c) Mn doped CsPbI₃ with low energy excitation NCs and average lifetime of hot carrier cooling for Mn-doped CsPbI₃ with different doping concentrations at (d) 400 nm (3.1 eV), (e) 500 nm (2.48 eV) and (f) 570 nm (2.18 eV) excitation energies, respectively. The added orange lines in Fig. 5b and c represent Mn dopant orbitals.

equilibrium phonon population where a LO hot-phonon bottleneck arises. In the undoped CsPbI₃ NCs, the majority of the LO vibrational modes are the Pb–I stretching vibrations with frequencies at around 4.4 meV ($\hbar\omega_{\text{LO2-min}}$) and 13.5 meV ($\hbar\omega_{\text{LO1-min}}$), while the maximum acoustic LA phonon frequency lies around 2.9 meV ($\hbar\omega_{\text{LA-max}}$) (Fig. 4d). The gap between LO and LA ($\hbar\omega_{\text{LO-min}} - \hbar\omega_{\text{LA-max}}$) is calculated to be about 1.5 meV. The lower LO phonon energy compared with twice the LA phonon energy guarantees an efficient Klemens decay in the undoped NCs. In contrast, the Pb–I stretching vibration (LO) frequencies in the doped NCs are around 4.1 meV ($\hbar\omega_{\text{LO2-min}}$) and 9.9 meV ($\hbar\omega_{\text{LO1-min}}$), while the maximum acoustic phonon frequency LA lies around 1.3 meV. The gap between LO and LA ($\hbar\omega_{\text{LO-min}} - \hbar\omega_{\text{LA-max}}$) is about 2.8 meV. Such enlargement of the phonon bandgap between LO and acoustic phonons should be induced from the strain due to Mn doping in the local structures.⁵³ The separation between the LO and LA phonon branches ($\hbar\omega_{\text{LO-min}} > 2\hbar\omega_{\text{LA-max}}$) after Mn doping should significantly hinder the Klemens channel, so that the LO phonons can only decay *via* alternative less efficient channels, such as the Ridley channel.⁵¹ This suggests that more LO phonons will be emitted to cool down the HC with the same excess energy, which inevitably leads to a large non-equilibrium LO phonon population.

We believe that the three factors above, *i.e.* integration of the doping levels, electron–LO phonon coupling, and the phononic band structure, all influence HC cooling dynamics. Therefore, the excitation wavelength dependence of HC cooling dynamics as shown in Fig. 6 should be induced by the competition among all of these factors as summarized in Fig. 6a–c. Under band-edge excitation (*e.g.* excited at 2.18 eV), the influence of additional Mn orbitals within the CB and VB can be neglected as their energies are well above the excited states, as shown in Fig. 5c. We also demonstrated that at high excitation intensity ($\langle N \rangle > 1$), the influence of Mn doping on HC cooling dynamics is significantly diminished (Fig. S23†). Firstly, under a high excitation fluence, the carriers will accumulate towards energy states higher than the Mn dopant orbitals even at low excitation energy (*i.e.* 2.2 eV) due to the so-called Moss–Burststein effect. In this case, Mn dopant orbitals can participate in HC cooling both under band-edge and high energy excitations. Secondly, the pronounced Auger heating effect and the hot phonon bottleneck may overwhelm the influence of intrinsic electronic and phononic structural changes induced by Mn doping. As a result, the HC cooling dynamics between undoped and doped NCs become harder to distinguish (Fig. S4, S5, S8 and S9†). Here the increased phononic bandgap induced by Mn doping is the dominant factor for HC cooling dynamics. As discussed, it hinders the decay of excited LO phonons and promotes the non-equilibrium phonon population, while enhancing the hot-phonon bottleneck. This accounts for the slow HC cooling and high T_r in power loss for doped NCs as shown in Fig. 6c.

Under high energy excitation (*e.g.* excited at 400 and 2.48 eV), the participation of the Mn orbital in the cooling pathways, together with other factors induced by Mn doping should all play a role in HC cooling dynamics as discussed above (Fig. 6b). The faster cooling rates for doped NCs in this scenario indicate the influence of the Mn orbital participation, and the enhanced

e–ph coupling competes with the enlargement of the phonon bandgap to accelerate the cooling process.

Summarizing the role of Mn doping in the HC with various energies, we noticed that such a situation does fit the optimal scenario for the materials applied in HCSCs. The HC at very high energy will undergo strong electron–phonon coupling to be efficiently thermalized to the quasi-equilibrium state integrating the carriers with LO phonons to keep the thermal pool ‘warm’ enough. In this case, the carrier temperature reaches 400 to 600 K reflected by the T_r values. The phonon bandgap enlargement prevents further heat dissipation when the quasi-equilibrium is established and the HC possesses lower energy.

Role of the dopant concentration in HC cooling dynamics

The samples with different doping levels are now considered. From the average HC cooling time t_{ave} shown in Fig. 6d–f, we find that the cooling rates become slower with increasing doping concentration under low excitation energies (2.18 eV, Fig. 6f). Since the HC cooling process at low excitation energy is exempt from the Mn orbital participation as discussed above, such a relationship indicates that the combined influence from the change of phononic structures and e–ph coupling evolves monotonously with the doping concentration. According to the XANES characterization above (Fig. 2), the local lattice disordering around the Mn atoms increases monotonously with the doping level increment. Such local distortion should modify the metal-halide vibrational modes, thus enhancing e–ph coupling and accelerating HC cooling in perovskite materials.⁵⁴ On the other hand, local structural distortion should also modify the phononic structure accounting for the enlargement of the phonon bandgap that hinders HC cooling according to the above DFT calculations. Apparently, the influence of phonon bandgap enlargement becomes more dominant at high doping concentrations.

On the other hand, at a high excitation energy of 3.1 eV, the average cooling time first decreases and then increases with the doping concentration. At an excitation energy of 2.48 eV, the average cooling time decreases with the doping concentration. The XANES characterization confirms the monotonously increased disordering of the Mn–I bonds with the doping level, which should weaken the mixing between Mn and I orbitals and affect the available states in the pathway for the cooling of the HC proved by the DFT calculations (Fig. 5c). The above dependences again indicate that Mn orbital pathways (*i.e.* factors that accelerate HC cooling) dominate HC cooling at low doping concentrations. In contrast, the phonon bandgap enlargement (*i.e.* factor that decelerates HC cooling) dominates the cooling dynamics at high doping concentrations.

Conclusions

In summary, the HC cooling dynamics in Mn-doped CsPbI₃ NCs have been studied using transient absorption spectroscopy combined with theoretical calculations and local structure characterization. Under a high energy excitation of 3.1 eV, Mn doping promotes fast HC cooling rates. However, Mn doping contributes to slowing the HC cooling rate after excitation at 2.18 eV. From

DFT calculations, Mn-doped CsPbI₃ shows higher effective electron/hole masses in comparison with undoped NCs. Meanwhile, temperature-dependent PL characterization further confirmed that Mn doping also helps to strengthen the electron-phonon coupling. However, a significant energy separation between the optical mode and acoustic modes is observed, implying that Mn doping suppresses the efficient Klemens channel for LO phonon decay. The HC cooling process is therefore the consequence of the competition between all the above factors, which leads to the excitation energy and doping concentration dependence. The enhanced electron-phonon coupling and efficient thermalization of the HC at high energy together with delayed heat dissipation after thermalization with the HC at low energy are optimal for HCSC application. Our results open up a new possibility to optimize HC cooling dynamics in HCSC materials *via* element doping with fine control of both electronic and phononic structures of host materials.

Author contributions

Jie Meng implemented the sample preparation, characterization, data analysis, and manuscript writing. Zhenyun Lan helped with the calculation with the supervision of Ivano E. Castelli. Weihua Lin helped to measure the transient absorption spectroscopies. Mingli Liang and Xianshao Zou helped to conduct the temperature-dependent PL measurement. Huifang Geng contributed to the TA fitting. Sophie E. Canton contributed to the X-ray experiment and analysis. Tõnu Pullerits participated in the data analysis and manuscript revision. Kaibo Zheng is the corresponding author and supervised the whole project.

Conflicts of interest

The authors declare no competing financial interest.

Acknowledgements

This work was funded by the Danish Council for Independent Research (No. 7026-0037B), Swedish Research Council (No. 2017-05337), Crafood foundation (no. 20200522), Swedish Energy Agency research grant, and Research Fund for International Young Scientists from NSFC, China (no. 21950410515) (K. Z.), J. M., Z. L., and Q. Z., acknowledge financial support from China Scholarship Council. S. E. C. acknowledges financial support from European XFEL. We thank DESY (Hamburg, Germany), a member of the Helmholtz Association HGF, for the provision of experimental facilities. Parts of this research were carried out at Petra III and we would like to thank Maria Naumova, Morgane Desmau, Edmund Welter and Vadim Murzin for assistance in working at P65 beamline.

References

- R. T. Ross and A. J. Nozik, *J. Appl. Phys.*, 1982, **53**, 3813–3818.
- S. S. Lim, D. Giovanni, Q. Zhang, A. Solanki, N. F. Jamaludin, J. W. M. Lim, N. Mathews, S. Mhaisalkar, M. S. Pshenichnikov and T. C. Sum, *Sci. Adv.*, 2019, **5**, eaax3620.
- Z. Guo, Y. Wan, M. Yang, J. Snaider, K. Zhu and L. Huang, *Science*, 2017, **356**, 59–62.
- T. R. Hopper, A. Gorodetsky, J. M. Frost, C. Müller, R. Lovrincic and A. A. Bakulin, *ACS Energy Lett.*, 2018, **3**, 2199–2205.
- Y. Takeda, T. Ito, T. Motohiro, D. König, S. Shrestha and G. Conibeer, *J. Appl. Phys.*, 2009, **105**, 074905.
- J. Fu, Q. Xu, G. Han, B. Wu, C. H. A. Huan, M. L. Leek and T. C. Sum, *Nat. Commun.*, 2017, **8**, 1300.
- S. H. Lee, H. S. Sim, J. Lee, J. M. Kim and Y. E. Shin, *Mater. Trans.*, 2006, **47**, 2835–2841.
- J. Yang, X. Wen, H. Xia, R. Sheng, Q. Ma, J. Kim, P. Tapping, T. Harada, T. W. Kee, F. Huang, Y.-B. Cheng, M. Green, A. Ho-Baillie, S. Huang, S. Shrestha, R. Patterson and G. Conibeer, *Nat. Commun.*, 2017, **8**, 14120.
- H. Zhu, K. Miyata, Y. Fu, J. Wang, P. P. Joshi, D. Niesner, K. W. Williams, S. Jin and X. Y. Zhu, *Science*, 2016, **353**, 1409–1413.
- Y. Yang, D. P. Ostrowski, R. M. France, K. Zhu, J. van de Lagemaat, J. M. Luther and M. C. Beard, *Nat. Photonics*, 2016, **10**, 53–59.
- G. Xing, N. Mathews, S. Sun, S. S. Lim, Y. M. Lam, M. Gratzel, S. Mhaisalkar and T. C. Sum, *Science*, 2013, **342**, 344–347.
- T. C. Sum, N. Mathews, G. Xing, S. S. Lim, W. K. Chong, D. Giovanni and H. A. Dewi, *Acc. Chem. Res.*, 2016, **49**, 294–302.
- M. Li, S. Bhaumik, T. W. Goh, M. S. Kumar, N. Yantara, M. Grätzel, S. Mhaisalkar, N. Mathews and T. C. Sum, *Nat. Commun.*, 2017, **8**, 14350.
- H.-H. Fang, S. Adjokatse, S. Shao, J. Even and M. A. Loi, *Nat. Commun.*, 2018, **9**, 243.
- Y. Zhou, J. Chen, O. M. Bakr and H.-T. Sun, *Chem. Mater.*, 2018, **30**, 6589–6613.
- Q. A. Akkerman, D. Meggiolaro, Z. Dang, F. De Angelis and L. Manna, *ACS Energy Lett.*, 2017, **2**, 2183–2186.
- D. Parobek, B. J. Roman, Y. Dong, H. Jin, E. Lee, M. Sheldon and D. H. Son, *Nano Lett.*, 2016, **16**, 7376–7380.
- W. Liu, Q. Lin, H. Li, K. Wu, I. Robel, J. M. Pietryga and V. I. Klimov, *J. Am. Chem. Soc.*, 2016, **138**, 14954–14961.
- A. K. Guria, S. K. Dutta, S. Das Adhikari and N. Pradhan, *ACS Energy Lett.*, 2017, **2**, 1014–1021.
- S. Ji, X. Yuan, S. Cao, W. Ji, H. Zhang, Y. Wang, H. Li, J. Zhao and B. Zou, *J. Phys. Chem. Lett.*, 2020, **11**, 2142–2149.
- J. Meng, Z. Lan, M. Abdellah, B. Yang, S. Mossin, M. Liang, M. Naumova, Q. Shi, S. L. Gutierrez Alvarez, Y. Liu, W. Lin, I. E. Castelli, S. E. Canton, T. Pullerits and K. Zheng, *J. Phys. Chem. Lett.*, 2020, **11**, 3705–3711.
- D. König, K. Casalenuovo, Y. Takeda, G. Conibeer, J. F. Guillemoles, R. Patterson, L. M. Huang and M. A. Green, *Phys. E*, 2010, **42**, 2862–2866.
- L. Protesescu, S. Yakunin, M. I. Bodnarchuk, F. Krieg, R. Caputo, C. H. Hendon, R. X. Yang, A. Walsh and M. V. Kovalenko, *Nano Lett.*, 2015, **15**, 3692–3696.
- B. Luo, F. Li, K. Xu, Y. Guo, Y. Liu, Z. Xia and J. Z. Zhang, *J. Mater. Chem. C*, 2019, **7**, 2781–2808.

- 25 M. Sikora, C. Kapusta, K. Knížek, Z. Jiráček, C. Autret, M. Borowiec, C. J. Oates, V. Procházka, D. Rybicki and D. Zajac, *Phys. Rev. B: Condens. Matter Mater. Phys.*, 2006, **73**, 1–5.
- 26 F. Thibault-starzyk, A. Ristic and N. Rajic, *Scanning*, 2003, 4745–4750.
- 27 J. Resasco, N. P. Dasgupta, J. R. Rosell, J. Guo and P. Yang, *J. Am. Chem. Soc.*, 2014, **136**, 10521–10526.
- 28 T. Ressler, S. L. Brock, J. Wong and S. L. Suib, *J. Synchrotron Radiat.*, 1999, **6**, 728–730.
- 29 F. Farges, *Phys. Rev. B: Condens. Matter Mater. Phys.*, 2005, **71**, 1–14.
- 30 J. M. Chen, J. M. Lee, S. W. Huang, K. T. Lu, H. T. Jeng, C. K. Chen, S. C. Haw, T. L. Chou, S. A. Chen, N. Hiraoka, H. Ishii, K. D. Tsuei and T. J. Yang, *Phys. Rev. B: Condens. Matter Mater. Phys.*, 2010, **82**, 1–8.
- 31 L. Hozoi, A. H. de Vries and R. Broer, *Phys. Rev. B: Condens. Matter Mater. Phys.*, 2001, **64**, 4–7.
- 32 Y. Hu, C. N. Borca, E. Kleymenov, M. Nachtegaal, B. Delley, M. Janousch, A. Dönni, M. Tachibana, H. Kitazawa, E. Takayama-Muromachi, M. Kenzelmann, C. Niedermayer, T. Lippert, A. Wokaun and C. W. Schneider, *Appl. Phys. Lett.*, 2012, **100**, 252901.
- 33 M. Croft, D. Sills, M. Greenblatt and C. Lee, *Phys. Rev. B: Condens. Matter Mater. Phys.*, 1997, **55**, 8726–8732.
- 34 A. H. De Vries, L. Hozoi and R. Broer, *Int. J. Quantum Chem.*, 2002, **91**, 57–61.
- 35 J. Chaboy, C. Prieto, M. Hernando, M. Parras and J. González-Calbet, *Phys. Rev. B: Condens. Matter Mater. Phys.*, 2006, **74**, 1–11.
- 36 M. B. Price, J. Butkus, T. C. Jellicoe, A. Sadhanala, A. Briane, J. E. Halpert, K. Broch, J. M. Hodgkiss, R. H. Friend and F. Deschler, *Nat. Commun.*, 2015, **6**, 8420.
- 37 N. R. Yogamalar and A. Chandra Bose, *Appl. Phys. A*, 2011, **103**, 33–42.
- 38 P. D. Cunningham, A. T. Hanbicki, K. M. McCreary and B. T. Jonker, *ACS Nano*, 2017, **11**, 12601–12608.
- 39 M. Li, J. Fu, Q. Xu and T. C. Sum, *Adv. Mater.*, 2019, **31**, 1802486.
- 40 W. Cao, L. Yuan, R. Patterson, X. Wen, P. C. Tapping, T. Kee, B. P. Veetil, P. Zhang, Z. Zhang, Q. Zhang, P. Reece, S. Bremner, S. Shrestha, G. Conibeer and S. Huang, *Nanoscale*, 2017, **9**, 17133–17142.
- 41 V. Klimov, P. Haring Bolivar and H. Kurz, *Phys. Rev. B: Condens. Matter Mater. Phys.*, 1995, **52**, 4728–4731.
- 42 L. Wang, Z. Chen, G. Liang, Y. Li, R. Lai, T. Ding and K. Wu, *Nat. Commun.*, 2019, **10**, 4532.
- 43 F. Sekiguchi, H. Hirori, A. Shimazaki, T. Nakamura, A. Wakamiya and Y. Kanemitsu, *Phys. Rev. Lett.*, 2021, **126**, 077401.
- 44 X. Jia, J. Jiang, Y. Zhang, J. Qiu, S. Wang, Z. Chen, N. Yuan and J. Ding, *Appl. Phys. Lett.*, 2018, **112**, 143903.
- 45 J. Chen, M. E. Messing, K. Zheng and T. Pullerits, *J. Am. Chem. Soc.*, 2019, **141**, 3532–3540.
- 46 S. Feldmann, M. K. Gangishetty, I. Bravić, T. Neumann, B. Peng, T. Winkler, R. H. Friend, B. Monserrat, D. N. Congreve and F. Deschler, *J. Am. Chem. Soc.*, 2021, **143**, 8647–8653.
- 47 H. Kawai, G. Giorgi, A. Marini and K. Yamashita, *Nano Lett.*, 2015, **15**, 3103–3108.
- 48 J. Even, L. Pedesseau and C. Katan, *J. Phys. Chem. C*, 2014, **118**, 11566–11572.
- 49 B. S. S. Rudin and T. L. Reinecke, *Phys. Rev. B: Condens. Matter Mater. Phys.*, 1990, **42**, 218–231.
- 50 A. D. Wright, C. Verdi, R. L. Milot, G. E. Eperon, M. A. Pérez-Osorio, H. J. Snaith, F. Giustino, M. B. Johnston and L. M. Herz, *Nat. Commun.*, 2016, **7**, 11755.
- 51 S. Kahmann and M. A. Loi, *J. Mater. Chem. C*, 2019, **7**, 2471–2486.
- 52 G. J. Conibeer, D. König, M. A. Green and J. F. Guillemoles, *Thin Solid Films*, 2008, **516**, 6948–6953.
- 53 A. Shafique and Y. H. Shin, *Phys. Chem. Chem. Phys.*, 2017, **19**, 32072–32078.
- 54 D. B. Straus, S. Hurtado Parra, N. Iotov, J. Gebhardt, A. M. Rappe, J. E. Subotnik, J. M. Kikkawa and C. R. Kagan, *J. Am. Chem. Soc.*, 2016, **138**, 13798–13801.

Supporting Information

Optimizing the quasi-equilibrium state of hot carriers in all-inorganic lead halide perovskite nanocrystals through Mn-doping: fundamental dynamics and device perspectives

Jie Meng^{†,1}, Zhenyun Lan^{‡,1}, Weihua Lin[#], Mingli Liang[†], Xianshao Zou[#], Qian Zhao[†], Huifang Geng[¶], Ivano E. Castelli[‡], Sophie E. Canton[§], Tönu Pullerits[#], and Kaibo Zheng^{*,†,#}

[†]Department of Chemistry, Technical University of Denmark, DK-2800 Kongens Lyngby, Denmark;

[‡]Department of Energy Conversion and Storage, Technical University of Denmark, DK-2800 Kongens Lyngby, Denmark;

[#]Chemical Physics and NanoLund, Lund University, Box 124, 22100 Lund, Sweden;

[¶]Ultrafast Electron Microscopy Laboratory, The MOE Key Laboratory of Weak-Light Nonlinear Photonics, School of Physics, Nankai University, Tianjin 300071, China;

[§] European XFEL, Holzkoppel 4, 22869 Schenefeld, Germany.

*Corresponding Author

Kaibo Zheng: kzheng@kemi.dtu.dk, kaibo.zheng@chemphys.lu.se.

¹This authors contribute equally in this work

Experimental Section

Materials and Chemicals. Cesium carbonate (Cs_2CO_3 , ReagentPlus 99%, Sigma-Aldrich), Lead iodide (PbI_2 , 99%, Sigma-Aldrich), Manganese iodide (MnI_2 anhydrous, 99.99% trace metals basis, Sigma-Aldrich), Oleylamine (OAm, technical grade 70%, Sigma-Aldrich), Oleic acid (OA, technical grade 90%, Sigma-Aldrich), 1-Octadecene (ODE, technical grade 90%, Sigma-Aldrich), Toluene (anhydrous 99.8%, Sigma-Aldrich).

Preparation of Cs-OA. Cs_2CO_3 (0.407 g), OA (1.5 mL), and ODE (20 mL) were added to a 50-mL 3-neck round-bottomed flask, evacuated and refilled with argon, dried at 120 °C for 30 min, then heated to 150 °C for at least 10 minutes until all Cs_2CO_3 reacted with OA before using.

Synthesis of Mn-doped CsPbI_3 NCs. Typically, PbI_2 (0.087 g, 0.188 mmol), MnI_2 (precursor: 0-0.01-0.02-0.03 g), OAm (0.5 mL), OA (0.5 mL), ODE (5 mL) were added to a 25-mL 3 neck round bottom flask and were evacuated and refilled with Ar followed by heating the solution to 120 °C for 30 minutes. Then dried OAm (0.5 mL) and dried OA (0.5 mL) were subsequently injected to solubilize the solution. The solution was then increased to 160 °C. At 160 °C, the Cs-oleate (0.4 mL) was swiftly injected and after 1 minute the solution was cooled with an ice/water bath. After reaction, the aggregated NCs were centrifuged at 6000 rpm for 5 min. After centrifugation, the supernatant was discarded and the precipitate was redispersed in dried toluene. And then, the solution will be centrifuged at 6000 rpm for 5 min and the supernatant will be redispersed in toluene for further measurement. The dopant concentration (0%, 5%, 7%, 10%) are obtained by Inductively coupled plasma mass spectrometry (ICP-MS).

Characterization. The absorption spectra were measured in a UV-Vis absorption spectrophotometer from Agilent Technologies (Santa Clara, USA). Steady-state

photoluminescence was measured using a FluoroMax@-4 spectrofluorometer (HORIBA JOBIN YVON, Inc., Edison, NJ) with the excitation at 500 nm. Transmission electron microscopy (TEM) imaging was conducted on Tecnai G² T20 TEM. The Mn doping concentration was determined by coupled mass spectrometry (*ICP-MS*)

TA measurement. The transient absorption (TA) experiments were performed on a femtosecond pump-probe setup. Laser pulses (800 nm, 80 fs pulse length, 0.5 kHz repetition rate) were generated by a femtosecond oscillator (Mai Tai SP, both Spectra Physics). The pump pulses at 400 nm, 500 nm and 570 nm were generated by an optical parametric amplifier (Topas, Light Conversion). For the probe, we used the super-continuum generation from a thin CaF₂ plate. The mutual polarization between pump and probe beams was set to the magic angle (54.7°) by placing a Berek compensator in the pump beam. The probe pulse and the reference pulse were dispersed in a spectrograph and detected by a diode array (Pascher Instruments). Excitation power and spot size measurements were used to determine the excitation fluence. To prevent sample degeneration, several strategies have been carried out: 1) the sample will be prepared only before spectroscopic measurement. 2) For each measurement, we will change the fresh sample. After measurement, we also checked the UV-vis absorption spectroscopies to check the samples.

Absorption cross-section determination. NCs can be excited to multiple exciton states by high excitation fluence. With a usual assumption, the initially generated multiple exciton population follows the Poissonian distribution

$$P_N = \frac{e^{-\langle N \rangle} \cdot \langle N \rangle^N}{N!} \quad (\text{S1})$$

where $\langle N \rangle$ is the average number of excitons per NCs, N is the number of excitons, and P_N is the fraction of NCs with N excitons. We can use $\langle N \rangle = \sigma \cdot I$ to present the average number of excitons

per NCs, where σ is the absorption cross-section at the excitation wavelength and I is the excitation intensity in units of the number of photons per pulse per excitation area. From equation S1, we can calculate the fraction of excited NCs, P_{exc} , as:

$$P_{exc} = \sum_{N=1}^{\infty} P_N = 1 - P_0 = 1 - e^{-\langle N \rangle} = 1 - e^{-\sigma I} \quad (S2)$$

If we know P_{exc} , σ can be calculated from (S2). We obtain P_{exc} by measuring the excitation intensity dependence of the late-time region signal ($t > 1$ ns), which corresponds to the last remaining exciton after the Auger process. Due to multiple excitations generated at high pump intensity excitation in NCs is rapidly lost via Auger process leaving only one excitation at late time region ($t > 1$ ns). The signal $\Delta A_0(I, t > 1$ ns) intensity can be rescaled to the corresponding signal at $t=0$, which we call $\Delta A_0(I)$. We use the lowest excitation intensity as reference excitation intensity and corresponding average number of excitons per NCs, $\langle N \rangle_0$, as reference number of excitons per NCs.

$$\Delta A_0(I) = \frac{\Delta A(I, t > 1 \text{ ns})}{e^{-t/\tau}} = \Delta A_{0,max} \cdot (1 - e^{-(I/I_0) \cdot \langle N \rangle_0}) \quad (S3)$$

ΔA_0 denotes the largest possible single-exciton signal rescaled to $t=0$.

Based on the rescaled signal $\Delta A_0(I)$, we perform exponential fit to equation S3. From the fitting, we get the value of $\langle N \rangle_0$, and absorption cross-section σ of Mn doped CsPbI₃ NCs at 400 nm (3.1 eV) were calculated. The absorption cross-section σ at 500 nm and 570 nm were calculated based on the values of σ at 400 nm and absorption spectra.

Power loss of the hot carriers. The power loss of hot carriers is obtained from the time-dependent hot carriers temperature T_c using follow equation. k_B is Boltzmann constant.

$$P = \frac{d\left(\frac{3}{2} k_B T_c\right)}{dt} \quad (\text{S4})$$

Average lifetime calculation

A multi-exponential model was used to fit the cooling process curves. The model is described as follows:

$$f(x) = A + \sum B_i \exp(-x/t_i)$$

where t_i represents the time constants and B_i represents the amplitudes of the fast and slow components, respectively. The average lifetime was calculated as follows:

$$t_{\text{ave}} = (\sum B_i t_i^2) / (\sum B_i t_i)$$

DFT calculation

The density functional theory (DFT) calculations were performed using Perdew-Burke-Ernzerhof (PBE) exchange correlation functional,¹ as implemented in the Vienna ab initio package (VASP).² The electronic wave functions were calculated by using projected augmented wave (PAW)³ with a plane-wave cutoff of 520 eV. Due to the heavy Pb atom in CsPbCl₃, spin-orbit coupling (SOC) was included for the electronic properties calculation. The unit cell CsPbCl₃ structure is cubic containing 5 atoms with lattice parameter of 6.401 Å. A single Pb atom was replaced by a Mn atom in the 2 x 2 x 2 supercell corresponding to Mn concentration of 6.25%. Phonon spectrum was calculated using the DFPT method by the Phonon code. The Brillouin zone samplings were carried out with a Γ -center 4 x 4 x 4 k-point mesh. The atomic forces were relaxed to be less than

0.01 Å⁻¹. While for the HSE06 band structure calculation, the plane wave cutoff was set as 300 eV and the Brillouin zone was sampled by 2 x 2 x 2 Γ -centered k-point grid. It should also be noted that the imaginary phonon modes with a negative frequency result from the metastable lattice of the perovskite where the permanent displacement of the atoms is possible through distortions of the crystal lattice.

X-ray absorption measurements

X-ray absorption spectra were acquired at P65 beamline of Petra III, Deutsches Elektronen - Synchrotron (DESY), Hamburg.⁴ The beam was monochromatized using Si(111) crystal pair. Higher harmonics rejection was done with two Si-coated mirrors. Solutions of Mn-doped nanoparticles in toluene were filled into 2 mm quartz capillaries (wall thickness 0.02 mm) which were positioned horizontally at 45 degrees to the incoming beam. Beam size on the sample was 2 mm (hor.) * 0.5 mm (ver.). Data were acquired in fluorescence mode using a 4 pixel Silicon drift detector. Spectra were taken in continuous scanning mode. First, damage tests were done by performing 30 s scans in -50 to 100 eV energy range around Mn K-edge. Then, based on the data quality, extended XANES range was chosen for the study: -100 to 300 eV measured for 120 s; many repetitions were done to improve the data quality. Mn foil was installed downstream of the sample for energy calibration. The maximum of first derivative of the foil was calibrated to 6539 eV.

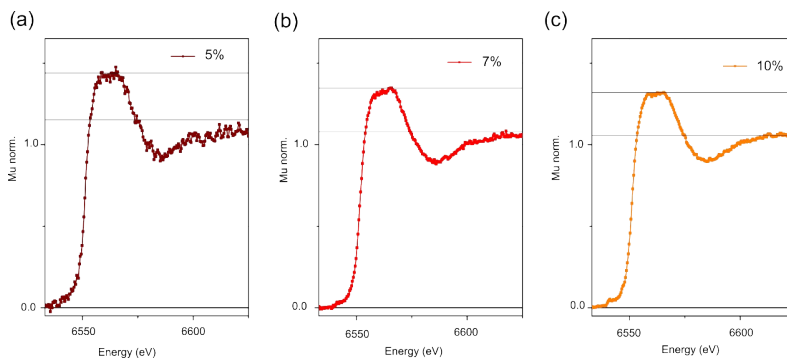


Figure S0. Normalized XANES feature for 5% (a), 7% (b) and 10% (c) doping. The solid lines indicate the maximum intensities and their values at 80% of the maximum in order to estimate the width of the white line features.

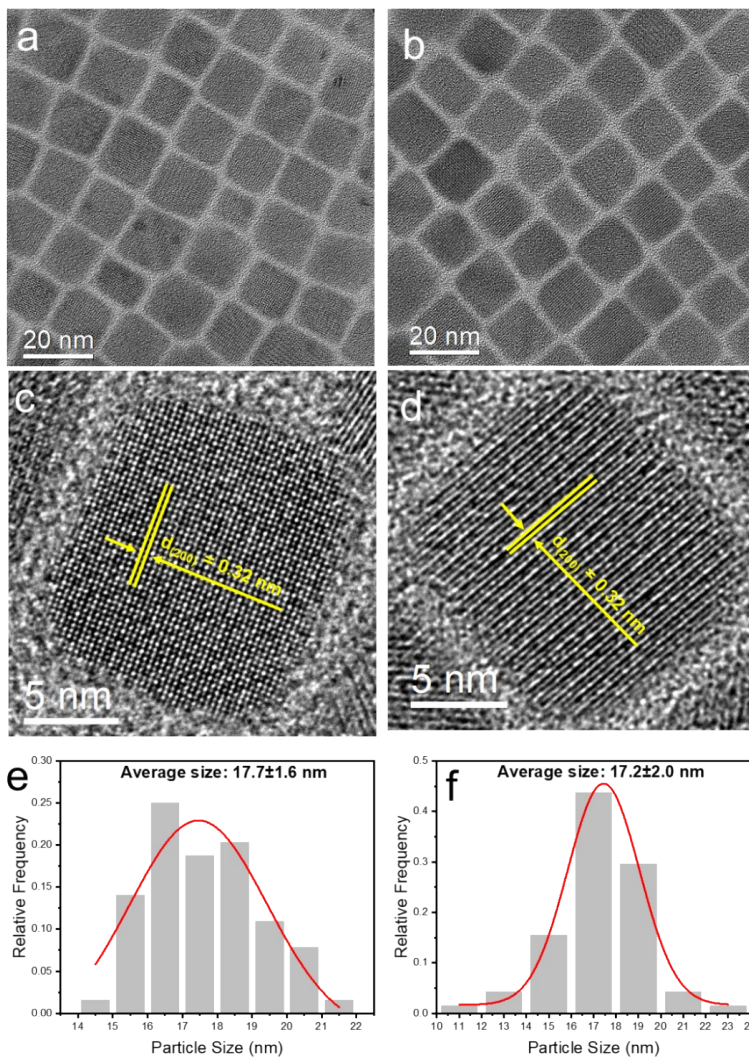


Figure S1. The TEM images and size distribution of samples. The TEM images of (a) undoped CsPbI₃ and (b) Mn doped CsPbI₃. The HRTEM images of (c) undoped and (d) doped NCs. The corresponding size distribution of (e) undoped CsPbI₃ and (f) Mn doped CsPbI₃.

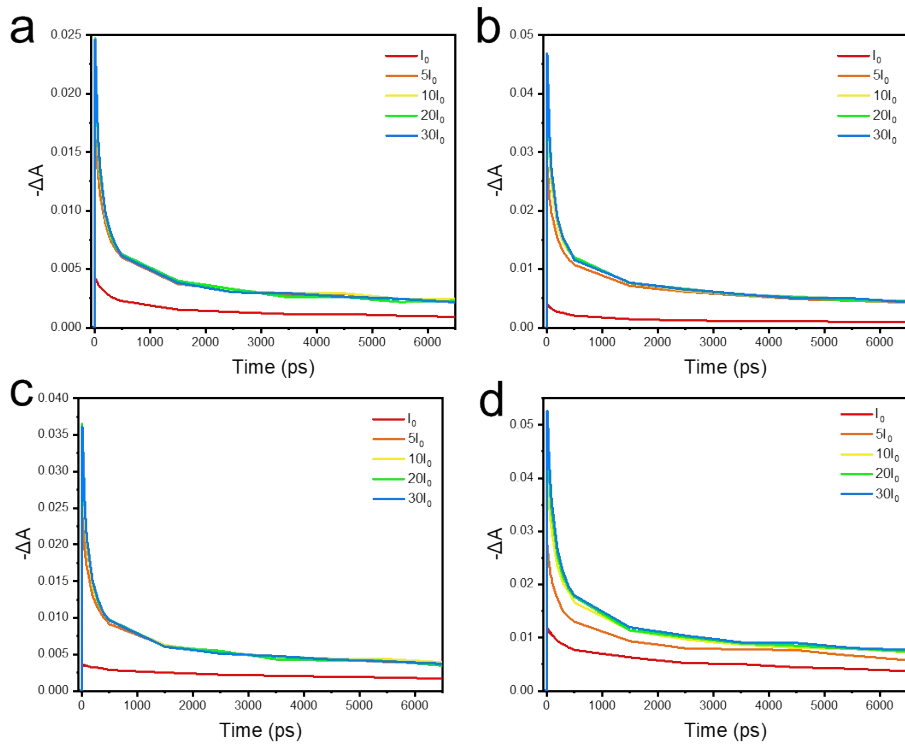


Figure S2. Pump fluence dependent TA kinetics for Mn doped CsPbI₃ NCs pumped at 400 nm (3.1 eV) probed at band-edge, $I_0=1.603 \times 10^{13}$ photons/cm²/pulse. (a) 0%, (b) 5%, (c) 7% and (d) 10%.

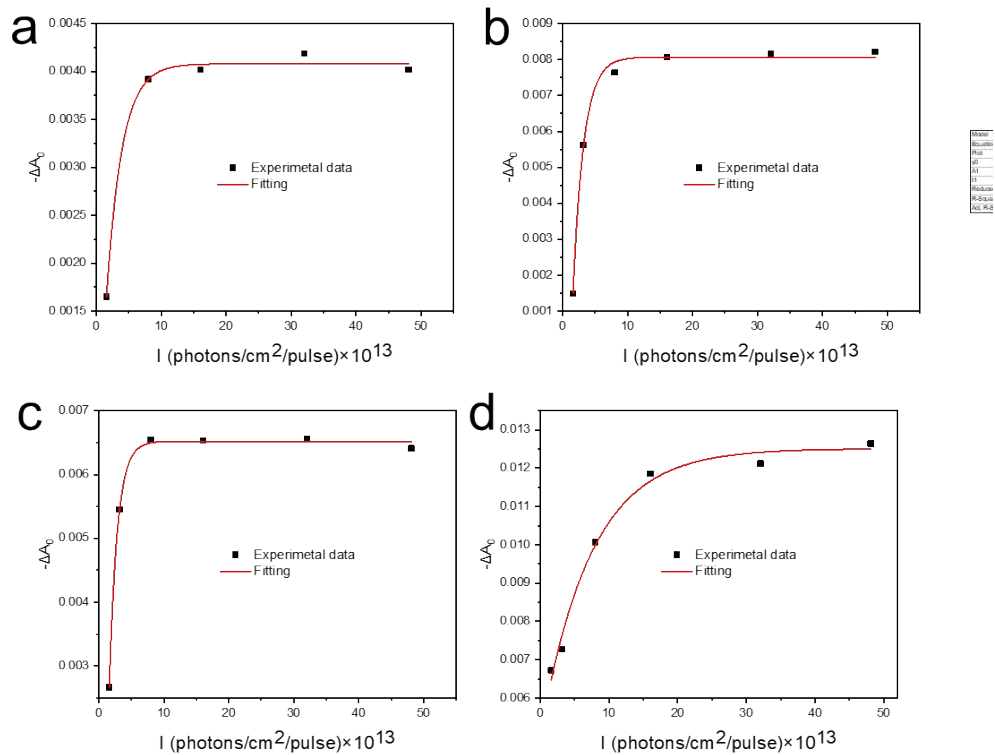


Figure S3. TA signal ΔA_0 rescaled from $\Delta t \geq 1$ ns as a function of pump fluence for Mn doped CsPbI₃ NCs pumped at 400 nm (3.1 eV) and probed at band-edge. (a) 0%, (b) 5%, (c) 7% and (d) 10%.

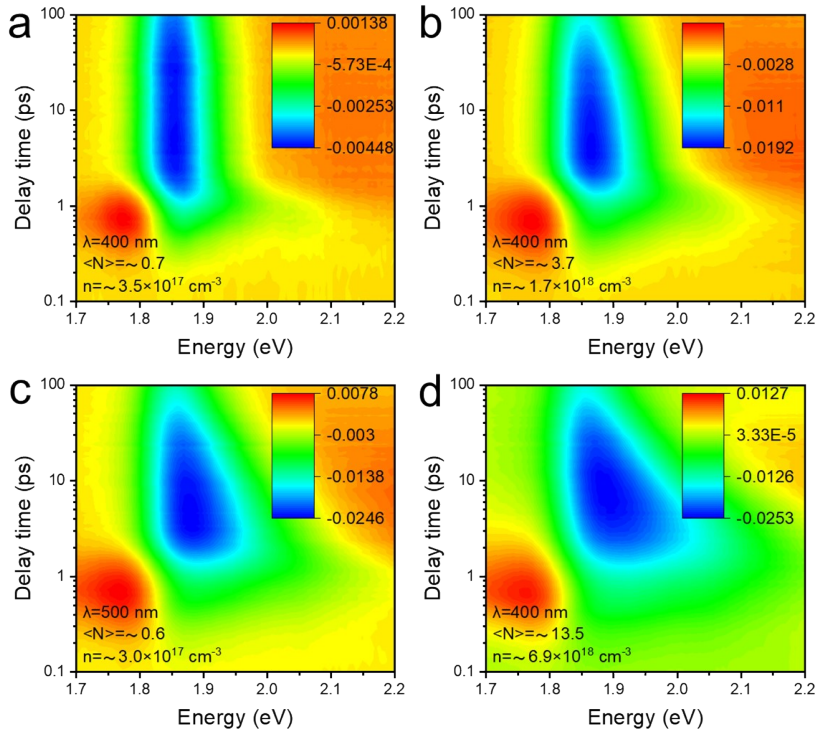


Figure S4. Pseudocolor representation TA spectra of undoped CsPbI₃ NCs for 400 nm excitation with different excitation intensities. (a) I1, (b) I2, (c) I3 and (d) I4.

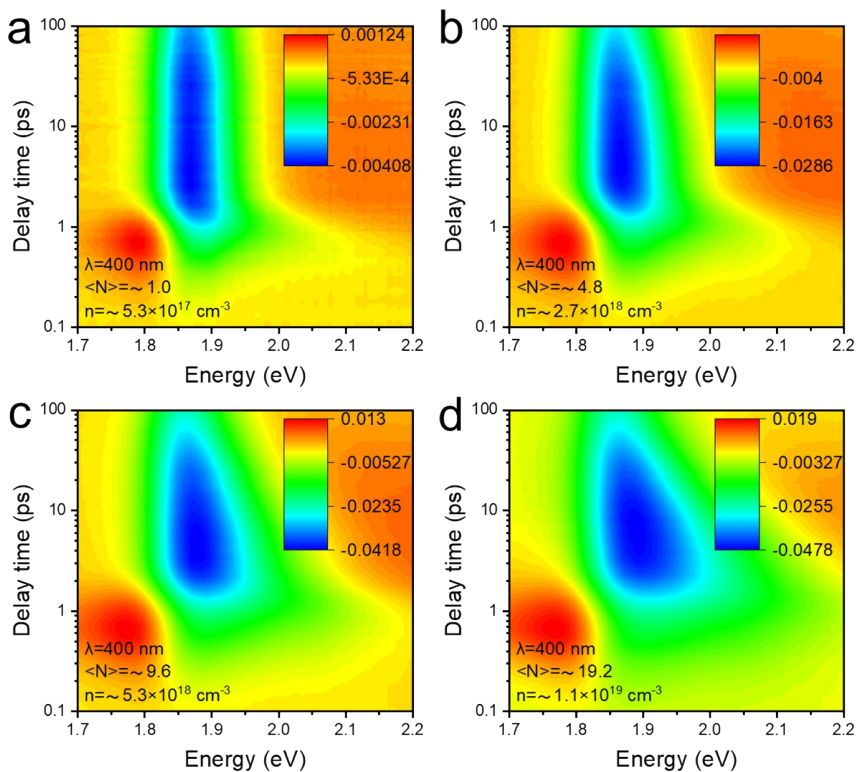


Figure S5. Pseudocolor representation TA spectra of Mn doped CsPbI₃ NCs for 400 nm excitation with different excitation intensities. (a) I1, (b) I2, (c) I3 and (d) I4.

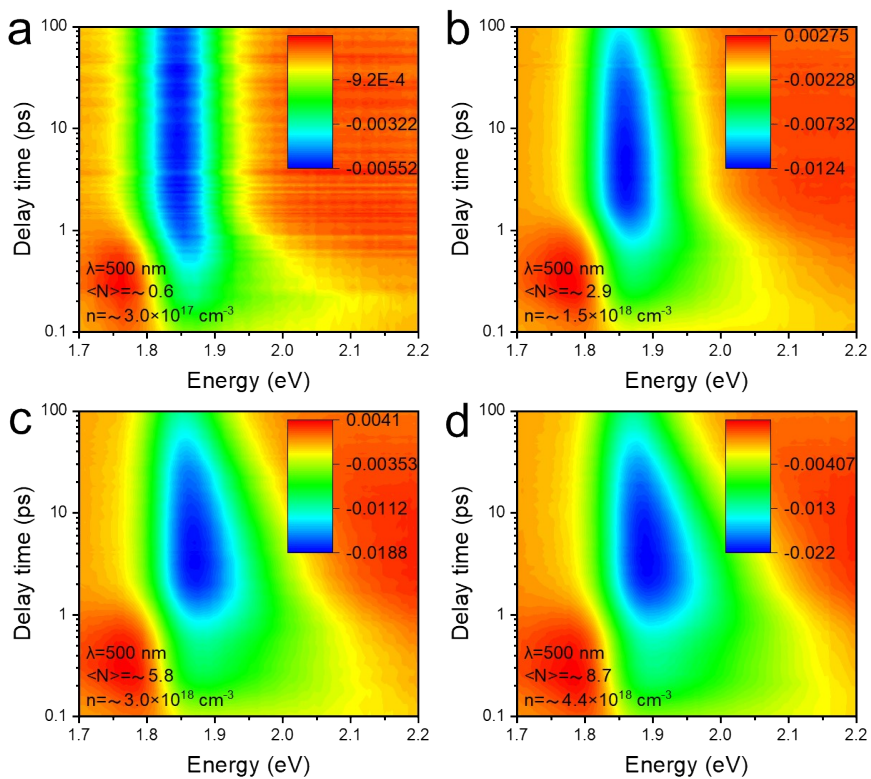


Figure S6. Pseudocolor representation TA spectra of undoped CsPbI₃ NCs for 500 nm excitation with different excitation intensities. (a) I1, (b) I2, (c) I3 and (d) I4.

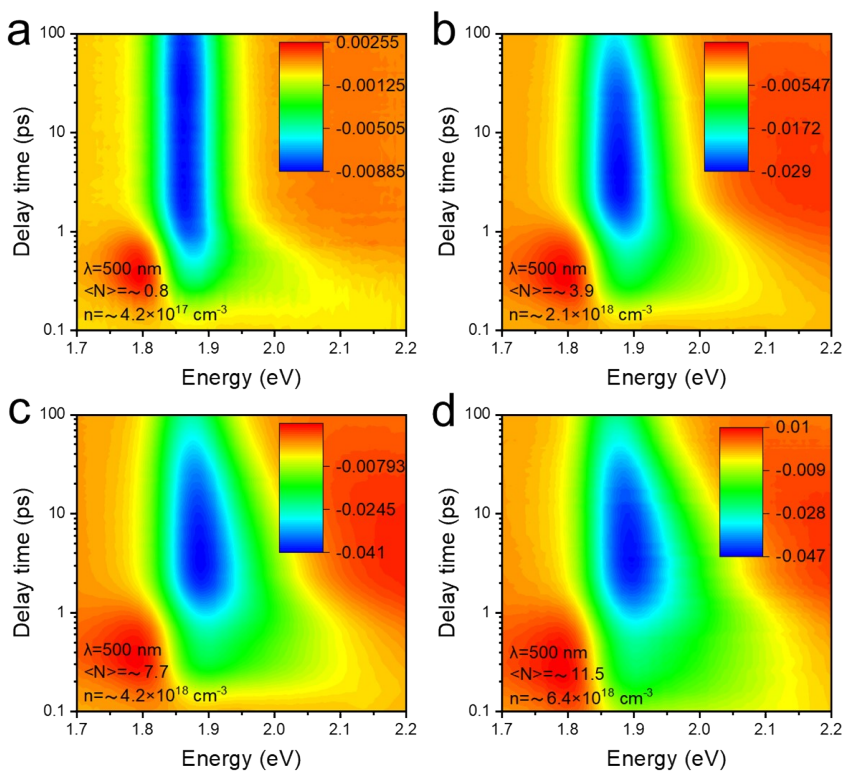


Figure S7. Pseudocolor representation TA spectra of Mn doped CsPbI₃ NCs for 500 nm excitation with different excitation intensities. (a) I1, (b) I2, (c) I3 and (d) I4.

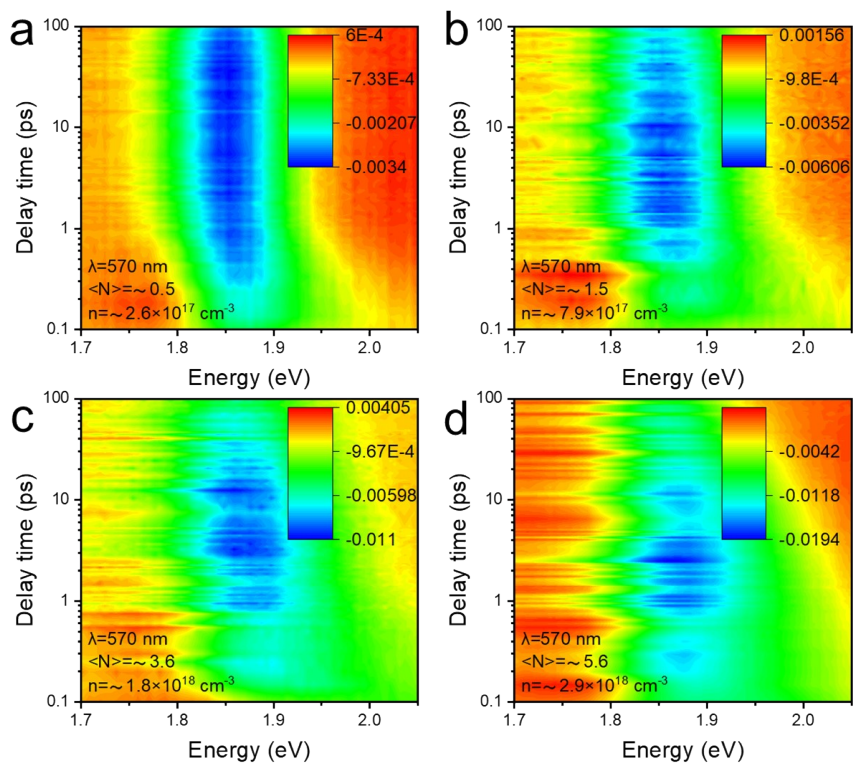


Figure S8. Pseudocolor representation TA spectra of undoped CsPbI₃ NCs for 570 nm excitation with different excitation intensities. (a) I1, (b) I2, (c) I3 and (d) I4.

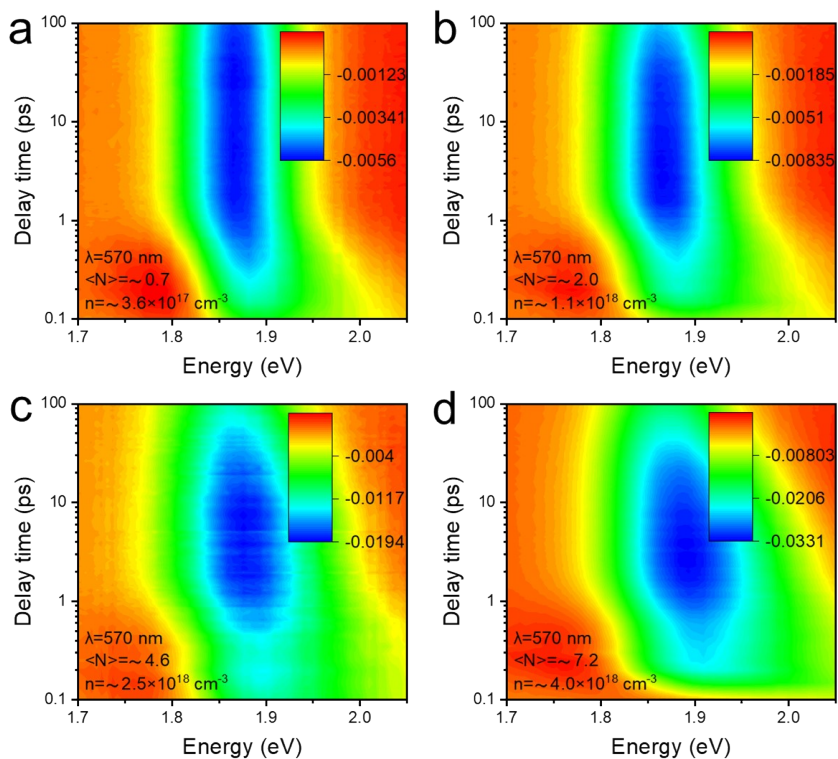


Figure S9. Pseudocolor representation TA spectra of Mn doped CsPbI₃ NCs for 570 nm excitation with different excitation intensities. (a) I1, (b) I2, (c) I3 and (d) I4.

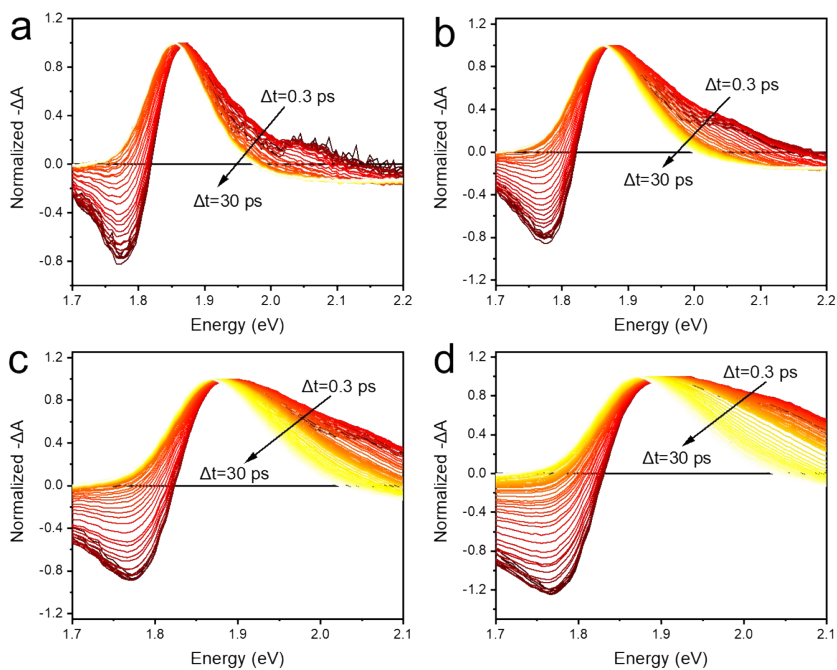


Figure S10. Normalized TA spectra of undoped CsPbI₃ NCs under 400 nm excitation with different excitation energies. (a) I1, (b) I2, (c) I3 and (d) I4. The shortest time delay (red) is 0.3 ps and the longest (yellow) is 30 ps.

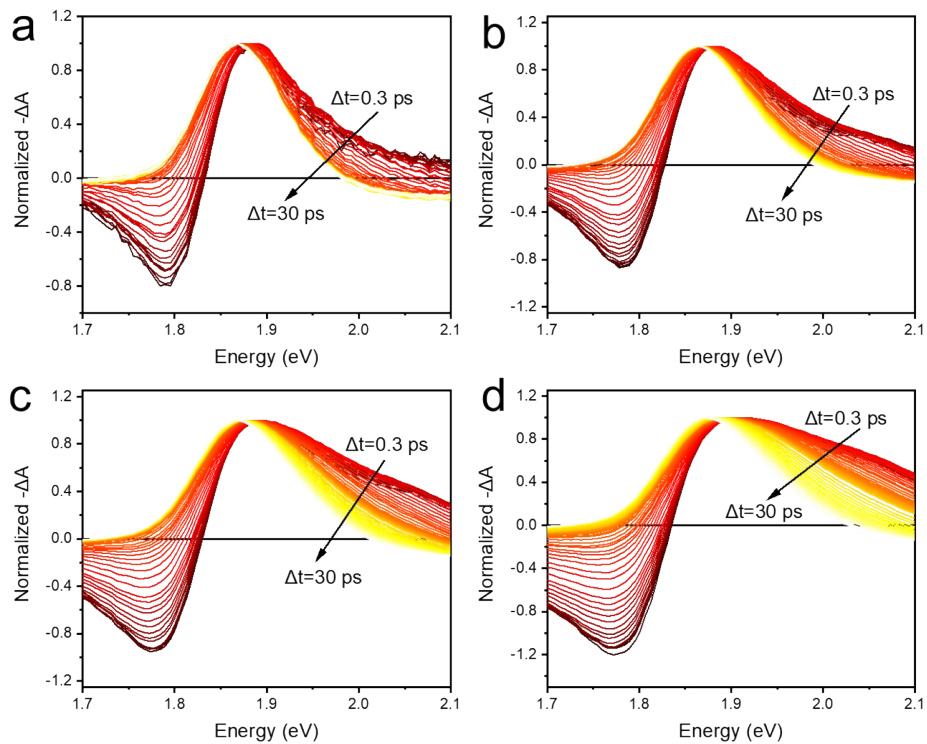


Figure S11. Normalized TA spectra of Mn doped CsPbI₃ NCs under 400 nm excitation with different excitation energies. (a) I1, (b) I2, (c) I3 and (d) I4. The shortest time delay (red) is 0.3 ps and the longest (yellow) is 30 ps.

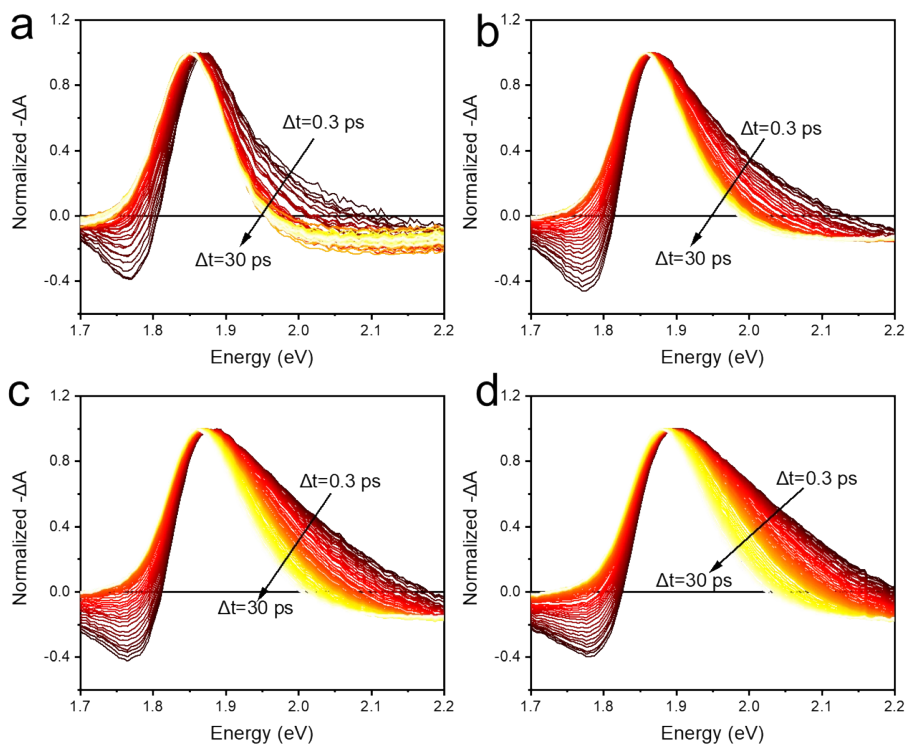


Figure S12. Normalized TA spectra of undoped CsPbI₃ NCs under 500 nm excitation with different excitation energies. (a) I1, (b) I2, (c) I3 and (d) I4. The shortest time delay (red) is 0.3 ps and the longest (yellow) is 30 ps.

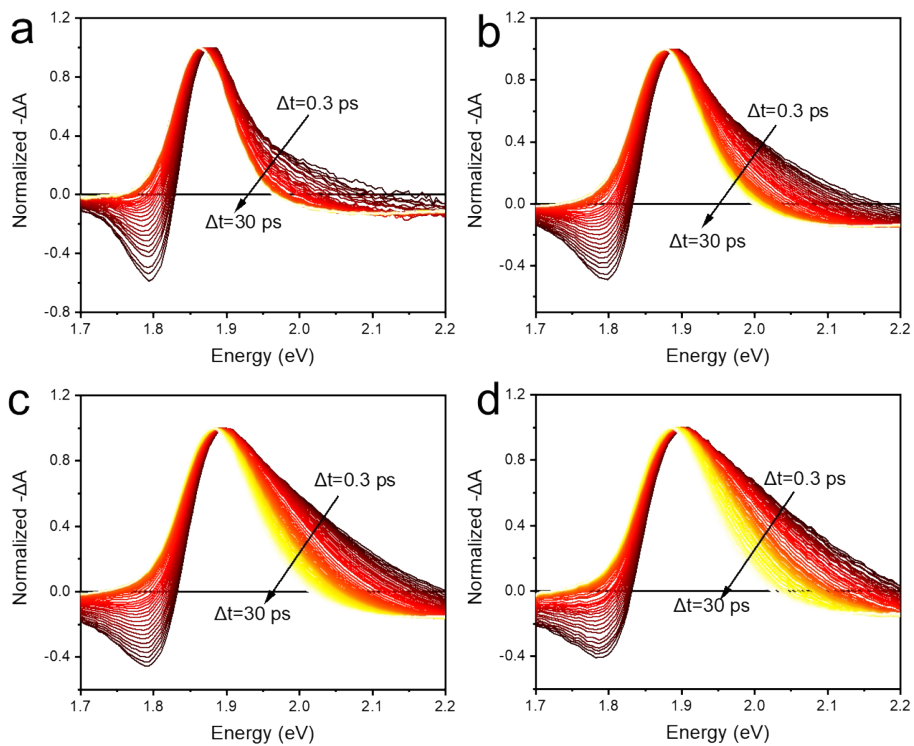


Figure S13. Normalized TA spectra of Mn doped CsPbI₃ NCs under 500 nm excitation with different excitation energies. (a) I1, (b) I2, (c) I3 and (d) I4. The shortest time delay (red) is 0.3 ps and the longest (yellow) is 30 ps.

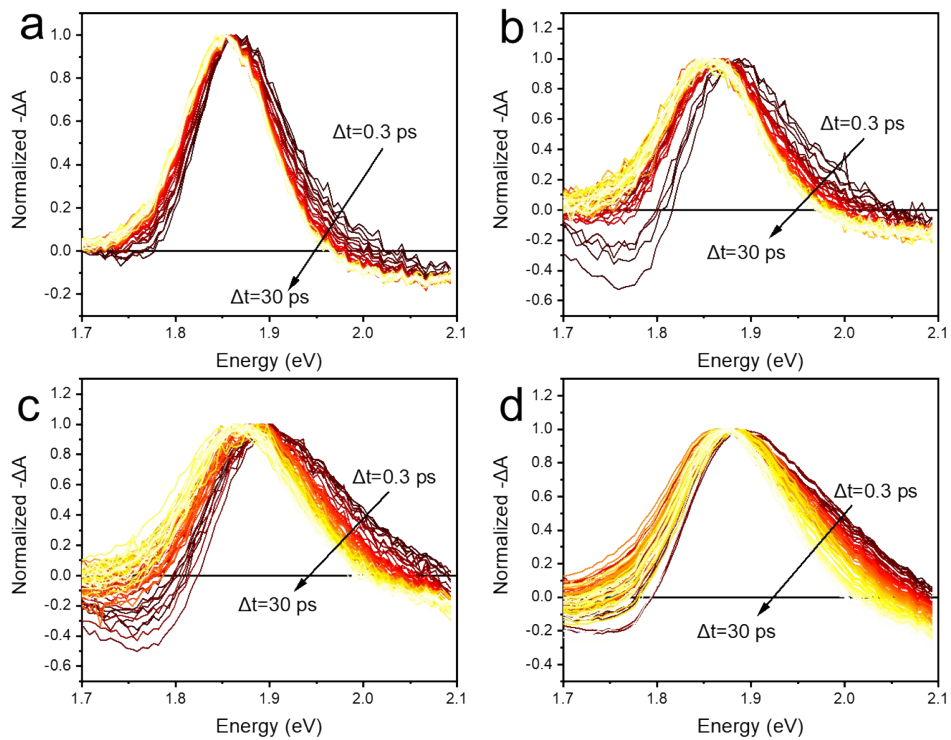


Figure S14. Normalized TA spectra of undoped CsPbI₃ NCs under 570 nm excitation with different excitation energies. (a) I1, (b) I2, (c) I3 and (d) I4. The shortest time delay (red) is 0.3 ps and the longest (yellow) is 30 ps.

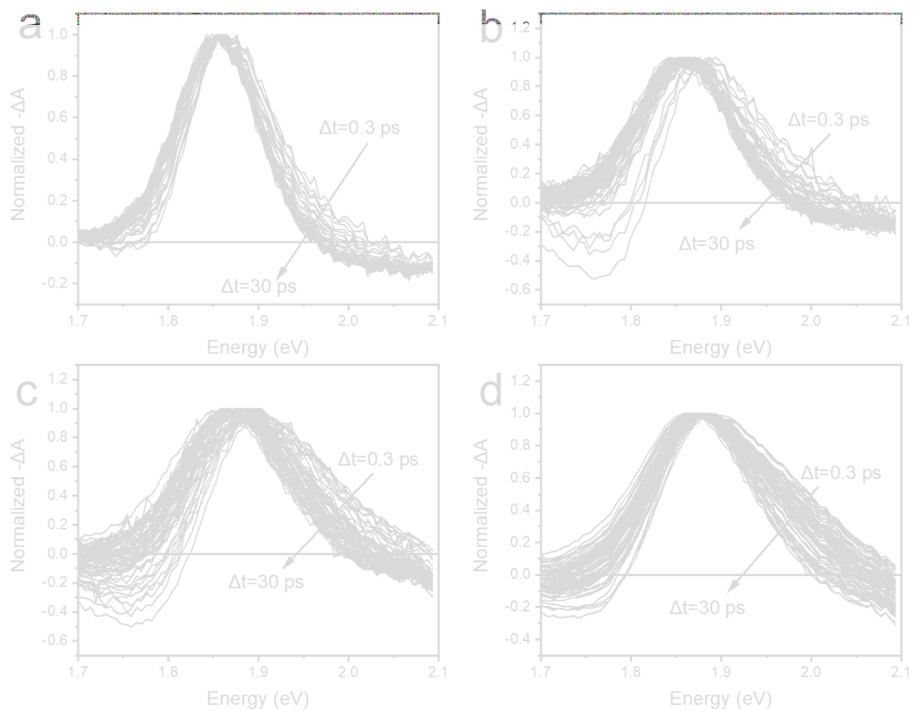


Figure S15. Normalized TA spectra of Mn doped CsPbI₃ NCs under 570 nm excitation with different excitation energies. (a) I1, (b) I2, (c) I3 and (d) I4. The shortest time delay (red) is 0.3 ps and the longest (yellow) is 30 ps.

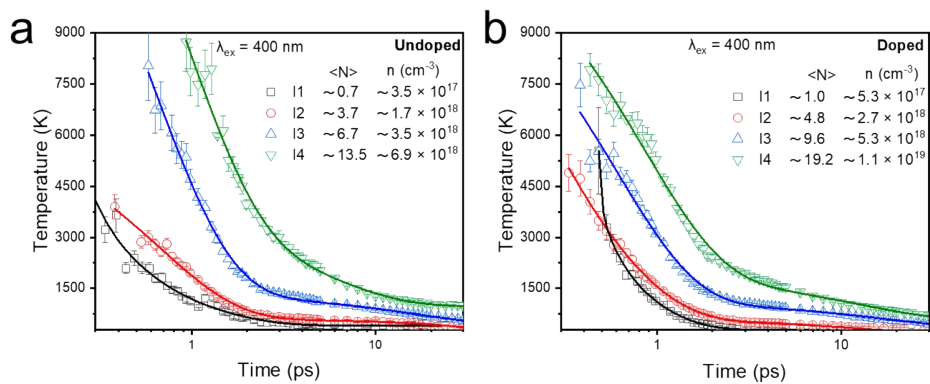


Figure S16. Time-dependent carrier temperature with 400 nm excitation at four different excitation intensities for (a) undoped and (b) Mn doped CsPbI₃ NCs.

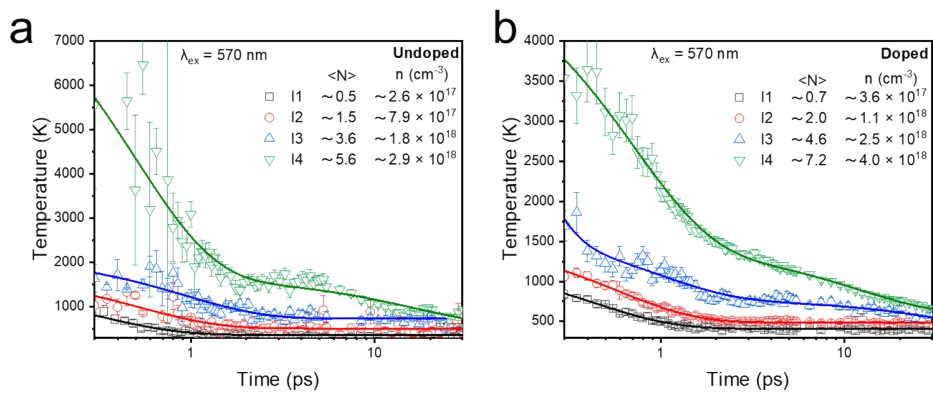


Figure S17. Time-dependent carrier temperature with 570 nm excitation at four different excitation intensities for (a) undoped and (b) Mn doped CsPbI₃ NCs.

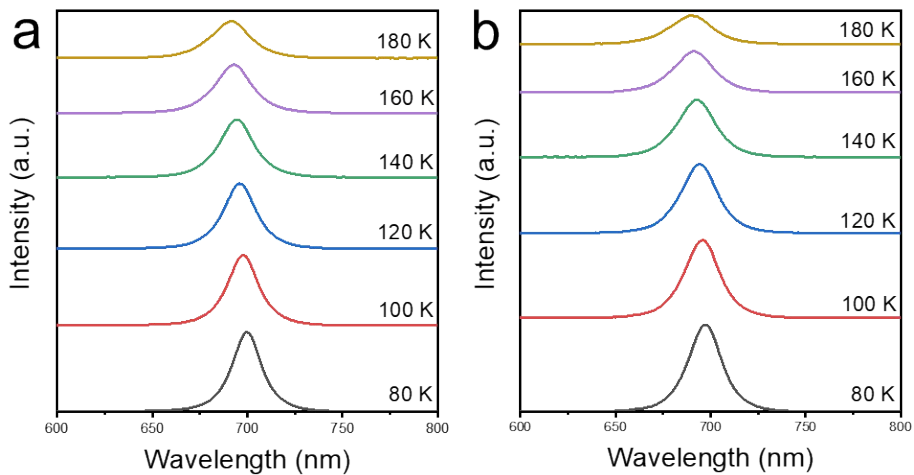


Figure S18. Temperature dependent PL emission spectra of Mn doped CsPbI₃ NCs as function of temperature (80 K to 180 K) for different doping concentration. (a) 0% and (b) 5%.

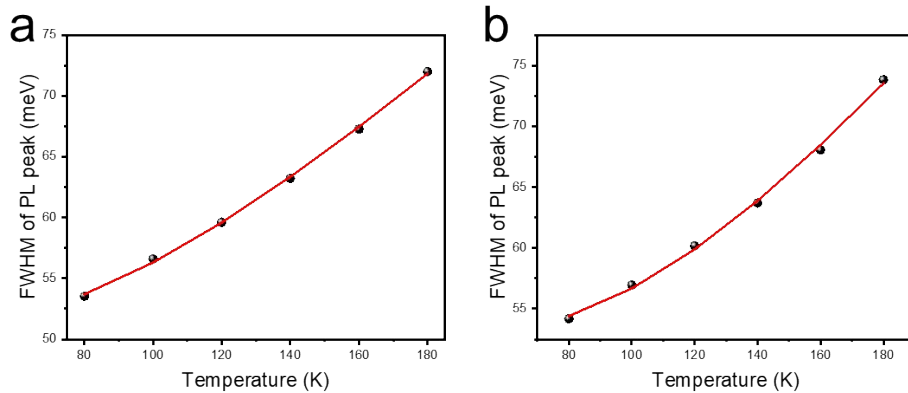


Figure S19. FWHM of the steady-state PL spectra as a function of temperature for of Mn doped CsPbI₃ NCs (80 K to 180 K) for different doping concentration. (a) 0% and (b) 5%.

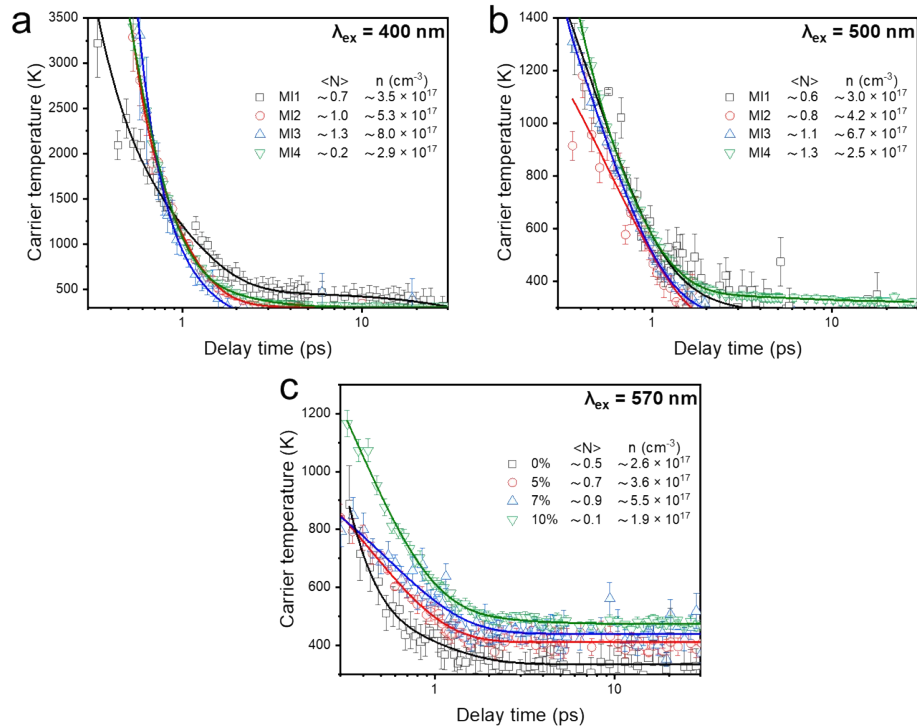


Figure S20. Time-dependent carrier temperature for different doping concentration at low excitation intensity with (a) 400 nm, (b) 500 nm and (c) 570 nm excitation energy.

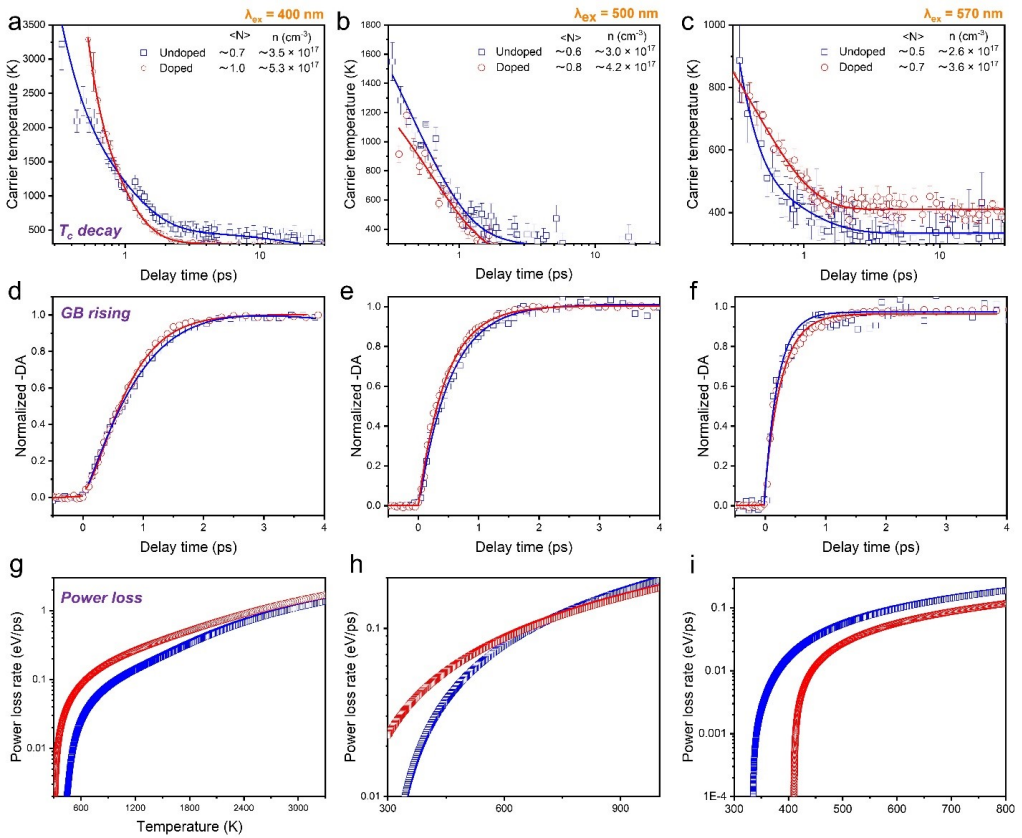


Figure S21. Time-dependent carrier temperature for undoped and Mn-doped CsPbI₃ NCs at low excitation density ($\langle N \rangle < 1$) with (a) 400 nm, (b) 500 nm and (c) 570 nm excitation energy. Normalized GB dynamics probed at the band-edge for undoped and Mn-doped CsPbI₃ NCs at low excitation intensity with (d) 400 nm, (e) 500 nm, and (f) 570 nm excitation energy. Power loss as a function of the inverse carrier temperature for the exponential fitting data from Figure 4a-3c of undoped and Mn-doped CsPbI₃ NCs at low excitation intensity with (g) 400 nm, (h) 500 nm, and (i) 570 nm excitation energy.

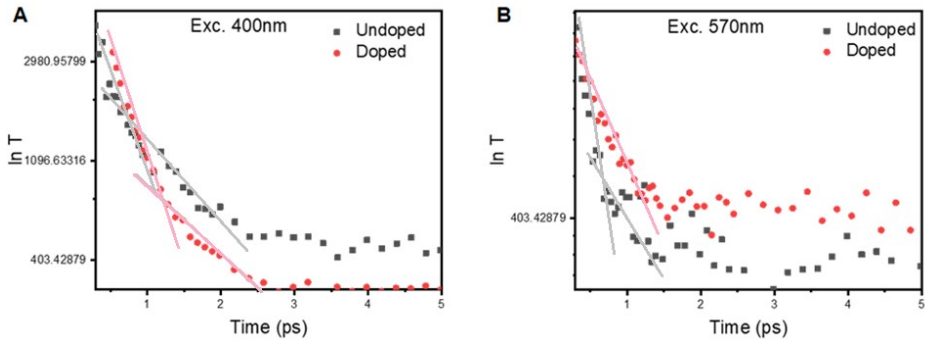


Figure S22. Time-dependent carrier temperature ($\ln T$) for undoped and Mn-doped CsPbI_3 NCs at low excitation density ($\langle N \rangle < 1$) with (a) 400 nm (3.1 eV) and (b) 570 nm (2.18 eV) excitation energy.

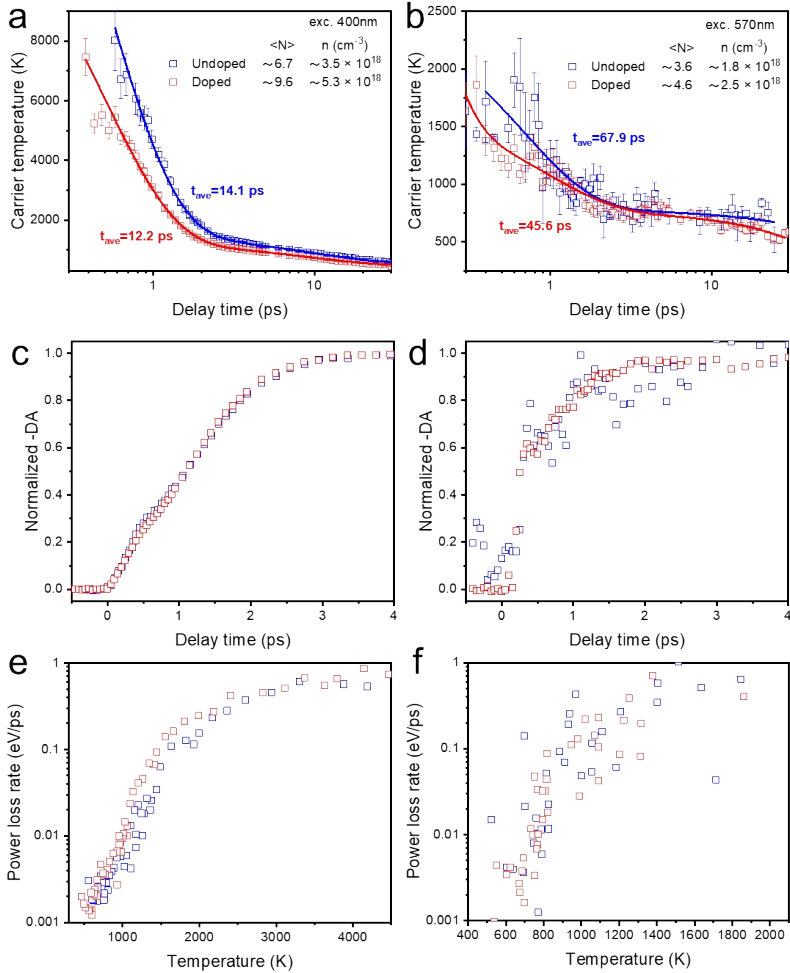


Figure S23. Time-dependent carrier temperature for undoped and Mn-doped CsPbI₃ NCs at high excitation density ($\langle N \rangle \gg 1$) with (a) 2.18 eV and (b) 3.1 eV excitation energy. Normalized GB dynamics probed at the band-edge for undoped and Mn-doped CsPbI₃ NCs at low excitation intensity with (c) 2.18 eV and (d) 3.1 eV excitation energy. Power loss as a function of the carrier temperature of Mn-doped CsPbI₃ NCs and corresponding exponential fitting at low excitation intensity with (e) 2.18 eV and (f) 3.1 eV excitation energy.

Table S1. The Absorption cross-sections of Mn doped CsPbI₃ at 400 nm, 500 nm and 570 nm. The values for 500 nm and 570 nm are calculated combining the absorption cross-section at 400 nm and absorption spectra in Figure 1c.

	0%	5%	7%	10%
400 nm (3.10 eV)	$4.2 \times 10^{-14} \text{ cm}^2$	$6.0 \times 10^{-14} \text{ cm}^2$	$8.0 \times 10^{-14} \text{ cm}^2$	$1.4 \times 10^{-14} \text{ cm}^2$
500 nm (2.48 eV)	$1.5 \times 10^{-14} \text{ cm}^2$	$2.0 \times 10^{-14} \text{ cm}^2$	$2.8 \times 10^{-14} \text{ cm}^2$	$0.5 \times 10^{-14} \text{ cm}^2$
570 nm (2.18 eV)	$0.7 \times 10^{-14} \text{ cm}^2$	$0.9 \times 10^{-14} \text{ cm}^2$	$1.2 \times 10^{-14} \text{ cm}^2$	$0.2 \times 10^{-14} \text{ cm}^2$

Table S2. Fit parameters for time-dependent carrier temperature of undoped CsPbI₃ NCs with 400 nm excitation at different intensities $n \approx 3.5 \times 10^{17}$ (I₁), 1.7×10^{18} (I₂), 3.5×10^{18} (I₃) and 6.9×10^{18} (I₄) photon/cm²/pulse, corresponding to $\langle N \rangle \approx 0.7, 3.7, 6.7$ and 13.5 , respectively. The unit of time t is *ps*.

	A ₁	t ₁	A ₂	t ₂	A ₃	t ₃	t _{ave}
I ₁	0.77	0.2	0.22	0.7	0.02	19.2	9.9
I ₂	0.74	0.7	0.21	0.7	0.05	24.0	16.4
I ₃	0.60	0.6	0.35	0.6	0.06	20.8	14.1
I ₄	0.56	0.9	0.32	0.9	0.13	5.4	3.0

Table S3. Fit parameters for time-dependent carrier temperature of Mn doped CsPbI₃ NCs with 400 nm excitation at different intensities $n \approx 5.3 \times 10^{17}$ (I₁), 2.7×10^{18} (I₂), 5.3×10^{18} (I₃) and 1.1×10^{19} (I₄) photon/cm²/pulse, corresponding to $\langle N \rangle \approx 1.0, 4.8, 9.6$ and 19.2 , respectively. The unit of time t is *ps*.

	A ₁	t ₁	A ₂	t ₂	A ₃	t ₃	t _{ave}
I ₁	0.97	0.1	0.03	0.4	0.0005	29.4	3.8
I ₂	0.97	0.7	0.03	14.0	-	-	8.3
I ₃	0.93	0.6	0.07	17.7	-	-	12.2
I ₄	0.89	0.8	0.11	12.4	-	-	8.2

Table S4. Fit parameters for time-dependent carrier temperature of undoped CsPbI₃ NCs with 500 nm excitation at different intensities $n \approx 3.0 \times 10^{17}$ (I₁), 1.5×10^{18} (I₂), 3.0×10^{18} (I₃) and 4.4×10^{19} (I₄) photon/cm²/pulse, corresponding to $\langle N \rangle \approx 0.6, 2.9, 5.8$ and 8.7 , respectively. The unit of time t is *ps*.

	A ₁	t ₁	A ₂	t ₂	A ₃	t ₃	t _{ave}
I ₁	0.94	0.4	0.06	4.1	-	-	1.8
I ₂	0.89	0.5	0.11	27.4	-	-	23.7
I ₃	0.84	0.6	0.16	23.2	-	-	20.2
I ₄	0.87	0.7	0.13	12.7	-	-	9.7

Table S5. Fit parameters for time-dependent carrier temperature of Mn doped CsPbI₃ NCs with 500 nm excitation at different intensities $n \approx 4.2 \times 10^{17}$ (I₁), 2.1×10^{18} (I₂), 4.2×10^{18} (I₃) and 6.4×10^{18} (I₄) photon/cm²/pulse, corresponding to $\langle N \rangle \approx 0.8, 3.9, 7.7$ and 11.5 , respectively. The unit of time t is *ps*.

	A ₁	t ₁	A ₂	t ₂	A ₃	t ₃	t _{ave}
I ₁	1	0.6	-	-	-	-	0.6
I ₂	0.93	0.6	0.07	18.8	-	-	13.1
I ₃	0.86	0.7	0.14	21.4	-	-	17.9
I ₄	0.86	0.6	0.14	11.7	-	-	9.0

Table S6. Fit parameters for time-dependent carrier temperature of undoped CsPbI₃ NCs with 570 nm excitation at different intensities $n \approx 2.6 \times 10^{17}$ (I₁), 7.9×10^{17} (I₂), 1.8×10^{18} (I₃) and 2.9×10^{18} (I₄) photon/cm²/pulse, corresponding to $\langle N \rangle \approx 0.5, 1.5, 3.6$ and 5.6 , respectively. The unit of time t is *ps*.

	A ₁	t ₁	A ₂	t ₂	A ₃	t ₃	t _{ave}
I ₁	0.95	0.1	0.05	0.7	-	-	0.3
I ₂	1	0.5	-	-	-	-	0.5
I ₃	0.82	0.7	0.18	71	-	-	67.9
I ₄	0.87	0.5	0.13	16.8	-	-	14.1

Table S7. Fit parameters for time-dependent carrier temperature of Mn doped CsPbI₃ NCs with 570 nm excitation at different intensities $n \approx 3.6 \times 10^{17}$ (I₁), 1.1×10^{18} (I₂), 2.5×10^{18} (I₃) and 4.0

$\times 10^{18}$ (I_4) photon/cm²/pulse, corresponding to $\langle N \rangle \approx 0.7, 2.0, 4.6$ and 7.2 , respectively. The unit of time t is ps .

	A_1	t_1	A_2	t_2	A_3	t_3	t_{ave}
I_1	1	0.4	-	-	-	-	0.4
I_2	1	0.6	-	-	-	-	0.6
I_3	0.92	0.1	0.05	0.9	0.03	49.4	45.6
I_4	0.81	0.7	0.19	12.1	-	-	9.8

Table S8. Fit parameters for time-dependent carrier temperature of Mn doped CsPbI₃ NCs with 400 nm excitation at different doping concentration. $n \approx 3.5 \times 10^{17}$ (0%), 5.3×10^{17} (5%), 8.0×10^{17} (7%) and 2.9×10^{17} (10%) photon/cm²/pulse, corresponding to $\langle N \rangle \approx 0.7, 1.0, 1.2$ and 0.2 , respectively. The unit of time t is ps .

	A_1	t_1	A_2	t_2	A_3	t_3	t_{ave}
0%	0.85	0.2	0.15	0.9	-	-	0.5
5%	0.97	0.1	0.03	0.5	-	-	0.2
7%	0.91	0.1	0.09	0.4	-	-	0.2
10%	0.97	0.3	0.03	1.4	-	-	0.5

Table S9. Fit parameters for time-dependent carrier temperature of Mn doped CsPbI₃ NCs with 500 nm excitation at different doping concentration. $n \approx 3.0 \times 10^{17}$ (0%), 4.2×10^{17} (5%), 6.7×10^{17}

(7%) and 2.5×10^{17} (10%) photon/cm²/pulse, corresponding to $\langle N \rangle \approx 0.6, 0.8, 1.1$ and 0.2 , respectively. The unit of time t is ps .

	A ₁	t ₁	A ₂	t ₂	A ₃	t ₃	t _{ave}
0%	0.94	0.1	0.06	4.1	-	-	1.8
5%	1	0.6	-	-	-	-	0.6
7%	1	0.4	-	-	-	-	0.4
10%	0.95	0.1	0.03	0.2	0.02	0.5	0.1

Table S10. Fit parameters for time-dependent carrier temperature of Mn doped CsPbI₃ NCs with 570 nm excitation at different doping concentration. $n \approx 2.6 \times 10^{17}$ (0%), 3.6×10^{17} (5%), 5.5×10^{17} (7%) and 1.9×10^{17} (10%) photon/cm²/pulse, corresponding to $\langle N \rangle \approx 0.5, 0.7, 0.9$ and 0.1 , respectively. The unit of time t is ps .

	A ₁	t ₁	A ₂	t ₂	A ₃	t ₃	t _{ave}
0%	0.95	0.1	0.05	0.7	-	-	0.3
5%	1	0.4	-	-	-	-	0.4
7%	1	0.6	-	-	-	-	0.6
10%	0.55	0.3	0.42	0.4	0.03	2.0	0.6

Table S11. Fit parameters of Figure S21 for carrier temperature decay kinetics of Mn-doped CsPbI₃ NCs (N≤1) with 400 nm and 570 nm excitation at low intensity (N≤1). The unit of time t is ps .

Exc. Wavelength		A ₁	t ₁	A ₂	t ₂	t _{ave}
400 nm	Undoped	0.85	0.2	0.15	0.9	0.5
	Doped	0.97	0.1	0.03	0.5	0.2
500 nm	Undoped	0.94	0.1	0.06	4.1	1.8
	Doped	1	0.6	-	-	0.6
570 nm	Undoped	0.95	0.1	0.05	0.7	0.3
	Doped	1	0.4	-	-	0.4

References

- (1) Perdew, J. P.; Burke, K.; Ernzerhof, M. Generalized Gradient Approximation Made Simple. *Phys. Rev. Lett.* **1996**, *77*, 3865–3868.
- (2) Kresse, G.; Hafner, J. Ab Initio Molecular Dynamics for Liquid Metals. *Phys. Rev. B* **1993**, *47*, 558–561.
- (3) Blöchl, P. E. Projector Augmented-Wave Method. *Phys. Rev. B* **1994**, *50*, 17953–17979.
- (4) Welter, E.; Chernikov, R.; Herrmann, M.; Nemausat, R. A Beamline for Bulk Sample X-Ray Absorption Spectroscopy at the High Brilliance Storage Ring PETRA III. *AIP Conf. Proc.* **2019**, *2054*, 1–6.

Paper V



Article type: Full Paper

Spatially Resolved Local Electronic Properties of Two-Dimensional Lead Halide Perovskite Single Crystals Studied by X-ray Photoemission Electron Microscopy

Mingli Liang,[†] Weihua Lin,[†] Qian Zhao, Lin Zhu, Brice Sarpi, Alexei Zakharov, Tõnu Pullerits, Yuran Niu, Sophie E. Canton*, and Kaibo Zheng**

Dr. M. Liang, Q. Zhao, Dr. K. Zheng, Dr. S. E. Canton

Department of Chemistry, Technical University of Denmark, DK-2800 Kongens Lyngby, Denmark.

Email: kzheng@kemi.dtu.dk; secanton03@yahoo.com; yuran.niu@maxiv.lu.se

W. Lin, Prof. T. Pullerits, Dr. K. Zheng

Chemical Physics and NanoLund, Lund University, Box 124, 22100 Lund, Sweden

Dr. L. Zhu, Dr. B. Sarpi, Dr. A. Zakharov, Dr. Y. Niu

MAX IV Laboratory, Lund University, P.O. Box 118, 22100 Lund, Sweden

Keywords: 2D lead halide perovskite, edge state, lattice mismatch, local electronic property, X-ray photoemission electron microscopy

Recently, the research on the edge state of two-dimensional (2D) lead halide perovskites (LHPs) has been attracting much attention. Lower-energy edge state (LES) is believed to provide an efficient pathway for the dissociation of photo-excited excitons. However, the mechanism of the edge state formation remains controversial, and studies that precisely positioned local electronic properties are lacking. Herein, we present the first study of spatially resolved core level electronic structures, especially at the edge area of the 2D LHP crystals by X-ray photoemission electron microscopy (XPEEM). The results show that blue shifts occur in the Pb 5d core levels at the edge area, which becomes more pronounced as n varies from 1 to 3 (~ 0.2 to 1.0 eV). This phenomenon is attributed to the lattice expansion induced by mechanical strain release at the edge area. Furthermore, we expounded on the relationships between the local structure and electronic properties by the lattice mismatch theory. This work provides an important reference on the origin of the edge state of 2D LHPs and is beneficial for future optoelectronic device applications.

1. Introduction

Two-dimensional (2D) lead halide perovskites (LHPs) are a class of quantum well (QW)-like materials described by the formula $(B)_2(A)_{n-1}Pb_nX_{3n+1}$, where B is a long-chain organic spacing cation, A is a small cation, X is a halogen ion (Cl^- , Br^- , and I^-), n is the number of octahedral layers and determines the QW thickness.^[1-3] In recent years, 2D LHPs have been extensively studied due to their excellent photo- and chemical stability coupled with good performance in optoelectronic devices (e.g. solar cells, light-emitting diodes (LEDs), photodetectors, *etc.*), which emerged as a potential alternative to 3D LHPs.^[4-11] In addition, unlike the classical 3D perovskite structure, the integral structural anisotropy of 2D LHPs makes their photophysics highly correlated with the local structures. Of great interest is the lower-energy edge state (LES) of 2D LHPs, which is observed at the edge area of the crystal. It was believed to facilitate the dissociation of photo-generated excitons, thus, further improving the performance of optoelectronic devices.^[12-14]

However, since first reported by Blancon *et al.*, the detailed formation mechanism of LES remains controversial. In the subsequent work from Mikaël and Blancon *et al.*, they attributed the formation of LES to the release of mechanical energy arising from the interface lattice mismatch at the edge area by creating a generic elastic model.^[15] Such model also predicts that there will be significant LES only when $n \geq 3$ in $(BA)_2(MA)_{n-1}Pb_nI_{3n+1}$ (BA = Butylamine, MA = Methylamine). However, LES in $(BA)_2(MA)Pb_2I_7$ ($n = 2$) was experimentally observed by other researchers.^[16-18] They attributed the formation of the edge state to the surface chemical reaction where new surface components were formed. These include the hydrodated reaction

triggered by moisture^[17], and the loss of B-site cations at the edge area^[18]. Very recently, it is also reported that LES can be manually induced by femtosecond laser treatment to ablate the surface of the crystal, which would also lead to the loss of the B-site cations.^[19]

Since the above argumentations are either based on theoretical calculation or deduction from the optical measurement, precise characterization of local electronic structures especially at the edge area of the 2D LHP crystals is urgently needed to provide more direct proof for the origin of edge states. Herein, we conducted the X-ray photoemission electron microscopy (XPEEM) study on the exfoliated $(\text{BA})_2(\text{MA})_{n-1}\text{Pb}_n\text{I}_{3n+1}$ ($n = 1, 2, 3$) fresh single crystal flakes to establish a spatial resolution of elementary compositions as well as electronic structures between the bulk area and edge area. We found that the binding energies of Pb 5d core levels at the edge area shift to the high energy (blue-shift) compared with that at the bulk area. Such a shift becomes more predominant with the increasing n values. On the other hand, the I 4d core levels exhibit negligible differences between bulk area and edge area. The blue-shifts of Pb core levels can be well rationalized by the lattice expansion at the edge area, which supports the lattice mismatch theory that interprets the formation of edge state in 2D LHP crystals.

2. Experimental Section

2.1 Chemicals

PbI_2 (99 %), MAI (98 %), BAI (98 %), hypophosphorous acid solution (50 %, H_3PO_2 in water), and hydroiodic acid (57 %, HI in water) have been utilized without further treatment. All the chemicals were supplied by Sigma-Aldrich.

2.2 Synthesis of 2D LHP Single Crystals

The cm-scale crystals of $(\text{BA})_2(\text{MA})_{n-1}\text{Pb}_n\text{I}_{3n+1}$ ($n = 1, 2, 3$) were obtained by the temperature gradient growth method.^{[20] [21]} PbI_2 , MAI, BAI, hydroiodic acid (5 ml), and hypophosphorous acid solution (0.25 ml) were initially formulated as the precursor solutions in 20 ml glass bottles. To prepare three samples with different n values ($n = 1, 2, 3$), the $\text{PbI}_2/\text{MAI}/\text{BAI}$ contents are varied to be 1.5/0.0/2.0 mmol, 1.5/1.5/2.0 mmol, and 1.5/2.5/2.0 mmol, respectively. The precursor solutions were then sealed and stirred for 30 min at room temperature. After that, they were heated at 80 °C until the solutions become completely clear, followed by a slow cooling process from 55 °C at a rate of -5 °C/day. The bulk crystals can finally be obtained after about one week of the recrystallization process (**Figure S1**). The as-obtained dried crystals were directly vacuum-sealed for further characterization.

2.3 Powder X-ray Diffraction (XRD) and UV-vis Absorption Measurements

To verify the purity of the bulk crystals, powder XRD data were collected on a Rigaku MiniFlex 136 II diffractometer using $\text{Cu-K}\alpha$ radiation with $\lambda = 1.5406 \text{ \AA}$. The results showed that all three samples were pure in phase (**Figure S1**). Furthermore, the UV-vis absorption spectra were used to study the absorption edges and optical bandgaps (**Figure 1b and c**), they were measured from PerkinElmer (Lambda 1050) at room temperature.

2.4 Low-energy Electron Diffractions (LEEDs) and XPEEM Measurements

The LEED and XPEEM patterns were measured in a spectroscopic photoemission and low energy electron microscope (SPELEEM III, Elmitec) in MAXPEEM beamline at the MAX-IV laboratory in Lund, Sweden. The instrument has a single-digit nanometer spatial resolution.

Before being placed in the loadlock of the microscope, the surface of the 2D LHP crystal was attached to a tape, while the other end of the tape is fixed on the surface of the loadlock. After pumping down the loadlock, the sample holder was taken out from the loadlock by a transfer arm, the tape was then automatically removed from the sample surface. By using this method, a cleaved clean surface was obtained. Finally, the sample was transferred quickly into the main chamber that has a base pressure better than 1×10^{-10} torr for further analysis. LEED patterns were taken at start voltage of 10 eV. The kinetic energy was corrected to be 9.86 eV with a small difference of 0.14 eV due to the relation between the sample's work function and the gun's electron. XPEEM patterns were measured with a low X-ray photon energy of 80 eV.

3. Results and Discussion

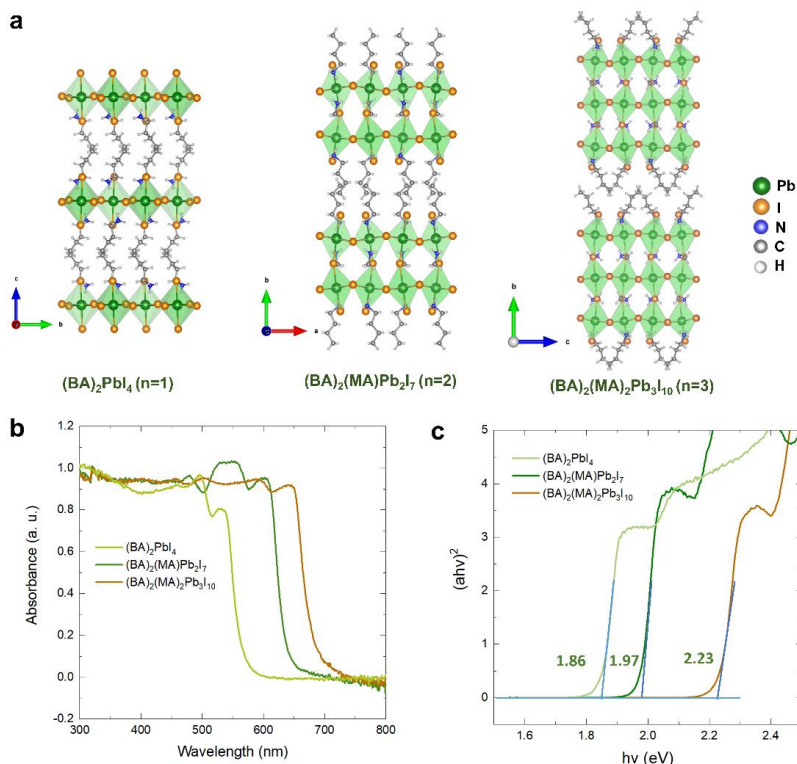


Figure 1. The structures of the $(\text{BA})_2(\text{MA})_{n-1}\text{Pb}_n\text{I}_{3n+1}$ ($n=1, 2, 3$) established from their crystallographic data extracted from the Cambridge Crystallographic Data Centre (CCDC) (CCDC No.: 1879292, 252315, 252316, respectively).^{[22] [2]} (a); UV-vis absorption spectra (b) and Tauc-plot representing the optical bandgap (c) of the three samples.

Figure 1a showed the ball-and-stick structural models of $(\text{BA})_2(\text{MA})_{n-1}\text{Pb}_n\text{I}_{3n+1}$ ($n=1, 2, 3$), respectively. The perfect agreement between our measured powder XRD spectra and the simulated powder XRD spectra from their crystallographic data confirms the phase purity of our as-synthesized crystals (**Figure S1**). The optical bandgaps of the 2D perovskites are dominated by the n -values (i.e. thickness of the 2D layers) which modulate the quantum confinement of the 2D quantum wells. This can be confirmed by the red-shift of the absorption band edges with the increasing n values as shown in **Figure 1b** [556.1 nm ($n=1$), 629.4 nm ($n=2$), and 666.7 nm ($n=3$)]. Their optical bandgaps can be calculated from the Tauc-plot to

be 2.23 eV, 1.97 eV, and 1.86 eV, respectively (**Figure 1c**), which correspond well with the reports in the literature.^[2]

Before being placed in the vacuum chamber for the XPEEM measurement, we peeled off the surfaces of the bulk crystals more than three times and transferred the obtained fresh flakes onto a silicon substrate using scotch tapes (**Figure S2**). The dispersed crystals are then exfoliated again when transferring into the main chamber in order to preserve the fresh surface for the measurement. These flakes are about 0.5-2.0 μm in thickness with lateral dimensions in hundreds of micrometers as confirmed by scanning electron microscope (SEM) images (**Figure S3**).

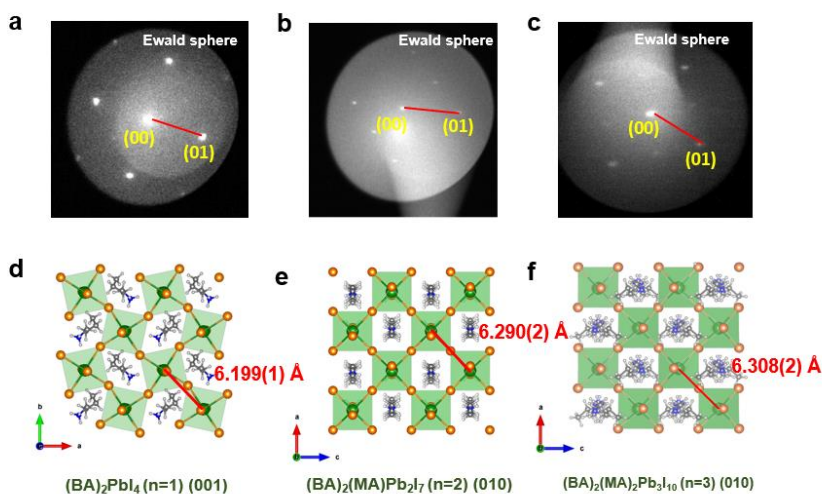


Figure 2. LEED patterns of $(\text{BA})_2(\text{MA})_{n-1}\text{Pb}_n\text{I}_{3n+1}$ ($n=1, 2, 3$) (a-c); and the corresponding crystal facets of their structures: (001) facet of $n = 1$, (010) facets of $n = 2, 3$ (d-f).

In order to confirm whether the long-range lattice order of the single crystal flakes still retains after exfoliation, we first conducted LEED measurements of all three samples. As seen in **Figure 2a** to **c**, the clear brag diffraction points of all three samples indicate intact crystallinity

of the crystal surfaces. The primary lattice vectors can be calculated via the comparison of the average distance from the central (00) spot to four (01) spots and the radius of Ewald sphere. The results show that the (00)-(01) distances of the three samples are close to 6.2 \AA , which are consistent with theoretical Pb-to-Pb distances at (001) facet of $(\text{BA})_2\text{PbI}_4$ ($n=1$),^[2] (010) facet of $(\text{BA})_2(\text{MA})\text{Pb}_2\text{I}_7$ ($n=2$), and (010) facet of $(\text{BA})_2(\text{MA})_2\text{Pb}_3\text{I}_{10}$ ($n=3$)^[22] (i.e. $6.199(1)$, $6.290(2)$, $6.308(2) \text{ \AA}$ for $(\text{BA})_2(\text{MA})_{n-1}\text{Pb}_n\text{I}_{3n+1}$ ($n=1, 2, 3$) (**Figure 2d-f**).

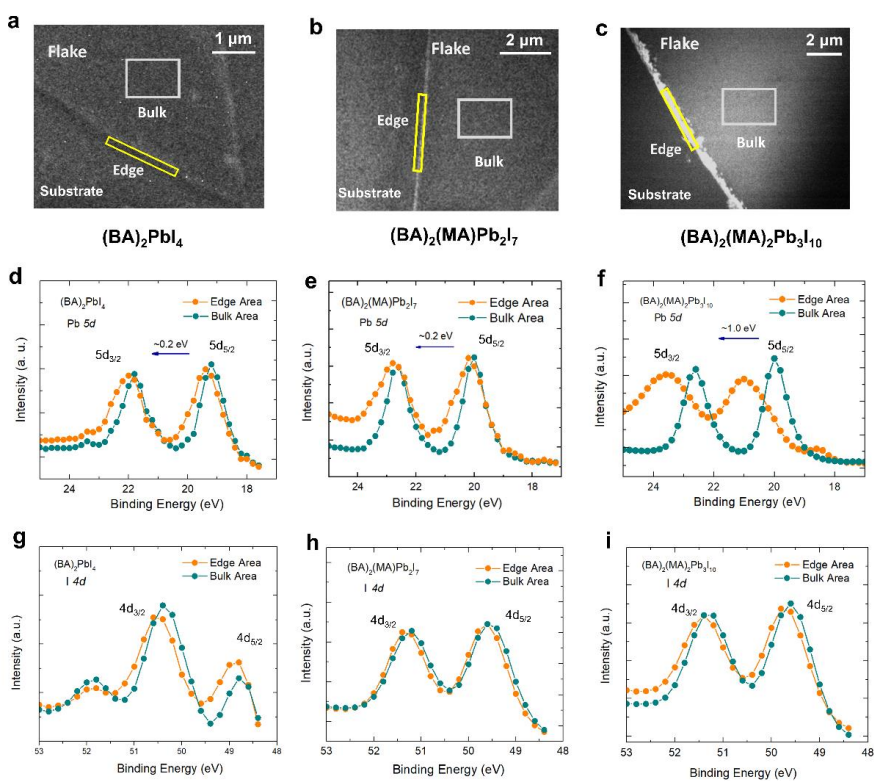


Figure 3. XPEEM mapping images of $(\text{BA})_2(\text{MA})_{n-1}\text{Pb}_n\text{I}_{3n+1}$ flakes ($n=1, 2, 3$) (a-c); Pb 5d (d-f) and I 4d (g-i) core level mission spectra at both bulk and edge area of them.

Next, we established the spatial resolution of the local electronic structures by mapping the element core level emission of individual single crystals for all three samples via XPEEM with

special focus on Pb 5d and I 4d core levels. **Figure 3a-c** show the typical XPEEM mapping images at a binding energy of 20.0 eV for a single crystal flake of $(\text{BA})_2(\text{MA})_{n-1}\text{Pb}_n\text{I}_{3n+1}$ ($n=1, 2, 3$), respectively. The noticeable contrast of the emission intensity between bulk and edge areas indicates distinguished electronic structures. We then selected two rectangle zones in each flake to represent these two areas, where the representative Pb 5d and I 4d core level spectra were extracted for comparison as exhibited in **Figure 3d-i**. The detailed peak positions of all core level emissions have also been summarized in **Table 1**. For $(\text{BA})_2\text{PbI}_4$ ($n = 1$), the Pb 5d core level emission at the edge area shifted slightly to higher binding energies (blue-shift) by ~ 0.2 eV compared to that at the bulk area (**Figure 3d**). For $(\text{BA})_2(\text{MA})\text{Pb}_2\text{I}_7$ ($n = 2$), the same blue-shift of the Pb 5d core level at the edge area can be observed with a similar value of ~ 0.2 eV considering the energy resolution (0.2 eV) of the setup (**Figure 3e**). However, in $(\text{BA})_2(\text{MA})_2\text{Pb}_3\text{I}_{10}$ ($n = 3$), such blue-shift of Pb 5d emission is drastically increased to be ~ 1.0 eV (**Figure 3f**). On the other hand, the I 4d core level emissions at the edge areas of all three samples have negligible blue-shifts ($\ll 0.2$ eV) regardless of the n values (**Figure 3g-i**). Overall, as the thickness of the PbI_6 octahedral layers increases ($n = 1$ to 3) the blue-shift of Pb 5d core level emissions at the edge areas increases, while the I 4d core level emission remains constant independent of the n values.

Table 1. The Binding Energies (eV) of Pb 5d and I 4d core levels at the edge area and bulk area of all three samples. (The energy resolution is 0.2 eV)

Samples	Bulk area		Edge area		Bulk area		Edge area	
	Pb 5d _{5/2}	Pb 5d _{3/2}	Pb 5d _{5/2}	Pb 5d _{3/2}	I 4d _{5/2}	I 4d _{3/2}	I 4d _{5/2}	I 4d _{3/2}
$(\text{BA})_2\text{PbI}_4$ ($n = 1$)	19.2	21.8	19.4	22.0	49.6	51.2	49.6	51.2

$(\text{BA})_2(\text{MA})\text{Pb}_2\text{I}_7$ ($n = 2$)	20.0	22.6	20.2	22.8	49.6	51.2	49.6	51.2
$(\text{BA})_2(\text{MA})_2\text{Pb}_3\text{I}_{10}$ ($n = 3$)	20.0	22.6	21.0	23.6	49.6	51.2	49.6	51.2

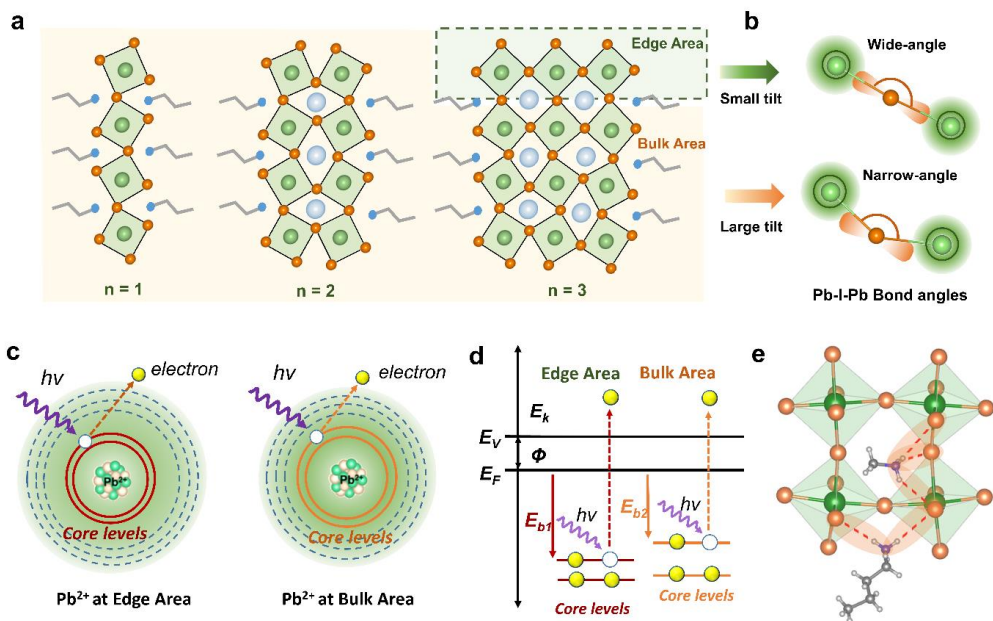


Figure 4. Schematic diagrams of local structures of both bulk and edge areas (a), and the diagrams of the effect of Pb-I-Pb tilting angles on the hybrid orbitals ($n = 3$) (b). Schematic diagram of electron escape from the core levels (c, d); Here, $h\nu$ is the energy of the X-ray photon, E_k is the kinetic energy of photoelectrons, E_{b1} and E_{b2} are the binding energy of Pb core levels at edge and bulk areas, E_F is the Fermi level, E_V is the vacuum level, Φ is the work function. N-H...I hydrogen bond interactions between N and I (e).

In order to rationalize the blue-shifts of Pb 5d core levels, we first exclude the changes in the chemical composition at the edge area. The coordination among Pb and I atoms in the lattice is mainly established via Pb-I metavalent bonds with Pb as electron donor and I as electron acceptor. In this scenario, any composition changes that lead to the deviation of the Pb to I ratio (e.g. the formation of PbI_x compounds or 3D MAPbI_3), an opposite shift of the Pb 5d and I 4d core levels should be observed with response to the modification of the charge transfer degree

in a D-A system, which is not the case here. On the other hand, the asymmetric shifts of Pb 5d and I 4d core levels at the edge state can be well rationalized via the Mikael's lattice mismatch theory^[15]. As shown in **Figure 4a**, in the 2D perovskite structures, the lattice strains accumulate within the inorganic layers and would be released differently along in-plane and out-of-plane directions. Along the out-of-plane direction (i.e. perpendicular to the 2D layers), the lattice strain is periodically relaxed by the soft organic spacer layers, while along the in-plane direction (i.e. parallel to the 2D layers) is accumulated within a long distance and can be released at the edge area. According to the lattice mismatch theory, such release of the mechanical energy results in the lattice expansion at the edge area. This can be manifested as a reduction in PbI_6 octahedral tilting (Pb-I-Pb bond angles are closer to 180°), and results in the formation of edge state.^[15] In addition, the edge state formation is strongly determined by the n value. When the octahedral layers are thin (i.e. $n = 1$ or 2), the in-plane lattice strain accumulation can largely be buffered by the organic spacer layers diminishing the edge state formation. Consequently, the lattice conformation of the PbI_6 octahedra at the edge state is more identical to that at the bulk state.

Figure 4b demonstrates the effect of Pb-I-Pb tilting angles on the hybrid orbitals in both bulk and edge areas when the n value is large ($n = 3$). At the edge area, the near-linear Pb-I-Pb angles (i.e. 180°) enhance the overlap between the Pb and I outer electron orbitals. This means that the Coulomb attraction of the Pb nucleus to core level electrons becomes stronger leading to the higher electron density. Therefore, at the edge states core level electrons are more difficult to delocalize with larger binding energy (**Figure 4c**). In this way, Pb 5d core level emission should

exhibit a significant blue-shift as summarized in **Figure 4d**, where the binding energy of edge state (E_{b1}) is bigger than that of bulk state (E_{b2}). On the contrary, the I 4d core levels are identical between bulk and edge areas in all samples. We believe it is due to the contribution of N-H...I hydrogen bonds between N and I that could balance the charge reorganization within the Pb-I metavalent bonds as shown in **Figure 4e**. Therefore, they are not significantly affected by the n value and local structures. A similar phenomenon also appeared in our previous XPS measurements on two 2D perovskite structures with the similar Pb halide compositions but different PbI_6 octahedra conformations.^[23]

In summary, we obtained spatial resolution of element core level emission of 2D LHP fresh crystal flakes via the XPEEM. XPEEM results show that at the edge area of 2D LHPs, the binding energies of the Pb 5d core levels are shifted to higher energy with the I 4d core level unchanged compared with bulk area. As the n value increases (from 1 to 3), such blue-shift increases from ~ 0.2 to ~ 1.0 eV. We have explained the blue-shift using the lattice mismatch theory caused by the lattice expansion at the edge area of the 2D perovskite crystals. This work provides an important reference to guide 2D perovskite engineering and device applications in the future.

Supporting Information

Supporting Information is available from the Wiley Online Library or from the author.

Acknowledgements

M. L and W. L. contributed equally to this work. This work was funded by the Danish Council for Independent Research (No. 7026-0037B), Swedish Research Council (No. 2017-05337), Crafood foundation (no. 20200522), Swedish Energy Agency research grant, and Research Fund for International Young Scientists from NSFC, China (no. 21950410515) (K. Z.).

Received: ((will be filled in by the editorial staff))

Revised: ((will be filled in by the editorial staff))

Published online: ((will be filled in by the editorial staff))

References

- [1] L. Mao, C. C. Stoumpos, M. G. Kanatzidis, *J. Am. Chem. Soc.* **2019**, *141*, 1171.
- [2] C. C. Stoumpos, D. H. Cao, D. J. Clark, J. Young, J. M. Rondinelli, J. I. Jang, J. T. Hupp, M. G. Kanatzidis, *Chem. Mater.* **2016**, *28*, 2852.
- [3] Y. Chen, Y. Sun, J. Peng, J. Tang, K. Zheng, Z. Liang, *Adv. Mater.* **2018**, *30*, 1703487.
- [4] H. Tsai, W. Nie, J. C. Blancon, C. C. Stoumpos, R. Asadpour, B. Harutyunyan, A. J. Neukirch, R. Verduzco, J. J. Crochet, S. Tretiak, L. Pedesseau, J. Even, M. A. Alam, G. Gupta, J. Lou, P. M. Ajayan, M. J. Bedzyk, M. G. Kanatzidis, *Nature* **2016**, *536*, 312.
- [5] Z. Wang, Q. Lin, F. P. Chmiel, N. Sakai, L. M. Herz, H. J. Snaith, *Nat. Energy* **2017**, *2*, 17135.
- [6] F. Yuan, X. Zheng, A. Johnston, Y. K. Wang, C. Zhou, Y. Dong, B. Chen, H. Chen, J. Z. Fan, G. Sharma, P. Li, Y. Gao, O. Voznyy, H. T. Kung, Z.H. Lu, O. M. Bakr, E. H. Sargent, *Sci. Adv.* **2020**; *6*, eabb0253.
- [7] K. Zheng, Y. Chen, Y. Sun, J. Chen, P. Chábera, R. Schaller, M. J. Al-Marri, S. E. Canton, Z. Liang, T. Pullerits, *J. Mater. Chem. A* **2018**, *6*, 6244.
- [8] N. Zhou, Y. Shen, L. Li, S. Tan, N. Liu, G. Zheng, Q. Chen, H. Zhou, *J. Am. Chem. Soc.* **2018**, *140*, 459.
- [9] Y. Chen, Y. Sun, J. Peng, W. Zhang, X. Su, K. Zheng, T. Pullerits, Z. Liang, *Adv. Energy Mater.* **2017**, *7*, 1700162.
- [10] J. Gu, R. Ji, W. Xu, C. Yin, K. Wen, H. Gao, R. Yang, Z. Pan, K. Wang, C. Zhang, R. Li, J. Lin, L. Xie, J. Wang, W. Huang, *Solar RRL* **2020**, *4*, 2000184.
- [11] J. Y. Ye, J. Tong, J. Hu, C. Xiao, H. Lu, S. P. Dunfield, D. H. Kim, X. Chen, B. W. Larson, J. Hao, K. Wang, Q. Zhao, Z. Chen, H. Hu, W. You, J. J. Berry, F. Zhang, K. Zhu, *Solar RRL* **2020**, *4*, 2000082.
- [12] J. C. Blancon, H. Tsai, W. Nie, C. C. Stoumpos, L. Pedesseau, C. Katan, M. Kepenekian, C. M. M. Soe, K. Appavoo, M. Y. Sfeir, S. Tretiak, P. M. Ajayan, M. G. Kanatzidis, J. Even, J. J. Crochet, A. D. Mohite, *Science* **2017**, *355*, 1288.
- [13] Z. Zhang, W. H. Fang, R. Long, O. V. Prezhdo, *J. Am. Chem. Soc.* **2019**, *141*, 15557.
- [14] K. Wang, C. C. Wu, Y. Y. Jiang, D. Yang, K. Wang, S. Priya, *Sci. Adv.* **2019**, *5*, 3241.

- [15]M. Kepenekian, B. Traore, J. C. Blancon, L. Pedesseau, H. Tsai, W. Nie, C. C. Stoumpos, M. G. Kanatzidis, J. Even, A. D. Mohite, S. Tretiak, C. Katan, *Nano. Lett.* **2018**, *18*, 5603.
- [16]J. Bao, V. G. Hadjiev, *Nano. Lett.* **2019**, *11*, 26.
- [17]E. Shi, S. Deng, B. Yuan, Y. Gao, Akriti, L. Yuan, C. S. Davis, D. Zemlyanov, Y. Yu, L. Huang, L. Dou, *ACS Nano.* **2019**, *13*, 1635.
- [18]C. Zhao, W. Tian, J. Leng, Y. Zhao, S. Jin, *J. Phys. Chem. Lett.* **2019**, *10*, 3950.
- [19]Y. Miao, Z. Xiao, Z. Zheng, D. Lyu, Q. Liu, J. Wu, Y. Wu, X. Wen, L. Shui, X. Hu, K. Wang, Z. Tang, X. F. Jiang, *Adv. Sci.* **2022**, *9*, e2201046.
- [20]S. Wang, L. Li, W. Weng, C. Ji, X. Liu, Z. Sun, W. Lin, M. Hong, J. Luo, *J. Am. Chem. Soc.* **2020**, *142*, 55.
- [21]M. Liang, W. Lin, Q. Zhao, X. Zou, Z. Lan, J. Meng, Q. Shi, I. E. Castelli, S. E. Canton, T. Pullerits, K. Zheng, *J. Phys. Chem. Lett.* **2021**, *12*, 4965.
- [22]M.-H. Jung, *CrystEngComm* **2021**, *23*, 1181.
- [23]M. Liang, W. Lin, Z. Lan, J. Meng, Q. Zhao, X. Zou, I. E. Castelli, T. Pullerits, S. E. Canton, K. Zheng, *ACS Appl. Electron. Mater.* **2020**, *2*, 1402.

Supporting Information

Spatially Resolved Local Electronic Properties of Two-Dimensional Lead Halide Perovskite Crystals Studied by X-ray Photoemission Electron Microscopy

Mingli Liang,[†] Weihua Lin,[†] Qian Zhao, Lin Zhu, Brice Sarpi, Alexei Zakharov, Tõnu Pullerits, Yuran Niu*, Sophie E. Canton*, and Kaibo Zheng*

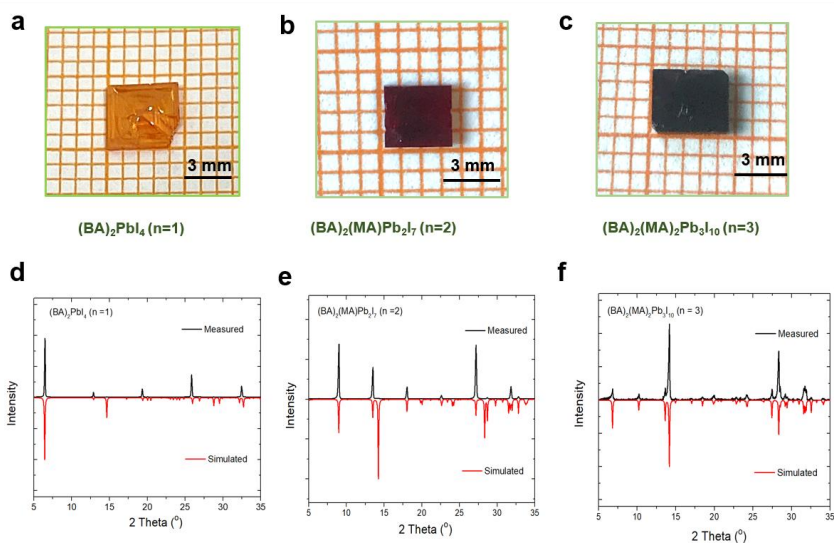


Figure S1 The obtained cm-scale crystals of $(\text{BA})_2(\text{MA})_{n-1}\text{Pb}_n\text{I}_{3n+1}$ ($n=1, 2, 3$) (a-c); and their comparison between the measured powder XRD and simulated powder XRD from crystallographic data (CCDC No.: 1879292, 252315, 252316), respectively (d-f)

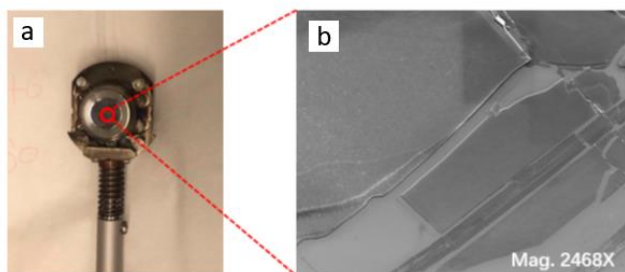


Figure S2 The sample holder with Si as a substrate (a); single crystal flakes dispersed on the substrate (b).

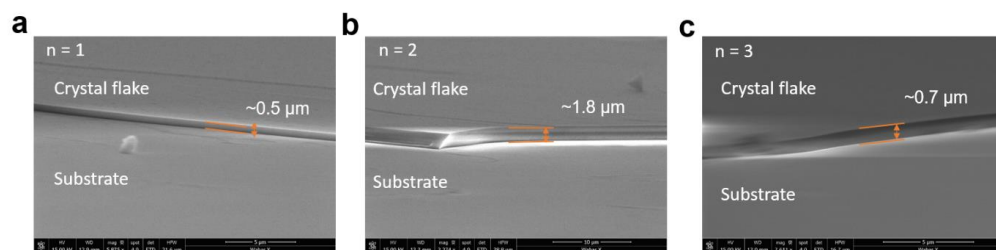


Figure S3 SEM sectional view of the single crystal flakes of $(\text{BA})_2(\text{MA})_{n-1}\text{Pb}_n\text{I}_{3n+1}$ ($n = 1, 2, 3$), respectively (a-c).



Faculty of Science
Department of Chemistry
Division of Chemical Physics

ISBN 978-91-7422-916-5

